

UC Berkeley

UC Berkeley Electronic Theses and Dissertations

Title

Applications of Nanotechnology to the Life Sciences

Permalink

<https://escholarship.org/uc/item/5sn92179>

Author

Dunn, Gabriel

Publication Date

2017

Peer reviewed|Thesis/dissertation

Applications of Nanotechnology to the Life Sciences

By
Gabriel Dunn

A dissertation submitted in partial satisfaction of the
Requirements for the degree of
Doctor of Philosophy
in
Physics
in the
Graduate Division
of the
University of California, Berkeley

Committee in charge:

Professor Alex Zettl, Chair
Professor Mike DeWeese
Professor Michel Maharbiz

Fall 2017

Abstract

Applications of Nanotechnology to the Life Sciences

by

Gabriel Purvin Dunn

Doctor of Philosophy in Physics

University of California, Berkeley

Professor Alex Zettl, Chair

This thesis describes three experimental thrusts applying nanotechnology to develop novel tools for the life sciences.

Part I (chapters 2 and 3) covers the development of a graphene based nanofluidic platform for in-situ electron microscopy. The Graphene Flow Cell (GFC), as we have referred to it, consists of a nanofluidic channel integrated into a SiN/SiO₂/SiN stack on a Silicon chip, with a layer of graphene sealing the channel. The graphene serves as an electron transparent membrane as well as a scavenger of oxidative radicals during imaging. We discuss the fabrication and testing of the GFC, as well as a few demonstrations of its capabilities. The GFC outperforms commercial nitride cells in resolution and contrast, and allows for the introduction of reactants during imaging and precise control of sample concentration, features sealed liquid cell architectures lack. These advantages have already allowed for advances in our understanding of nanobubble geometry and stability, as well nanoparticle dynamics. Finally, we discuss some future applications and improvements for the GFC.

Part II (chapters 4 and 5) discusses work towards carbon nanotube intracellular neural electrodes. Due to their nanoscale nature, extreme aspect ratios, and unique mechanical and electrochemical properties, carbon nanotubes make an ideal electrophysiological probe. We demonstrated their capability using a single-unit probe device, and further demonstrated that such a probe is scalable, having the potential to record from a high-density of neurons in a small volume. We walk through the micro- and nano-fabrication considerations in developing such a probe, and progress we have made towards this aim. Finally, we discuss an alternative application of CNTs as neural probes, using them to bias plasmonic nanoparticles to create a voltage sensitive optical probe.

Finally, Part III (chapters 6 and 7) covers ongoing work applying atomically precise nanopores in hexagonal boron nitride (hBN) to DNA sequencing. Previous work out of our lab has demonstrated that defects in hBN introduced by electron beam irradiation grow in atomically-quantized metastable triangles. Taking advantage of this property, it is possible to produce individual triangular nanopores in hBN with atomically precise diameters. This precision allows us to create nanopores for DNA sequencing in which the pore size is tailored to the size of DNA strands. Currently, solid-state nanopore sequencing has been limited by the

speeds at which DNA passes through the pore, as well as limited blocking current signatures of the nucleotide bases. Atomically precise pores address both of these issues and will likely mark a significant advance in the field. We cover the progress we have made towards this goal, as well as aims that are still outstanding.

DEDICATION

For Caroline,

A slippery path is not feared by two people who help each other.

Table of Contents

| | |
|---|------------|
| Acknowledgements | vii |
| Chapter 1: Introduction | 1 |
| PART I: GRAPHENE-ENABLED IN-SITU ELECTRON MICROSCOPY..... | 3 |
| Chapter 2: Background – Graphene Flow Cell and Associated Liquid Cell Technology | 4 |
| 2.1 Overview | 4 |
| 2.2 Introduction..... | 5 |
| 2.3 In-Situ Transmission Electron Microscopy Background..... | 6 |
| 2.3.1 History and Devices..... | 6 |
| 2.3.2 Graphene Liquid Cell..... | 10 |
| 2.4 In-Situ TEM Nanotechnology Applications | 12 |
| 2.4.1 Nanobubbles | 12 |
| 2.4.2 Nanoparticle Dynamics..... | 18 |
| 2.4.3 Mineral Precipitation and Dissolution | 22 |
| 2.5 In-Situ TEM Biological Applications..... | 23 |
| 2.5.1 Cryo- and Stain-Based TEM..... | 23 |
| 2.5.2 Resolution in In-Situ Biological Imaging | 25 |
| 2.5.3 Contrast in In-Situ Biological Imaging..... | 26 |
| 2.5.4 Beam Damage in In-Situ Biological Imaging..... | 28 |
| 2.5.5 Graphene Liquid Cells for Biological Imaging | 29 |
| Chapter 3: Graphene-Enabled Static & Flow Cells – Fabrication and Scientific Results.... | 32 |
| 3.1 Graphene-Sealed Si/SiN Cavities | 32 |
| 3.1.1 Overview..... | 32 |
| 3.1.2 Design and Fabrication | 32 |

| | |
|---|-----------|
| 3.1.3 Results..... | 34 |
| 3.1.4 Conclusion | 38 |
| 3.2 Graphene Flow Cell | 38 |
| 3.2.1 Overview | 38 |
| 3.2.2 Fabrication | 40 |
| 3.2.2.1 Bottom Chip..... | 40 |
| 3.2.2.2 Top Chip | 44 |
| 3.2.3 Bonding..... | 46 |
| 3.2.4 Channel Wetting and Bottom Chip Improvements..... | 51 |
| 3.3 Results and Discussion | 53 |
| 3.3.1 Testing..... | 53 |
| 3.3.2 Nanobubbles | 54 |
| 3.3.3 Nanoparticle Imaging..... | 62 |
| 3.3.4 Uranyl Acetate Crystallization and Dissolution | 67 |
| 3.3.5 Stained Biological Sample Imaging..... | 69 |
| 3.4 Future Applications..... | 70 |
| 3.4.1 DNA Transcription – RNA Polymerase | 70 |
| 3.4.2 Antibody Binding on Viral Capsid | 72 |
| 3.4.3 MAC Complex on Vesicles | 75 |
| 3.4.4 Dynein on Microtubules | 77 |
| 3.5 References..... | 80 |
| | |
| PART II: CARBON NANOTUBE NEURAL PROBES | 86 |
| Chapter 4: Background – Electrophysiology and Nanoprobe..... | 87 |
| 4.1 Overview..... | 87 |
| 4.2 Introduction..... | 88 |
| 4.3 Electrophysiology | 89 |
| 4.3.1 Electrochemical Impedance | 90 |

| | |
|---|------------|
| 4.3.2 Biocompatibility | 91 |
| 4.4 Standard Neural Probes..... | 93 |
| 4.5 Nanowire Neural Probes | 97 |
| 4.6 Carbon Nanotube Properties | 102 |
| 4.6.1 Mechanical Properties..... | 102 |
| 4.6.2 Biocompatibility | 103 |
| 4.6.3 Electrochemical Properties | 104 |
| 4.6.4 CNTs as Neural Probes Examples | 106 |
| Chapter 5: Carbon Nanotube Neural Probes – Fabrication and Scientific Results..... | 108 |
| 5.1 Overview..... | 108 |
| 5.2 Single-Unit CNT Probe..... | 109 |
| 5.2.1 Direct Attachment..... | 109 |
| 5.2.2 Insulation..... | 110 |
| 5.2.3 Electrochemical Impedance Spectroscopy | 112 |
| 5.2.4 Visualization | 113 |
| 5.2.5 Precision Stage Movement | 115 |
| 5.2.6 Neurons | 116 |
| 5.2.7 CNT Probe Results | 117 |
| 5.3 Scalable Multi-Unit Array | 118 |
| 5.3.1 Tip Growth of CNTs..... | 118 |
| 5.3.2 Planar Process | 119 |
| 5.3.2.1 Microfabrication | 119 |
| 5.3.2.2 Controllable Placement of CNTs | 127 |
| 5.3.2.3 Insulation and Exposure of CNT Tip..... | 129 |
| 5.3.2.4 Selective Parylene Deposition | 130 |
| 5.3.2.5 Electrochemical Impedance Spectroscopy | 135 |
| 5.3.2.6 Cantilevered Probe..... | 138 |
| 5.4 CNT Plasmonic Push Pin..... | 140 |

| | |
|--|------------|
| 5.4.1 Proposed Experimental Methods | 143 |
| 5.5 References..... | 146 |
| | |
| PART III: BORON NITRIDE NANOPORES FOR DNA SEQUENCING..... | 155 |
| Chapter 6: Nanopores for DNA Sequencing Background | 156 |
| 6.1 Overview..... | 156 |
| 6.2 DNA Sequencing | 156 |
| 6.3 Nanopore Sequencing | 157 |
| 6.3.1 Biological Nanopores..... | 161 |
| 6.3.2 Solid-State Nanopore Sequencing | 163 |
| 6.3.2.1 2D Materials for Nanopore Sequencing | 167 |
| 6.3.2.2 hBN for Nanopore Sequencing..... | 168 |
| 6.3.2.3 Edge Functionalization | 173 |
| Chapter 7: Boron Nitride Nanopores for DNA Sequencing Fabrication and Results | 176 |
| 7.1 Overview..... | 176 |
| 7.2 Pore Fabrication | 177 |
| 7.3 Experimental Design..... | 183 |
| 7.3.1 Reservoir Chuck Design | 183 |
| 7.3.2 Electronics..... | 187 |
| 7.3.3 Setup Procedure | 190 |
| 7.4 Preliminary Results..... | 192 |
| 7.4.1 Noise | 192 |
| 7.4.2 Ionic Current | 194 |
| 7.4.3 DNA Translocation Events | 195 |
| 7.4.4 BN Nanopore Impedance Measurement..... | 196 |
| 7.4.5 BN Nanopore Double-Stranded DNA Translocation Events | 196 |
| 7.4.6 BN Nanopore Single-Stranded DNA Translocation Events | 197 |
| 7.5 Troubleshooting | 198 |

| | |
|--|-----|
| 7.5.1 No Voltage Response (or only transients) | 198 |
| 7.5.2 Extremely High Pore Impedance | 198 |
| 7.5.3 Extremely Low Pore Impedance..... | 198 |
| 7.5.4 High Current Offset | 199 |
| 7.5.5 High Noise Levels..... | 199 |
| 7.6 Conclusion | 200 |
| 7.7 References..... | 201 |

ACKNOWLEDGEMENTS

I owe a number of people a deep debt of gratitude for all they have done throughout my graduate career. First and foremost, I would like to thank **Professor Alex Zettl** for being an unparalleled research adviser. The lab you have built has given me the freedom and support to pursue my own scientific path, something I am immensely grateful for. Your tenacity and resourcefulness have made you a truly remarkable scientist, adventurer, and mentor; always ready with a river map to help me navigate even the most perilous stretches of graduate school.

I would also like to thank all of the **graduate students** and **postdoctoral researchers** I have worked with. I have learned more from all of you than in any classroom or textbook.

During my time here at Berkeley, I have also had the honor of working with over a dozen **undergraduate researchers**. Having played a role in shaping the futures of such talented researchers has been life-changing. Learning to be a better mentor through you may prove to be one of the most valuable things graduate school has taught me.

To Professor **Mike DeWeese**, whose infectious energy and enthusiasm for science was always a reminder of what we were working towards.

To **Anne Takizawa**, who always went above and beyond to make graduate school better for myself and every graduate student in the department. You have done a tremendous service to this department that will never be forgotten.

To my family, whose love and support has meant the world to me and will never be taken for granted.

To **my mother**, who always valued creativity and intelligence over being well-behaved.

To **my father**, who answered every question I ever had with, “let’s look it up!” You taught me that curiosity should never be dismissed.

To **my grandparents**, who supported and pushed me towards being a third generation of Dr. Dunn’s.

And finally, to my incredible wife and partner **Caroline**. Meeting you will always be the greatest thing I did in graduate school.

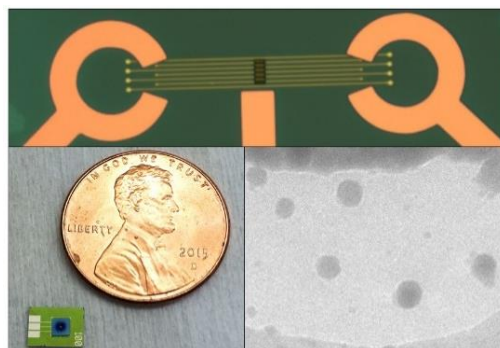
Chapter 1

Introduction

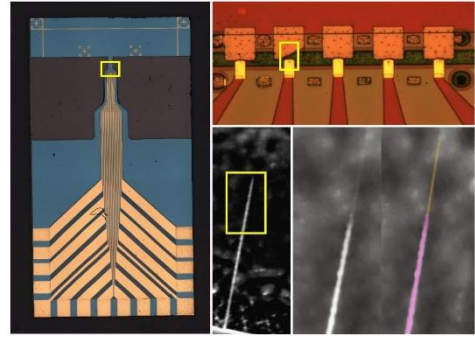
As biologists push to better understand life, consciousness and disease, they are far too often limited by the tools at their disposal. As much of the inner workings of cells take place at nanometer length scales, it seems natural to turn towards nanotechnology to develop the tools necessary to probe these phenomena. This intersection of nanotechnology and life sciences has been the focus of much of my doctoral studies.

While interdisciplinary research has become increasingly popular, in no small part due to increased funding, it is by no means new. From super resolution and electron microscopy, to nuclear magnetic resonance imaging and x-ray crystallography, techniques born out of interdisciplinary research have allowed for incredible advances in our understanding of biological processes. By its nature, interdisciplinary research requires collaboration, and the work I will speak of in this thesis could not have been done without the efforts, viewpoints and advice of a number of students and professors from a range of disciplines. As such, I will begin each topic section by recognizing those who participated in this work.

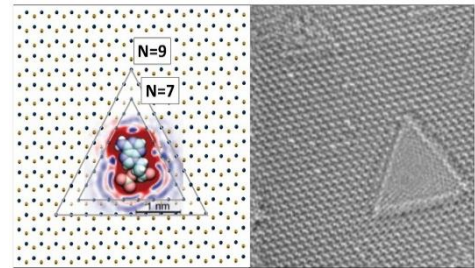
This thesis consists of three parts, each dedicated to a different experiment. **Part I** (chapters 2 and 3) covers the development of a graphene-based nanofluidic platform for imaging liquid specimen in-situ in an electron microscope. Graphene acts as an electron transparent membrane improving resolution and contrast compared to silicon nitride based cells. This platform was used to study a variety of nanoscale liquid phenomena. We demonstrate that this can be used to image biological processes at length scales beyond those currently accessible, and outline some of these potential applications.



Part II (chapters 4 and 5) will cover work we have done towards using carbon nanotubes as electrochemical probes. In particular, we have evaluated the probe for application as a neural probe. The further advancement of neuroscience relies on improved methods of recording neural activity from a large-scale, high-density of neurons. Existing probes fall well short of this, and seem theoretically incapable of this kind of scaling. We believe that by shrinking the probe size to the nanoscale, and entering the interior of the cell where the signal amplitudes are their largest, we could demonstrate a sufficiently scalable probe.



Part III (chapters 5 and 6) covers ongoing work on atomically precise nanopores in hexagonal boron nitride (hBN) for DNA sequencing. Nanopore sequencing has the potential to significantly disrupt DNA sequencing, a crucial tool for a wide-range of fields. Still, nanopore sequencing faces a number of hurdles in realizing its full potential. We have shown that by taking advantage of properties unique to hBN, we can fabricate triangular nanopores with atomically precise diameters. Applying these pores to DNA sequencing may very well help solve a number of the issues still facing solid state nanopore sequencing.



In each chapter, I provide an introduction and foundation for the work being done – its importance, as well as where the field is currently. In my description of my own experimental work, I have tried to be as detailed as possible to allow a researcher continuing on in this path to easily pick up where I have left off.

Part I:

Graphene Flow Cells

Chapter 2

Background – Graphene Flow Cell and Associated Liquid Cell Technology

2.1 Overview

In this section we will discuss the development of a graphene-enabled nanofluidic platform for imaging liquid samples by transmission electron microscopy (TEM). In this chapter, we will start by taking a closer look at in-situ liquid TEM and its progress over the last few decades, including the application of graphene as an electron transparent encapsulating layer. We will discuss some of the applications of in-situ liquid TEM, such as nanobubble research, nanoparticle research and the precipitation and dissolution of salts. Finally, we will discuss the imaging of biological specimen. In the following chapter, we will first discuss the development of graphene-sealed SiN cavities for imaging of hermetically sealed samples. Next, we will discuss the development and fabrication of the graphene flow cell (GFC) as well as some applications. The GFC provides a unique means of studying nanobubbles, which has allowed us to shed further light on the methods of their stabilization. The improved resolution of the GFC showed significant promise for the study of nanoparticle dynamics, crystallization processes, and biological materials. We will go on to discuss further potential applications of the GFC.

2.2 Introduction

Electron microscopy has been vital in ushering in the age of nanotechnology research. However, this represents a particular challenge for imaging nanoscale phenomena occurring in liquid. While air is relatively optically transparent, the scattering of electrons off nuclei means air in the beam path would obscure the image. Electron microscope samples are typically held under high vacuum for imaging, seemingly incompatible with liquid samples. Additionally, the liquid medium itself causes electron scattering which reduces resolution. Further understanding the behavior and synthesis of nanoparticles in solution, nanoscale liquid phenomena such as nanobubbles, and dissolution and crystallization, has required the development of novel techniques and tools for in-situ liquid electron microscopy.

In particular, there is great need for better imaging of dynamic processes in the life sciences. As many of the biological structures we are interested in are tens of nanometers or less, traditional optical techniques typically lack the resolution required. While advances in super-resolution optical microscopy have allowed for the imaging of structures at smaller length scales, they typically do so at the cost of temporal resolution and require labelling [1], [2]. Electron microscopy is an attractive alternative to achieving high resolution imaging of dynamic processes at the relevant spatial and temporal scales. However, the imaging of dynamic biological phenomenon under electron microscope is met with a number of challenges.

Nearly all biological processes of interest occur in solution, representing a major challenge for electron microscopy of biological samples. In addition to the limitations mentioned above, the low nuclear mass of biological molecules limits contrast as well. Furthermore, because the atomic numbers of the primary components of biological material – Carbon, Hydrogen and Oxygen – are so similar (C=6, H=1, O=8) to that of the surrounding water, obtaining enough contrast for effective imaging is a challenge. Finally, electron beam irradiation can have deleterious effects on biological samples, the mechanisms of which are just beginning to be understood.

2.3 In-Situ Transmission Electron Microscopy

2.3.1 History and Devices

In-situ electron microscopy, in which the liquid sample is encapsulated and hence separated from the high-vacuum environment of the TEM column, remains as the only means by which we can view real-time, high frame rate, dynamic nanoscale processes in solution. While in-situ TEM of liquid samples was reported soon after the development of electron microscopy, advances in silicon microfabrication and thin films have led to a renewed interest and tremendous progress in the field over the past two decades [3]. The original designs for in-situ electron microscopy relied on differential pumping to create a region in the beam column not held at high vacuum, while the electron source and most of the beam path are still held in high vacuum. While such environmental electron microscopes are still available, the resolution suffers considerably due to scattering in the higher pressure region as well as limited control of sample thickness [4]. Instead, samples encapsulated in silicon nitride thin-films have gained popularity, with nitride based holders now commercially available. Silicon nitride based cells have a number of advantages. The growth of Silicon Nitride has been extremely well characterized and optimized, so it is straightforward to control the thickness of the encapsulating film. The freestanding SiN membranes are also robust even at small thicknesses (10nm thickness is stable over tens of microns). Planar processing on top of SiN is also extremely well developed, allowing for easy integration of electrodes and fluidics.

Typically, nitride based cells are formed by sandwiching two SiN membranes together with a spacer in between them, encapsulating the sample between the two membranes. The first example of modern SiN liquid cell technology came from F. M. Ross et al. in 2003, whose initial designs can be seen in Figure 2.1. Two reservoirs are formed by the mating of two silicon chips. Each chip has a SiN membrane between the two reservoirs, where liquid samples are confined for TEM imaging. The two chips are then epoxied together along with two electrodes in contact with each reservoir. Using this setup, Ross et al. demonstrated the electrochemical growth of Cu in a closed liquid environment [5]. Since then, a number of advances have been made beyond this original design.

The first major advance was in introducing the ability to flow liquids into the sealed liquid cell. In 2010, de Jonge et al. demonstrated a homebuilt flow cell similar in design to the cell described previously, but with fluidic tubing in place of the electrodes. This design can be seen in Figure 2.2 [6]. Beyond the addition of flow, groups have demonstrated such cells can be used for gas phase studies as well, and heating and cooling techniques have also been developed [7], [8].

While the two chip epoxy-sealed approach has shown tremendous success, there are a number of downsides. It is difficult to unseal the two chips if necessary, the sealing and alignment can be technically demanding, and the epoxy can leach into the reservoirs contaminating the sample. Because of this, the trend has been towards o-ring sealed two-chip

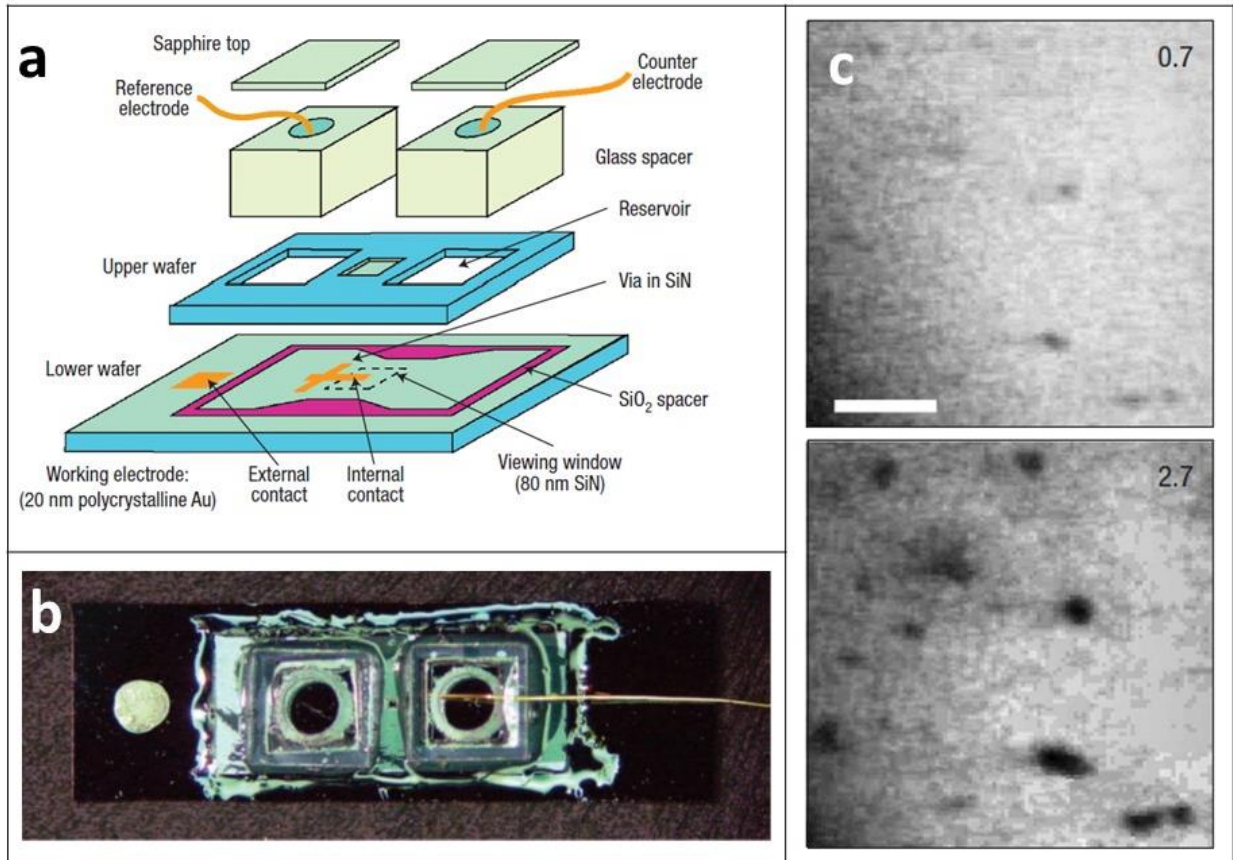


Figure 2.1: Static Silicon Nitride Electrochemical Liquid Cell. a) Cartoon schematic of cell assembly. b) Optical image of cell. c) TEM images of copper cluster electrodeposition. Image times shown at top right. Scale bar is 500nm. Adapted from Ref [5].

assemblies. The first example of this sealing design came from Chen et al., as shown in Figure 2.3 [9]–[11]. Due to the ease of sample preparation and the versatility of this approach, two commercial TEM liquid cell holders have been developed utilizing o-ring sealing: the Protochips Poseidon and Hummingbird. These two holders are shown in Figure 2.4. As we shall discuss later, our lab has purchased a Protochip Poseidon holder and our graphene flow cell chips have been fabricated to be compatible with this system.

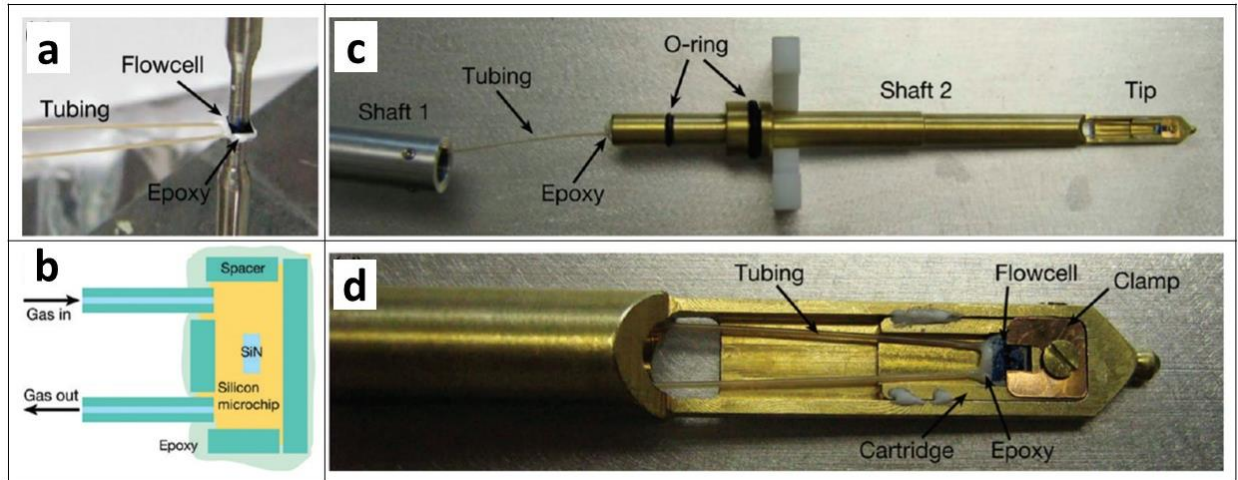


Figure 2.2: Silicon Nitride Flow Cell. a) Assembly of flow cell. b) Cartoon schematic of flow cell. c) TEM holder components. d) Close up image of the viewing area of the TEM holder. Adapted from Ref [6].

Recently, Jensen et al. demonstrated further improvement with a monolithic chip system in which the two chip sandwiches are replaced by an integrated microfluidic channel on a single chip, shown in Figure 2.5 [12]. While this technology is still in its infancy, it holds a critical advantages in precise control of sample thickness and thinner SiN encapsulating windows. Typical sandwiched nitride cells typically use SiN membranes which are tens of microns wide, which can create significant bowing when the two chips are sealed together. An integrated channel can be made significantly narrower ($2\mu\text{m}$ in Jensen et al.'s work), allowing for a more uniform sample thickness and higher resolution. In order to ensure membrane stability during the sandwiching process, the nitride membranes are typically at least 50nm thick. An integrated fluidic channel does not require the same thickness as it does not undergo the same stresses as sandwiching and the comparably narrow channel areas are less prone to rupture. The approach we ultimately undertook for the graphene flow cell similarly utilized a monolithic integrated channel for these same reasons.

Sample encapsulation solves only one of the difficulties of imaging liquid specimen, separating it from the high vacuum environment of the TEM. However, it does nothing to address the issues of limited resolution, contrast and beam damage in samples. In fact, sample encapsulation can introduce additional difficulties as the encapsulating material itself serves to scatter electrons and reduce resolution.

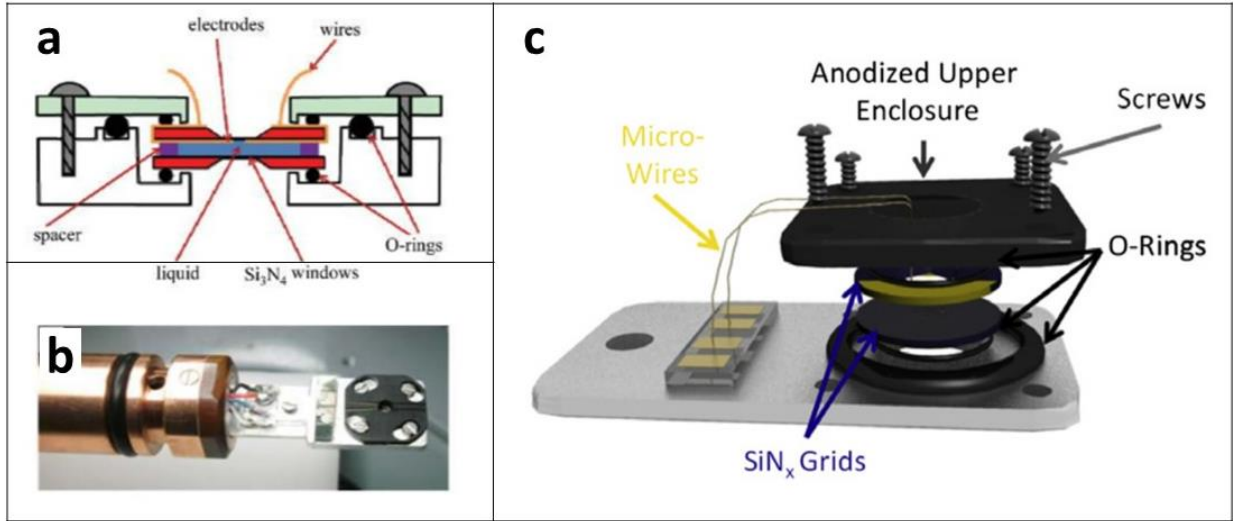


Figure 2.3: O-ring sealed TEM flow cells. A) Schematic of homebuilt holder. O-rings separate liquid environment from high-vacuum of TEM. B) Optical image of holder. C) Cartoon of enclosure. Adapted from Ref [10].

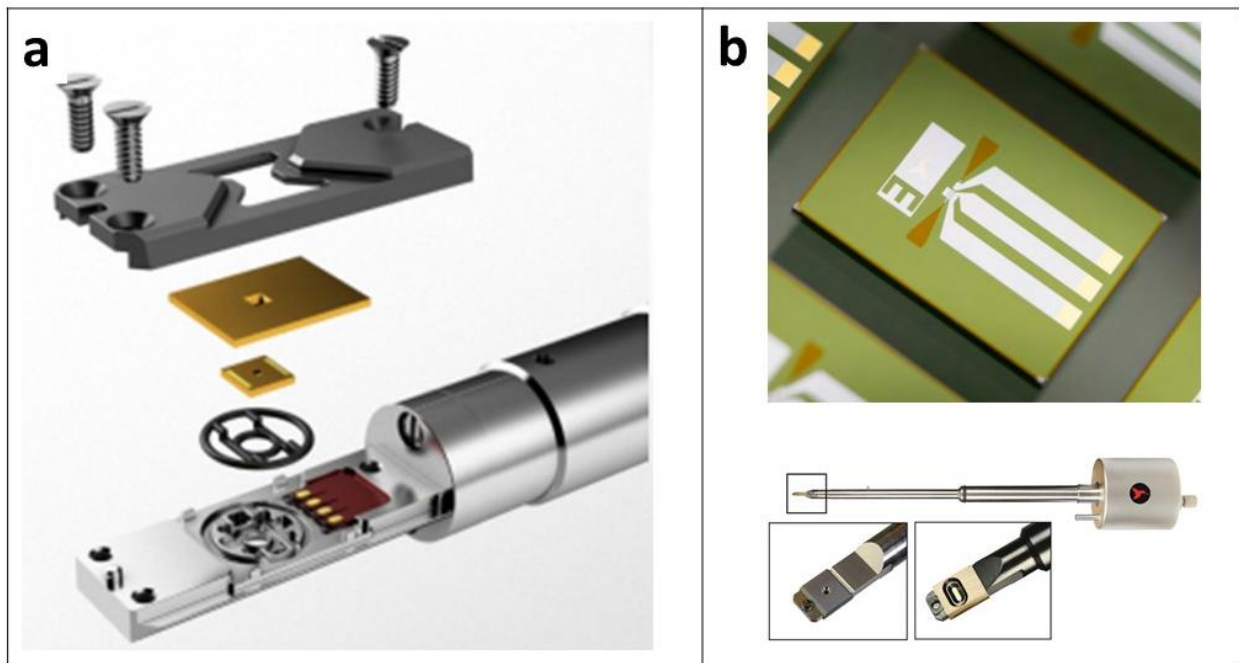


Figure 2.4: Commercial SiN TEM Flow Cells. A) Illustration of the Protochips Poseidon™ flow holder. B) Hummingbird™ holder. (top) Silicon fluidic chip for bottom half of the flow holder. (bottom) image of the TEM holder and close ups of the top and bottom of the headpiece. Courtesy of Protochips and Hummingbird.

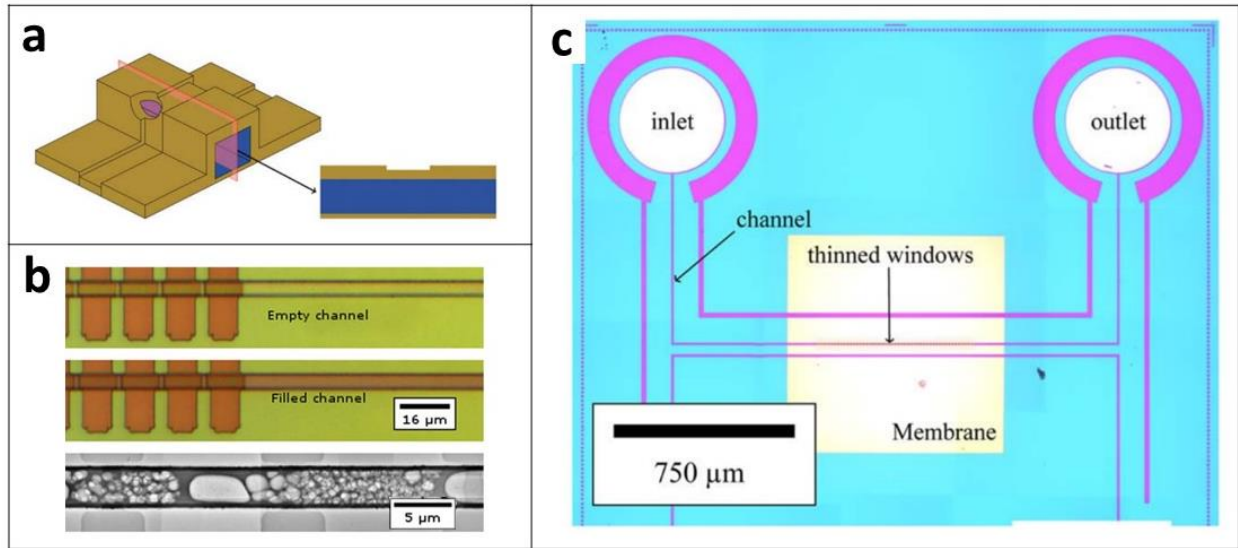


Figure 2.5: Monolithic SiN Flow Cell. a) Cartoon cross section view of the SiN channel. The channel is thinned in areas for improved resolution and contrast. b) Channel filling. The top image shows an optical image of the empty channel. The middle is an optical image of the channel filled. The bottom is a TEM image of the filled channel. c) Optical image of chip design. Adapted from Ref [12].

2.4 Graphene Liquid Cells

In 2012, Yong Min Yuk, a visiting graduate student in the Zettl lab, demonstrated that by using graphene to encapsulate liquids, one could get significantly higher resolution and contrast, allowing for atomic-resolution imaging of nanoparticle growth in solution [13]. Thus, the graphene liquid cell (GLC) was born. In many ways, graphene proved to be an ideal material for imaging liquid samples. At a single atom thick, the graphene is as thin as an encapsulating layer one can possibly achieve, limiting additional electron scattering from the encapsulating layer. Graphene is also conductive, which limits the charging effects seen in SiN based cells. The encapsulation method creates liquid layers that range in thicknesses, but can be tens of nanometers in some area, allowing for the high-resolution imaging seen by Yuk et al [14].

In addition to the improved resolution, the simplicity of GLC assembly works to its advantage. No specialized fluidic equipment or holder is necessary, and these graphene liquid cells could be safely loaded into most TEMs. In brief, a liquid droplet is placed on a sheet of graphene suspended on a quantifoil TEM grid. A second graphene TEM grid is then placed on top of the droplet, sandwiching the solution. As the solution evaporates, the van der Waals force

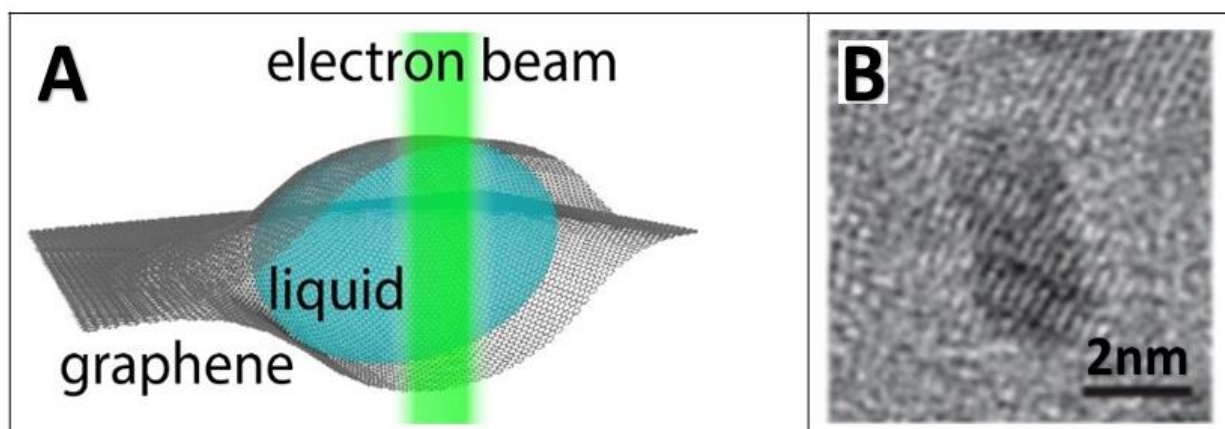


Figure 2.6: Graphene Liquid Cell (GLC). A) Schematic. Liquid sample is sealed between two sheets of graphene. B) Platinum nanoparticle in GLC imaged with atomic resolution in aberration corrected TEAM microscope at 80keV. Adapted from Ref [13].

between the two graphene layers seals the solution between the two sheets. The seal is extremely strong and trapped samples remain so for a considerable time (we have seen at least months and never checked longer). A schematic of the GLC is shown in Figure 2.6.

As we shall discuss in the next chapter, this initial assembly method was improved upon in order to give more control over the volume and thickness of the trapped samples. In addition to this change in architecture, a more modest improvement was demonstrated by Sasaki et al., in which a mist generator is used to wet the graphene before sealing [15].

This original GLC architecture allowed for number of advances in chemistry and nanotechnology [13], [14], [16]–[21]. Work has been done on the growth, behavior and dynamics of nanoparticles in liquid [13], [14], [16], [17]. Other work has focused on the dissolution and formation of salt crystals in solution [19]–[21]. Park et al. were able to go beyond just atomic resolution 2D imaging of Pt nanoparticles, and were able to use the rotation of the nanoparticle in the liquid cell to reconstruct a full 3D atomic model of the nanoparticle [14]. Despite these successes, the technique has a number of limitations which we shall further discuss. Briefly, the static nature of the sealed cells, as well as the large uncertainty in sample concentration after evaporative sealing represent significant hurdles to some of the further applications of GLCs.

2.5 In Situ TEM Applications

In-situ TEM has found considerable success studying a number of nanoscale phenomena. As discussed above, it stands as one of the only means of imaging nanoscale phenomena in real-time, with high frame rate, and high resolution.

2.5.1 Nanobubbles

Surface nanobubbles – gaseous bubbles on a solid surface in a liquid medium – have been a contentious area of research since the first evidence of their existence [22], [23]. In-situ liquid microscopy is an ideal tool for the study of nanobubbles. Owing to their nanoscale size and low optical contrast, it is not possible to image nanobubbles with optical microscopy. The use of fluorescent labelling would directly interfere with nanobubble formation and stability, so the use of super-resolution optical techniques is also off-limits. The primary method of direct nanobubble detection and measurement has been with AFM – as shown in Figure 2.7 – but as we shall discuss, this holds a number of drawbacks. TEM not only gives us the resolution and contrast necessary to image nanobubbles at unprecedented length scales, the production of gaseous byproducts by electron beam irradiation can act to nucleate and grow nanobubbles during imaging.

The reason for initial skepticism surrounding reports of nanobubble observation was that traditional theory suggested bubbles with this small of a diameter would be inherently unstable and dissolve on the order of microseconds. Instead, researchers were seeing long-lived nanobubbles stable for days. The pressure inside of a bubble is described by the Young-LaPlace equation:

$$P - P_L = \frac{2\gamma}{R}$$

where P_L is the pressure of the surrounding liquid, γ is the surface tension of the bubble, and R is the radius of the bubble. For a bubble with a 10nm radius, the difference in pressure between inside the bubble and outside would be 143atm. As the liquid-air interface should be permeable, gas in the high-pressure interior should cross over into the liquid, further reducing the volume of the nanobubble. As such, the radius would decrease as well, further increasing the pressure, and leading to runaway process of nanobubble dissolution.

Despite this, nanobubbles were being regularly produced and reported, and their stability remained unexplained. Efficient sample preparation methods were developed, such as by solvent exchange. A hydrophobic sample was first immersed in ethanol, which has greater solubility for

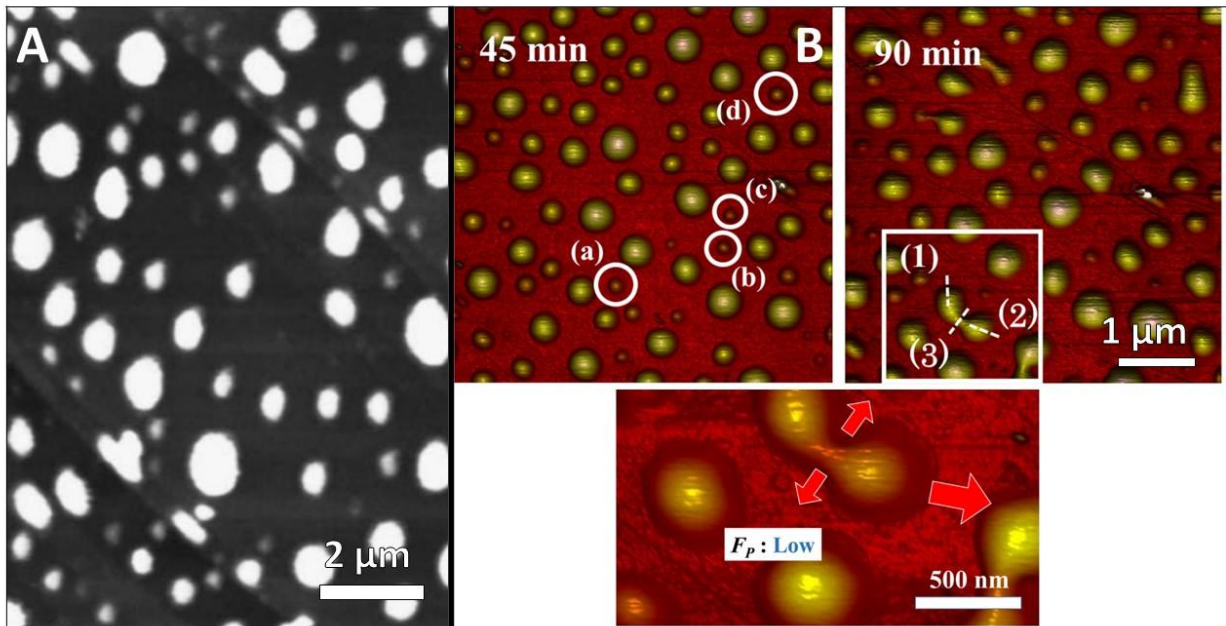


Figure 2.7: Nanobubble AFM. A) Tapping mode AFM image of nanobubbles on HOPG. Adapted from Ref [23]. B) Nanobubbles imaged by Peak Force Measurement AFM. Combining nanobubbles show a structural stability that is not present in macroscopic nanobubbles. This is cited as evidence of contact line pinning. Adapted from Ref [32]

nitrogen than water, and is then immersed in water. As the ethanol readily mixes with water, the nitrogen becomes supersaturated, and nucleates at the hydrophobic surface [24], [23].

Interestingly, in addition to their anomalous stability, nanobubbles also showed different contact angles than those reported for their macroscopic counterparts. In macroscopic bubbles, the contact angle is predicted by Young's equation:

$$\cos \theta = \frac{\gamma_{SV} - \gamma_{SL}}{\gamma_{LV}}$$

where γ_{ij} are the interfacial tensions between the solid, vapor, and liquid, as shown in Figure 2.8. In nanobubble experiments on highly ordered pyrolytic graphite – which owing to its hydrophobicity typically has a large contact angle of $\sim 120^\circ$ – the contact angle is estimated by AFM to be significantly smaller. In early work, the angle was found to be between $10\text{-}40^\circ$ for

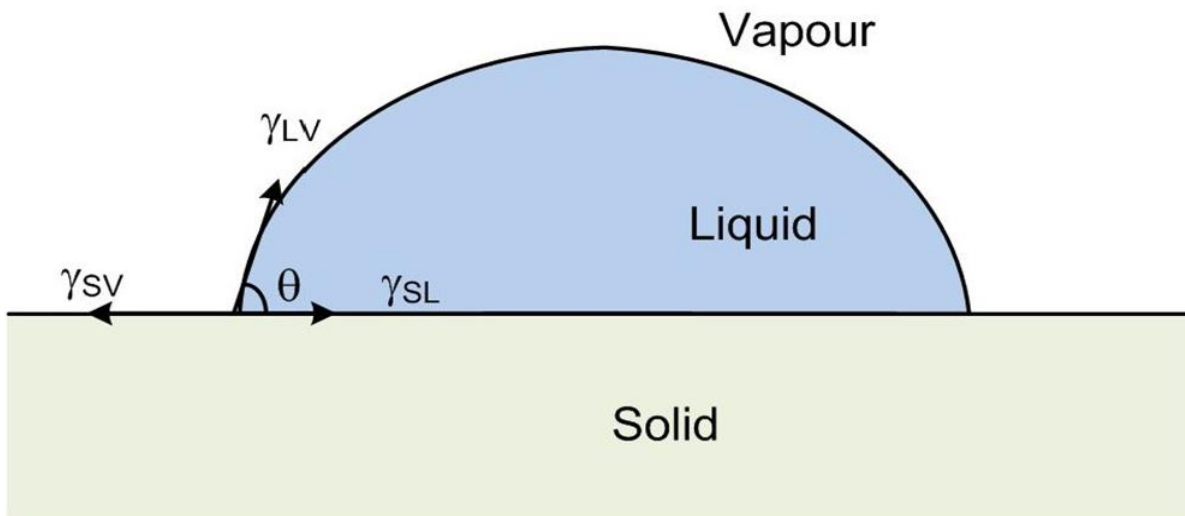


Figure 2.8: Young's Equation Tensions. Force diagram at three-phase contact point for classical unmodified Young's equation.

nanobubbles on HOPG. This suggested that Young's equation does not hold for nanobubbles, and needs to be modified. An additional term has been suggested which would factor in an additional force from line tension – a force originating from the vapor-liquid interface. This term would be inversely proportional to the size of the nanobubble, explaining why its effects are no longer seen in macroscopic bubbles. The modified Young's equation can be expressed as

$$\cos \theta = \frac{\gamma_{SG} - \gamma_{SL}}{\gamma_{LG}} - \frac{\gamma_{SLG}}{r}$$

where γ_{SLG} is the line tension, and r the radius [25]–[28].

A number of possible explanations were provided for the stability of nanobubbles. One possibility was that jamming of contaminants in the solvent made the nanobubbles impermeable to gas. This jamming effect could contribute an additional term to Young's equation which would account for the change in contact angle. A similar theory suggests that surfactant contamination or charged ions on the surface of the bubble could end up providing a repulsive force, effectively reducing the surface tension and therefore the LaPlace pressure. The fact that the nanobubbles are still stable in a range of pH's stand in direct contradiction of this explanation [22].

An explanation that has been gathering support is the idea of contact line pinning. In this case, either surface features or chemical heterogeneities cause the nanobubble interface to pin to a certain radius on the surface. Due to this pinning, as the bubble grows (shrinks), the height of

the bubble, H , increases (decreases) while the radius of curvature, R , increases (decreases), and the lateral size of the bubble remains constant. In this case, the Young-LaPlace equation can be rewritten as

$$P - P_L = \frac{2\gamma}{\left(\frac{(L/2)^2 + H^2}{2H}\right)} = \frac{4\gamma H}{(L/2)^2 + H^2}$$

As the bubble shrinks, the LaPlace pressure actually decreases, stabilizing the bubble [29], [30]. There has been evidence to support the contact line pinning of nanobubbles. In AFM time series of surface nanobubbles taken over the course of 24 hours, shown in Figure 2.9, the lateral size of the nanobubbles are relatively constant, while the height and radius of curvature decrease [31]. Additional evidence for this has been found in the coalescence of nanobubbles. As shown in Figure 2.7(B), as two nanobubbles coalesce, they tend to maintain their independent morphology, in contrast to macroscopic bubbles which will typically combine to form a larger sphere. Despite this evidence for contact line pinning, the source of the contact line pinning is still not understood. While changes in the lateral length are small compared to the changes in height, the lateral length does still change slightly [32].

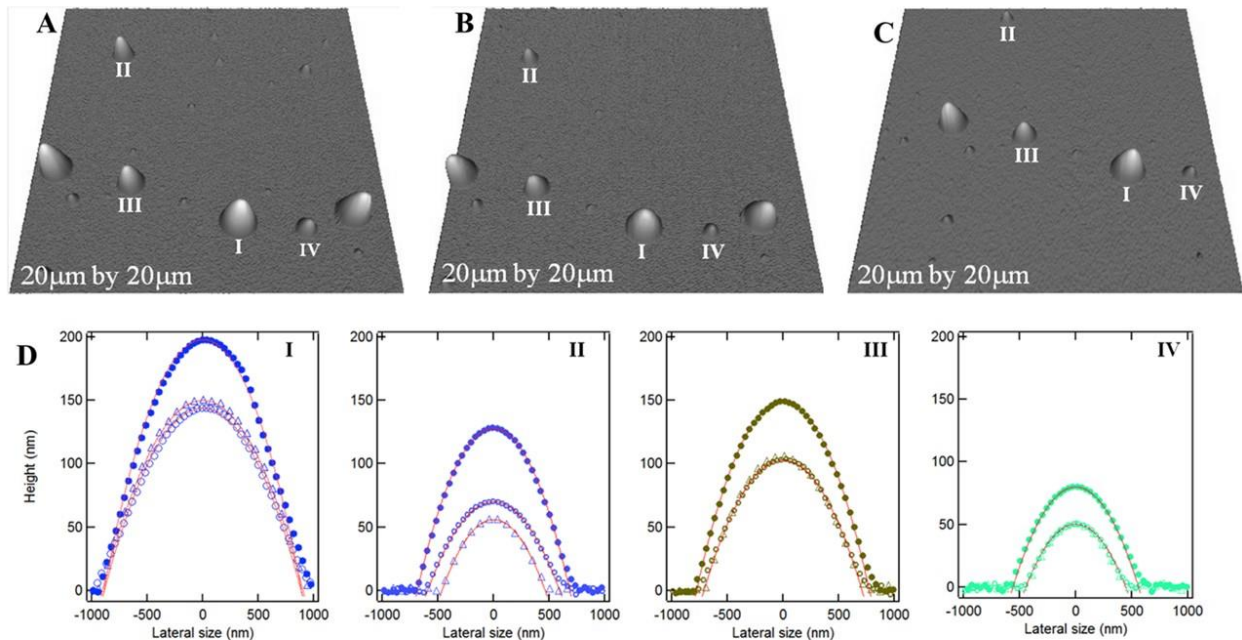


Figure 2.9: Contact Line Pinning. A)-C) AFM images of nanobubbles in a degassed environment in which the nanobubbles can be seen to shrink over time. D) AFM line profiles of the nanobubbles labelled in (A)-(C). The height and radius of curvature of the nanobubbles change considerably more than the lateral length of them, supporting the contact line pinning theory. Adapted from Ref [31].

The most common method of observing nanobubbles has been with atomic force microscopy (AFM) [24], [23], [32], [22]. While AFM can have exceptional spatial resolution, there are a number of drawbacks in imaging nanobubbles. First, the force the cantilever tip exerts on the bubble will cause one to underestimate the height of the bubble, and surface tension forces on the cantilever itself will alter the resulting image. Additionally, AFM is incapable of measuring any undercut features, the pyramidal structure of the cantilever tip can interfere with imaging high angle features. Additional characterization tools have been applied to nanobubbles. Recently, in-situ electron microscopy has been utilized to image nanobubbles.

Nanobubble formation was initially seen as an unwanted side-effect of imaging liquid samples in a TEM. Radiolysis from the electron beam irradiation of water would cause the nucleation of H₂ filled nanobubbles. Bau and Ross et al. first imaged nanobubbles in-situ in a SiN based flow cell driven by radiolysis, as shown in Figure 2.10(A) [33], [34]. Regan et al. followed this up by studying the stability of nanobubbles created by the local heating of water to vaporization. They found the nanobubbles to be unstable below a radius of around 50-300nm, and saw rapid nanobubble collapse, as shown in Figure 2.10(B) [35]. Novoselov et al. looked at the growth dynamics and coalescence of nanobubbles in graphene liquid cells, as shown in Figure 2.10(C) [36]. Because each of these studies were looking at nanobubbles from a top-down point of view, little was able to be said about the three-phase contact point, and no light was shed on the mechanism of their stability.

In summary, a clear explanation for the stability of nanobubbles has remained elusive. A number of peculiar characteristics of surface nanobubbles have been discovered: the stark difference in the contact angle of nanobubbles compared to those of macroscopic bubbles; the changing radius of curvature and contact angle with nanobubble growth; the geometric integrity of merging nanobubbles. It is clear that a better understanding of the behavior at the three-phase contact line would be helpful in explaining these phenomena.

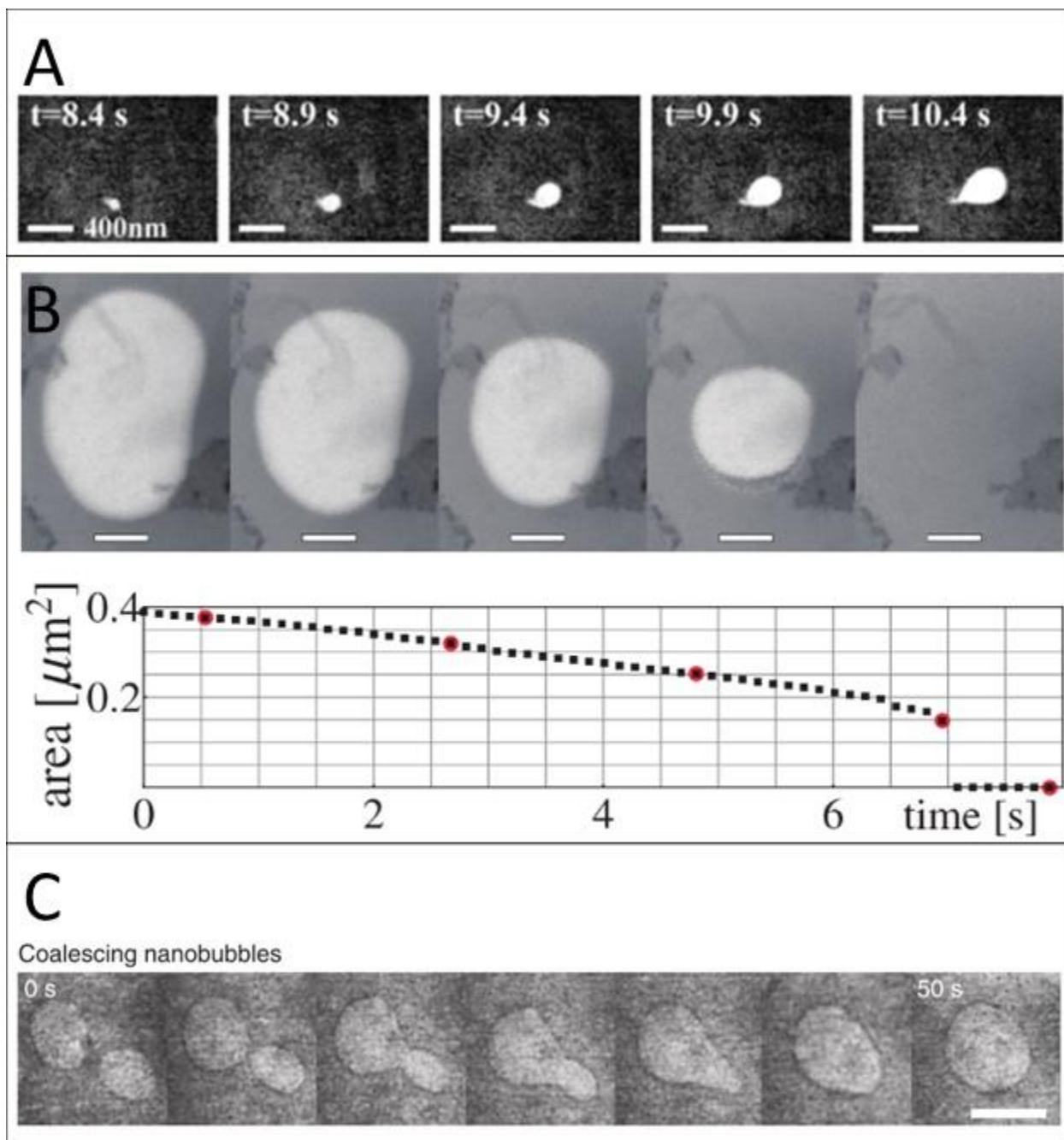


Figure 2.10: Nanobubble In-Situ Liquid TEM Studies. A) Formation of a nanobubble by radiolysis in a SiN liquid cell. Adapted from Ref [33]. B) Collapse of a nanobubble formed by local heating. Nanobubble is seen to collapse when radius reaches 50-300nm in radius. Adapted from Ref [35]. C) Nanobubble dynamics in a graphene liquid cell. Two nanobubble coalesce. While they do combine into one nanobubble, they maintain their individual structure for an extended period of time. Adapted from Ref [36]

2.5.2 Nanoparticle Dynamics

Nanoparticle dynamics is a natural area of research for in-situ electron microscopy. Heavy element nanoparticles offer a high contrast sample with high stability under electron beam irradiation, and their nanoscale dimensions make optical imaging less effective. Due to this ease of use, some of the earliest work with liquid cells has been concerned with the growth or dissolution of metallic nanoparticles. Despite the breadth of this work, study of the dynamics of nanoparticles in liquid cell has been limited, and that which has been done raises a number of questions.

The movement of spherical nanoparticles in solution from Brownian motion can be described by the Einstein-Stokes equation:

$$D = \frac{k_B T}{6\pi\eta R}$$

where k_B is the Boltzmann constant, T is the temperature, η is the liquid medium viscosity, and R is the nanoparticle's radius. For rotational movement, this formula is adapted as:

$$D_r = \frac{k_B T}{8\pi\eta R^3}$$

For water at room temperature, for a 10nm radius nanoparticle, $D = 3.65 \times 10^{-7} \text{ nm}^2/\text{s}$. A typical TEM camera has a frame rate of around 10 frame/s. This suggests that in between images, a freely diffusing nanoparticle could move upwards of $2\mu\text{m}$ across the screen. This means that such a nanoparticle would be moving too quickly to be resolved by our TEM camera. Similarly, the same nanoparticle would be expected to rotate at around 40 rad/s .

Despite this, in situ TEM has had tremendous success imaging nanoparticles in solution, and dynamics have been observed, as shown in Figure 2.11 [37]. The diffusivity has been measured to be many orders of magnitude smaller than what the Einstein-Stokes equation would suggest [38], [39]. Evidence suggests that nanoparticles in the bulk solution are moving at speeds

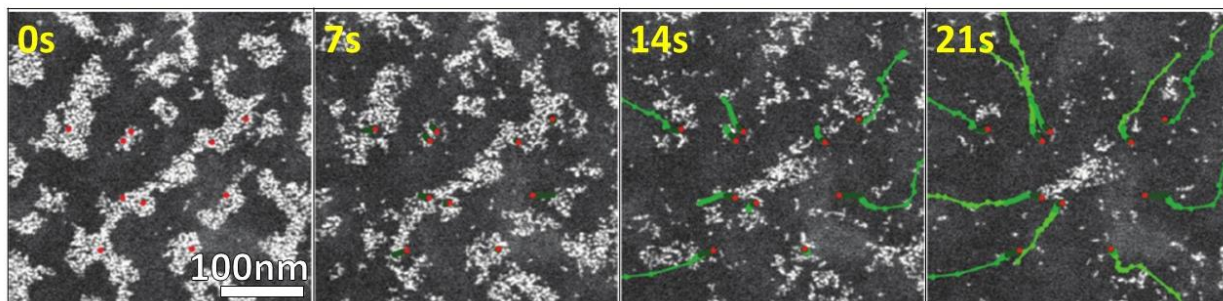


Figure 2.11: Charged Nanoparticle Dynamics. STEM time-series of Pt nanoparticles in buffer solution. After continued imaging, the charging of the SiN from the electron beam causes the nanoparticles to scatter. Adapted from Ref [37].

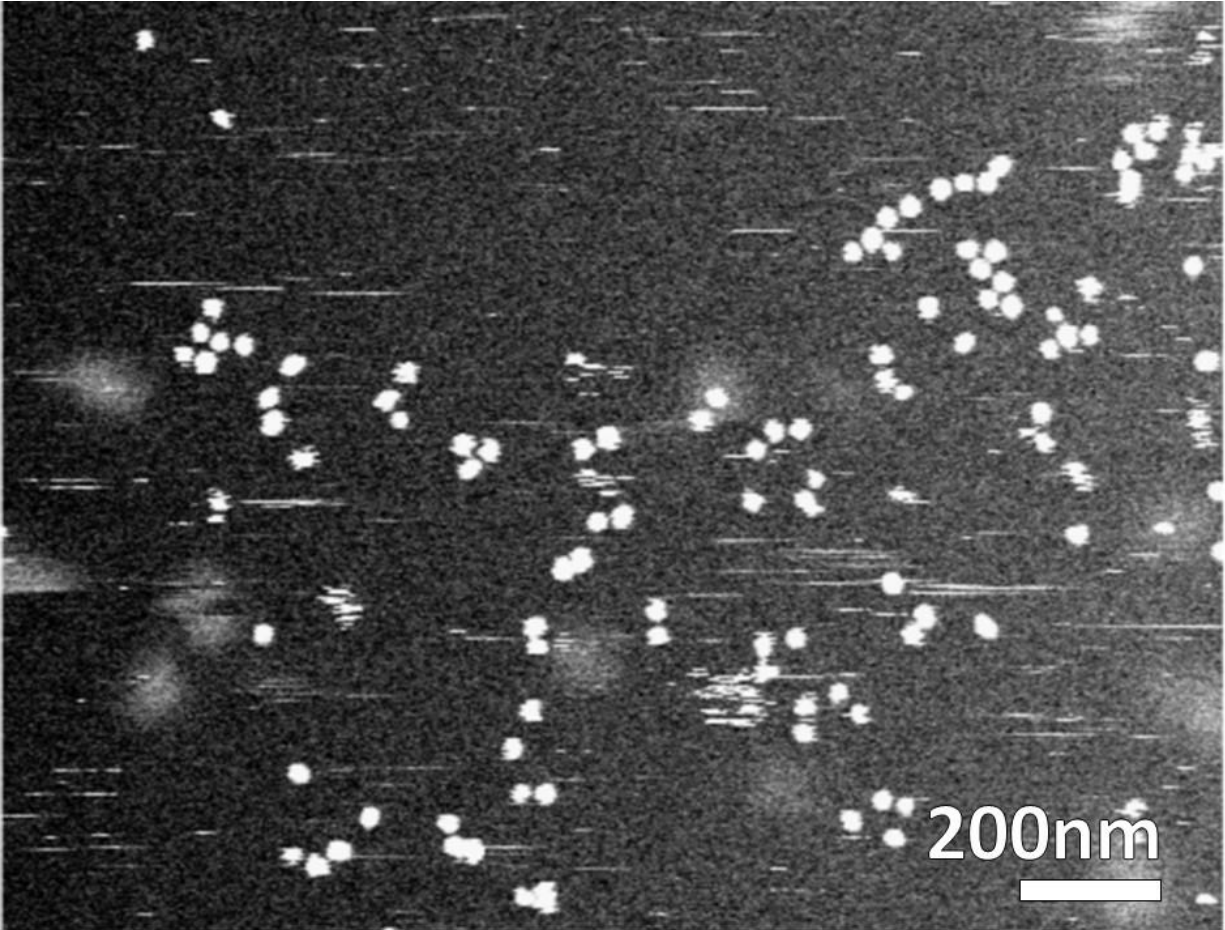


Figure 2.12: Fast Diffusing Non-Adsorbed Nanoparticles. STEM image shows stationary or slow moving adsorbed nanoparticles clearly resolved, while streaks are thought to be quickly moving nanoparticles diffusing in the bulk solution. Poorly resolved, fuzzy images are thought to be nanoparticles adsorbed on the bottom membrane. Adapted from Ref [39].

in accordance with the Einstein-Stokes equation and are moving too quickly to resolve, but particles close to the encapsulating substrate are moving slowly enough to be resolved, as suggested in Figure 2.12. However, the reason for this slower movement has been an issue of debate. One possibility is that the particles are adsorbing to the surface and movement is the result of two mechanisms: the rolling of nanoparticles along the substrate and the rapid desorption and re-adsorption of nanoparticles causing a jump movement [40]. Nanoparticle tracking, as shown in Figure 2.13, shows clear evidence of these two diffusion modes. The second explanation is that a highly ordered phase of water near the substrate surface is increasing the viscosity locally by orders of magnitude. A third explanation, that hydrodynamic hindrance near the nitride surface, has been shown to produce too small an effect to explain the drastic change in diffusion that has been witnessed.

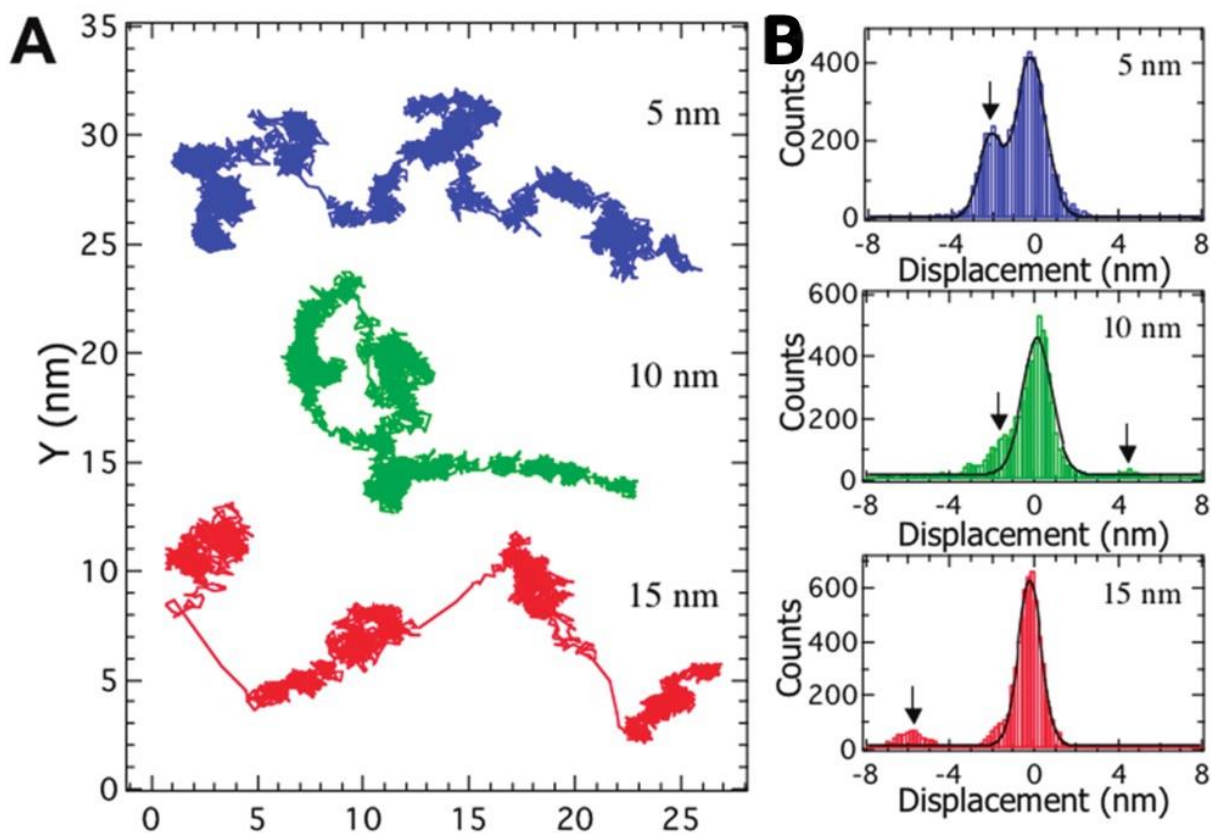


Figure 2.13: Two Distinct Modes of Diffusive Motion. A) 2D tracking of three nanoparticles from STEM imaging. B) Histograms of step length of nanoparticle movement. In each case, there are clearly two distinct modes of nanoparticle movement – fast jumps and small steps. Adapted from Ref [40]

Beyond just their diffusion characteristics, the assembly and coalescence of nanoparticles in solution has also been studied. Nanoparticles have been observed to self-assemble into 1D chains, 2D sheets, and 3D crystal structures. The degree to which this assembly is driven by diffusion or other long-range forces has been studied by a number of groups. This can be largely affected by the makeup of the nanoparticles as well as ligand interactions on the nanoparticle shell. As shown in Figure 2.14, after extended electron beam irradiation, PtFe nanoparticles are seen to self-assemble into chains. This is primarily driven by the magnetic dipole interactions of the PtFe nanoparticles [41].

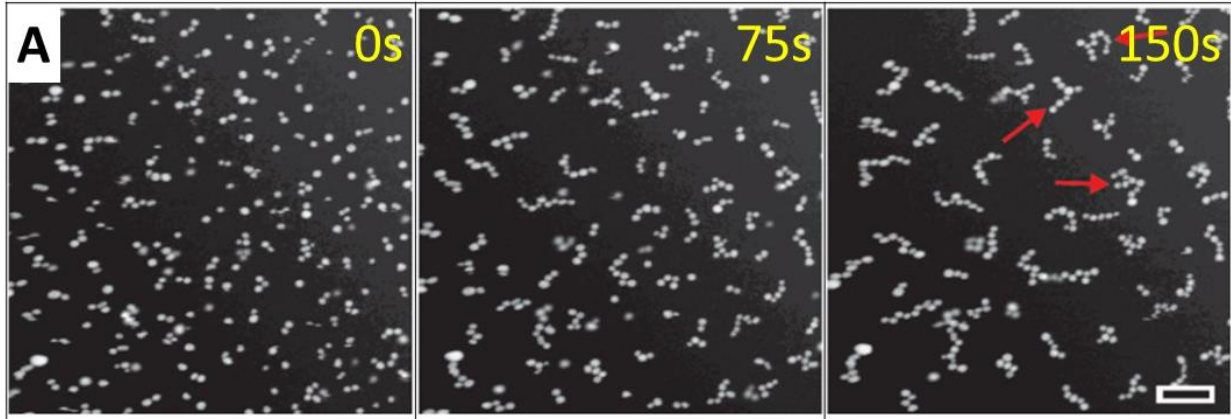


Figure 2.14: Chain Self-Assembly. STEM time series of AuNP chains self-assembling primarily via diffusion.

The dynamics of nanoparticles in bulk liquids is not the only area of application for in-situ electron microscopy. As nanoparticles have found a number of potential applications, placement of nanoparticles from solution onto a dry substrate has become critical. Techniques using nanopatterned surfaces have shown that nanoparticles can be essentially lithographically patterned, as nanoparticles in a drying solution can be drawn to specific spots by capillary forces, as shown in Figure 2.15 [42]. As such, understanding the surface diffusion and behavior of nanoparticles in the final seconds of drying is then critical in improving this process.

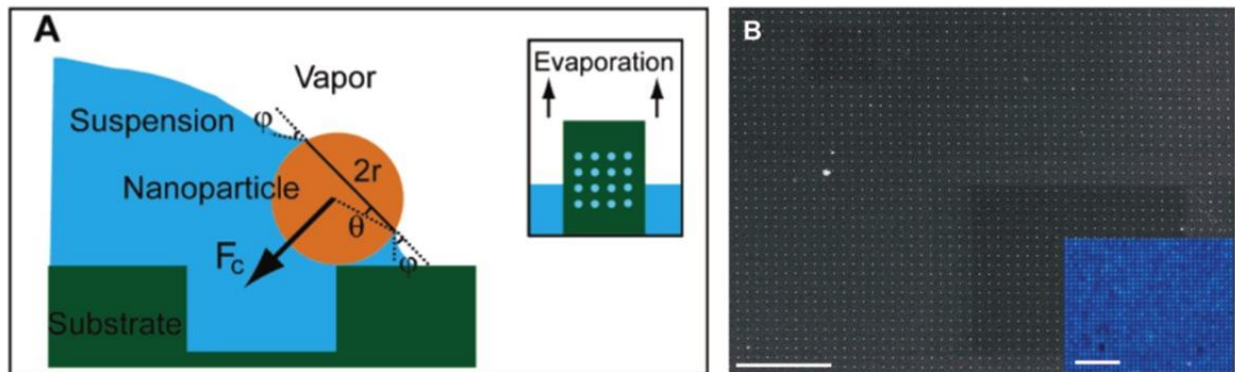


Figure 2.15 Lithographic Patterning of Nanoparticles in Solution. A) Cartoon of nanoparticle trapping method. B) SEM of resulting patterned nanoparticles. Adapted from Ref [42].

2.5.3 Mineral Precipitation and Dissolution

A better understanding of the crystallization of minerals in solution would benefit a number of fields. Mineralization is common in nature and biology, and is involved in a number of chemical processes of interest. However, our tools for studying mineralization are fundamentally limited. Optical microscopy, AFM, and Grazing-Incidence Small-Angle X-Ray Scattering (GISAXRS) have all been used to study mineralization in-situ, but each has inherent limitations, be it spatial or temporal resolution, or complicated sample preparations [43]–[47].

Our lab has already demonstrated that in-situ liquid TEM can be a valuable tool for investigating mineralization processes. Yuk et al. showed that mineralization could be initiated in a sealed graphene liquid cell by radiolysis. As shown in Figure 2.16, the grain boundaries of the precipitate could be resolved and mapped. It was then possible to directly image the grain growth and dynamics in real time [19].

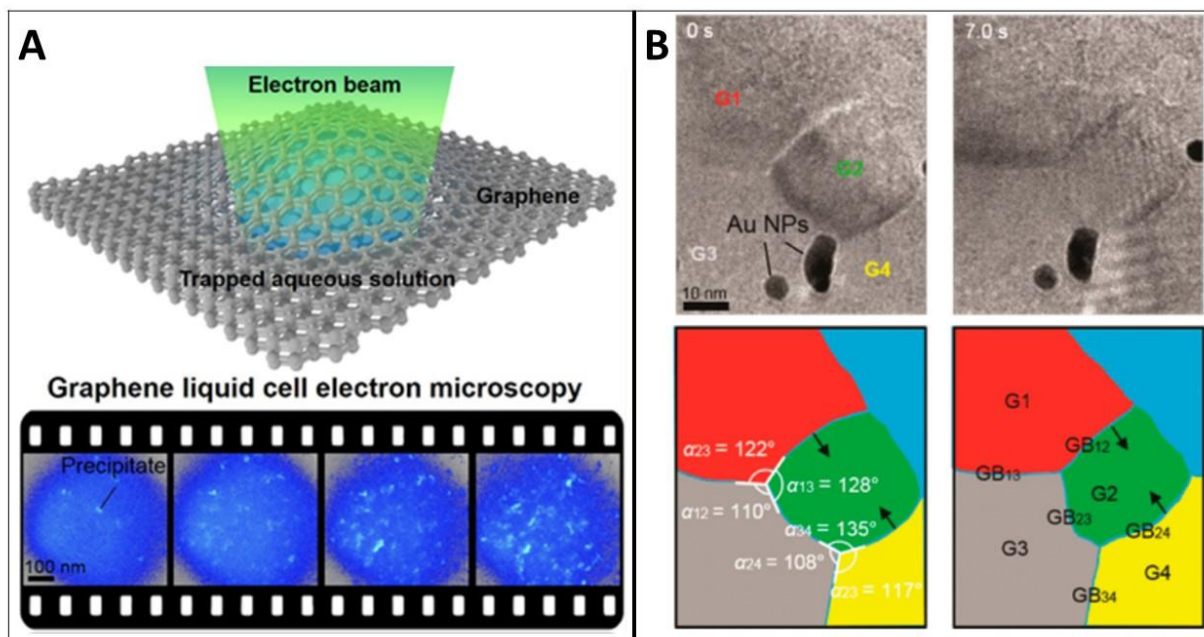


Figure 2.16: Thenardite Precipitation in GLC A) Cartoon of experimental setup (top). Dark-Field TEM time series of crystal precipitation. B) TEM image of thenardite precipitating under e-beam irradiation (top). Mapping of crystal domains and growth (bottom). Adapted from Ref [19]

2.6 Biological Specimen – Cryo- and Stain-Based TEM

While in-situ liquid TEM holds significant promise for imaging biological specimen, the low-contrast light elements that make up most biological material, as well as damage from electron beam irradiation represent major hurdles in its application. Two methods of electron microscopy commonly used for biological specimens, stain-based imaging and cryo-TEM, have found different ways of mitigating these challenges and have become mainstays of biological imaging. Stain-based electron microscopy gets around the difficulties mentioned above by removing the surrounding liquid media and creating a mold of the specimen in a heavy element salt. Typically, dilute uranyl acetate (UA), sodium phosphotungstate (PTA) or methylamine tungstate is introduced into the sample solution. The salt preferentially adheres to the specimen and the sample is allowed to dry, leaving a shell of the heavy-element salt [48]. Depending on the concentration of the salt, this stain can have a positive staining or negative staining effect as shown in Figure 2.17 [49], [50]. Samples prepared in this manner do not have the same dose limitations as the original biological specimen, are not sensitive to the high-vacuum environment of the TEM, and do not have the same resolution loss from electron scattering in the solution.

Cryo-TEM instead flash freezes samples to make them stable under high-vacuum. A droplet of the sample solution is placed on a TEM grid which is then rapidly passed through liquid nitrogen. While the resolution and contrast difficulties of biological samples remain, cryo-TEM utilizes low-dose imaging averaged over lengthy acquisition times, and often averaged over a number of nearly identical samples, in order to produce extremely high-resolution images

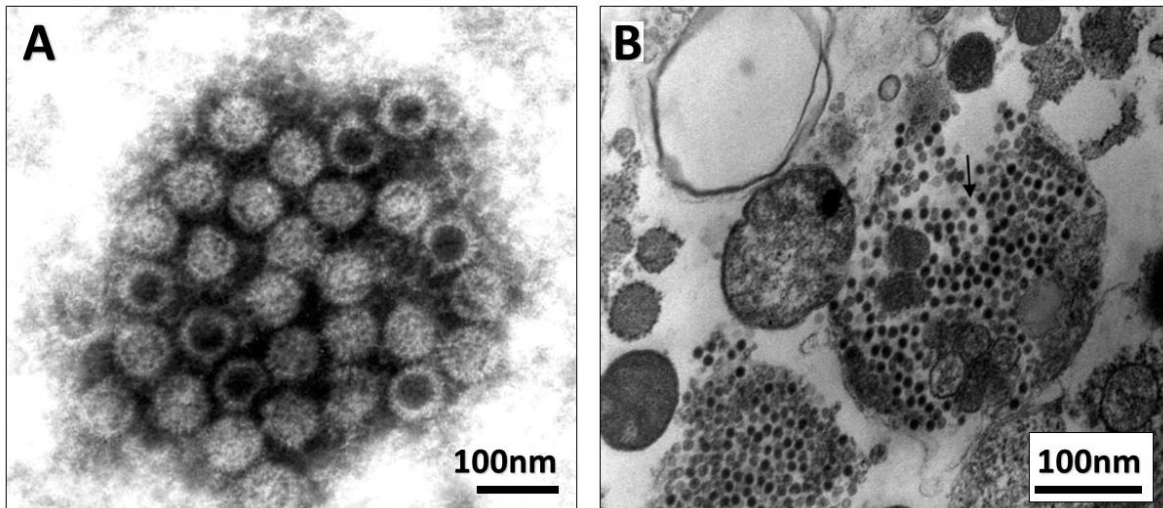


Figure 2.17: Negative and Positive Staining for TEM. A) A group of rotavirus capsids negatively stained with 1% phosphotungstic acid (PTA). B) Dengue virus positively stained with lead citrate [50].

of biological structures [51]–[54]. In contrast to stain-based imaging, the specimen are rigidly preserved in their natural environment and not prone to structural collapse or conformation change during drying. As imaging equipment and analysis has continued to improve, so has the applicability of cryo-TEM, with it becoming a powerful tool in structural biology. Figure 2.18 shows the structural reconstruction of β -galactosidase, a common enzyme protein, demonstrating the incredible resolution that can now be achieved [54]. While both cryo- and stain-based electron imaging have been critical in advancing our understanding of the structure of a number of proteins and cellular machinery, these techniques provide only snapshots, where dynamics must be pieced together and inferred.

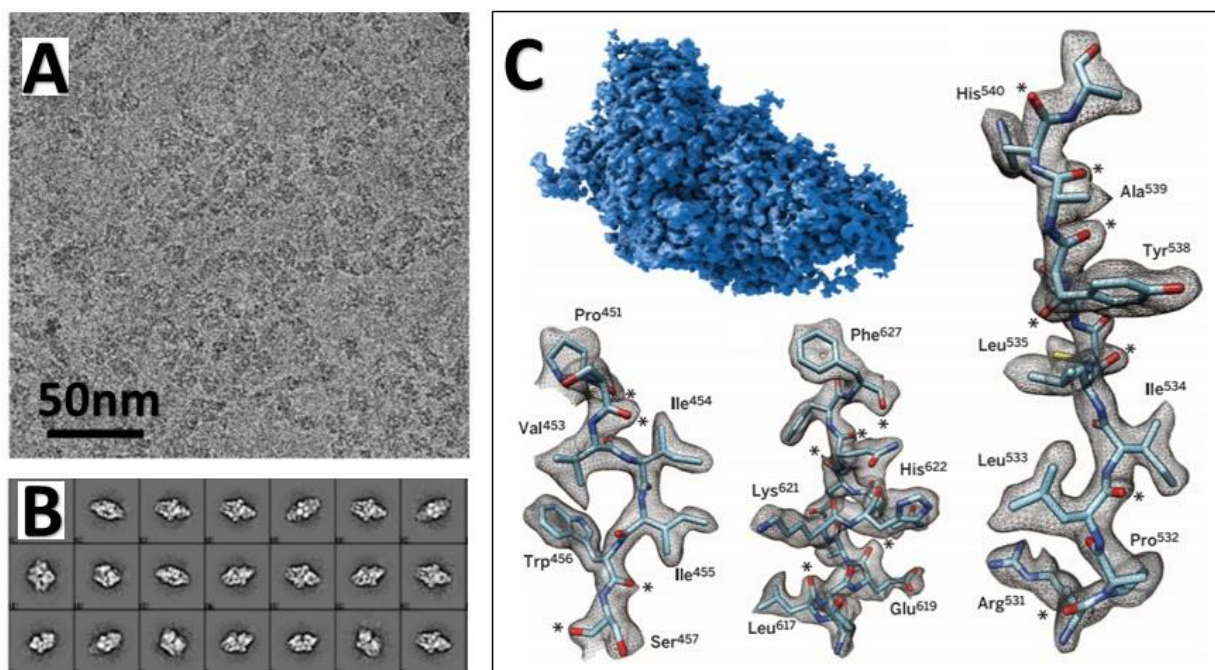


Figure 2.18: CryoTEM. A) Average of 38 aligned movie frames acquired over a 7.6 s exposure window ($45 \text{ e}^-/\text{\AA}^2$ total accumulated dose) of β -galactosidase. B) Various 2D projection views from averaging over multiple similar proteins. C) Simulated reconstruction of the 3D structure of β -galactosidase with resolution of 2.2\AA . Adapted from Ref [54].

2.6.1 Resolution in In-Situ Biological Imaging

The issue of resolution of specimen in liquid is a general one and is not just limited to biological samples. For a standard TEM, both the liquid itself and the encapsulating layer will cause the inelastic scattering of electrons, leading to chromatic aberration which reduces the resolution. The top and bottom encapsulating material and the liquid can be treated as three separate layers which each contribute to the chromatic aberration. The change in energy distribution of the electrons due to this inelastic scattering in each layer is given by

$$\Delta E = \frac{N_A e^4 Z \rho T}{2\pi \epsilon_0^2 W m_0^2 v^2}$$

where N_A is Avagadro's number, e is the electron's charge, W the atomic weight, m_0 the mass of the electron, v its velocity, Z is the effective atomic number of the scattering layer, ρ its density, and T its thickness. The effect on the resolution of the image is given by

$$d_c = \alpha C_c \frac{\Delta E}{2E}$$

where α is the objective semi-angle, C_c is the chromatic aberration coefficient and E is the beam energy.

From these equations, one can see that for samples in which $T_{water} \gg T_{SiN}$, the scattering from the SiN is negligible. However, as these two thicknesses become similar, the SiN scattering becomes more important. This is especially true when one considers that $Z_{SiN} = 12.1$, nearly twice that of water, $Z_{water} = 7.4$, and that $\rho_{SiN} = 3.44 \text{g/cm}^3$ compared to $\rho_{water} = 1 \text{g/cm}^3$ [3], [55]–[58]. This means that every 10nm of SiN has a similar effect on the resolution as 60nm of H₂O.

The resolutions arrived at from these equations represent the optimal resolution. For 1 μm of water being imaged in a 200keV, the resolution is limited to 4nm. This assumes the sample of interest is at the bottom side of the liquid – if it is instead on the top of the liquid the resolution would be ~12nm [55]. It is also worth noting that these equations do not hold for aberration corrected and scanning-TEM (STEM). STEM in particular has been shown to have particularly impressive resolutions for thick liquid samples [58]. It is also worth noting that in the case of STEM, the resolution is optimal with the focus at the top of the liquid chamber, on the beam incident side, than on the bottom of the chamber.

The resolution limits discussed above do not incorporate the scattering cross section of the sample, and for biological samples, the structures that can be resolved will depend just as critically on the contrast.

2.6.2 Contrast in In-Situ Biological Imaging

As discussed above, a great deal of biological structures consist of carbon, hydrogen, and oxygen, making it very difficult to resolve when surrounded by water. While some work has been done on heavy element containing biological materials such as ferretin, this greatly limits the reach of in-situ microscopy in biology [59], [60]. In order to account for this, we have looked to both nanoparticle labelling and heavy element staining schemes. Due in large part to the successes of fluorescent optical imaging in biology, there are a number of straightforward labelling schemes that apply for nearly all systems of interest [61]–[64]. A number of groups have used gold nanoparticles (AuNPs) as a means of labelling items and areas of interest [56], [65]–[67]. Thiol chemistry makes it simple to attach them to biomolecules with great selectivity. With these labels attached, the dynamics could be inferred by the relative motion of the attached NPs, and could be resolved with higher temporal and spatial accuracy than could be realized with optical approaches. As an example of this, Sugi et al. were able to further elucidate the mechanism for muscle contraction by labelling muscle filaments with AuNPs and imaging under TEM, as shown in Figure 2.19. ATP was introduced into the liquid cell in order to drive muscle contraction [68]. However, these labelling based approaches still provide only discrete points of reference.

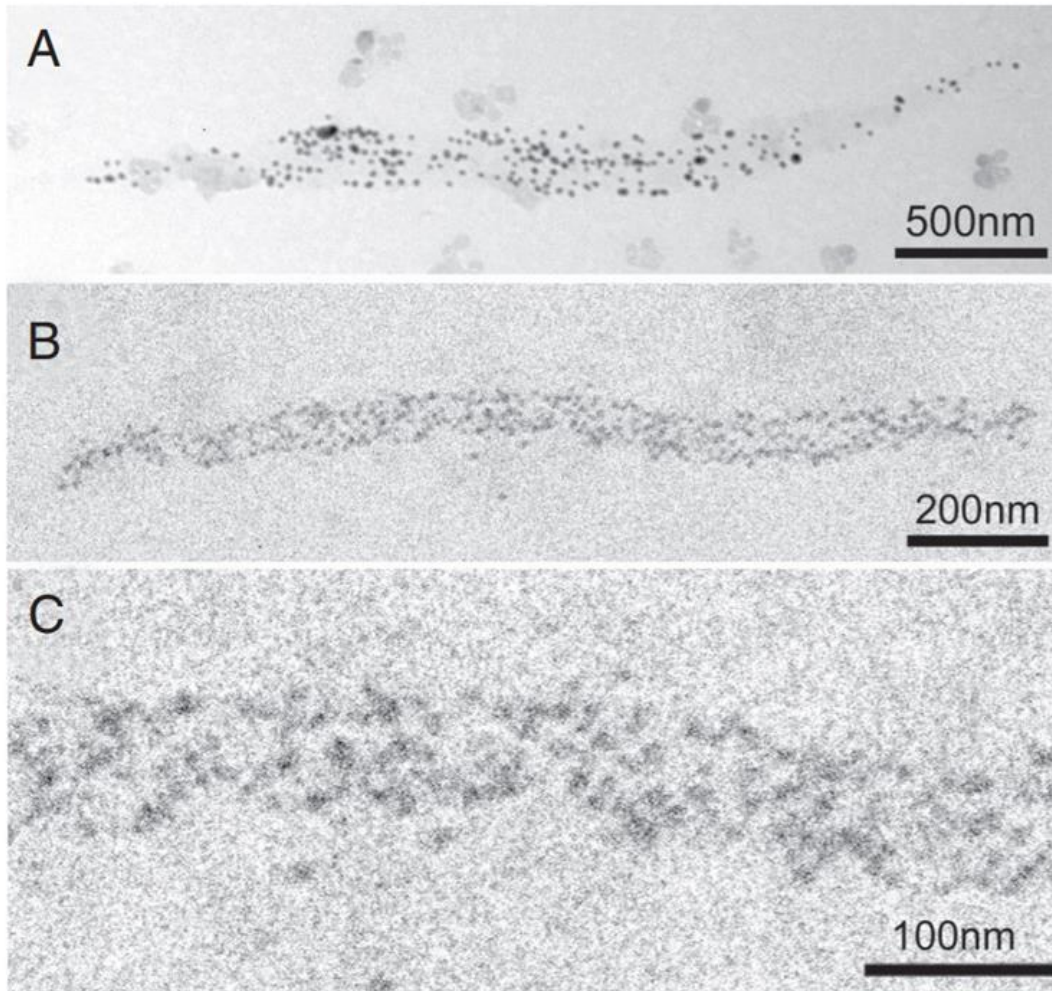


Figure 2.19: AuNP labelling of muscle filaments. (A)-(C) TEM images of muscle filaments with AuNP labelling. Adapted from Ref [68]

Instead, for more complicated dynamics, or dynamics in which the whole structure is of interest, a stain-based approach can be used. While the higher stain concentrations used for negative staining will end up interfering with cellular function, the effects can be less pronounced with lower positive staining contributions. Kennedy et al. demonstrated that with 0.01%-0.1% uranyl acetate stain, they could image the P1 bacteriophage infection of an E. Coli cell with 5nm resolution using a Scanning Transmission Electron Microscope (STEM) as shown in Figure 2.20 [69]. This work demonstrated that positive staining was not only viable for in-situ imaging, but in smaller concentrations can preserve biological function. When using such a staining technique, it is critical to confirm that the stain is not interfering with biological function. The stain can alter the pH of the solution causing degradation of the sample. It can also act to block key sites on the biological structure which are involved in the process you are

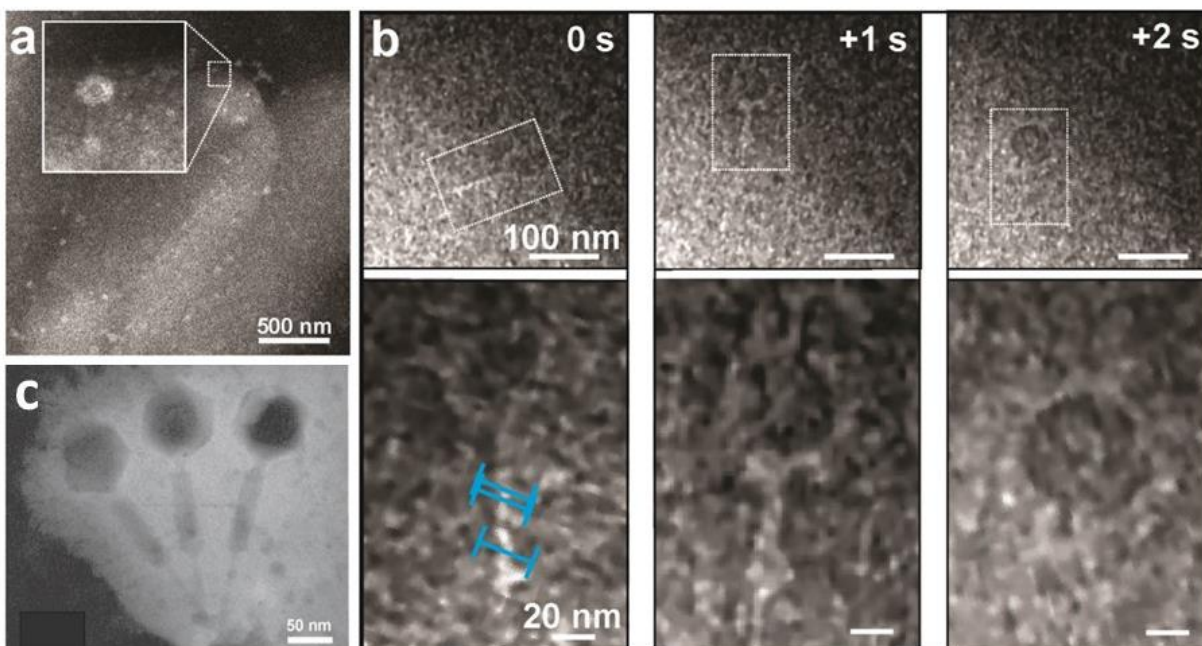


Figure 2.20: Positively stained imaging of P1 bacteriophage infecting *E. coli* cell. a) STEM image of bacteriophage on cell membrane stained with 0.01-0.1% UA. b) STEM images of bacteriophage injection process. c) Dried negative stain image of bacteriophages for reference. Scale bar is 50nm. Adapted from Ref [69].

looking to study. The viability of the stain you are looking to employ should be confirmed with traditional assays before using.

2.6.3 Beam Damage in In-Situ Biological Imaging

In order to address the issue of dose limitations, it is important to understand the various potential sources of beam damage to biological samples. While there has been a great deal of work on electron beam damage in cryo samples, there has been significantly less work on beam damage for in-situ samples. While for some types of beam damage, the two systems may behave similarly, for others the switch to a liquid environment has a significant impact. Towards this point, dramatic difference in beam dose damage has been seen between the two [70].

Knock-on damage, in which direct collisions between electrons and the sample eject atoms or introduce defects directly into the material of interest, as well as ionize or chemically alter it, is a clear path for degrading biological samples. These effects are likely similar for cryo samples as they are for in-situ [71]. The next is heating effects from the electron beam that would heat the sample beyond where the biological specimen is stable. This effect is expected to be particularly low in liquid samples in which the heat is well dissipated [55]. Instead, what appears to be the dominant effect of beam damage in in-situ EM is the creation of deleterious radicals and the changing pH from radiolysis of the water, as opposed to mechanisms of direct damage to

the biological structure. OH and hydrogen radicals, and aqueous electrons are readily formed during radiolysis, and are strongly reactive [71]–[73]. As we will discuss later, the choice of encapsulating material can affect the concentration of these harmful radicals. In the case of heating and radical species formation, it is worth noting that cumulative dose is not the only factor that needs to be considered, but dose rate can be more critical, as radicals and heat can diffuse away from the sample.

In work by Matsudaira et al., the dose limit for a protein bundle is shown to be as low as $1,100 \text{ e}^-/\text{nm}^2$ at 120kV. In this work, the structural integrity of an acrosomal bundle is inferred by monitoring the Fourier peaks of the protein image. A drop of $1/e$ is seen as intolerable damage to the protein. Interestingly, they found that the damage was worse for cryo samples than in-situ ones [70]. What little work has been done on beam damage of biological samples in-situ has primarily looked at structural effects, and ignored function or dynamics. The work of Kennedy et al. described above was some of the first to look at a dynamic process under beam irradiation and suggests that while a critical factor, beam damage is a surmountable obstacle.

While SiN based cells have demonstrated a great deal of utility, new materials have shown great promise in further improving in-situ microscopy. While in-situ microscopy has shown potential for biological specimens, it has not made the substantial contributions to our understanding of cellular processes that cryo-EM has made for structural biology. Improving resolution through thinner samples and encapsulating materials, improved contrast through evolving staining and labelling schemes, and reducing the effects of beam damage would push in-situ microscopy into this realm.

2.6.4 Graphene Liquid Cells for Biological Imaging

Driven by the successes of GLCs in studying nanoparticles and crystallization, as well as cryo-TEM and the increasing role of electron microscopy in biology, applying the newly developed GLC technique to biological samples became a clear target for a number of groups. Park et al demonstrated a technique for imaging fixed biological cells as well as viruses encapsulated in GLCs, as shown in Figure 2.21A&B [74]. Chen et al demonstrated that AuNPs linked by DNA could also be stably imaged in GLCs, as shown in Figure 2.21C [75]. Beyond improved resolution, graphene has also been shown to improve sample stability, particularly for biological systems. In the study mentioned above, Chen et al. first demonstrated that DNA-AuNP barbells in a graphene liquid cell appear to remain intact for significantly longer times in graphene liquid cells than typical SiN cells [75]. Cho et al. later showed that this improved stability is owed to graphene's role as a radical scavenger, reducing the presence of reactive radicals that would otherwise degrade biological specimens [76]. This suggests that the dominant source of biological specimen damage is not knock-on damage from the electron beam, or

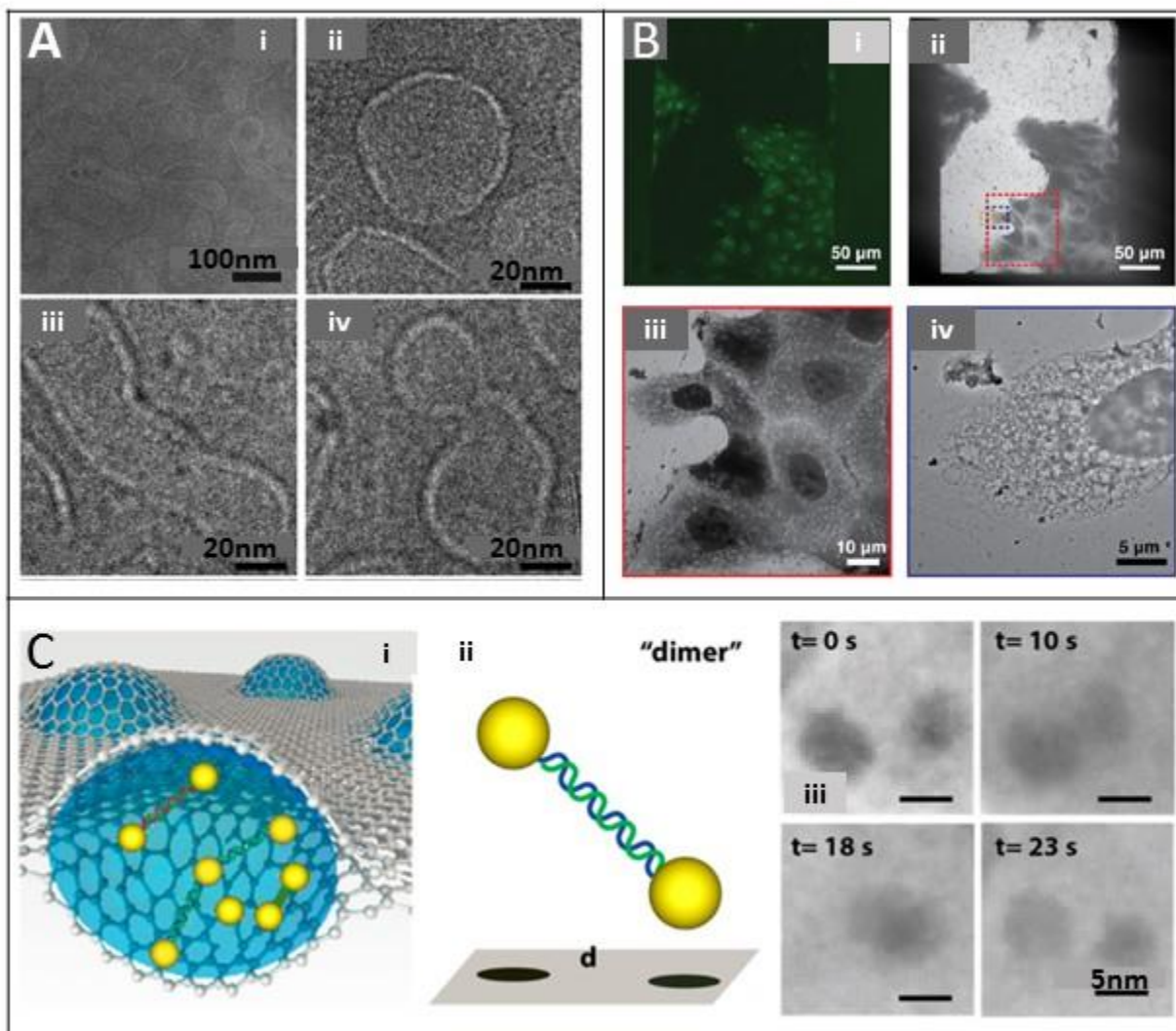


Figure 2.21: Biological Specimen in Graphene Liquid Cells. A) H3N2 virus. i-iv) TEM images of unstained H3N2 viruses. Contrast is attributed to hemagglutinin in the cell membrane. B) MDCK cells. i) Fluorescence image of MDCK cells encapsulated in graphene. ii-iv) TEM images of same MDCK cells. A-B adapted from Ref [74]. C) AuNP DNA barbells. i) Cartoon of GLCs. ii) Cartoon of AuNP DNA barbell and the TEM projection image. iii) TEM images showing the rotation of the barbell in a time series. Adapted from Ref [75]

thermal degradation caused by heating from the beam, but from beam induced changes in the solution itself. It is worth noting that each of the above studies focused on structural stability, and little to no work has been done on studying the functional stability of biological processes in graphene liquid cells under electron irradiation [74]. In fact, while this work suggests the incredible potential that graphene liquid cells have in imaging dynamic biological processes, as is the case with SiN cells, there has been very little work demonstrating this.

Despite the promise and advantages of graphene liquid cells, they hold a number of drawbacks which have greatly limited their application. For starters, the liquid trapping is highly random, creating pockets of varying size, morphology, and concentrations throughout an individual sample. The size and shape of the liquid container can be critical in evaluating the reactions and particle dynamics in the cell. In addition to this, the static nature of the sealed cells means it is impossible to introduce reactants during imaging. While there has been some success using the electron beam itself to initiate reactions, this severely limits the applications [16]. For attempting to image biological dynamics, this proved to be a major difficulty. The reactants needed to drive a process were either spent by the time imaging took place, or their levels were so low that the dynamics would be too slight to be seen. The evaporative nature of the sealing of the two graphene sheets introduced another major difficulty for samples, in particular biological ones. The reliance on evaporation to encapsulate the sample makes concentration impossible to control. For most biological processes and systems, pH and salt concentration are critical. In addition to this, heavy-atom stains need to be precisely balanced and reactants concentrations need to be controlled.

We first worked to address these issues in a new generation of graphene liquid cells, which allowed for consistent and repeatable pocket sizes and volumes. Then, in order to fully realize the promise of graphene as an encapsulating material for in-situ electron microscopy, we set out to combine its benefits with those of SiN flow cells, developing the Graphene Flow Cell.

Chapter 3

Graphene Enabled Static & Flow Cells – Fabrication and Scientific Results

3.1 Graphene-sealed Si/SiN cavities

3.1.1 Overview

As discussed earlier, while the original Graphene Liquid Cell (GLC) architecture demonstrated that graphene is an ideal sealing layer and electron-transparent viewing window, they trapped irregular geometries of liquid with unknown sample volumes. In order to produce more controlled samples, we developed a technique for the leak-proof confinement of liquids of precise volume in the tens of attoliter range, while maintaining the benefits of graphene as a viewing window [77].

This work was done with postdoc Dr. Haider Rasool, and former graduate student Dr. Aidin Fathalizadeh. Dr. Rasool took part in the design, fabrication, microscopy and analysis of this work. Dr. Fathalizadeh took part in the fabrication, and I took part in the fabrication and analysis.

3.1.2 Design and Fabrication

Two different liquid cell geometries are made using graphene as the sealing material: a well-type cavity where pits are etched into a silicon chip and graphene is used to seal the top-side, and a channel-type cavity where ~500nm diameter holes are etched into a suspended silicon nitride membrane and graphene is used to seal both sides, as shown in Figure 3.1. In both cases, the cavities are formed by focused ion beam (FIB) milling. The channel-type cavity is ideal for

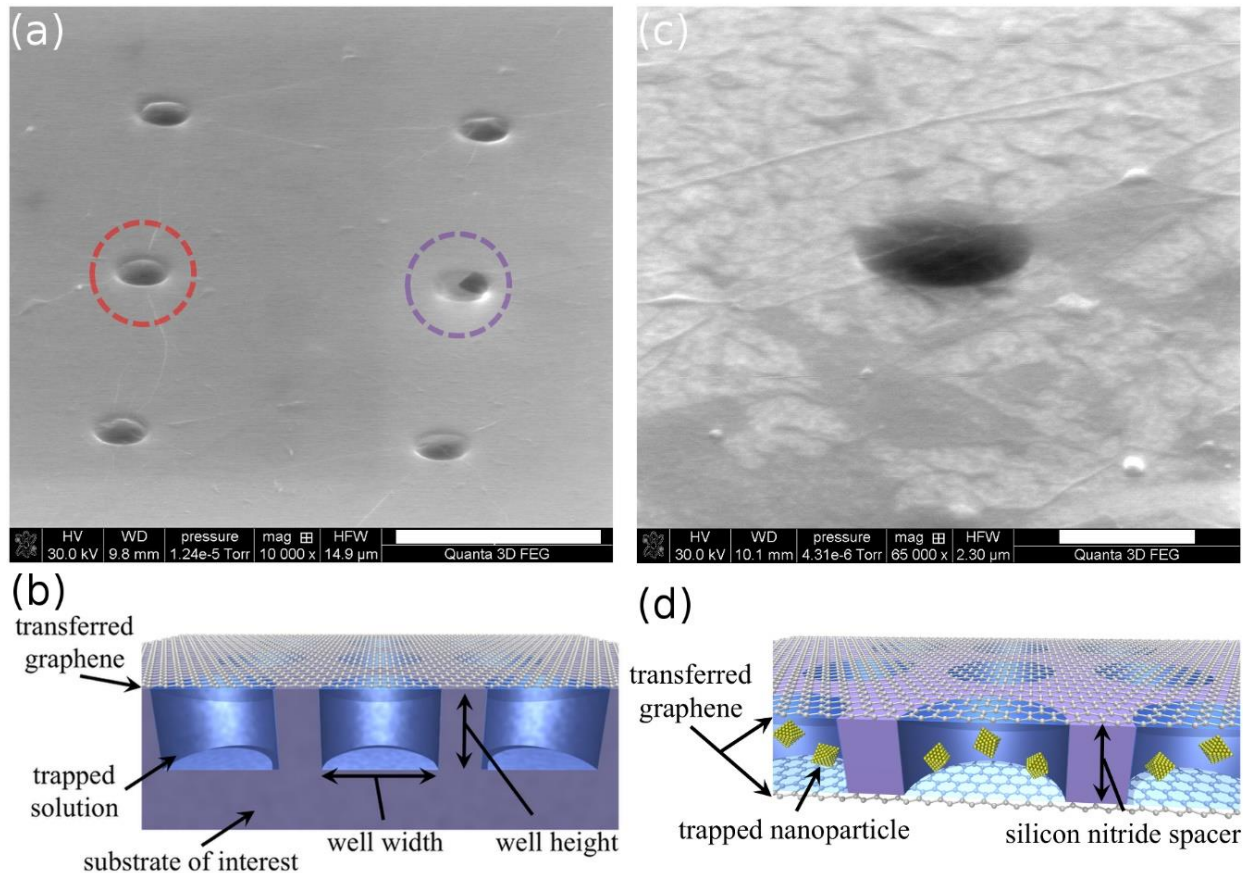


Figure 3.1: Graphene Sealed SiN Cavities. (a) SEM image of well-type liquid cell. Red circle shows in-tact graphene sealing layer with trapped liquid creating a bulge in the graphene film. Purple circle shows torn graphene sealing layer where no liquid is trapped. Scale bar is $5\mu\text{m}$ (b) Schematic of well-type liquid cell. Scale bar is 500nm . (c) SEM image of channel-type liquid cell. The smaller hole size shows less bulging. (d) Schematic of channel-type liquid cell.

in-situ TEM, as the total sample thickness is determined by the silicon nitride membrane, and the viewing path consists of only our sample and single atom thick layers of graphene.

A schematic of the assembly and sample encapsulation of the graphene capped liquid cells is presented in Figure 3.2. Single-layer graphene is first grown by chemical vapor deposition (CVD) on copper foil and one side is subsequently etched by oxygen plasma. A thin layer of PMMA A4 is spun onto the graphene side of the copper foil, and the copper foil is then placed in an etchant bath of sodium persulfate in water ($\sim 2\text{g/mL}$) to remove the copper substrate. The film is then transferred to multiple baths of DI water to prevent any residual sodium persulfate. The film is again transferred to a bath of the desired trapping solution. A substrate with fabricated wells or holes is submerged into the bath and, in a single step, the receiving substrate is withdrawn from the solution pulling the graphene-PMMA film onto the surface and encapsulating the solution. Excess solution is removed from the surface with an absorbent. The sample is allowed to sit for 12 – 16 hours to enhance graphene adhesion to the substrate before

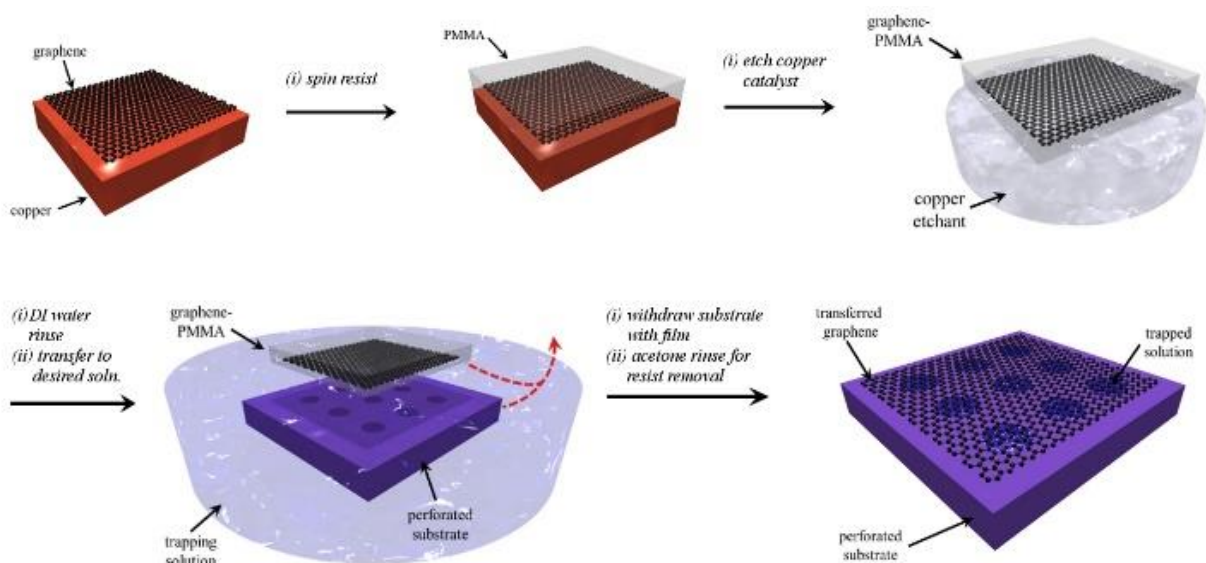


Figure 3.2: Graphene is CVD grown on a copper substrate, then coated in a thin layer of PMMA. The Cu substrate is etched away and the graphene/PMMA is transferred to a DI water rinse followed by the desired trapping solution. The sheet is then scooped out by the substrate with patterned cavities. For the capped-hole type cell, this procedure is repeated for both sides of the nitride membrane.

the PMMA is removed with acetone, and the sample is rinsed in IPA. In the case of the double-sided graphene sealed channel-type cells, the process is only slightly modified. The above steps are followed to apply the first graphene film to one of the sides of the silicon nitride after the water rinse and allowed to adhere to the substrate for 12 – 16 hours. The graphene then provides the base of the well for the trapping of a desired solution in the above steps [25-26].

Sample encapsulation can be confirmed by SEM as is shown in Figure 3.1(a)-(b). Slight bulging can be seen by the shading on the graphene film under SEM and is due to the pressure differential between the trapped liquid and high-vacuum environment of the SEM, as well as the surface tension of the sample. When the graphene is torn or a hole is present, the liquid readily evaporates, and the remaining suspended graphene shows no bulging and the shading is then absent in the SEM scan.

3.1.3 Results

Using the described trapping method for a channel-type cell, we trap a solution of 10nm gold nanoparticles (AuNPs) suspended in a phosphate buffer solution (PBS) to study the motion and interactions of the nanoparticles. PBS is a common solution used in biological experiments, which mimics the physiological conditions of a cell and is easily trapped using the above procedure. It is worth noting that were the acetone or isopropyl alcohol used to remove the

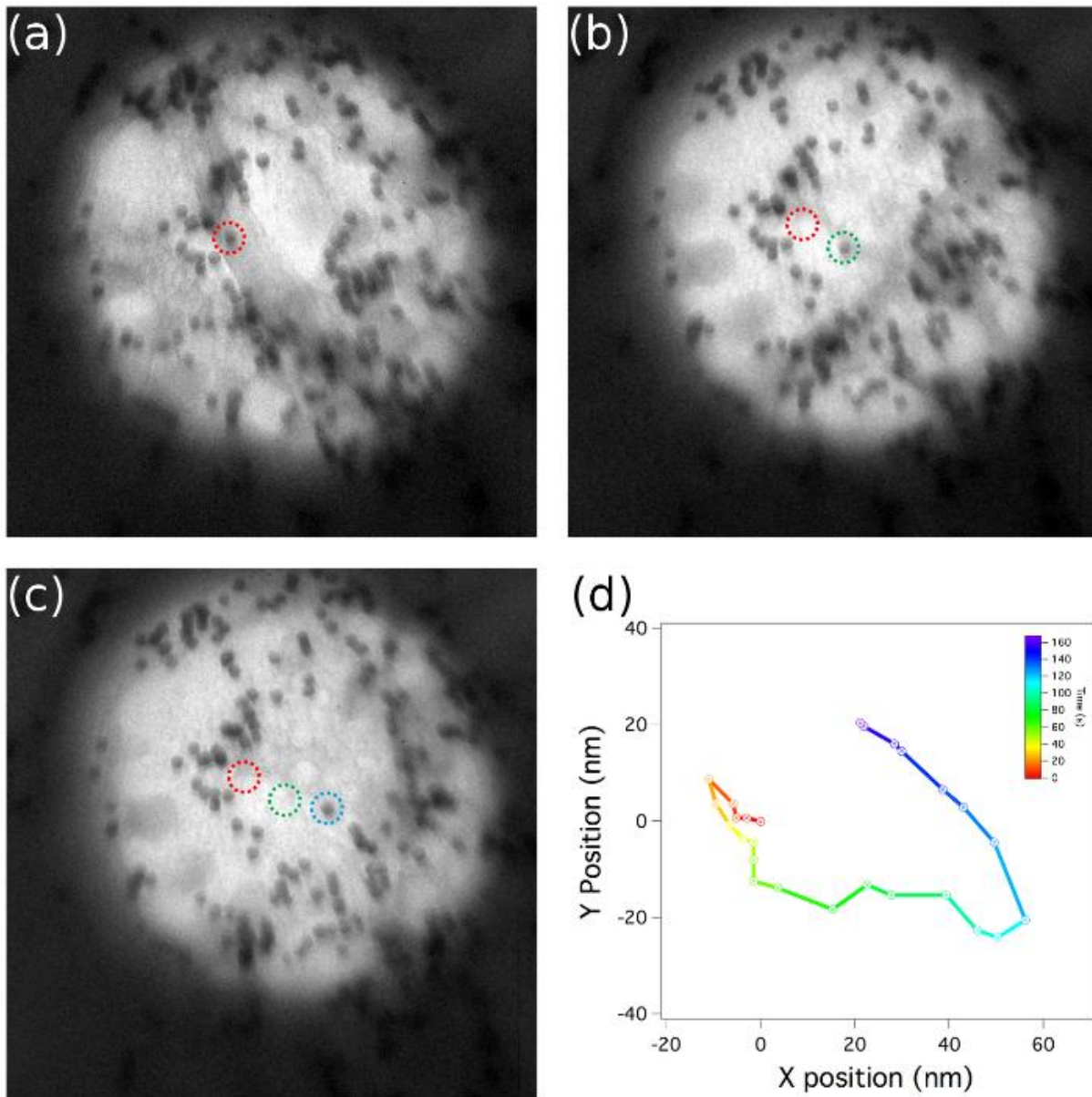


Figure 3.3: AuNP Dynamics. (a)-(c) TEM time series snapshots of Au-NPs trapped in a phosphate buffer solution. Bubbles formed by the hydrolysis of water under the electron beam drive the nanoparticle's movement. (d) Time series plot of the motion of the circled nanoparticle as it moves around the cell.

PMMA from the graphene to have entered the cell, the buffer solution and the AuNPs would crash out of solution.

At lower dose rates, the cells appear stable and can be imaged indefinitely. However, upon exposure to a high intensity beam of illuminating electrons, the AuNPs begin to move within the cavity. The motion of one of the 10nm AuNPs inside a 400nm wide and 200nm thick liquid cavity is highlighted in Figure 3.3 using the Zettl lab's JEOL 2010 TEM at an acceleration

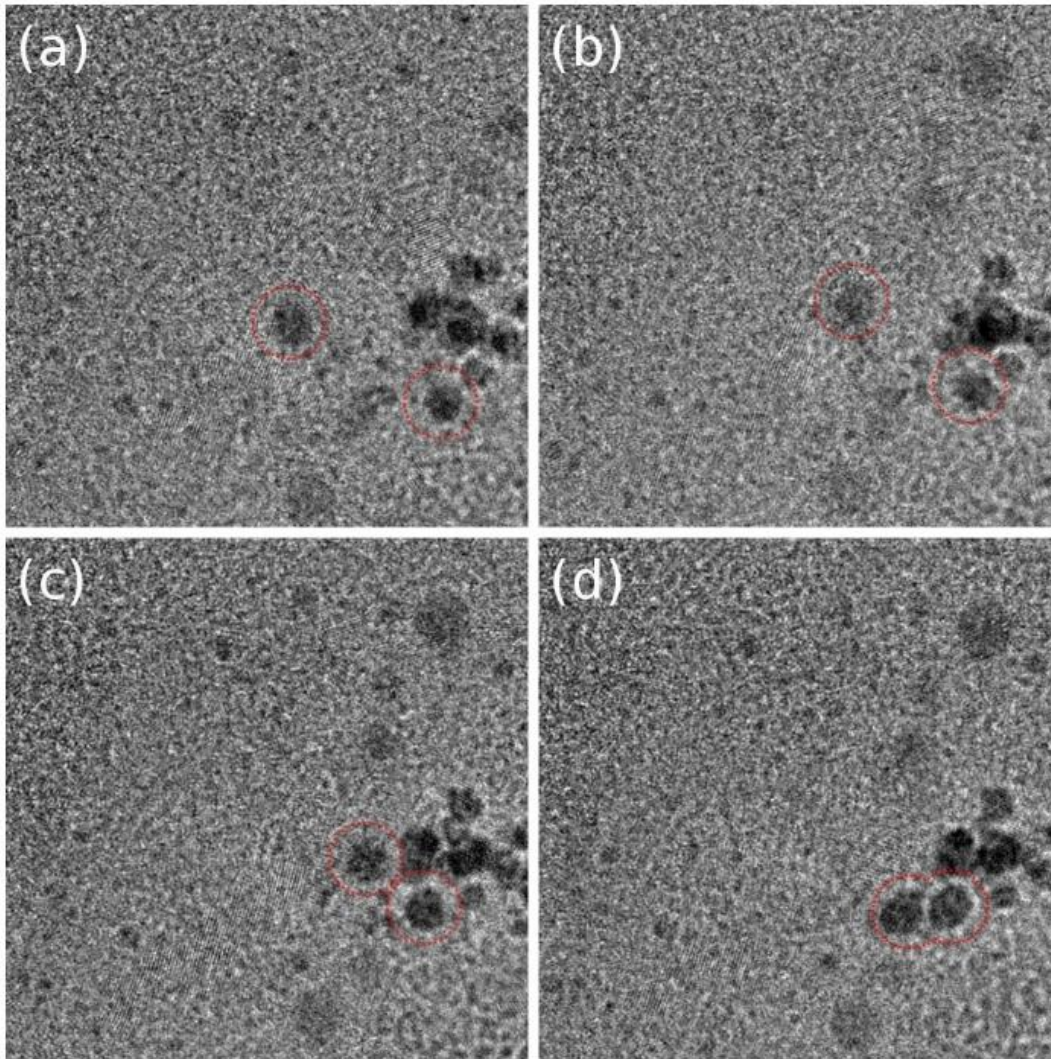


Figure 3.4: 3D Nanoparticle Tracking. (a)-(d) TEM images of the axial motion of the two circled nanoparticles. While the other particles remain in the focal plane, these two fall out of focus and develop a bright ring around them, consistent with travelling out of the focal plane.

voltage of 80kV. The particle begins with small movements with subsequent motion likely driven by the formation of expanding bubbles generated by radiolysis of water under electron beam irradiation. As the fluid current and oscillations evolve with time, the dynamic forces on the NP evolve as well, and generate large motions within the liquid chamber. After imaging at high intensity for upwards of ten minutes, particle motion will cease and the cell will appear dry. This is likely due to a combination of tears in the graphene produced by electron beam damage or etching from radiolytic byproducts, and hydrolysis of the solution.

In addition to being able to image large-scale particle motion in the liquid cavity, it is possible to observe three dimensional (3D) particle motion at atomic resolution. Figure 3.4 shows a sequence of images taken with the Transmission Electron Aberration-Corrected Microscope 0.5 (TEAM 0.5) managed by the National Center for Electron Microscopy operated

at 80kV, where two particles move toward each other in the lateral plane while simultaneously changing their height within the cell. This change in height is evidenced by the change in the focus of the particles with time. In Figure 3.4a the two particles appear close to the focal condition of minimum contrast and as the particles move to the positions imaged in Figure 3.4b, they develop Fresnel fringes indicating a change in height of the particles. The magnitude of this axial motion can be estimated from the transport of intensity equation as shown by Zhang and Oshima [27]. While observing three-dimensional motion of the NPs in Figure 3.4 and in Figure 3.5, we observe clear atomic lattice fringes, allowing for further studies on particle rotations and surface reactions. With the ability to observe three-dimensional motion with atomic resolution it is now possible to consider developing 3D particle tracking to observe a particle for an extended period of time and understand particle motion in confined space.

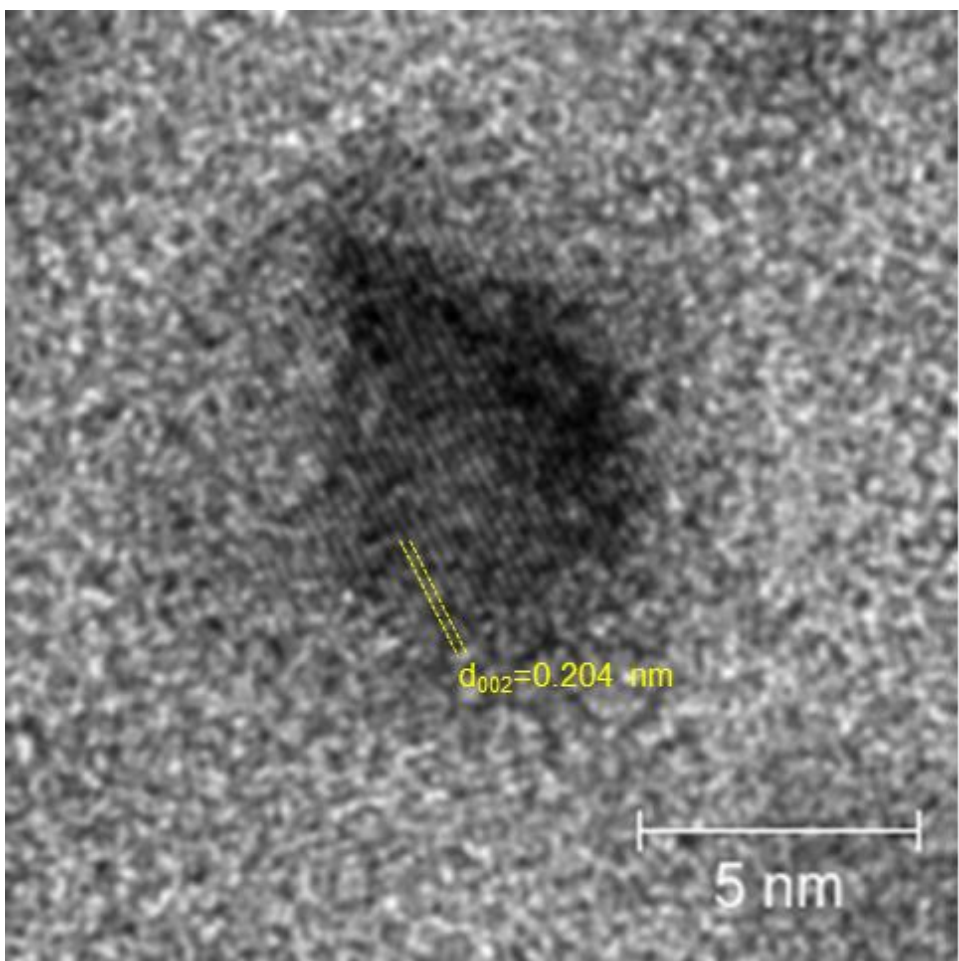


Figure 3.5: Atomic Scale Resolution of AuNP. In-situ TEM image of Au-NP in PBS demonstrates atomic-scale resolution. Lattice planes are clearly visible and spacing is consistent with the Au lattice constant.

3.1.4 Conclusion

While the liquid cell architecture described above represents a significant improvement to the initial GLC design, a number of the issues we described above still remain. The static nature of these liquid cells mean that new reactants can not be introduced shortly before or during imaging. The reliance on evaporative sealing also makes the final concentration of the solution being imaged highly variable.

3.2 Graphene Flow Cell – Design and Fabrication

3.2.1 Overview

In developing the Graphene Flow Cell (GFC), we sought to combine the benefits of the graphene liquid cell – namely the increase in contrast and resolution, the absence of charging effects, and the improved dose limits for biological specimens – with the versatility of commercial SiN flow cells – being able to precisely control solution concentration and introduce reactants while imaging.

In addition to the incorporation of graphene as an imaging window, integrating a nanofluidic channel on a single chip marked a significant design improvement as opposed to relying on the sandwiching of two chips to form the sample. This allowed for a significantly thinner sample, and reduced the considerable bowing seen in commercial nitride flow cells. The design of the GFC was made to be compatible with the Protochip's Poseidon system, shown in Figure 3.6, so as to allow us to use their TEM holder and fluidics. In contrast to the Poseidon system, our top chip serves as an o-ring to isolate the sample from the high-vacuum environment of the TEM, as opposed to an encapsulating layer. An illustration of our two chip assembly is shown in Figure 3.7.

The two chips are sandwiched and bonded and then loaded into the Poseidon TEM holder. Samples can be introduced via a syringe pump connected to the holder. Two test setups were developed to verify the integrity of the setup: an optical setup allowing one to see liquid filling the channel as well as any large leaks, and a high-vacuum test setup which detects small leaks.

This work was performed primarily by postdoc Dr. Vivek Adiga, undergraduate Chris Bryant, and myself. Dr. Adiga and I were responsible for the design of the cell, while Chris and I were responsible for the device fabrication. TEM imaging was performed by Dr. Hamid Barzegar, Dr. Jongmin Yuk, and Thang Pham.

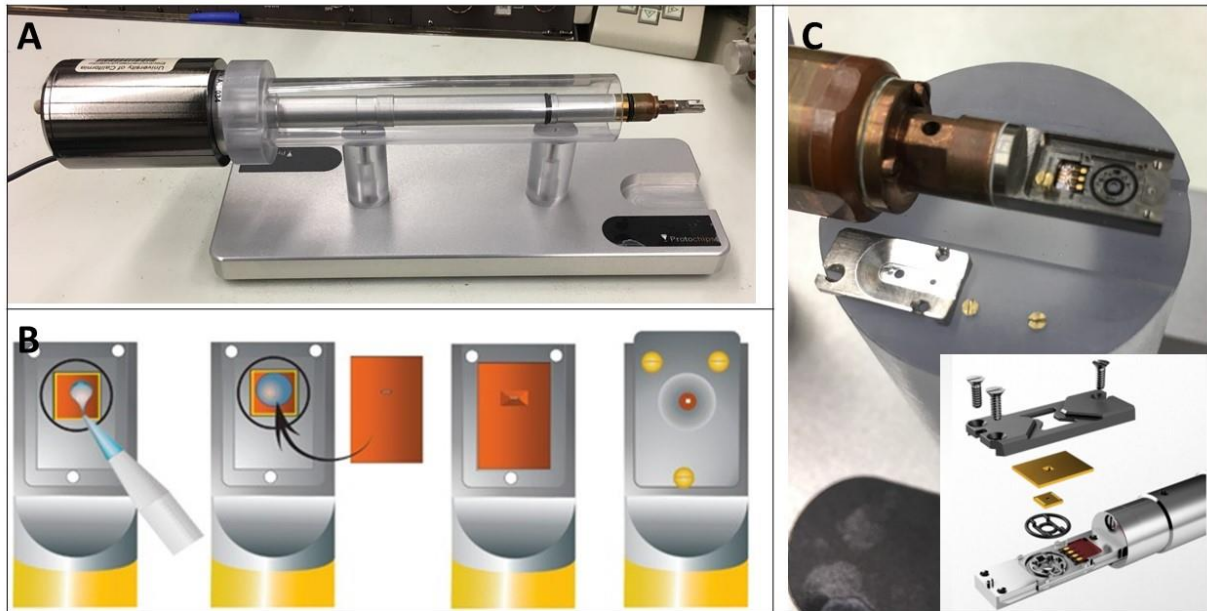


Figure 3.6: Protochips Poseidon Flow Holder. A) TEM holder. B) Chip loading for standard Poseidon use. Small chip is loaded, a droplet of solution is placed on top, this is then sealed by the top chip and the headpiece is screwed shut. This is distinct from the bonded chip setup we will be describing for the Graphene Flow Cell. C) TEM holder headpiece. Two o-rings seal the liquid environment between the two chips and isolate it from the vacuum of the TEM.

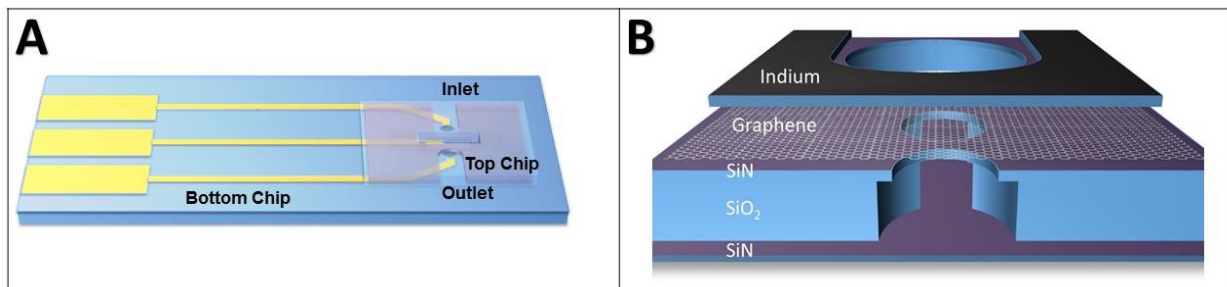


Figure 3.7: Illustration of Graphene Flow Cell (GFC). A) The two chips assembly which forms the GFC. B) Longitudinal cross section view of the nanochannel.

3.2.2 Fabrication:

The top and bottom chips were fabricated separately on 300 μm thick silicon wafers in the UC Berkeley Marvell Nanolab and using tools in the Zettl lab. The wafer thickness needs to be at a tolerance of $\pm 10\mu\text{m}$ or the o-rings won't create a seal. While the larger chip is referred to as the bottom chip, and the smaller chip as the top chip, the two are loaded into the TEM flipped upside down, so the electron beam is incident on the bottom side of the assembly first. I will discuss the fabrication of the two chips independently before describing the assembly and bonding process.

3.2.2.1 Bottom Chip

The fabrication steps for the bottom chip are shown in detail in Figure 3.8. A silicon nitride/silicon oxide/silicon nitride stack is grown by PECVD on the wafer using the tystar17 furnace in the nanolab (STDNITA recipe for nitride and HTOXIDE for the oxide). Our initial chips used SiN/SiO₂/SiN stacks with thicknesses of 50nm/100nm/50nm respectively. Our next chips used 14nm/75nm/7nm. The top (14nm) nitride layer will be etched and covered with graphene, so is less harmful to the imaging resolution than the thickness of the bottom layer (7nm). However, because the graphene will seal on top of the layer, this thickness will be replaced by the sample solution, so it is still advisable to keep it relatively thin. The oxide thickness will determine the channel thickness. Wetting the channel will be discussed in further detail later in this chapter, but channel thickness will play a major role in how easy it is to drive solution across the channel. While at 100nm, this was fairly straightforward, 75nm required more work, and much below this will require additional work.

Gold or platinum contacts are then patterned and evaporated onto the wafer using photolithography (nanolab ksaligner and iline photoresist) and electron beam evaporation (Zettl lab). It is worth noting that while these contacts were intended for electrochemistry experiments, the indium sealing method we ended up using shorts these contacts; however, they are still necessary as alignment patterns for subsequent steps. In the future, if a non-conducting bonding method like SU8 or other epoxy is used, these electrodes could provide a new avenue of research.

In order to release the SiN/SiO₂/SiN stacks from the silicon substrate, a KOH backside etch is performed. Before beginning, the top side of the wafer was coated in photoresist to protect it from scratches during processing. The backside of the chip is then coated in i-line and areas to be etched are patterned by photolithography (ksaligner). The exposed areas are etched using an SF₆ based reactive ion etch (RIE). While there are a number of SF₆ etchers on campus, the lam6 system in the nanolab provides the most conformal etch across the wafer as well as the highest selectivity for nitride and oxide over bare silicon. This will significantly improve device yield. Because lam6 uses an electrostatic chuck and both sides are covered in photoresist, the wafer is first bonded to a 6" dummy wafer before loading into the etcher. The wafer is placed in an acetone or photoresist stripper bath. Before KOH etching, the topside is spin coated in Protek B3, an alkaline etch resistant adhesive coating which protects the topside during the etch. It is




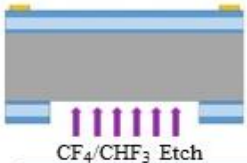
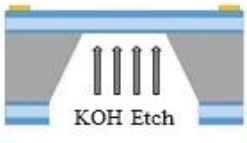
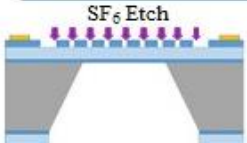
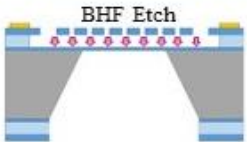
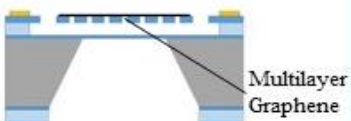
| <u>Schematic</u> | <u>Description</u> |
|---|---|
|  <p>A grey rectangular block representing a silicon wafer, with a label 'Si' pointing to its right side.</p> | 300±10um thick <1-0-0> orientation 4" silicon wafer. |
|  <p>A cross-section showing a grey silicon wafer with a stack of three thin layers on top: a blue layer labeled 'SiN', a white layer labeled 'SiO2', and another blue layer labeled 'SiN'.</p> | SiN:SiO2:SiN stack grown by PECVD in nanolab's tystar17. |
|  <p>The stack from the previous step with small yellow rectangular blocks labeled 'Au' deposited on the top surface.</p> | I-line photoresist was exposed in nanolab's ksaligner (10s) and developed. A brief oxygen plasma etch was done before evaporating Cr: Au::3nm:50nm in the Zettl lab e-beam evaporator, followed by lift-off. |
|  <p>The wafer with a protective layer of photoresist (PR) on top. Purple vertical lines represent the etched pattern. Below the wafer, the text 'CF4/CHF3 Etch' is written.</p> | I protective layer of PR was spun on the topside of the wafer. The bottom side was patterned using i-line and ksaligner's backside alignment. The backside pattern was etched to the underlying silicon in lam6 (nanolab). Oxygen plasma cleaned to remove etch byproducts. |
|  <p>The wafer with a trapezoidal channel etched into the silicon. Three vertical arrows point upwards from the channel. Below the wafer, the text 'KOH Etch' is written.</p> | Protek B3 protective coating was spun onto the topside of the wafer before etching in 20% KOH at 80C (5-6hr) on hotplate in Zettl lab. Followed with multiple DI baths to remove KOH residue, then protek removal in acetone and MIAK (protek remover). |
|  <p>The channel from the previous step with small purple rectangular blocks on top. Below the wafer, the text 'SF6 Etch' is written.</p> | Dot lines patterned in ZEP-520A with a dose of (?). SF6 plasma etched (5sccm SF6, (?W) in Zettl lab RIE (etch rate: ~(?))nm/s). Light oxygen plasma clean afterwards. |
|  <p>The channel with small red circular dots on top. Below the wafer, the text 'BHF Etch' is written.</p> | Channel opened in underlying SiO2 by BHF dip. With dot spacing of (?), 255s(?) etch required. ZEP then removed in (?). |
|  <p>The channel with a thin grey layer on top, labeled 'Multilayer Graphene' with a line pointing to it.</p> | Multilayer graphene CVD grown in atmospheric growth. Wet transfer to substrate with PMMA. A drop of IPA will ensure the graphene clings to the chip surface. PMMA removed with acetone or annealing. |

Figure 3.8: Schematics of bottom chip fabrication process.

then immersed in a 20% KOH solution at 73°C for ~6hrs to etch the exposed silicon. A slightly lower temperature than the standard 80°C was used to limit bubbles in the etch area which caused significant variation in etch times across the wafer. Small Teflon blocks were used to weight the wafer and prevent it from floating to the top. The wafer is then soaked in three sequential DI water baths to prevent residue from the KOH, then the Protek film is removed in Protek remover. The wafer was then diced into individual dies. In order to protect the membranes during dicing, a layer of photoresist is spun on top. The chips were then diced either using a commercial service or the nanolab's dicing saw (disco). The chips are made to be compatible with the Protochips Poseidon holder, so dicing to the correct chip size is important. With the mask layout I have made for these chips, it assumes a kerf of 45µm. All remaining work was done dye by dye and was performed in the Zettl lab.

In order to create an integrated channel in the SiN/SiO₂/SiN stack, small holes were etched into the top nitride layer and the underlying oxide was wet etched. The chip was coated in 2 or 3 layers of PMMA A4 depending on the thickness of the nitride to be etched. Dots were then e-beam patterned in an NPGS enabled SEM with a point dose of 500fC at 30kV. The dot spacing was set to 0.5µm, 1µm, or 1.5µm and would determine how much oxide would need to be removed to form a continuous channel. The top layer of SiN was etched using an SF₆ plasma etch at 100W w/ 5sccm of SF₆ for 90s for 14nm nitride and 270s for 50nm thick. The chip was then dipped in a buffered HF solution (BHF) which would etch the oxide at a rate of 38Å/s. For chips with 50nm spacing, I used an etch time of 120s. Especially for the chips with thinner nitride, longer etch times will result in the nitride layers collapsing onto one another. Figure 3.9 shows an example of a collapsed channel vs a suspended one. After the oxide etch, the photoresist is removed in an acetone bath.

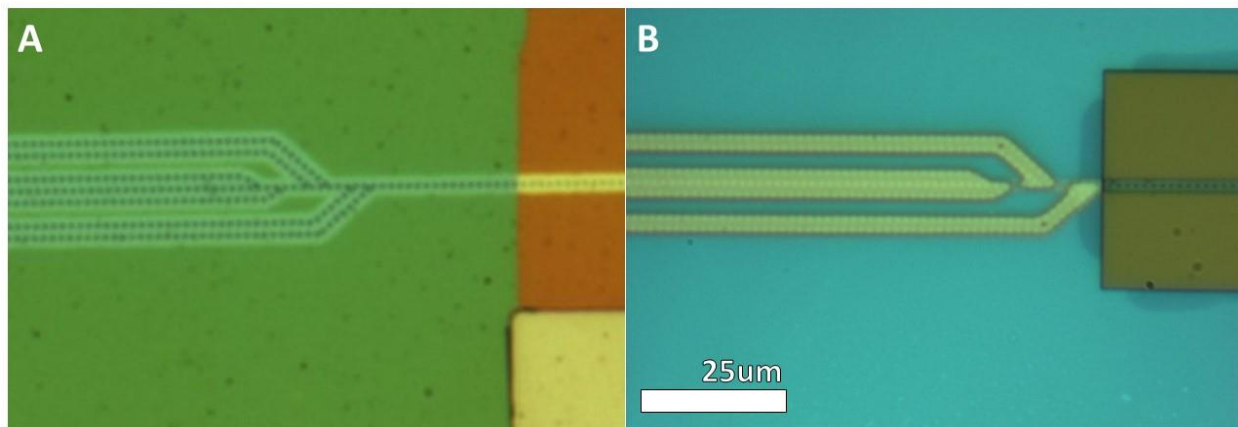


Figure 3.9: Channel collapse. A) Optical image of a non-collapsed channel. B) Optical image of a collapsed channel as seen by the contrast around the collapsed regions of the channel.

A square of multilayer graphene is then transferred onto the chip, sealing the holes in the nitride. Multilayer graphene is used instead of single layer because any tears in the graphene suspended over the nitride holes will cause a leak. Few-layer graphene is grown by chemical vapor deposition on copper foil at atmospheric pressure. The foil was coiled (for higher yield) inside a 1" quartz tube and annealed under 200sccm H₂ in vacuum at 1025°C for 1hr. The vacuum valve was then closed, and the tube was allowed to pressurize to 1atm before opening the exhaust valve. 18sccm CH₄ was then introduced in addition to the 200sccm H₂ for a 1hr growth time [78]. The presence of multilayer graphene was confirmed by Raman, where the G peak would be approximately twice the size of the 2D peak. The D peak was always present in all multilayer growths we performed using this method. The top side of the copper foil was then spin coated in PMMA, and the graphene on the backside was etched in an oxygen plasma. The foil was cut into small pieces which were floated in a bath of Na₂SO₃ solution to etch away the copper, leaving the graphene suspended on the liquid's surface. The graphene was then transferred to water baths and finally scooped onto our top chip. A small droplet of IPA ensures the graphene seals well to chip, then the PMMA is either baked off at 500°C under H₂ in a tube furnace, or dissolved in acetone. Figure 3.10 shows the resulting chip, as well as an SEM of the nanochannel both with and without graphene.

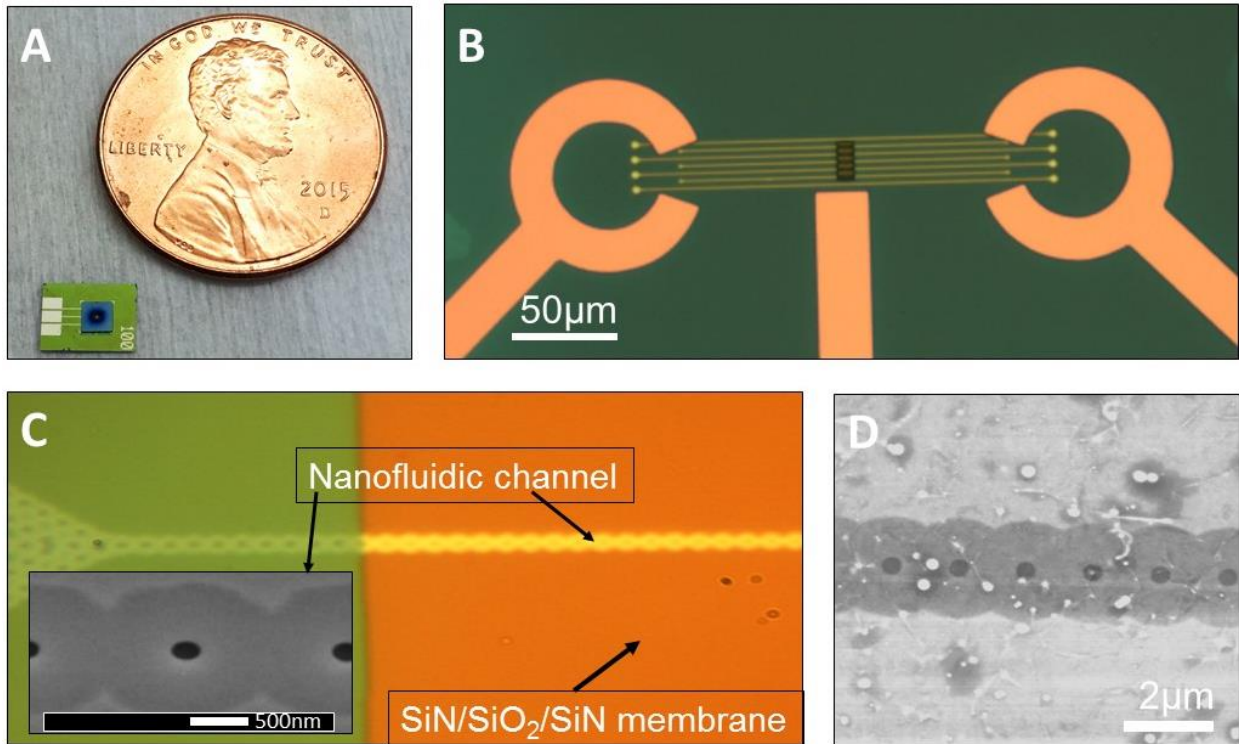


Figure 3.10: Finished bottom chips. A) Picture of assembled chip next to US penny for scale. B) Optical image of chip with multiple channels. C) Optical image of an individual channel, with an SEM inset of a typical section of the nanofluidic channel. D) SEM of a graphene covered channel. Circles of darkest contrast are the holes in the top SiN layer, and the concentric lighter contrast area around them is where the SiO₂ has been etched away.

3.2.2.2 Top Chip

The fabrication steps for the top chip are shown in detail in Figure 3.12. The process described here was that used for indium bonding of the chips together. As will be discussed later, these chips were originally designed for an SU8 spacer which would serve as the bonding material. Similar to the bottom chip wafer, the wafer must be $300\mu\text{m}$ thick with a tolerance of $\pm 10\mu\text{m}$. 20-50 μm deep channels are etched into the chips to allow for the sample liquid to reach the inlet and outlet ports. The channels are first patterned on the wafer in g-line photoresist. The channels are then etched with a deep reactive ion etch (DRIE) performed on the sts2 tool in the nanolab.

A layer of silicon nitride of arbitrary thickness was then deposited by PECVD to serve as a KOH etch mask. The nitride was grown in the tystar17 furnace using the STDNITA recipe. The backside of the wafer was then patterned and the nitride etched, followed by a KOH etch in the same manner as described above for the top chip. The SiN was then etched from the topside as well in order to remove the membrane. Optical images of the chip can be seen in Figure 3.11.

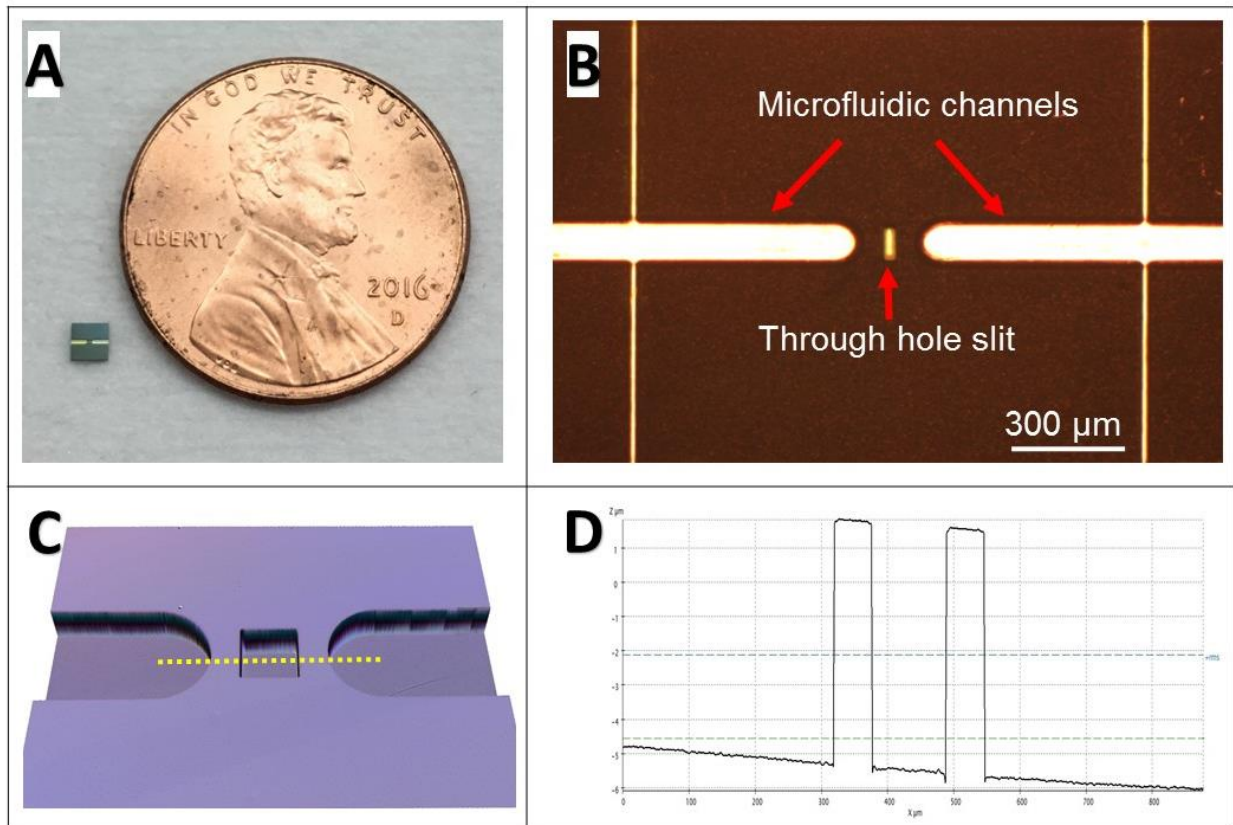


Figure 3.11: Finished top chip. A) Top chip shown next to a US penny for scale. B) Optical image of pattern on top chip. C) 3D confocal mapping image of the chip showing defined microfluidic channels. D) Height profile of dotted line shown in (C). The step height of the microfluidic channels is $7.2\mu\text{m}$.




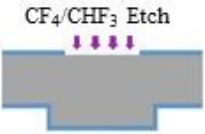

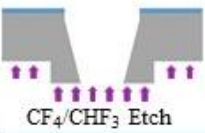

| <u>Schematic</u> | <u>Description</u> |
|---|--|
|  <p>A rectangular grey block representing a silicon wafer. A label 'Si' is positioned to the right of the block.</p> | <p>300±10µm thick <1-0-0> orientation 4" silicon wafer.</p> |
|  <p>A schematic showing a grey wafer with a central rectangular hole. Purple vertical bars on either side of the hole represent the etching process. The text 'C₄F₈/SF₆ DRIE' is written below the wafer.</p> | <p>Futurex negative resist spun on and patterned in nanolab's ksaligner. 10-20µm depth Deep Reactive Ion Etch (DRIE) using nanolab's sts2. Futurex removed with oxygen plasma asher – matrix in nanolab.</p> |
|  <p>A schematic showing a grey wafer with a central hole. A blue layer, representing SiN, is deposited over the entire surface, including the top of the hole. A label 'SiN' is positioned to the right of the layer.</p> | <p>SiN film of arbitrary thickness grown by PECVD using nanolab's tystar17 furnace.</p> |
|  <p>A schematic showing a grey wafer with a central hole. A blue SiN layer is on top. Purple vertical bars on the top surface of the wafer represent the etching process. The text 'CF₄/CHF₃ Etch' is written above the wafer.</p> | <p>Backside alignment and patterning using ksaligner. SiN etched until underlying Si using lam6 in nanolab. (Note: Backside facing up in schematic)</p> |
|  <p>A schematic showing a grey wafer with a central hole. A blue SiN layer is on top. Two vertical black arrows pointing downwards from the top surface of the wafer represent the KOH etch process. The text 'KOH Etch' is written above the wafer.</p> | <p>Protek B3 protective coating was spun onto the topside of the wafer before etching in 20% KOH at 80C (5-6hr) on hotplate in Zettl lab. Followed with multiple DI baths to remove KOH residue, then protek removal in acetone and MIAK (protek remover).</p> |
|  <p>A schematic showing a grey wafer with a central hole. A blue SiN layer is on top. Purple vertical bars on the top surface of the wafer represent the RIE etching process. The text 'CF₄/CHF₃ Etch' is written below the wafer.</p> | <p>Nitride membrane and remaining nitride are removed by RIE in nanolab's lam6. Wafer diced into 2mm x 2mm dyes using nanolab's Disco dicing saw.</p> |
|  <p>A schematic showing a grey wafer with a central hole. A thin blue layer (Au) is deposited on top. Below the blue layer, a thicker yellow layer (In) is deposited. Labels 'Au' and 'In' are positioned to the right of the layers.</p> | <p>Thin (~10nm) layer of gold followed by 2-4µm of Indium deposited by e-beam evaporator in Zettl lab. Requires you to pre-melt the indium in the crucible to increase packing volume and to evaporate the entire contents of the crucible. Store in inert environment to avoid oxidation.</p> |

Figure 3.12: Schematics of top chip fabrication process.

3.2.3 Bonding

Bonding the two chips together in a way that was both leak proof but preserved the channel was a considerable difficulty. Initially, we were planning to use SU8 – an epoxy-based negative photoresist – as a sealing layer [79]–[84]. We ran into significant problems with SU8 delaminating from the wafer, and as a result, very few chips would survive dicing. On top of this, we could not get a good seal with the SU8 chips we were able to produce. While I still believe SU8 is a promising approach that could allow for electrochemical studies to be done in the future, we had better initial results with indium sealing and chose to pursue this further [85]–[87]. Unfortunately, the use of indium shorts the device’s electrodes.

The assembly and sealing is shown in more detail in Figure 3.13. On the top chip, a thin layer of chrome and gold (3 and 25nm respectively) and a thick (5 μ m) layer of indium were evaporated in our e-beam evaporator. In order to achieve this thickness of indium in our standard crucibles, indium pellets must first be melted in the crucible on the hotplate outside of the evaporator to completely fill the crucible. The evaporator chamber should be wrapped in aluminum foil to prevent significant contamination from the indium. The quartz crystal monitor will also likely need to be replaced afterwards.

The bottom chips were also blanket coated in a thin (20nm) layer of gold to improve the bond with indium. Without this step, the indium chip would bond to silicon without too much difficulty, but failed to bond to the graphene. The evaporated gold allowed for a strong bond with the graphene film. The indium covered chips were kept under vacuum to avoid excessive oxidation while not being used.

The two chips were press-fitted together in a custom built press setup shown in Figures 3.14 and 3.15. The press has three screws which were each tightened to 0.12 lb·f-in. The entire setup was then heated to 200°C for 60s on a hotplate and allowed to slowly cool. The timing of this proved to be critical. The hotplate started at room temperature and was then set to 200°C and the temperature is allowed to ramp up for 60s before the hotplate is turned off. We found that if the chips weren’t heated enough a seal wouldn’t form, but if the chips were heated too much, the indium would become too soft and be pressed into the viewing window area. In the press setup we currently have, a small copper spacer is used under the top chip in order to get it to make good contact with the bottom chip. This is due to the chuck being machined out of tolerance.

After cooling, the chips were dipped in an iodine based gold etchant to remove the blanket-coated gold from the bottom chip. The iodine based etchant was chosen to avoid etching the graphene. In order to get the etchant to enter the backside of the KOH etched chip, a small droplet of IPA was used to first wet the area, then the etchant was introduced. Typically, an etch time of 10-20s sufficed.

After the chips have been assembled and the gold has been etched, the chips are loaded into the Protochips Poseidon TEM holder shown in Figure 3.6. The holder is connected to an external syringe pump and loaded into the optical test setup shown in Figure 3.16. With this setup, we can ensure that the channel fills with liquid and does not have any large leaks. A

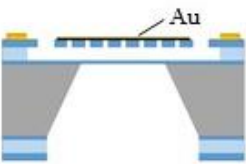
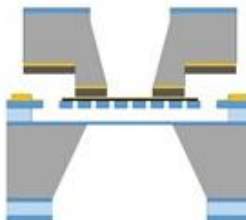
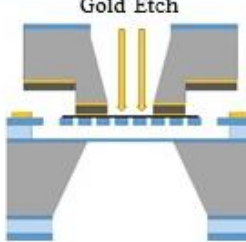
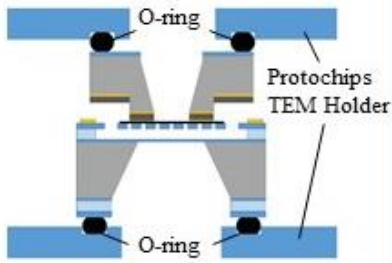
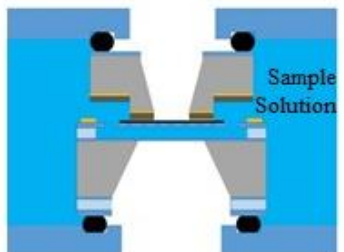
| <u>Schematic</u> | <u>Description</u> |
|---|--|
|  <p>A schematic diagram showing a cross-section of a chip. The top surface is coated with a thin layer of gold, labeled 'Au'. The chip is mounted on a substrate with a central channel.</p> | <p>Blanket coat bottom chip in thin layer of Au (~20nm) in e-beam evaporator in Zettl lab. Au will improve indium wetting and adhesion in subsequent step.</p> |
|  <p>A schematic diagram showing two chips sandwiched together in a homebuilt chuck. The top chip is positioned on a spacer grid. The assembly is held together by three screws.</p> | <p>Sandwich chips in homebuilt chuck with pair of o-rings (cut a small square of a spacer grid to place under top chip to ensure proper contact). Tighten each of the three screws to 0.12 lbf-in using precision torque-driver. Heat on hotplate to 200C. Turn off hotplate and allow to slowly cool. Remove chips from chuck (use small drill bit to dislodge the chips from the chuck).</p> |
|  <p>A schematic diagram showing the gold etching process. A small droplet of IPA is placed in the KOH etch pit of the top chip. The chip is then dipped in an iodine-based gold etchant.</p> | <p>Place a small droplet of IPA in KOH etch pit of the top chip to wet the surface. Dip chip in iodine based gold etchant for 7s to remove excess gold not bonded to the indium chip. Immediately transfer to DI bath followed by IPA.</p> |
|  <p>A schematic diagram showing the assembled and bonded chips being placed into the Protochips Poseiden TEM holder. The holder has o-rings and screws to secure the chips.</p> | <p>Place assembled and bonded chips into the Protochips Poseiden TEM holder with supplied o-rings in place. Tighten each of the three screws to 0.12 lbf-in. Confirm under optical microscope that the channel is within the viewing window and that the chips are properly seated within the holder.</p> |
|  <p>A schematic diagram showing the injection of sample into the chip. The sample solution is injected through a syringe pump connected to the chip via Luer lock connections and 200µm PEEK tubing.</p> | <p>Inject sample by connecting to the syringe pump. The connection is Luer lock on both ends, and the tubing used is 200µm PEEK tubing.</p> |

Figure 3.13: Schematics of chip assembly process.

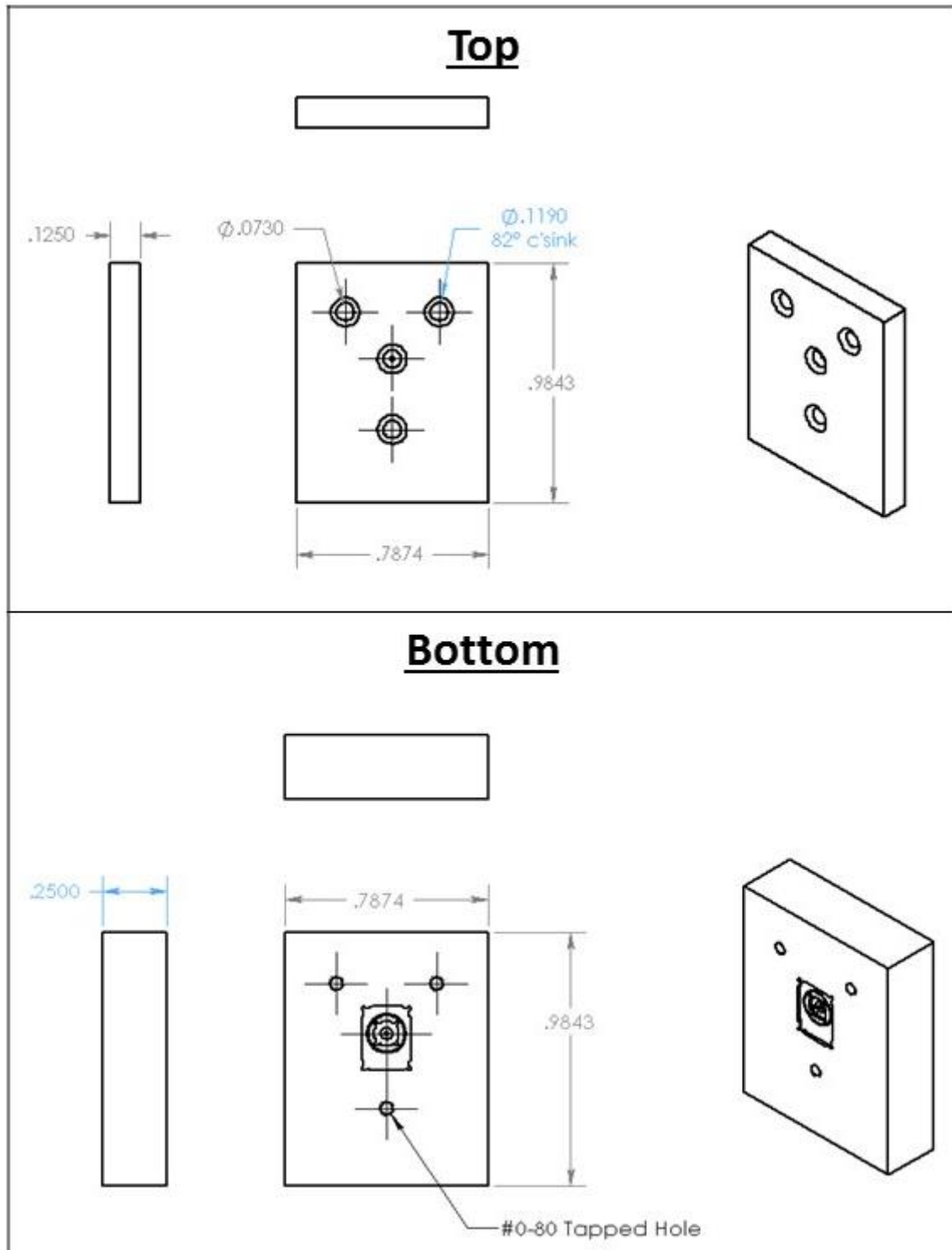


Figure 3.14: Indium sealing press chuck design. Top and bottom parts are screwed together in order to compress the evaporated indium on the top chip onto the graphene covered bottom chip.

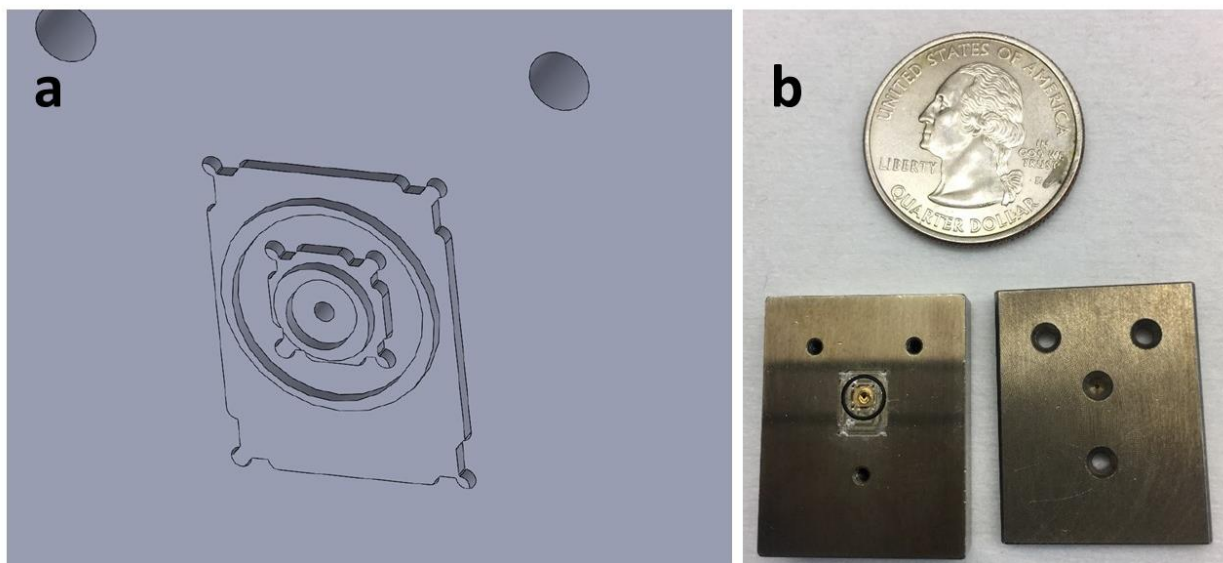


Figure 3.15: Indium sealing press chuck. (a) Close up of the recessed grooves for the chips and o-rings. b) Chuck machined out of steel - quarter for scale.

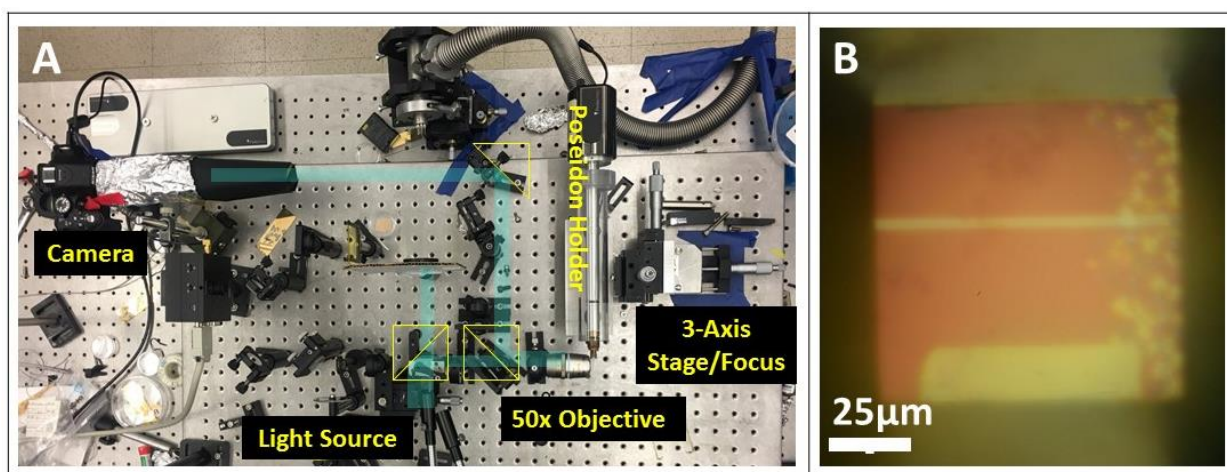


Figure 3.16: Optical test setup. A) Optical test setup image of empty channel. Optical path is shown in blue. B) After flowing at $100\mu\text{L}/\text{min}$ for 2min, the channel quickly fills which can be seen by a change in channel contrast.

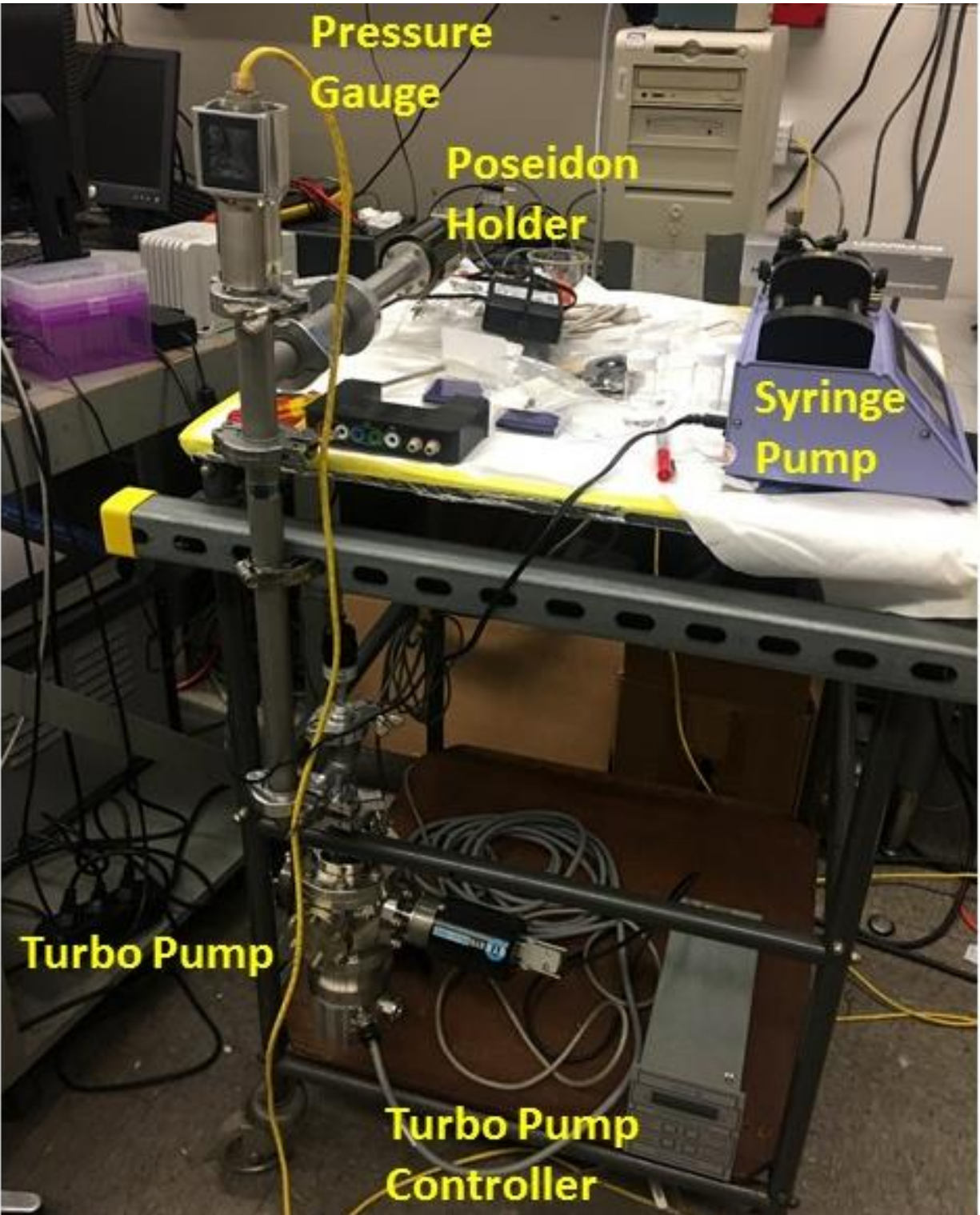


Figure 3.17: Vacuum test setup. Mimics the high-vacuum environment of the TEM. If a spike in pressure or significantly higher than base pressure is seen, this indicates a leak in the system. This is typically an o-ring issue, as chip bonding issues typically result in visible leaking during the optical test.

second test setup shown in Figure 3.17 is meant to mimic the high-vacuum environment of the TEM and ensures that no small leaks went undetected.

3.2.4 Channel Wetting and Bottom Chip Improvements

For the first version of bottom chip nanochannels, getting liquid to fill the channel was straight forward. DI water could be pumped into the TEM headstage at a rate of 50 μ L/min and would typically fill the channel. This would typically take no longer than 5min of fluid flow to happen.

While degassing the liquid was not necessary in order to wet the channel, we began to do this to avoid air bubbles blocking the channel, as well as to potentially limit bubbling during imaging. In order to degas the liquid, we would put it in a vacuum bell jar for ~1hr. For samples that did not contain any sensitive materials, we would sonicate as well to assist in the degassing.

After our initial successes with filling the 100nm thick channels with 50nm SiN layers, we developed a second generation of chips with narrower channels and thinner SiN layers. As shown in Figure 3.18, v.2 of our chips had 70nm thick channels and 14nm and 7nm thick SiN layers on the top and bottom respectively. We found these chips significantly more difficult to wet the channel.

With this new generation of chips, initially introducing DI into the chamber would not fill the channel. Instead, we started out with a 1:1 mixture of ethanol and water. The ethanol helps reduce the surface tension of the water and allows the mixture to readily wet the channel. We found the degassing to improve the wetting of the channel. After the channel has been filled, the ethanol could be diluted by flowing pure DI water. We typically did so for at least 10min to ensure that the ethanol had diffused from the channel.

As mentioned earlier, because of the thinner channels and thinner SiN layers, these channels were more likely to collapse due to stiction than the initial v.1 chips. While critical point drying (CPD) worked to avoid the collapse, this can be time consuming considering the number of acetone and IPA baths that the chips are put through. Instead, we found that making the channels narrower prevented them from collapsing. In order to do this, the spacing of the SiN holes was made smaller, and the SiO₂ etch time was reduced.

The final change we made for the v.2 chips was introducing multiple channels as shown in Figure 3.18B, as opposed to a single nanochannel. Because the channels often became blocked during imaging, multiple channels allowed the chips to be used for multiple experiments.

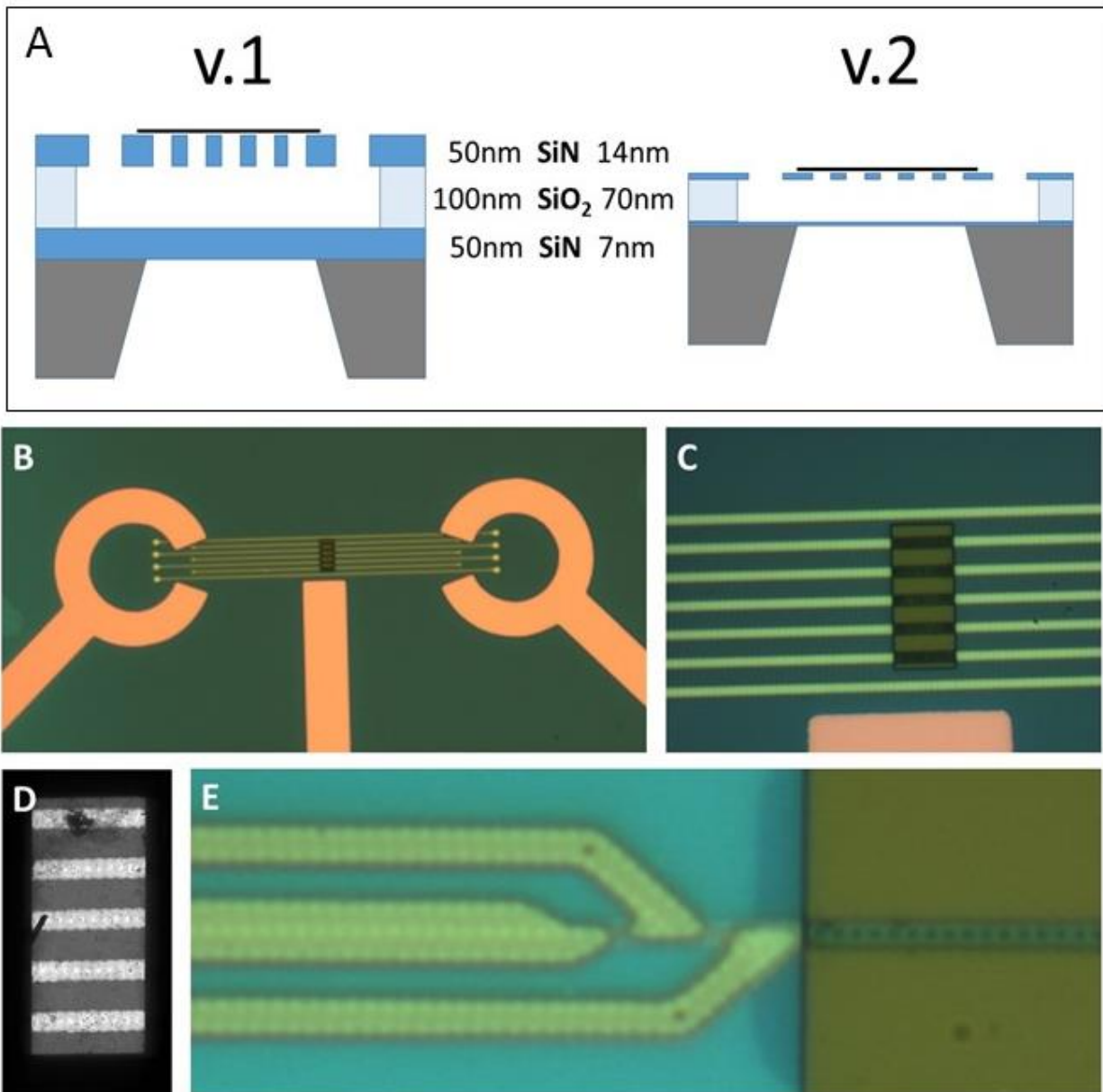


Figure 3.18: Bottom chip upgrades. A) Cartoon of v.1 vs. v.2 of bottom chip. SiN thicknesses have been substantially decreased as well as a thinner SiO₂. B)-C) Optical images of multichannel upgrade. D) TEM image of multichannel chip. E) Optical image of channel collapse caused by stiction. High contrast in wider channel areas on the left indicate collapse.

3.3 Results and Discussion:

3.3.1 Testing

With the TEM holder in the optical test setup, the nanochannel is filled with liquid as described above. When water fills the channel, the channel rapidly switches from light to dark as shown in Figure 3.19. If the channel is not clogged, this filling will typically happen in a few minutes, rarely more than 5 minutes, and never longer than 10 minutes. If the indium fails to seal, often a droplet will form on the surface of the chip along the edges of the top chip. The second test setup shown in Figure 3.17 meant to mimic the high-vacuum environment of the TEM and ensures that no small leaks go undetected. The setup allows one to continue to flow liquid through the enclosure, while bringing the external environment to high-vacuum with the pressure being carefully monitored. Initially, the holder is best loaded into the setup with the inlet and outlet ports blocked off. After pumping down to base pressure, the plugs on the inlet and outlet port are removed, with spikes in pressure indicating a problem. The syringe pump line is then attached to the inlet and flow begins, again with spikes in pressure indicating a leak. In the event of a leak, the chips are reheated to attempt to reseal them.

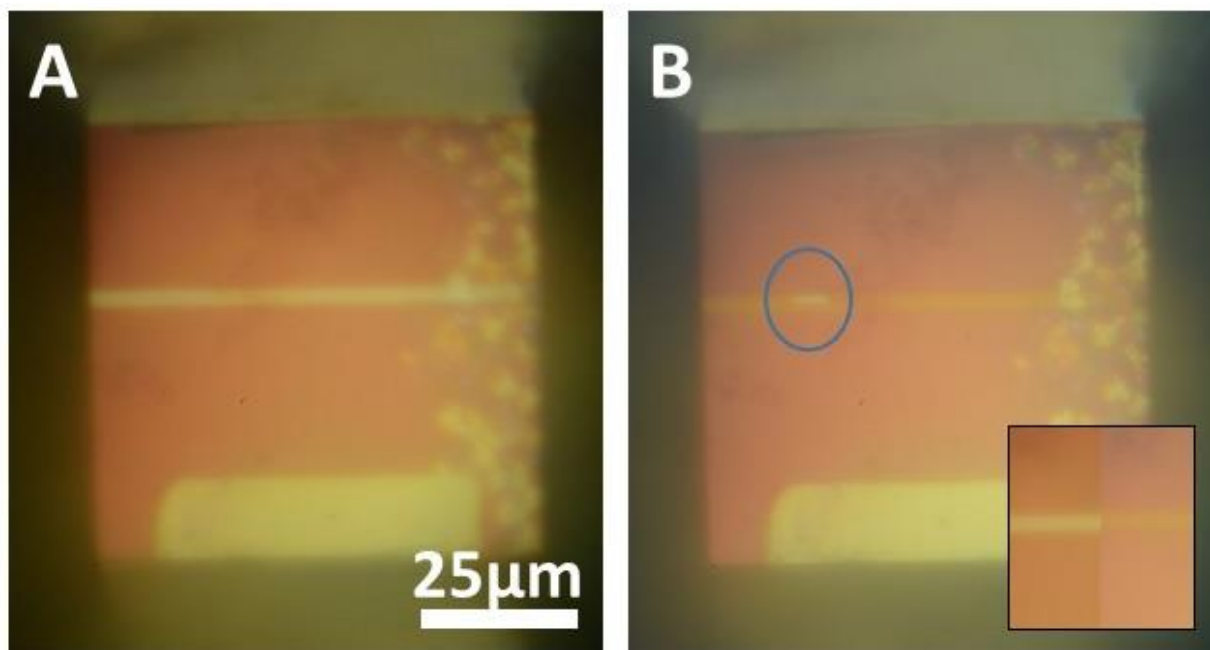


Figure 3.19: Filling of nanochannel. A) Optical test setup image of empty channel. B) After flowing at $100\mu\text{L}/\text{min}$ for 2min, the channel quickly fills which can be seen by the change in contrast. Circled in blue is a small air bubble that is trapped in the channel. Inset is side-by-side comparison of the empty and filled channel to demonstrate the difference in contrast.

3.3.2 Liquid Sample Imaging - Nanobubbles

Assuming no leaks were detected, the holder is safe to be loaded into the TEM. All of our images were taken in the Zettl lab TEM, a JEOL 2010 at 80keV with a LaB6 gun. Samples are injected into the holder using the syringe pump. We started by loading ethanol, and after stable imaging, we next looked at pure deionized water. The aqueous samples were significantly more stable under the electron beam. In addition to confirming that the channel was filled and stable under imaging, imaging DI provided a platform for imaging and studying nanobubbles. We saw three distinct modes of nanobubble formation, the last of which provided a novel way of studying nanobubbles in-situ.

The first mode of nanobubble formation saw nanobubbles form on the graphene viewing windows. These bubbles were typically on the order of ~40nm, as shown in Figure 3.20 and would appear and disappear often. The irradiation of water with an electron beam will generate a variety of species, primarily hydrated electrons, H_2 , OH^- , H_3O^+ , H , and H_2O_2 . As these byproducts are produced within the irradiated area, they are diffusing away and reverse reactions are taking place. In order for nanobubbles to form, the local concentration of these reactants needs to surpass a critical saturation concentration. For homogenous nucleation, in which nucleation occurs in the bulk liquid, the concentration typically must far exceed the critical concentration. For heterogeneous nucleation, in which the nucleation occurs at sites on the surface, conditions are more favorable for nucleation and can occur at concentrations between the critical concentration and that required for homogenous nucleation.

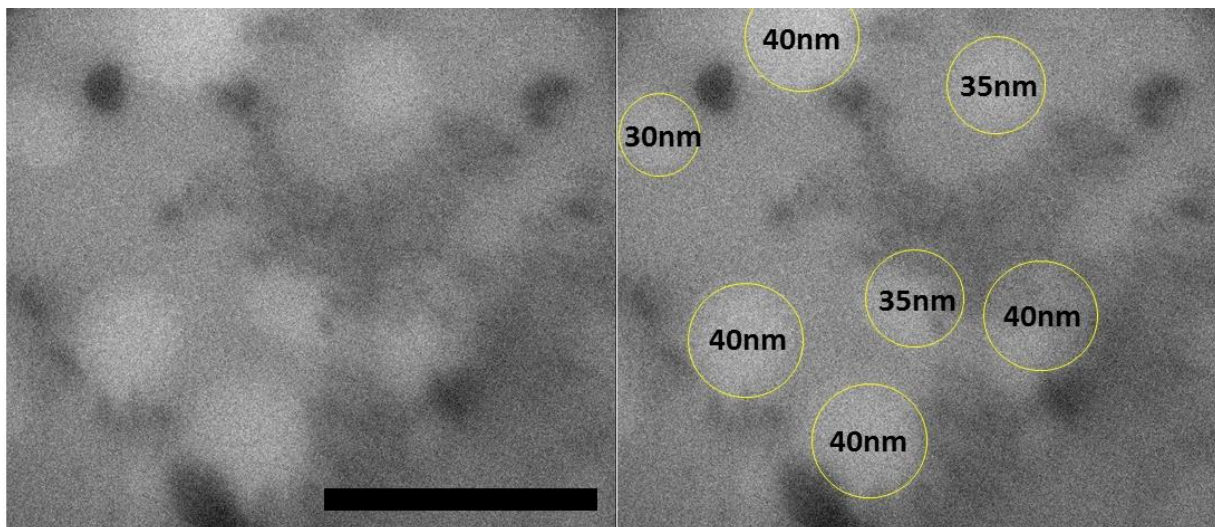


Figure 3.20: Radiolysis Driven Nanobubble Formation on Graphene. Left side shows a TEM image of nanobubbles formed on the graphene substrate during imaging. The lower resolution of these bubbles suggest that they are on the bottom viewing window, which is the graphene covered one. These were seen only on the graphene and not the SiN areas. The right shows the same image with the nanobubbles circled in yellow, with nanobubble diameters indicated inside the circle. Scale bar is 100nm.

The production of a particular chemical species X in M/s is given by

$$R_X = \rho D \frac{G(X)}{eN_A}$$

where ρ is the density of the liquid, D is the volumetric dose rate, e is the electron charge, N_A is Avogadro's number, and $G(X)$ is the G-value, an empirically arrived at number quantifying the number of molecules produced per 100eV. Under TEM conditions, the dominant contribution to bubble formation comes from H_2 as opposed to O_2 . While O_2 production will add to the growth of nanobubbles that have formed, H_2 should reach saturation more quickly. Molecular byproducts like OH^- may also be oxidize the graphene, creating additional H_2 and O_2 byproducts, but given the expected low rate of OH^- production, this is unlikely to be a significant effect.

The common radius suggests a minimum radius for nanobubble stability. Regan et al. found a similar minimum observable radius of around 10nm when using a metallic nanorod to locally boil water in an STEM [35]. As we shall discuss shortly, we see this similar 40nm limit in nanobubbles created by other means within the cell as well.

The second mode of nanobubble formation is an explosive bubble formation which quickly envelops the entire viewing area, as shown in Figure 3.21. This has been documented by other groups as well, but has defied sufficient explanation [33]. The effect appears to be

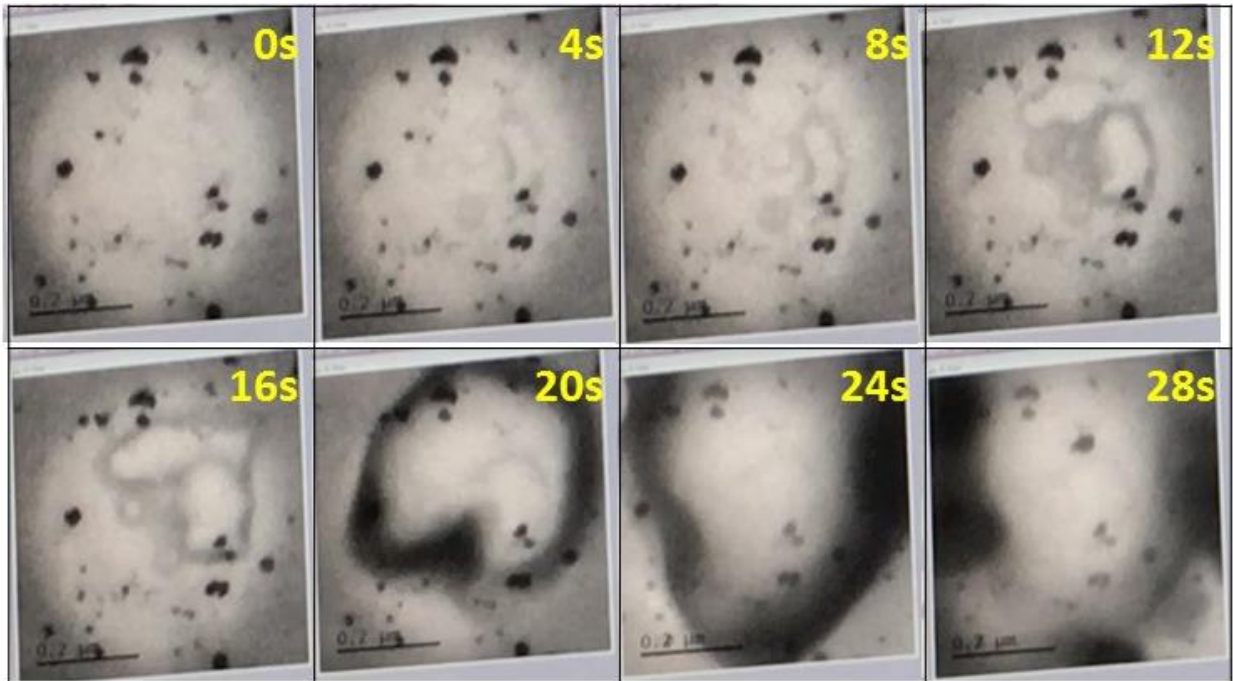


Figure 3.21: Explosive Bubble Formation. TEM time series of an explosive nanobubble rapidly forming. Multiple bubbles seem to nucleate at the graphene window, and rapidly combine and grow to take up the whole field-of-view. This typically occurred after extended imaging.

radiolysis driven, and may represent the concentration of gaseous byproducts surpassing the homogenous nucleation limit. While it is possible that, given the lengthy imaging time, enough oxidative radicals have been produced by the beam and etched a hole in the graphene. While imaging takes place at 80keV – below the knock-on damage threshold for graphene – it is still possible that this could also be damaging the graphene. The sudden exposure to vacuum would create the explosive bubble formation that we see. However, because this rapid bubble formation is seen by other researchers using SiN-based cells, I believe it is not an issue of graphene integrity. Furthermore, I would expect a hole in the graphene sealing to lead to a more catastrophic failure of the nanochannel.

The final mode of bubble formation was induced by the solvent exchange method described earlier and shown in Figure 3.22. The nanochannel was filled with ethanol, followed by DI water - neither had been degassed. The ethanol near the channel edges is nanoconfined and slower to mix than in the center of the channel. Because of this, when the remaining ethanol mixes with the DI, it leaves a supersaturated with nitrogen, nucleating a surface nanobubble at the silicon oxide edge. While it would energetically prefer a hydrophobic surface, nanobubbles have been observed on hydrophilic surfaces such as silicon oxide before [88]. The nanobubble quickly grows with beam irradiation as radiolysis byproducts are incorporated into the bubble. The side-view image of the nanobubble growth allows for direct study of the three-phase contact line and leads to a number of important insights about nanobubble mechanics.

The nanobubbles are seen in the first frame of imaging after the DI has been introduced. At that time, the nanobubbles are ~40nm in radius, similar to the nanobubbles on graphene we discussed earlier. While the graphene nanobubbles seemed to be metastable at 40nm, and would blink in and out of existence, the nanobubbles at the channel edge rapidly grew. The reason for this difference is unclear. The fact that we see growth of the nanobubbles suggests that they are gas permeable, ruling out the theory that this is the source of nanobubble stability.

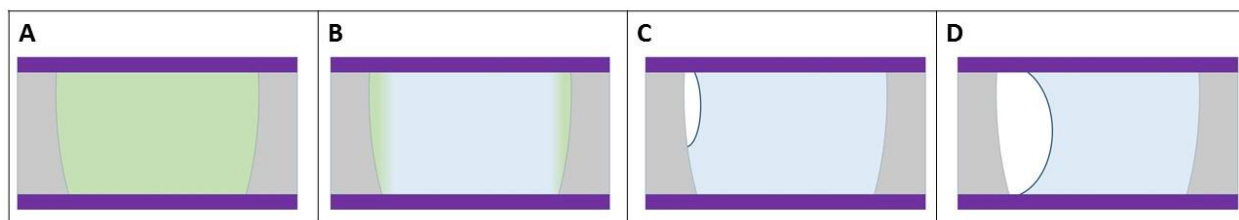


Figure 3.22: Nanobubble Formation by Solvent Exchange Schematic. A) Nanochannel is filled with ethanol (green). B) DI water (blue) is pumped into the channel, but the ethanol at the channels edge is slow to mix. C) As the residual ethanol mixes with the DI, N₂ is supersaturated in the channel and nanobubbles form. With radiolysis from electron beam irradiation, H₂ and O₂ are produced and contribute to nanobubble growth.

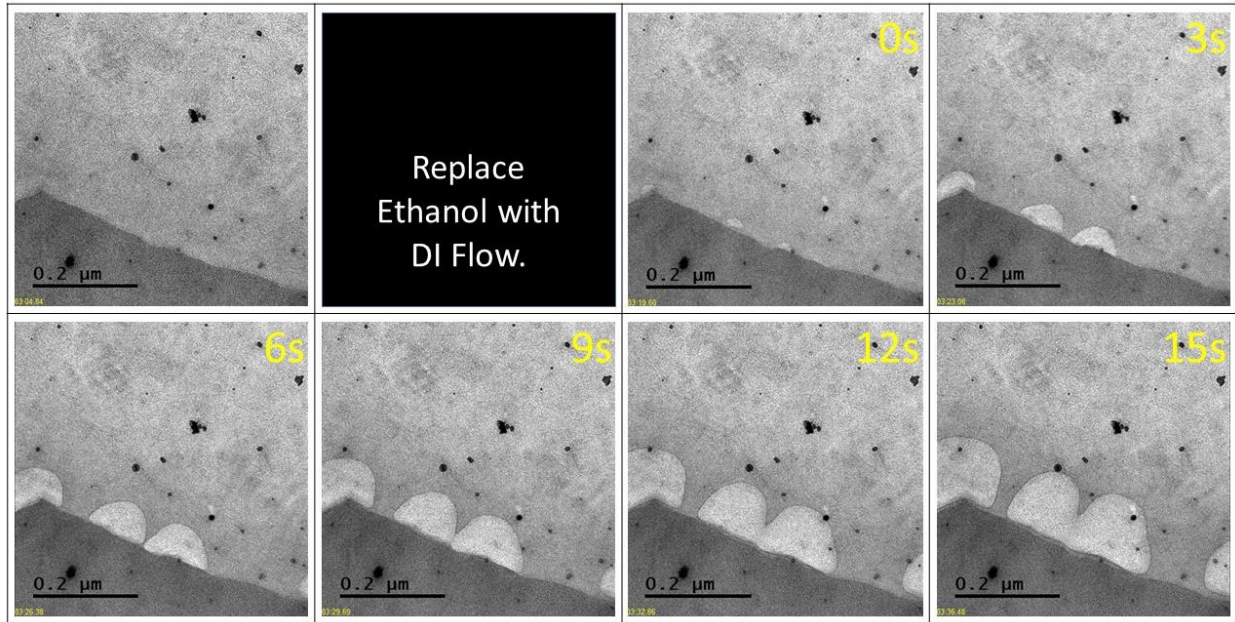


Figure 3.23: Nanobubble Growth. TEM time series of nanobubble nucleation and growth. Beam was blanked while DI was introduced into the nanochannel. Upon un-blanking the beam, small (40nm in width) nanobubbles were already present on the SiO₂ wall of the nanochannel.

A time series of the nanobubble growth can be seen in Figure 3.23. We can confirm a number of unique characteristics of nanobubbles that have been witnessed by other researchers, as well as gain further insight from the nanoscale resolution of the three-phase contact line region. For starters, the nanobubbles do appear to decrease their radius of curvature as they grow rather than maintaining a constant contact angle. This has been proposed by a number of groups as evidence of contact line pinning, which we shall address shortly. As the nanobubble grows, its length between contact points, L , initially grows, but seems to slow, and instead the height of the nanobubble increases to accommodate a higher vapor volume. In our own images, the bubbles can be seen to grow rapidly in both height and lateral dimension at first, but growth in the lateral dimension seems to slow.

In addition to this, we see the combining of two nanobubbles during the growth process. Interestingly, the two bubbles maintain their own structures to a large degree. One would expect that their lowest energy state would be a sphere, and the two would quickly reorganize into such a structure. As discussed in the previous chapter, this was seen as a potential consequence of contact line pinning. Early in their combination, a faint contrast line can be seen at the contact point between the two nanobubbles, as shown in Figure 3.24.

Of particular interest in the above images, is the three-phase contact line region. As can be seen in Figure 3.25, while the bulk of the nanobubble appears to be a spherical cap, the contact line area has a markedly different contact angle. As most of the previous work on nanobubbles contact angle and geometry has been done with AFM – which is incapable of seeing

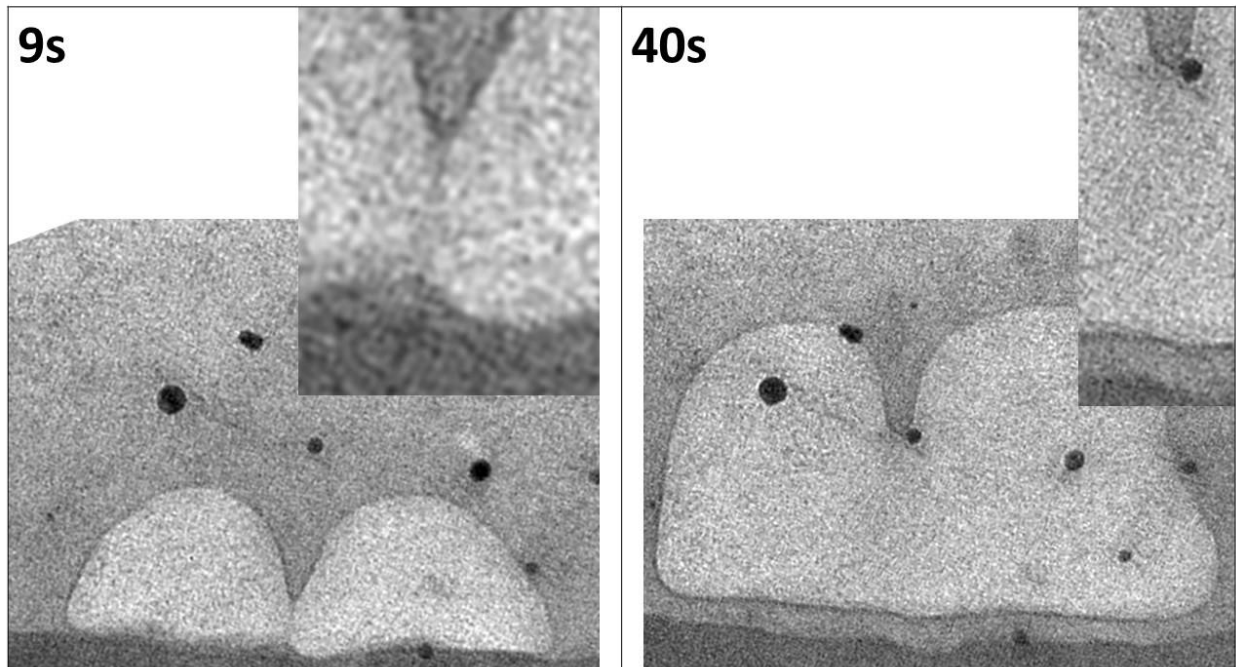


Figure 3.24: Nanobubble Coalescence. As the two bubbles first merge, a faint contrast region between the two suggests that they have maintained independent contact lines. At later times, the contact lines appear fully merged, yet the independent structure of each nanobubble remains. This has been seen in AFM studies as well and proposed as evidence of contact line pinning.

undercut surfaces and would have difficulty accurately imaging the final 10-20nm of the contact line area – the results we are seeing may be the first truly accurate look at the contact line. While a number of our experimental results to agree with observations which have been attributed to contact line pinning, these findings suggest that this explanation is not sufficient.

These images suggest that Young's equation does in fact hold at the nanoscale for the three-phase contact point, as shown in Figure 3.26. For SiO_2 , the expected contact line angle would be around 23° . While the spherical cap deduced contact angle differs from this substantially (85°), it would appear as if the nanoscale contact line is around 23° . This suggests that the forces at the three-phase interface are in fact the three forces described in the unmodified Young's equation. This Young's equation consistent contact line is only seen in 4-5nm from the SiO_2 substrate.

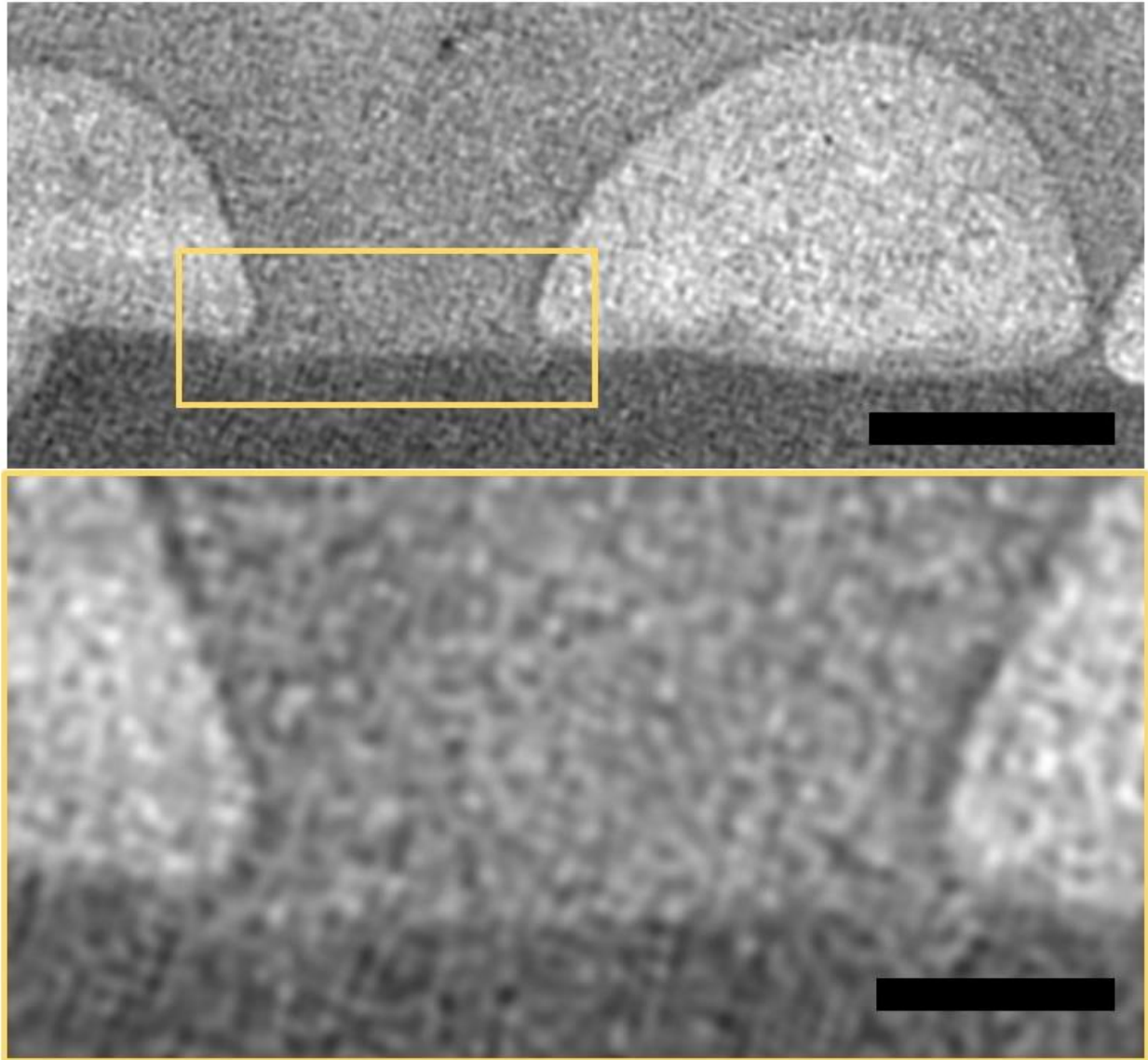


Figure 3.25: Contact Line Deviation at Three-Phase Interface. While the contact line appears spherical for the bulk nanobubble, near the substrate, a change in curvature can be seen. Scale bars are 50nm and 20nm respectively.

Looking back more carefully at previously published studies lends support to the hypothesis that Young's Equation holds, unmodified, at the three-phase contact point. HOPG's hydrophobicity means that such a nanobubble would have an extremely shallow angle, resulting in a tapered finish to the nanobubble. Figure 3.27 show a couple of examples of nanobubble results which suggest this may be the case. These were likely believed to be imaging artifacts, either from sample preparation in the case of Figure 3.27A, or the limitations of AFM discussed earlier for Figure 3.27B.

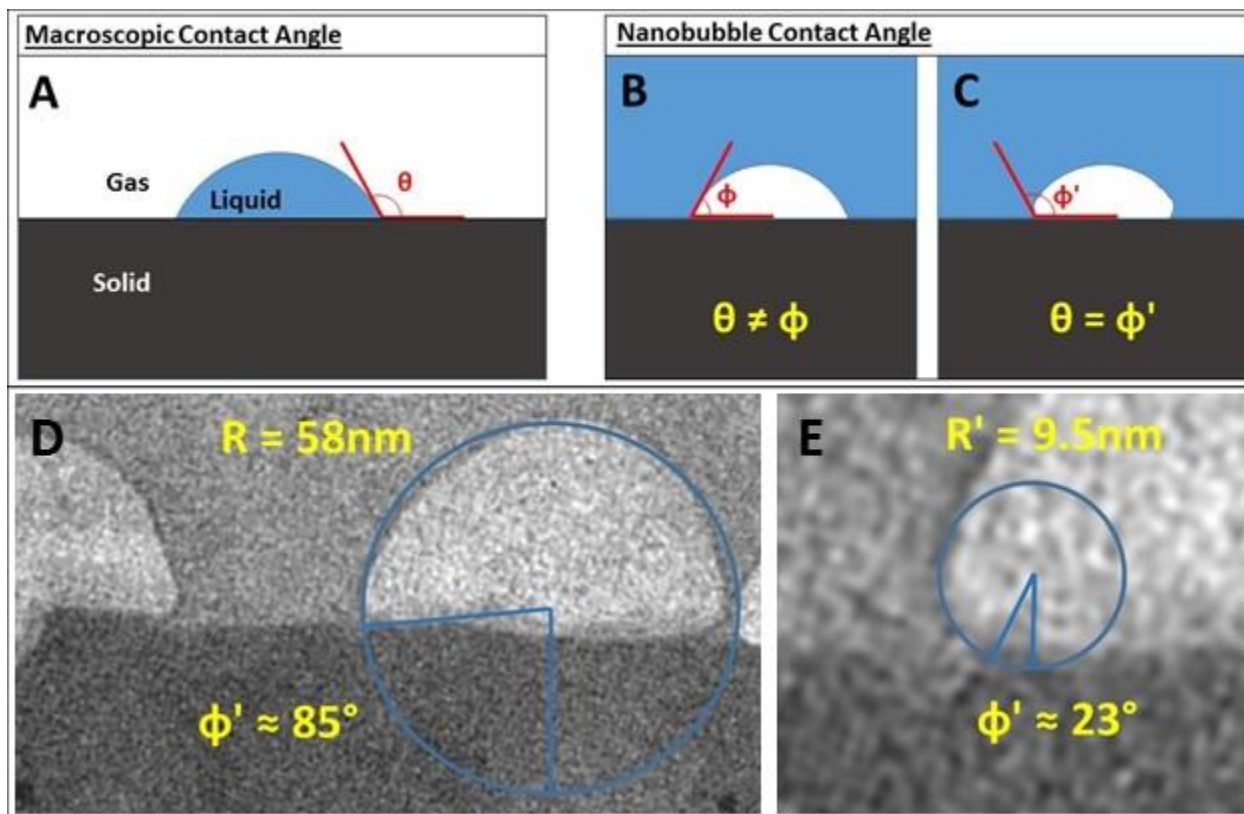


Figure 3.26: Young's Equation Holding at Contact Point. A) Cartoon of contact angle from macroscopic contact angle. B) Cartoon of contact angle for standard image of a nanobubble. Note that it is different from the macroscopic contact angle. C) Our updated picture of the nanobubble contact angle. Near the contact point, the contact angle is in agreement with the unmodified Young's equation.

This result has potentially profound implications for explanations of the stability of nanobubbles. Explanations which have focused on contact line pinning or an additional line tension force all require an additional modified term which would alter the contact angle. Our results suggest that while there does appear to be an additional force acting to stabilize the nanobubble and alter the general radius of curvature, this effect is not local to the surface interface.

In addition to this, our work calls into question the supposed mechanism of contact line pinning. While nanoscale surface features have been an often used explanation for pinning, our imaging shows no clear evidence of pinning effects at specific features. In fact, the nanobubble on the far left in Figure 3.23 can be seen to grow undeterred by the sharp pyramidal feature.

The unique nanochannel architecture of the GFC allows for an unprecedented look at the morphology of surface nanobubbles. While the morphology and stability of nanobubbles have defied explanation for years, GFC imaging may prove instrumental in arriving at a sufficient explanation.

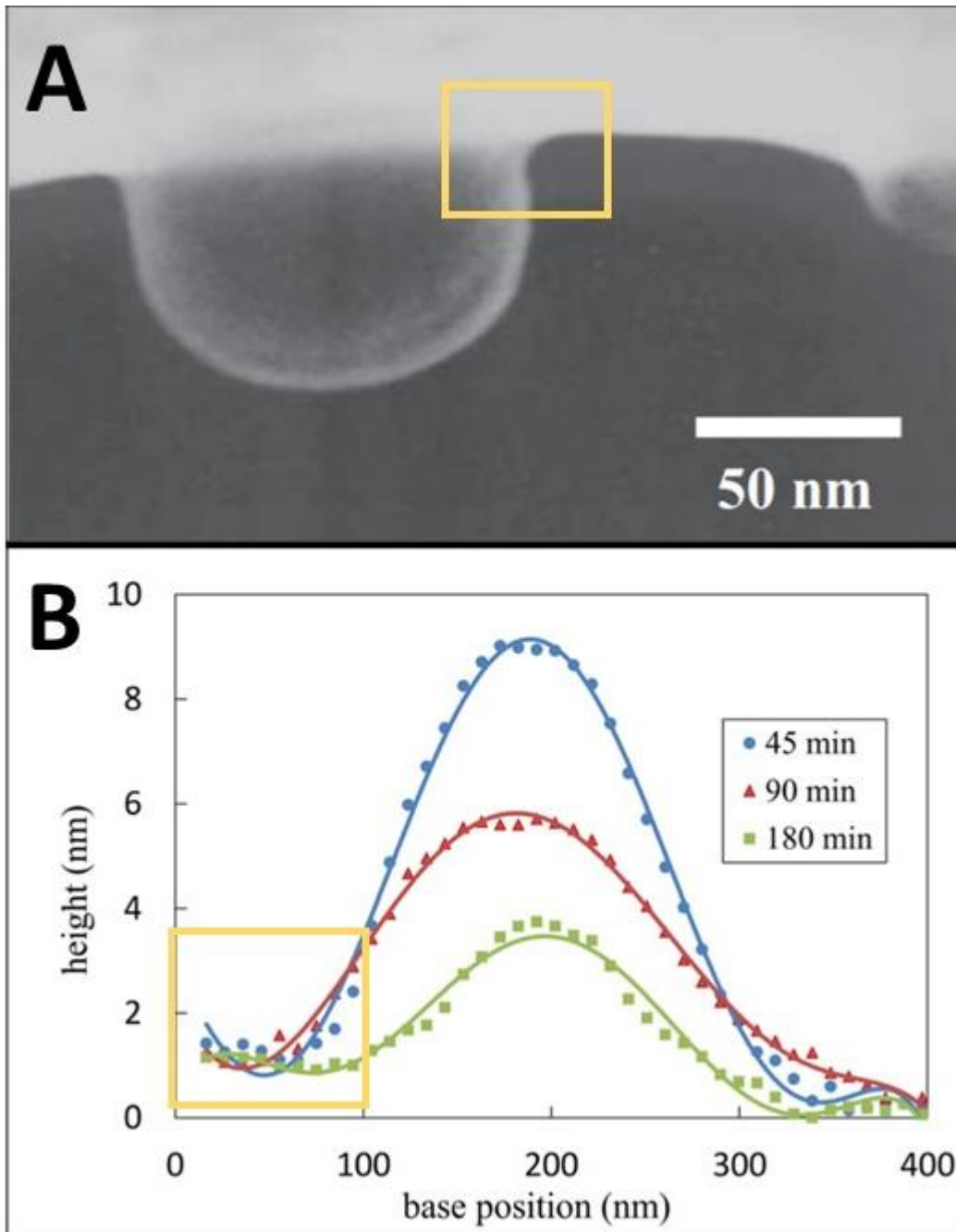


Figure 3.27: Further Evidence of Unmodified Young's Equation. A) Nanobubbles prepared by rapid freezing, carbon encapsulation and fracture. Adapted from Ref [90]. AFM height profile of shrinking nanobubbles. Adapted from Ref [32]

3.3.3 Nanoparticle Imaging

As a second test, we introduced a gold nanoparticle solution through the syringe pump. Within a matter of minutes, the nanoparticles could be seen in the nanochannel, demonstrating the GFC's ability to rapidly introduce reactants or new samples, as well as allowing for the study of nanoparticle dynamics. Clear dynamics could be seen as shown in Figure 3.28, further confirming that we are in fact trapping liquid. These dynamics shed light on a number of other characteristics of the GFC.

While we have referred to an inlet and outlet port, it was clear in imaging that flow through the channel was dominated by diffusion. There was no favorable motion along the nanochannel. This was to be expected, as there is significant dead volume between the two Protochips o-rings sealing the chips, creating a large bypass around the nanochannel. This bypass is necessary as a nanochannel would allow for too small of a fluid flux to introduce new samples at realistic pressures. In addition to this, significant convective currents caused by hydrolysis from beam irradiation dominate particle motion.

Closer imaging of the AuNPs allows us to establish the resolution which we were achieving with the GFC. By taking the FFT of our TEM images, we can establish the information limit of each image, or by looking at the distribution of pixel intensities around a nanoparticle we can determine resolution limits. Typical AuNP images, like those in Figure 3.29, showed sub-nanometer resolution. This resolution is on par with what we have observed

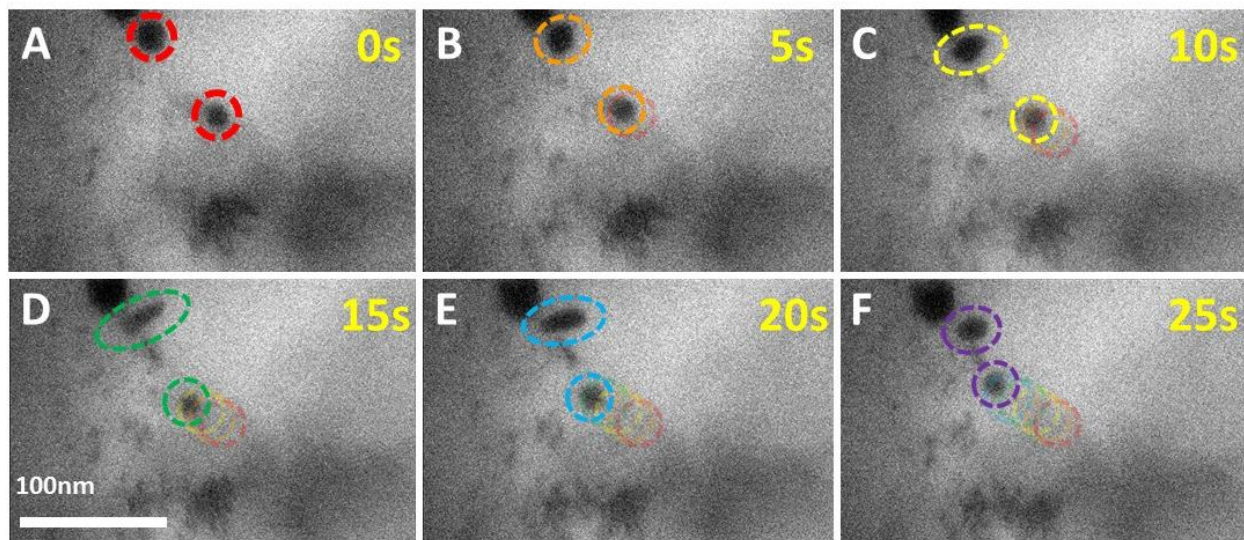


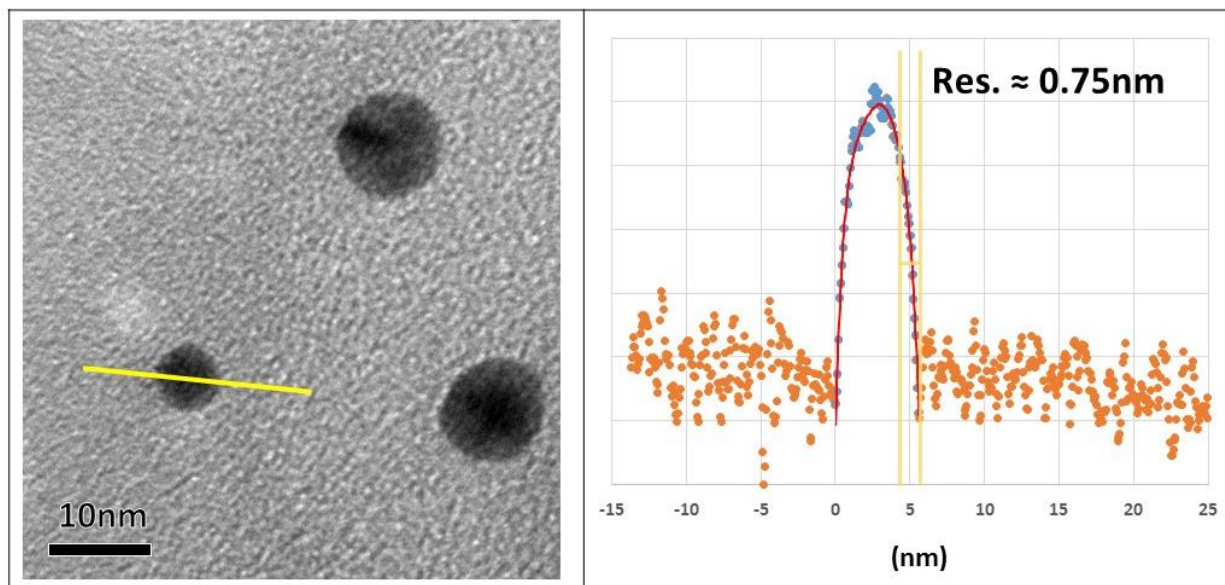
Figure 3.28: Nanoparticle dynamics. A)-F) Time series of nanoparticle movement. Circles track the particles movement through time, as well as highlight rotation of one nanorod particle. This demonstrates both that we are able to diffusively introduce new species into the chamber and that the channel is in fact filled with fluid allowing us to see in-situ dynamics of nanoparticles.

with the graphene liquid cell in our TEM, and superior to the resolution in the graphene encapsulated SiN cells, suggesting that were we to load the GFC setup into an aberration corrected TEM we could achieve atomic resolution. It also far outperforms the Poseidon silicon nitride flow cell, which typically has significantly larger sample thicknesses.

It is worth noting that the gold etch appears to leave some nanoparticles on the surface of the graphene. However, because the gold is on the top surface of the chips, it does not interact or interfere with the sample, and can be distinguished from samples in the cell by its lack of movement. We will discuss ways in which this issue could be ameliorated shortly. The nanoparticles in Figure 3.28 were all seen to move with the fluid in the GFC, and in some cases were seen to agglomerate.

Besides helping characterize the GFC, these nanoparticle behaviors can also shed light on the mechanisms that drive AuNP diffusion dynamics. The AuNP circled in the lower right hand corner of Figure 3.28 is seen to be moving at a speed of $\sim 4 \text{ nm/s}$, significantly less than the $20 \mu\text{m/s}$ (5,000 times larger) for a nanoparticle diffusing in bulk solution predicted by the Einstein-Stokes equation as described earlier. The Au nanorod circled on the top right of Figure 3.28 is seen to rotate at a rotation speed of $\sim 0.15 \text{ rad/s}$, while the rotational motion expected by stokes equation is closer to 450 rad/s – 3000 times larger. The fact that these are off by a similar multiplier adds some support to the explanation that the water near the substrate is in a highly ordered phase. This explanation causes a large increase in viscosity, which would explain the similar offset for both rotational and translational motion. This would not be the case with the adsorbed rolling motion.

Figure 3.30 shows another example of nanoparticles diffusing. The larger nanoparticle can be seen to travel at 0.172 nm/s , while the smaller travels at 0.5 nm/s . larger nanoparticle is 20 nm , while the smaller is approximately 7 nm . This once again suggests the $1/R$ scaling of the



solution. B) Line scan of pixel intensity for the yellow line in (A). Resolution limit is estimated at 0.75 nm based on the pixel intensity tail.

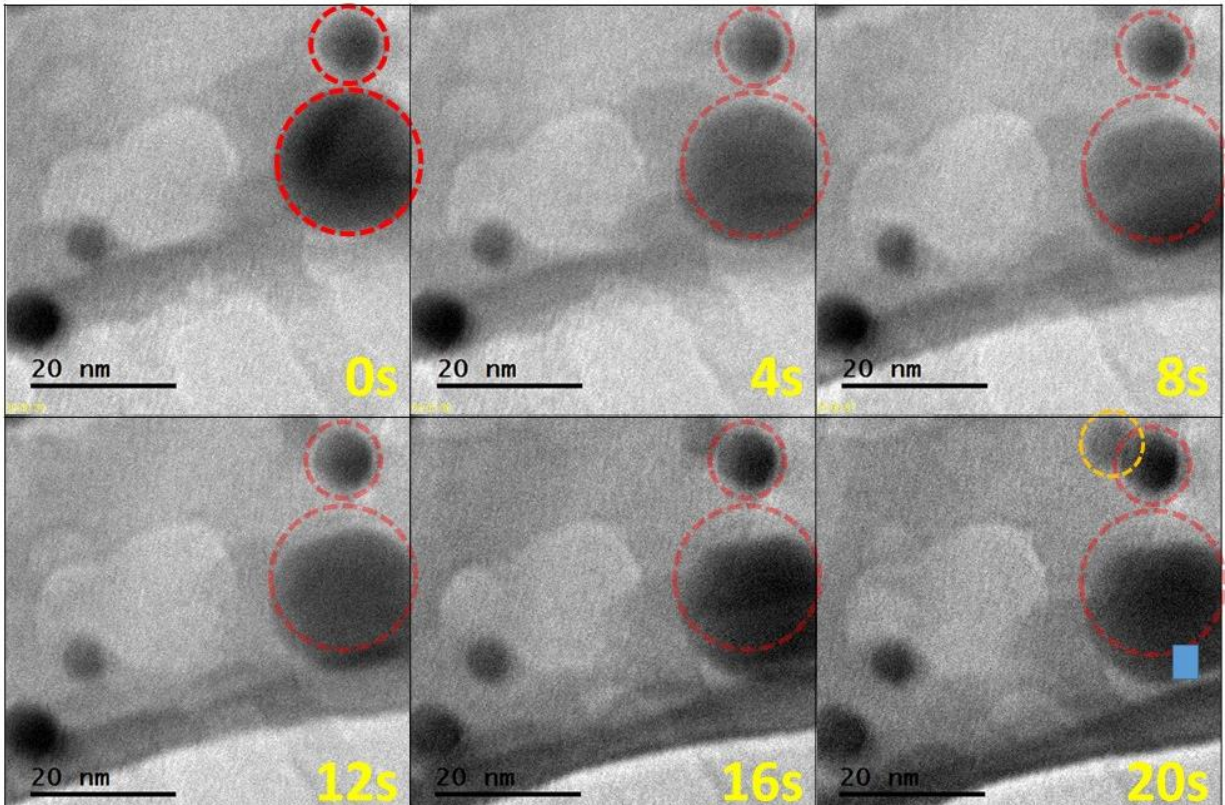


Figure 3.30: High Resolution Nanoparticle Dynamics. TEM time series of nanoparticles moving across liquid front.

Einstein-Stokes relation still holds. Furthermore, the smaller AuNP can be seen to be further from the substrate than the larger one, as evidenced by the lower contrast as well as the overlap with the other nearby nanoparticle. These results also point to the ordered liquid phase at the substrate boundary. Were movement to be explained by the surface diffusion and off substrate jumping, we would expect the smaller nanoparticle to be moving much more quickly as it is not in contact with the substrate. Instead the nanoparticle's speed is well explained by a smaller radius.

It is worth noting that the charging effects witnessed by Regan et. al, in which nanoparticles were seen to scatter from the irradiated area, were not seen in GFC imaging [37]. In fact, in many cases, an attractive force appeared to cause the nanoparticles to assemble, without any clear repulsion from the substrate. This may be due to the graphene encapsulation layer which acts as a charge sink reducing the SiN charging effects.

Similarly to the graphene-sealed SiN cavities, the GFC allowed for the high-resolution imaging of nanoparticle dynamics in 3D. Our results have lent support to the claim of anomalously high viscosities near a substrate. In addition, the jump-stick motion that was seen by Zheng et. al was never seen. Instead, particles were seen to diffuse steadily after initial irradiation made them mobile.

In addition to the bulk nanoparticle dynamics that were seen, the GFC proved useful for the study of additional nanoparticle behaviors. During the radiolysis driven drying of a nanochannel, the study of nanoparticle behavior in a drying thin film can be studied. As shown in Figure 3.31, we see a few distinct phases during the drying process. First, the bulk liquid appears to evaporate. Many of the nanoparticles move quickly with the evaporation front. Second, what appears to be a residual liquid layer begins to evaporate as well, forming smaller bubbles. Third, as this layer seems to dry, a number of the nanoparticles appear to move with this new drying

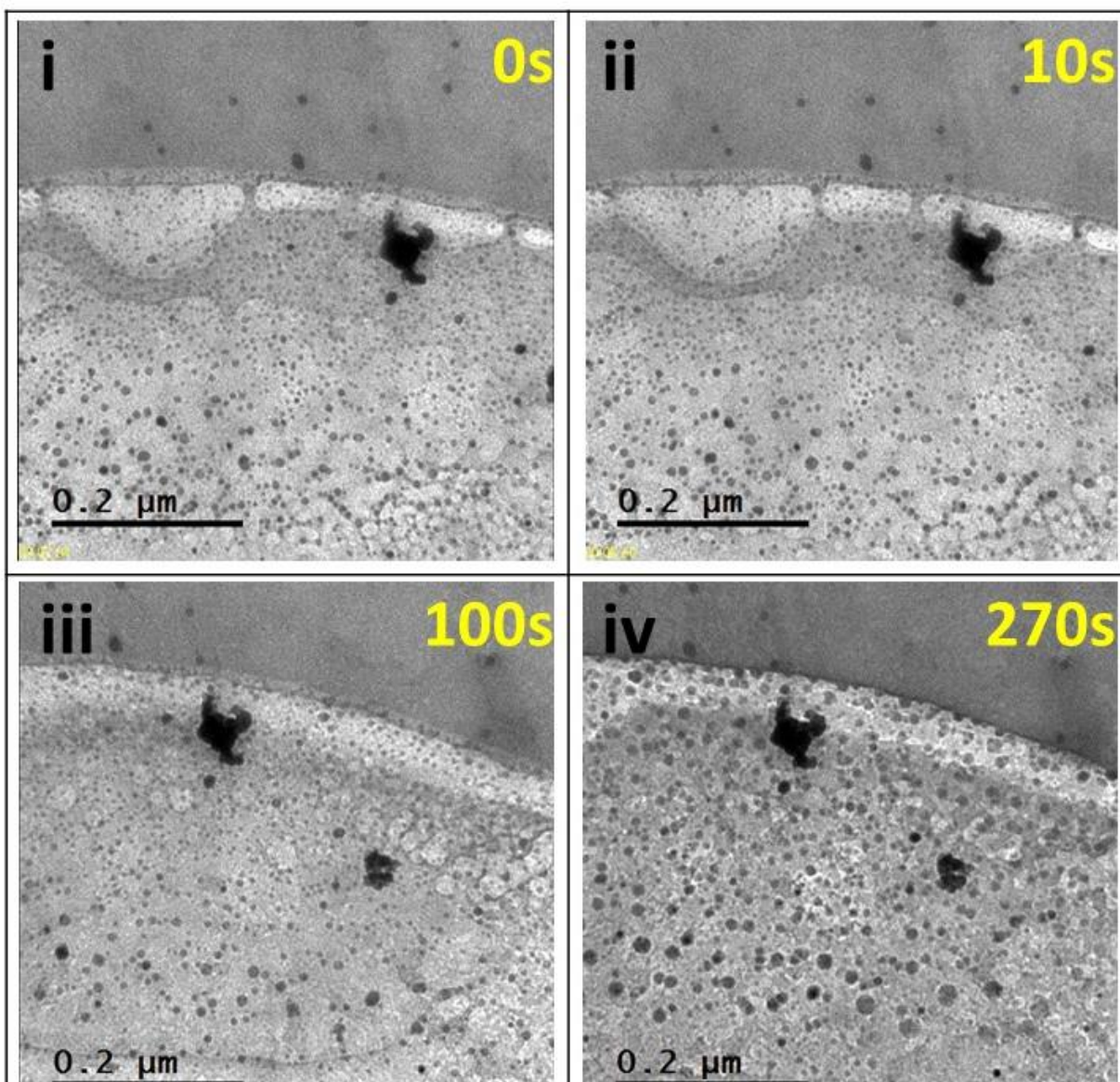


Figure 3.31: Nanoparticle Behavior During Thin Film Drying. TEM time series. i)-ii) Bulk liquid evaporating. iii) Nanobubbles appear in residual liquid thin film. iv) Nanoparticle radius increases likely by the addition of Au ions.

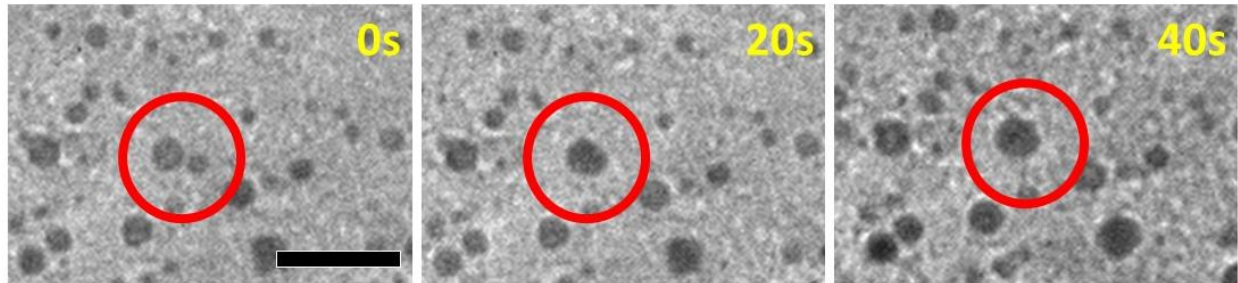


Figure 3.32: Nanoparticle Coalescence. TEM time series of two nanoparticles in liquid thin film coalescing. Scale bar is 50nm.

front, but much more slowly than before. During this time, it is common to see nanoparticle coalescence, as shown in Figure 3.32. The nanoparticles also grow in diameter. This may be because Au ions in the solution become supersaturated as the channel dries and are being incorporated into the crystalline nanoparticles. Alternatively, this could be indicative of the two sides of the channels collapsing and flattening the nanoparticles.

3.3.4 Uranium Acetate Crystallization and Dissolution

In order to image the dynamics of crystallization and dissolution within a liquid cell, unfiltered 0.1% uranyl acetate was introduced into the nanofluidic channel. Uranyl acetate was used for two reasons. First, the heavy uranium nuclei make for an excellent contrast agent for TEM imaging. Second, UA is a common stain for imaging biological material, so better understanding its behavior under electron beam irradiation was necessary. Uranyl acetate is known to precipitate under UV exposure, and while it has been used extensively as a contrast agent for stain-based imaging, its behavior under electron beam irradiation while in solution has been studied far less.

The presence of UA was markedly different than imaging DI or ethanol, as can be seen in Figure 3.33. Many areas of the nanochannel appeared to have a number of clear crystal facets. During imaging, a number of nanoplatelets could be seen either forming or rotating under beam irradiation. For example, the platelet circled in Figure 3.33 could clearly be seen to rotate during imaging.

In addition to this UA nanocrystal rotation, we also saw many instances that appeared to be the precipitation and dissolution of UA minerals. Clear facet lines and edges would appear

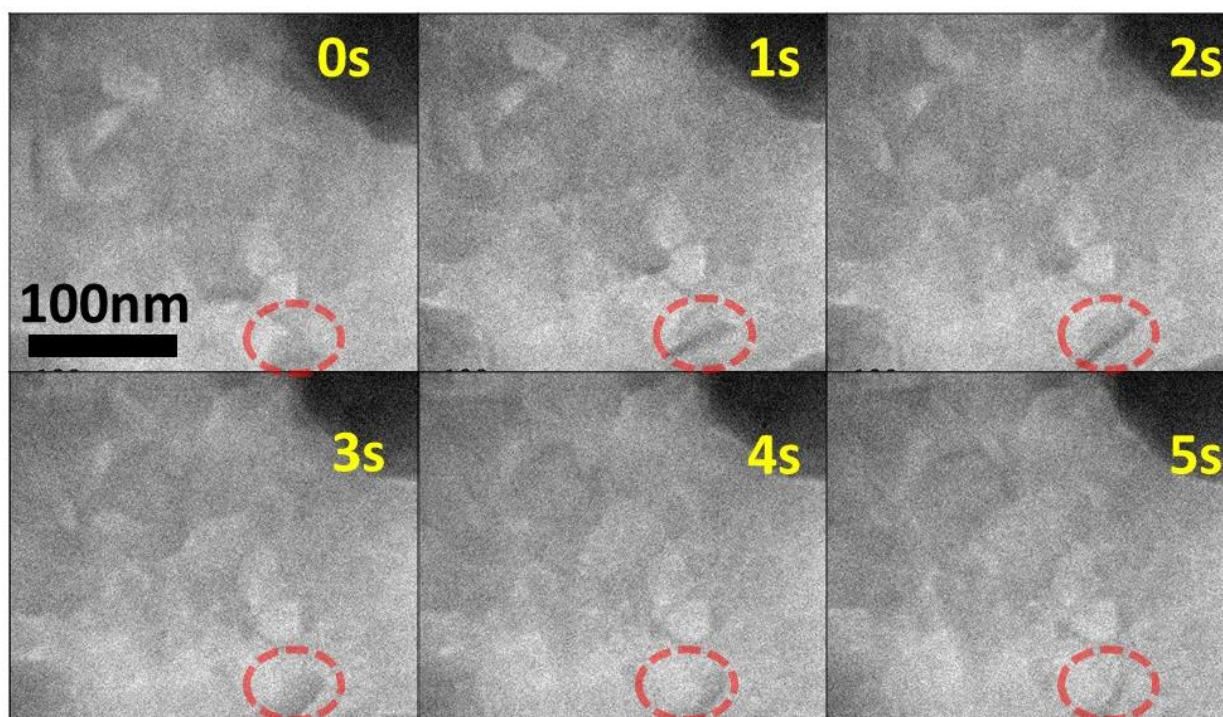


Figure 3.33: 0.1% Uranium Acetate (UA) in Phosphate Buffer Solution (PBS). A) TEM time series of facet appearing and disappearing. B) TEM Time series of multiple platelet-like structures. Red circle shows one example of what looks like a platelet rotating. Often these platelets seem to oscillate between being more liquid or solid.

and seemingly dissolve. Figure 3.34A shows the clear assembly of a facet, which was measured to have an angle of $113 \pm 2^\circ$, corresponding to the coordination angle of neighboring linear chains of UA hydrogen bonded around a remote water molecule. Shortly after this formed, it seemed to rapidly dissolve. Additional evidence of this phenomenon was seen in other areas of the channel. As shown in Figure 3.34B, clear facets would form along a UA area, and were dynamic under the beam. Facet lines would grow and shrink, but interestingly, the size of the bulk nanocrystal itself remained somewhat constant.

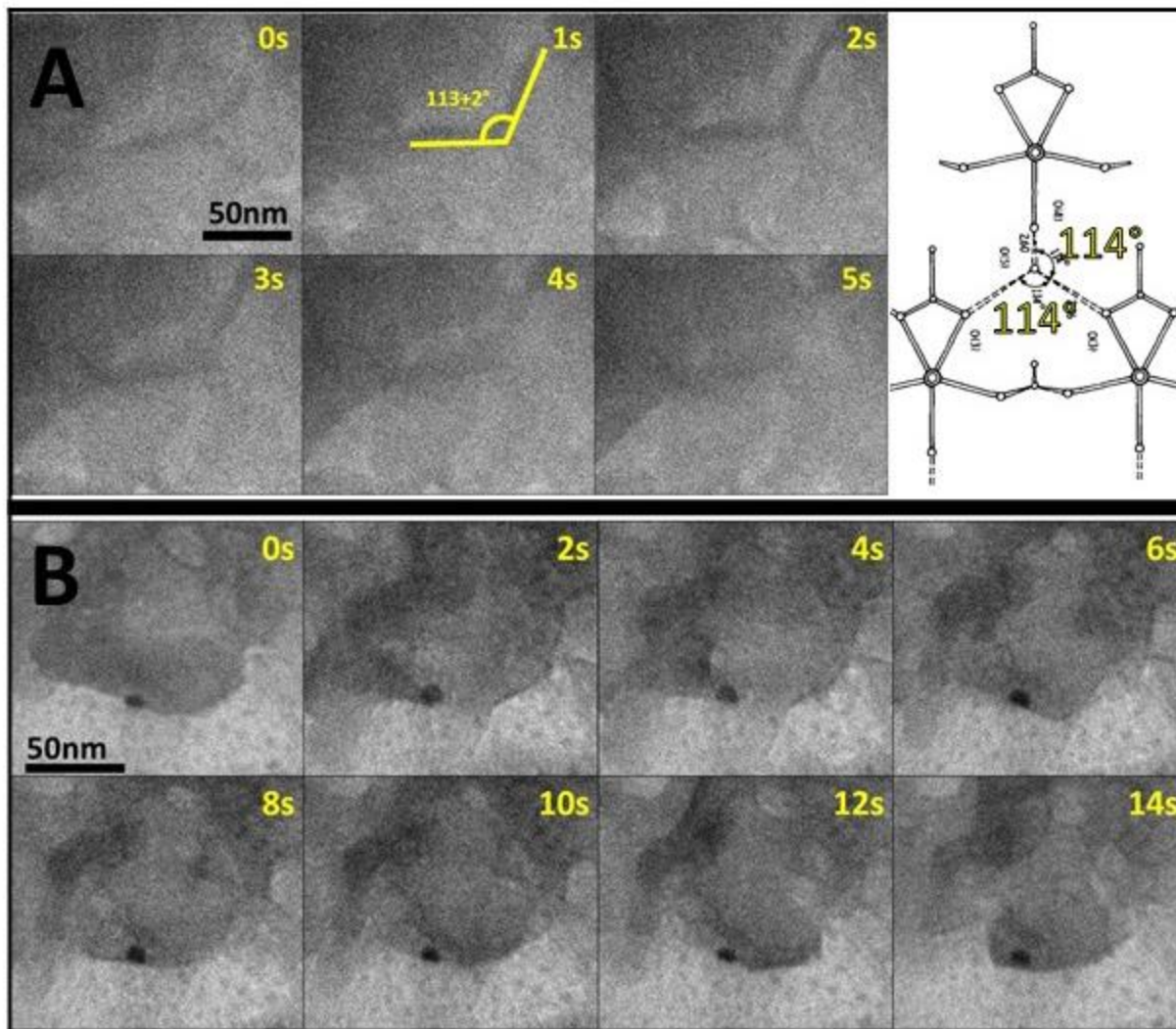


Figure 3.34: 0.1% Uranium Acetate (UA) in Phosphate Buffer Solution (PBS). A) TEM time series of facet appearing and disappearing. Right side is an image of UA chain hydrogen bonded around a remote water molecule. Adapted from Ref [91]. B) TEM Time series of multiple platelet-like structures. Red circle shows one example of what looks like a platelet rotating. Often these platelets seem to oscillate between being more liquid or solid.

3.3.5 Stained Biological Sample Imaging

Finally, to demonstrate that the holder was applicable for biological specimen, we loaded a solution of MS2 viral capsids in a 0.1% UA in DPBS into the first generation GFC with 100nm thick channels. The MS2 was obtained from graduate student Emily Hartman from Matt Francis' lab, and the UA was obtained from graduate student Ben LaFrance from Eva Nogales' lab. These viral capsids are nearly spherical polyhedrons with a typical diameter of 25-27nm. Prior to imaging in the GFC, we took a negatively stained dry image of the MS2 capsids for comparison. Under these stain concentrations used for GFC imaging, we would expect the capsids to be positively stained – contrasting as dark compared to their surroundings. As can be seen by the images in Figure 3.35, the MS2 capsids are clearly stained. Video images show that many are in fact still hydrated, as evidenced by fluid motion.

Successfully imaging MS2 capsids shows that, as expected, the GFC is capable of imaging biological samples and accommodating light heavy element staining. This opens the door to a number of potential applications which have been outside the grasp of conventional liquid cell technology.

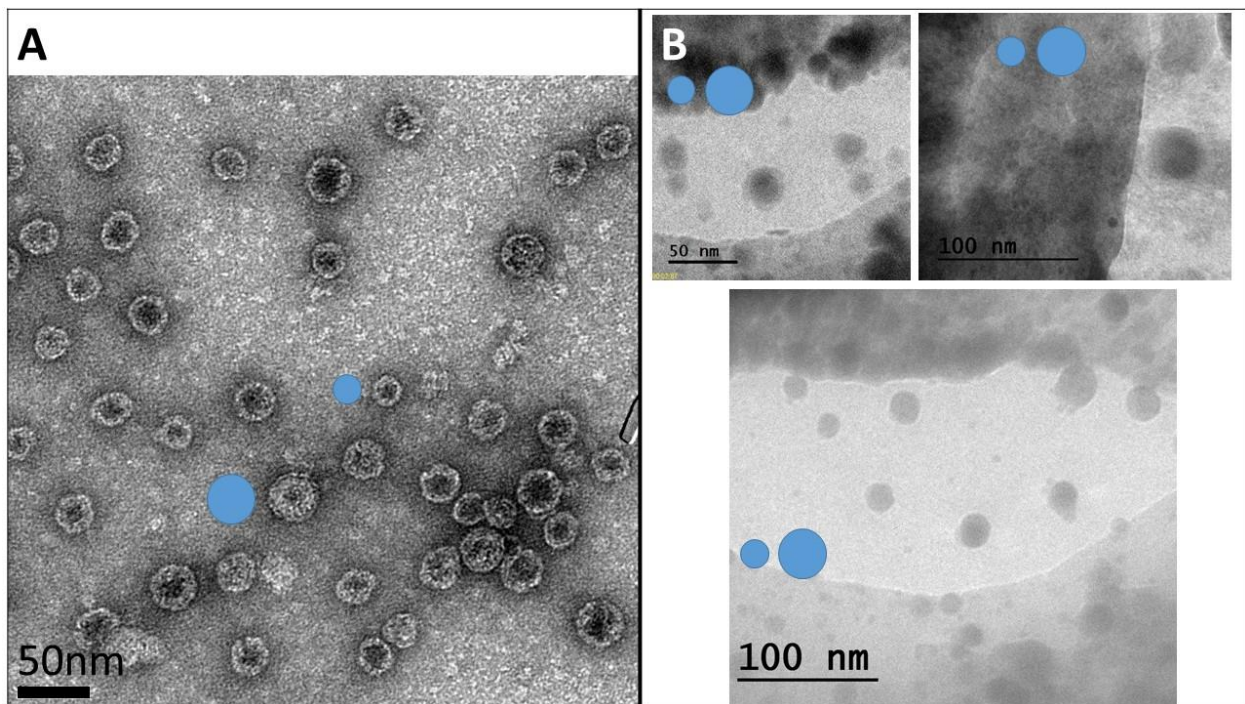


Figure 3.35: MS2 capsid imaging with positive stain. A) TEM images taken with our GFC. MS2 were positively stained with 0.1% UA. Blue circles are representative of the range of capsid sizes in our sample. The scale is the same in all images for easier comparison. B) Negative stained image of MS2 capsids taken for comparison.

3.4 Future Work

3.4.1 Applications

There are two directions future work with the graphene flow can take: using the design as-is for a number of potential applications; or improving the flow cell to allow for more advanced applications. I believe the graphene flow cell platform as-is lends itself to a tremendous range of applications in chemistry and biology, and extends the resolution of in-situ TEM into a region with incredible potential.

Many of the applications listed below are what originally inspired me to begin working on the graphene flow cell. In some instances, I had begun working towards the application described below using the static graphene liquid cell, and began to see its limitations and the necessity for a graphene-based platform capable of flow and not reliant on evaporative sealing.

3.4.1.1 Application: DNA Transcription – RNA Polymerase

The original motivation for this work was to look at a very specific biological process, DNA transcription by RNA Polymerase. This work began as a collaboration with the Bustamante group in biophysics. DNA transcription is the process by which RNA strands are created and informed by DNA. These RNA strands go on to serve a number of potential purposes, like the blueprints for a protein structure or as a messenger molecule. Essential to the process is the action of the protein RNA Polymerase (RNAP). RNAP consists of a number of subunits which attach at specifically coded sites in a double-strand of DNA. The RNAP sequentially unzips a local region of the double-strand, creates a complimentary RNA strand by incorporation of nucleotide triphosphates (NTP), and re-zips the DNA behind it. In this manner, the RNAP moves along the double-strand, being fueled by NTP. Our goal was to image this process in-situ and investigate the dynamics on the sub-nanometer scale. The intended experimental design is shown in Figure 3.36.

To do this, we would need to label the DNA and RNAP with some kind of heavy element to give them any contrast in the liquid cell. Our initial labelling scheme was to label the terminal end of the DNA strand with a 10nm AuNP, and the RNAP with a 5nm AuNP [89]. Eventually, we moved to labelling both ends of the DNA strand with AuNPs. By doing this, we would be able to observe the movement of the RNAP relative to the DNA strand. Initial imaging suggested that it was possible to make these assemblies and that they appeared to remain intact under the electron beam. Figure 3.37 shows one such example of an RNAP labelled with a 10nm AuNP attached to DNA with a single 5nm AuNP label. The two AuNP appear to be tethered to one another as they travel across the trapped GLC region.

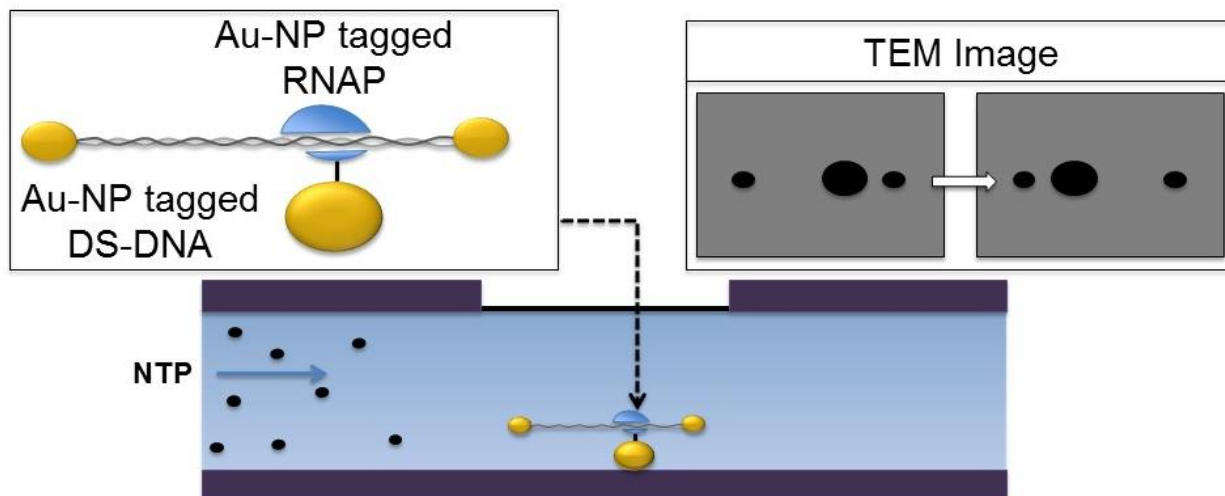


Figure 3.36: DNA Transcription Experimental Design. The DNA and RNAP are labelled with AuNPs. The assembly can be loaded into the flow cell, and then NTP can be introduced to initiate transcription. The transcription can be inferred by the relative motion of the larger AuNP (RNAP) to the two smaller AuNPs (DNA).

However, where the project got stuck was how to initiate the transcription while viewing in order to actually see the dynamics as they happened. Because the graphene liquid cell takes at least an hour to seal and load into the TEM, if we were to incorporate NTP in the initial sample liquid, the process would either have ceased by the time we loaded it into the TEM, or it would be happening so slowly that it would not be observable in the time window in which we could view it.

The graphene flow cell solves the problem in a simple straightforward manner. The RNAP can be initiated on the DNA and loaded into the flow cell. After initial imaging shows the static RNAP-DNA complex, the NTP can be introduced into the flow holder. The NTP will diffuse into the viewing area and drive the transcription process.

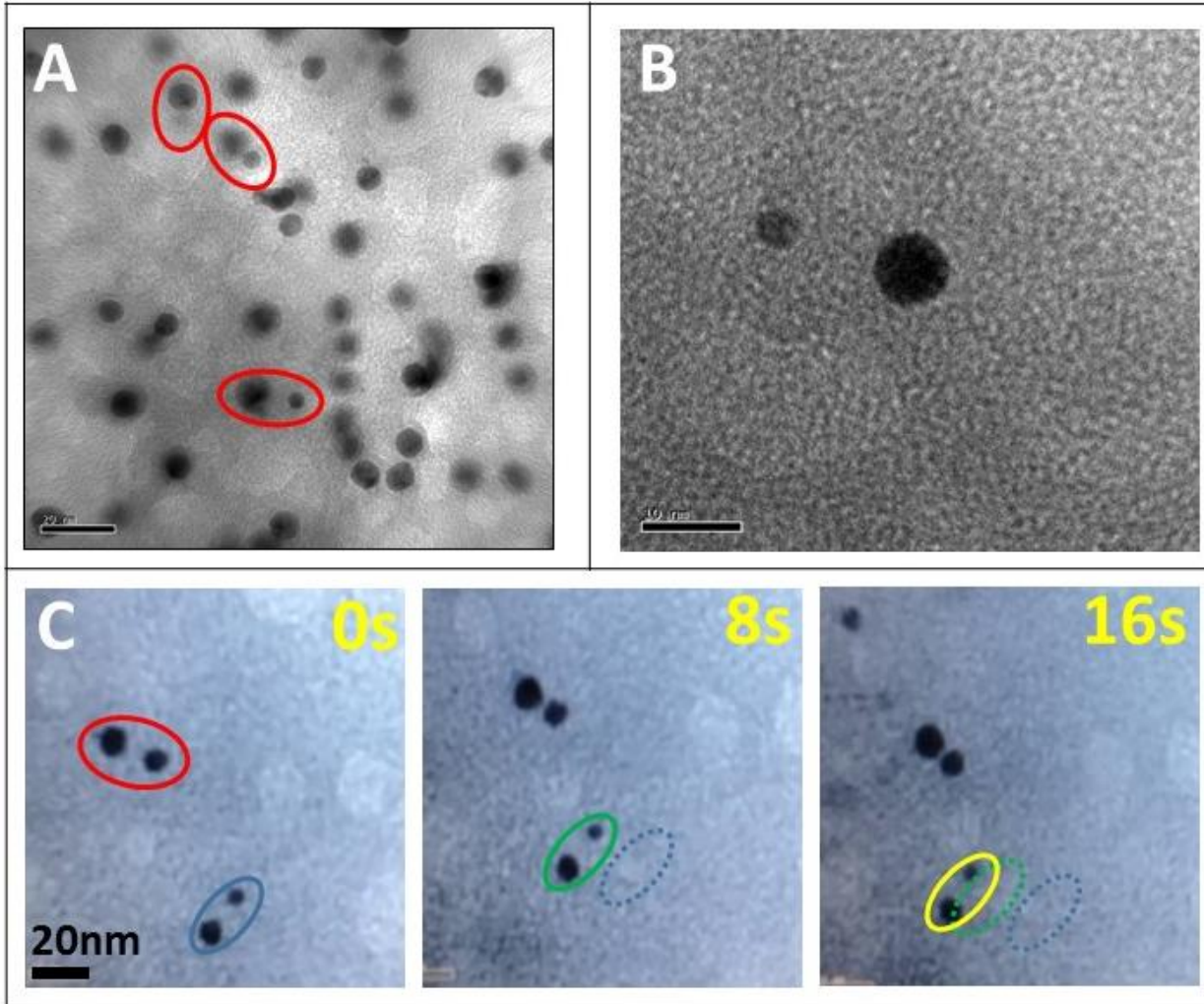


Figure 3.37: DNA Transcription Preliminary Results. A) TEM in Graphene Liquid Cells, we managed to trap RNAP-DNA complexes where the DNA was labelled with a 5nm AuNP (only one in this case) on the terminal end, and the RNAP was labelled with a 10nm AuNP. Multiple candidates circled, but significant background from extraneous AuNPs. B) TEM close-up of one such pair. C) Time series video of a RNAP-DNA complex moving within the GLC, demonstrating that the structure of the DNA and the adherence of the RNAP remained intact during electron beam irradiation.

3.4.1.2 Application: Antibody Binding on Viral Capsids

In order to demonstrate the potential for the GFC to image dynamic biological processes, one of the first applications we considered was the antibody binding on viral capsids. Our immune system uses antibodies to identify and bind to foreign bodies. An antibody is a Y-shaped protein with binding sites on each arm which complement sites on a specific foreign body. Antibody binding is critical in the performance and study of our immune system. They have found applications in pharmaceuticals and diagnostics as well as basic research. High-resolution

of antibody binding would allow for further study of these binding dynamics, as well as serve as a rapid screening method for the effectiveness of an antibody.

Antibody binding to viral capsids seemed like an ideal system for a number of reasons. The viral capsid we would use is Cowpea Mosaic Virus (CPMV). CPMV is typically found in cowpea leaves and can be readily harvested and isolated. The capsid is roughly spherical with an average diameter of 28.4nm – neither too large to fit in a thin nanochannel, nor too small to be difficult to resolve. It has also been extremely well studied and is readily available. CPMV is fairly robust to radiation, and should be structurally stable under electron beam irradiation. It is also stable in a large pH range (3.5-9), which will also improve its stability under the beam. In addition to this, the binding complex is localized to a small area on the capsid which is typically repeated a number of times on the capsid surface, and the binding area of the antibody is equally as localized. This reduces the chances that beam damage will hinder the binding, or that the UA stain will block binding sites. The antibody is also readily available, and can even be purchased with quantum dots or nanoparticles attached to the head of the antibody.

The experimental design is relatively straightforward and shown in Figure 3.38. CPMV would be loaded into the GFC along with a dilute 0.01-0.1% uranyl acetate stain. Shortly thereafter, the antibodies would be loaded alongside them into the channel. As a first attempt, I would try without labelling the antibodies and see if they are visible with only the uranium stain. If none are seen, using a AuNP labelled antibody would be your best bet. If you are seeing the antibodies, but they do not appear to be binding to the CPMV, an important next step would be doing a classic ligand binding assay to ensure that the UA is not interfering with proper binding.

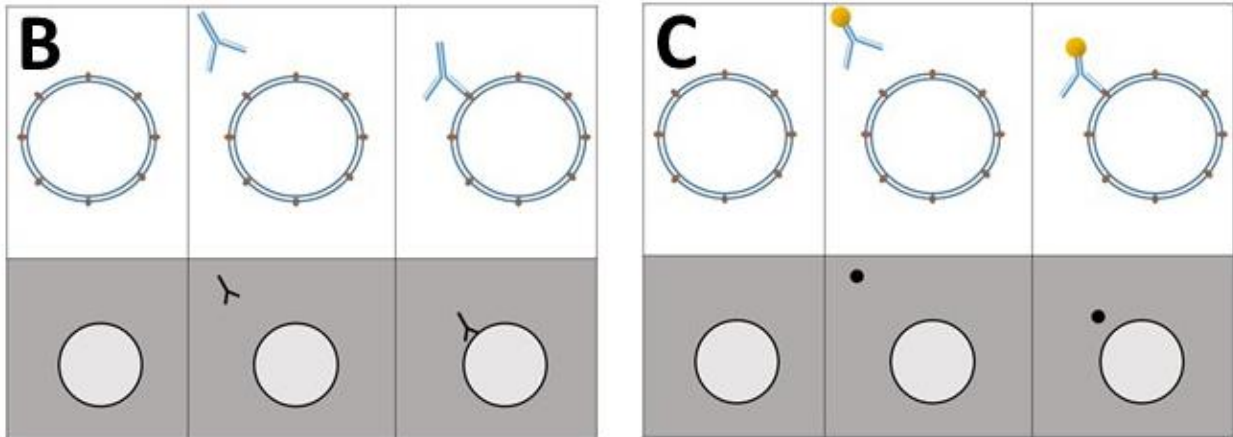
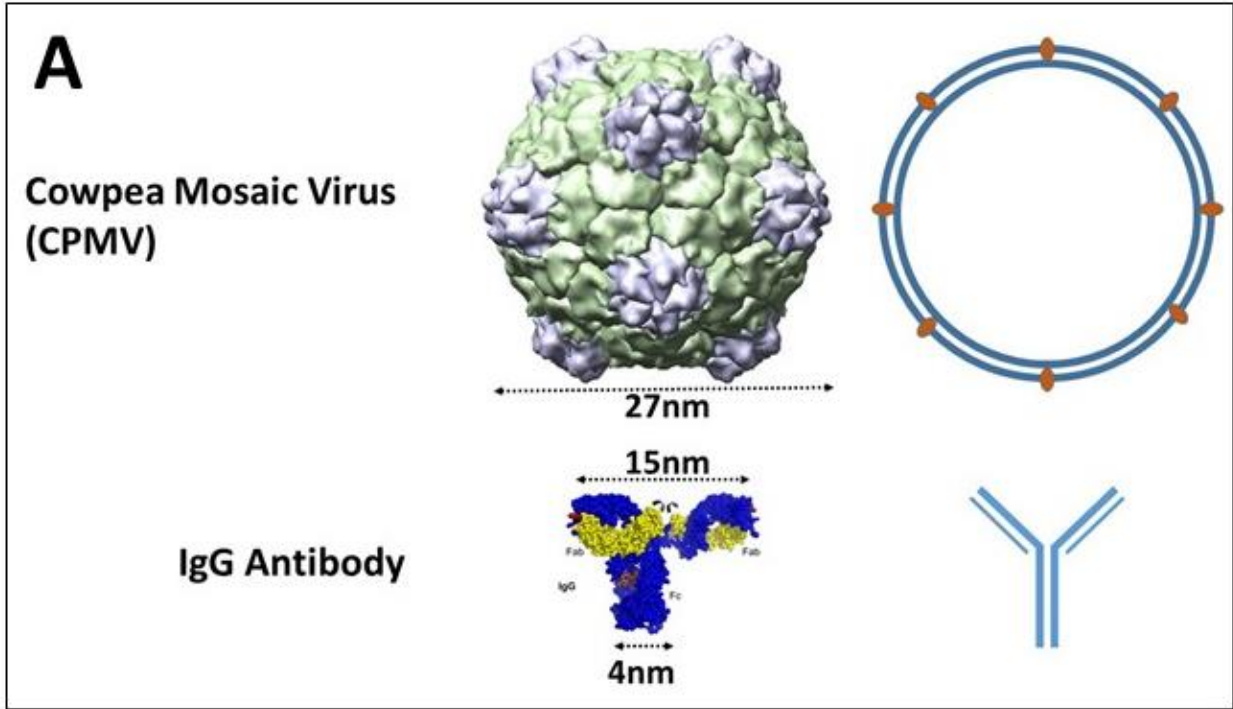


Figure 3.38: DNA Transcription Preliminary Results. A) TEM in Graphene Liquid Cells, we managed to trap RNAP-DNA complexes where the DNA was labelled with a 5nm AuNP (only one in this case) on the terminal end, and the RNAP was labelled with a 10nm AuNP. Multiple candidates circled, but significant background from extraneous AuNPs. B) TEM close-up of one such pair. C) Time series video of a RNAP-DNA complex moving within the GLC, demonstrating that the structure of the DNA and the adherence of the RNAP remained intact during electron beam irradiation.

3.4.1.3 Application: MAC Complex on Vesicles

Another particularly interesting application would be studying the Membrane Attack Complex (MAC) on vesicles. The MAC is a protein complex formed on a target pathogenic cell as part of an immune response from the host system referred to as the complement cascade. Typically, after an antibody attaches to some portion of the cell membrane, it recruits a series of complement proteins (labelled C5b, C6, C7, C8). These in turn induce the polymerization of 10-16 additional proteins (C9) which form an approximately 20nm pore in the plasma membrane of the cell. This leads to an influx of extracellular fluid into the cell, interferes with normal cell functioning, and eventually leads to cell death.

Performing this work on a whole cell would be near impossible as even the smallest cells are ~300nm and more typically in the 1-100 μ m range. By instead using vesicles, which can be 20-100nm in size and can have no other contents, we can hope to directly image the formation of a MAC in real time. Furthermore, demonstrating this use of vesicles for high resolution imaging of a membrane protein complex would open up the possibility of a range of further studies. A tremendous number of membrane proteins exist and play critical roles in cellular functioning. Currently, the best ways to study these complexes are statically with cryo-EM or X-Ray crystallography. Rather than snapshots, the graphene flow cell could allow for real-time videos of these essential cellular processes.

A proposed experimental design for this work is shown in Figure 3.39. The vesicles would be loaded into the GFC with the initial protein antibodies and protein complexes (except C9) already integrated into the lipid bilayer. In order to best image the MAC formation, a positive uranyl acetate stain would be best to provide contrast to the pore complex. Alternatively, heavy-atom nanoparticle (like gold) tagging could be used to indirectly image the formation. The positive staining approach may be particularly useful, as the vesicles should be free of stain on their interior before the pore has formed, giving it a significantly lighter contrast. The final C9 protein would then be loaded into the cell and when the complex is formed, you should be able to see the extracellular fluid with the stain enter the cell and see it darken.

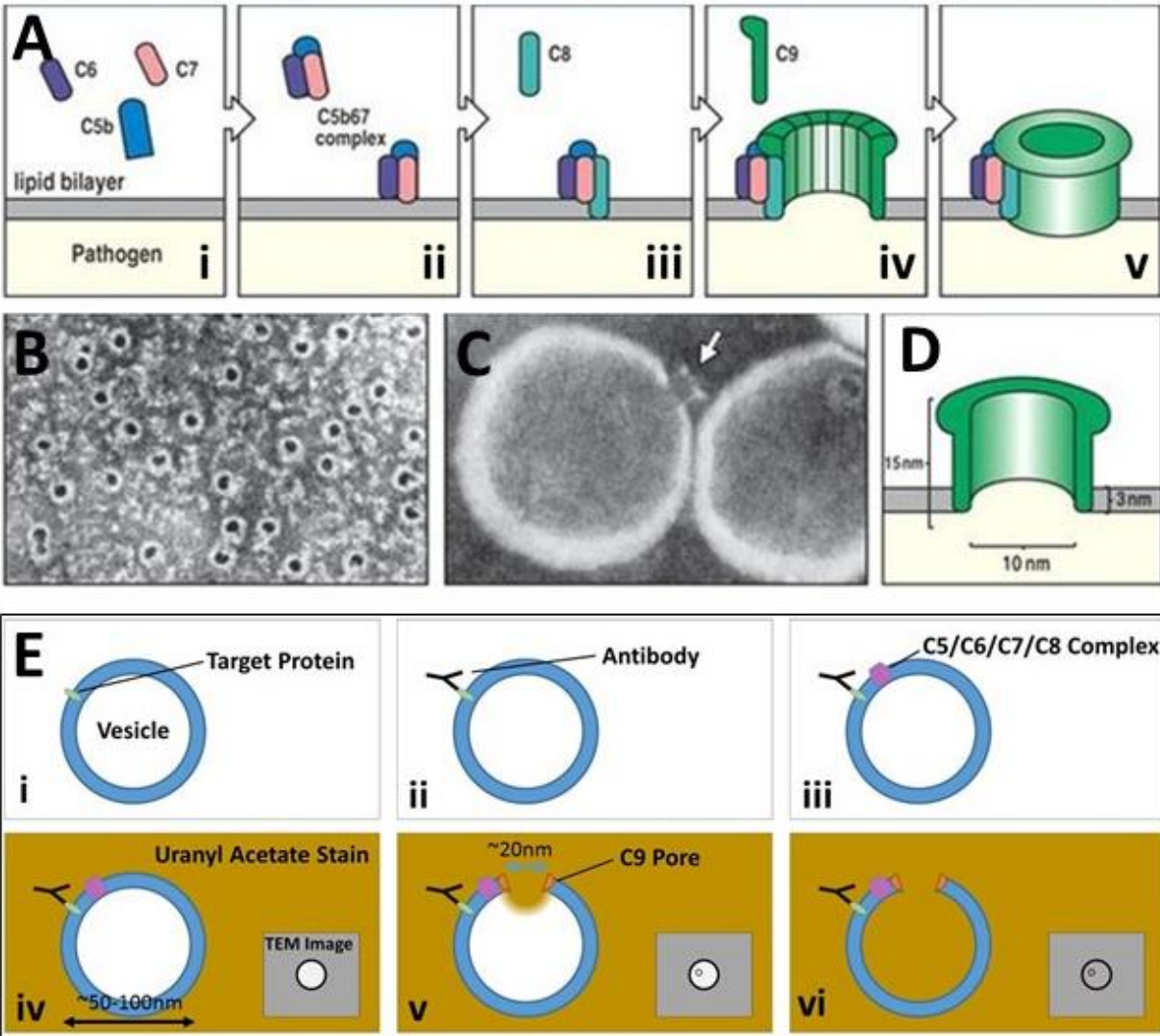


Figure 3.39: Membrane Attack Complex (MAC). A) i-v. Cartoon of MAC process. i) Antibody recruits protein cascade. ii) C5b, C6 and C7 form complex on membrane. iii) C8 protein recruited into complex. iv) Multiple C9 proteins recruited and incorporated into complex. v) C9's polymerize to form pore in membrane. B) SEM of multiple pores formed on a cell wall. C) TEM of pores on a vesicle. D) Schematic of C9 pore and sizes. E) i-v experimental design. i-iii) Vesicles are prepared with entire protein cascade except for C9 protein. iv) Vesicles are loaded into GFC w/ dilute uranyl acetate stain (0.01-0.1%). v) C9 protein is introduced and form pores in vesicle. vi) Uranyl acetate fills vesicle as evidenced by contrast change in TEM.

3.4.1.4 Application: Dynein on Microtubules

This represents work we performed with graduate student Ben LaFrance from Eva Nogales' group, and graduate student Sinan Can from Ahmet Yildiz's group. We had additional help from Postdocs Jongmin Yuk, Hamid Barzegar and Amin Azizi.

Dynein is a motor protein which carries cargo along microtubules inside of a cell along with other biological functions. Dynein is similar in structure and role to kinesin, another motor protein involved in transport along microtubules. Unlike RNAP work discussed above, where after the RNAP disengages from a DNA strand it is unable to re-link to another, when dynein falls off of a MT, it is capable of binding onto another and continue walking. This gave us hope that we would be able to load it into a static liquid cell and still be able to see dynamics at the time of imaging. This was an experiment we originally tried in the graphene liquid cell, which proved to be impossible due to the evaporative sealing of the liquid cell, and the lack of control over stain concentration. While the flow cell would solve this problem, the experimental design is not clear with the existing GFC channels, as microtubules are typically microns in length, so loading them into the nanochannels would be difficult. Eventually we used the Poseidon holder's standard nitride cells to try to image.

Cytoskeletal dynein typically present in a dimer, with each of the dynein consisting of a ring subunit, as well as a tail and a stalk. The dimer connects at the stalk, and the two tails act as legs as it walks along a microtubule. The ring is typically 15-20nm in radius, with the tail extending 20-25nm. The microtubule is around 25nm in diameter and consists of a spirally wound protein filaments. A cryo-TEM image of a Dynein monomer can be seen in Figure 3.40.

As is the case with most biological samples, there are too few heavy atoms to provide enough contrast for high resolution imaging, so either a stain or labelling scheme should be used. Staining would be preferable as it would give us a more complete picture of the dynamics of the dynein as it is walking, even if we couldn't fully resolve its tails. The downside to staining would be the potential effect it could have on functionality of the motor protein. To test this, we labelled dynein with quantum dots, and used an optical total internal reflection (TIRF) microscope to assess the viability of the dynein with 0.01% and 0.1% uranyl acetate (UA) stains. These are the stain concentrations necessary to positively stain the sample. We found that the UA interfered with the dynein's ability to bind to the microtubule at both 0.01 and 0.1%. However, if we introduced the UA after the dynein had the chance to bind to the microtubule, the dynein would remain attach and remain functional, as evidenced by the movement of the dynein along the microtubules. This suggests that the UA interference was from the binding of the UA salt on the bottom of the dynein stalks, and there was enough vacant space on the microtubules to still allow for the UA to walk along the microtubule.

We initially tried imaging the dynein/MT complexes in GLCs. However, because of the evaporative sealing, the final concentration of trapped solution had tremendous variability, even across a single sample. This was particularly a problem for the UA stain, which at low concentrations wouldn't provide enough contrast to see MTs, and at higher concentrations would

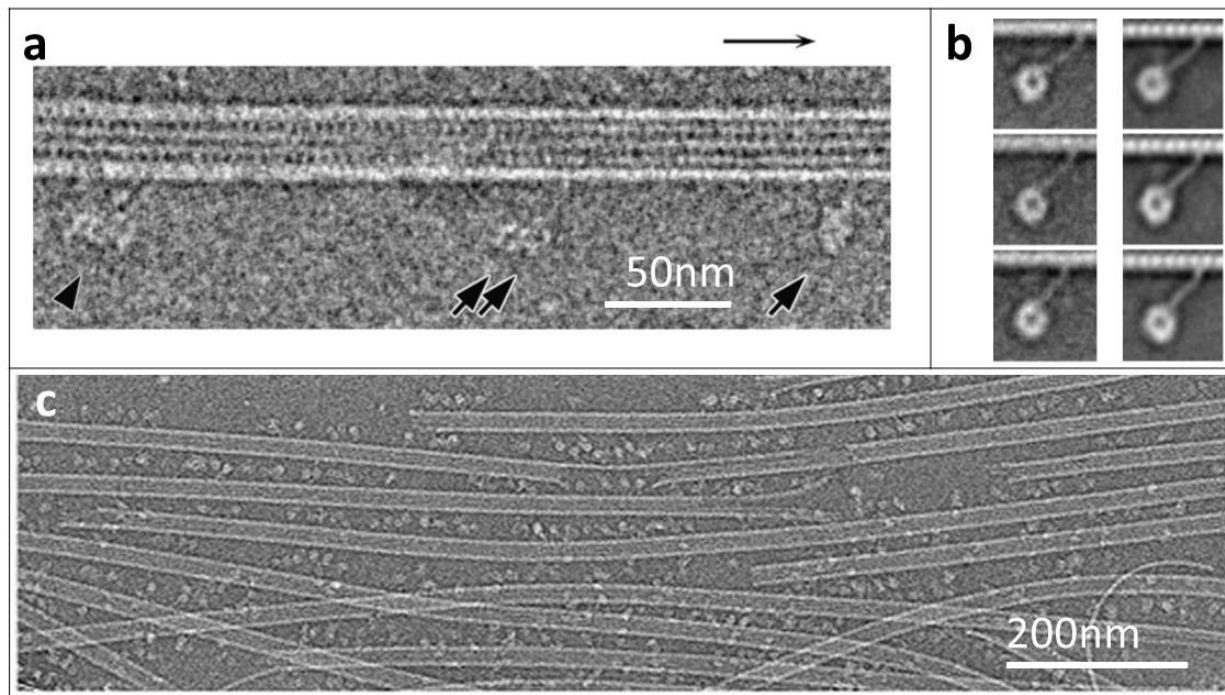


Figure 3.40: Dynein on Microtubule. a) Cryo-TEM image of dynein on a microtubule. b) Reconstructed image of dynein from multiple cryo-TEM images. c) Zoomed out cryo-TEM of dynein decorated microtubules. Adapted from Refs [92], [93].

be too opaque for imaging and the MTs would be too heavily caked in UA. Figure 3.41A shows an example of the best case for MT imaging in GLC. Although the UA salt is still too heavily concentrated, and there was no hope for resolving the dynein. After a number of unsuccessful attempts, we decided that the UA concentration was simply too variable. It is possible that using a STEM microscope with better resolution we would be able to resolve the dynein.

Instead, we finally turned to using the Poseidon flow holder, which while having significantly thicker encapsulating layers, and a thicker trapped liquid layer, is capable of precisely controlling the UA concentration. We first wanted to check to see that the Dynein is capable of decorating the MTs and that we can in fact see them under TEM. This work was therefore done in a static configuration, where the inlet and outlet ports are sealed. This means that ADP could not be added during imaging, so we were not expecting to see any dynamics. Dynein was loaded into a solution of MTs, followed by a short incubation period. The UA was then loaded into the solution at a 0.01% concentration. The results are shown in Figure 3.41B-C. As can be seen, it is possible that we are capable of resolving the dynein, but even this is speculative. The staining appears to be very faint.

This represents work that is ongoing. I believe by optimizing the UA concentration the Dynein could eventually be resolved, but at the resolutions we are now expecting, it does not appear that useful information about the dynamics of dynein could be discovered. Some improvement in either the flow holder or the microscope would be necessary to reach useful levels of resolution.

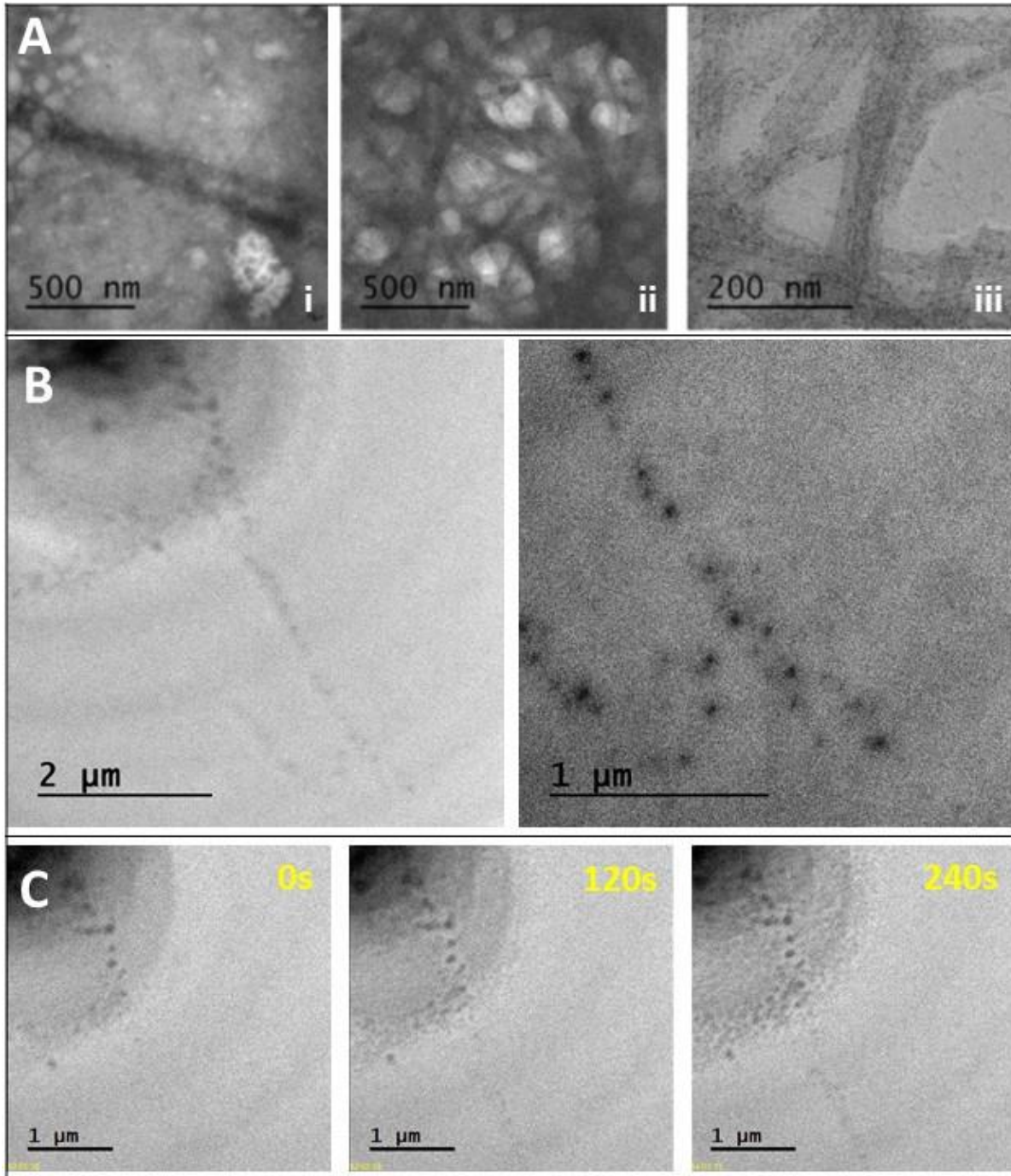


Figure 3.41: In-Situ TEM of Dynein on Microtubule. A) TEM images of dynein on MTs in a GLC. i) Best image of MT in GLC, and still significant background noise and no dynein visible. ii) Thick MT bundling in GLCs as the concentration is difficult to control. iii) Area in which the GLC had dried. B) TEM images of dynein on MTs in Protochips Poseidon SiN holder. Unclear if what we are seeing is the dynein. Resolution is much worse than (A) but much less background noise. C) Time series showing that the contrast of the MT/Dynein improves with imaging time.

Bibliography

- [1] E. Betzig *et al.*, “Imaging Intracellular Fluorescent Proteins at Nanometer Resolution,” *Sc*, vol. 1642, no. 2006, pp. 1642–1646, 2013.
- [2] R. Schmidt, C. A. Wurm, S. Jakobs, J. Engelhardt, A. Egner, and S. W. Hell, “Spherical nanosized focal spot unravels the interior of cells,” *Nat. Methods*, vol. 5, no. 6, pp. 539–544, 2008.
- [3] F. M. Ross, “Liquid Cell Electron Microscopy.” 2016.
- [4] M. E. Wise, G. Biskos, S. T. Martin, L. M. Russell, and P. R. Buseck, “Phase Transitions of Single Salt Particles Studied Using a Transmission Electron Microscope with an Environmental Cell,” *Aerosol Sci. Technol.*, vol. 39, no. 9, pp. 849–856, 2005.
- [5] M. J. Williamson, R. M. Tromp, P. M. Vereecken, R. Hull, and F. M. Ross, “Dynamic microscopy of nanoscale cluster growth at the solid-liquid interface,” *Nat. Mater.*, vol. 2, no. 8, pp. 532–6, 2003.
- [6] N. de Jonge, W. C. Bigelow, and G. M. Veith, “Atmospheric Pressure Scanning Transmission Electron Microscopy,” *Nano Lett.*, vol. 10, pp. 1028–1031, 2010.
- [7] S. Zhang *et al.*, “Dynamic structural evolution of supported palladium-ceria core-shell catalysts revealed by in situ electron microscopy,” *Nat. Commun.*, vol. 6, no. July, p. 7778, 2015.
- [8] S. Zhang, M. Cargnello, W. Cai, C. B. Murray, G. W. Graham, and X. Pan, “Revealing particle growth mechanisms by combining high-surface-area catalysts made with monodisperse particles and electron microscopy conducted at atmospheric pressure,” *J. Catal.*, vol. 337, pp. 240–247, 2016.
- [9] X. Chen, C. Li, and H. Cao, “Recent developments of the in situ wet cell technology for transmission electron microscopies,” *Nanoscale*, vol. 7, no. 11, pp. 4811–4819, 2015.
- [10] X. Chen, L. Zhou, P. Wang, C. Zhao, and X. Miao, “A study of nano materials and their reactions in liquid using in situ wet cell TEM technology,” *Chinese J. Chem.*, vol. 30, no. 12, pp. 2839–2843, 2012.
- [11] X. Chen, K. W. Noh, J. G. Wen, and S. J. Dillon, “In situ electrochemical wet cell transmission electron microscopy characterization of solid-liquid interactions between Ni and aqueous NiCl₂,” *Acta Mater.*, vol. 60, no. 1, pp. 192–198, 2012.
- [12] E. Jensen, A. Burrows, and K. Mølhave, “Monolithic chip system with a microfluidic channel for in situ electron microscopy of liquids,” *Microsc. Microanal.*, vol. 20, no. 2, pp. 445–51, 2014.
- [13] J. M. Yuk *et al.*, “High-Resolution EM of Colloidal Nanocrystal Growth Using Graphene Liquid Cells,” *Science (80-.)*, vol. 336, no. 6077, pp. 61–64, 2012.
- [14] J. Park *et al.*, “3D structure of individual nanocrystals in solution by electron microscopy,” *Science (80-.)*, vol. 349, no. 6245, pp. 290–295, 2015.
- [15] Y. Sasaki, R. Kitaura, J. M. Yuk, A. Zettl, and H. Shinohara, “Efficient preparation of graphene liquid cell utilizing direct transfer with large-area well-stitched graphene,” *Chem. Phys. Lett.*, vol. 650, pp. 107–112, 2016.

- [16] X. Ye *et al.*, “Single-particle mapping of nonequilibrium nanocrystal transformations,” vol. 354, no. 6314, pp. 345–348, 2016.
- [17] J. M. Yuk, M. Jeong, sang yun Kim, hyeon kook Seo, J. Kim, and jeong yong Lee, “In situ atomic imaging of coalescence of Au nanoparticles on graphene: rotation and grain boundary migration,” vol. 49, no. 98, 2013.
- [18] J. M. Yuk *et al.*, “Graphene Veils and Sandwiches,” pp. 3290–3294, 2011.
- [19] J. M. Yuk, Q. Zhou, J. Chang, P. Ercius, A. P. Alivisatos, and A. Zettl, “Real-time observation of water-soluble mineral precipitation in aqueous solution by in situ high-resolution electron microscopy,” *ACS Nano*, vol. 10, no. 1, pp. 88–92, 2016.
- [20] J. Young *et al.*, “Growth dynamics of solid electrolyte interphase layer on SnO₂ nanotubes realized by graphene liquid cell electron microscopy,” *Nano Energy*, vol. 25, pp. 154–160, 2016.
- [21] J. Y. Cheong, J. H. Chang, J. M. Yuk, J. Y. Lee, and I. Kim, “The Effect of Electron Beam Dosage in the Decomposition Behavior of Electrolytes Encapsulated Inside the Graphene Sheets Based on In Situ TEM Observation,” vol. 23, no. Suppl 1, pp. 2052–2053, 2017.
- [22] V. S. J. Craig, “Very small bubbles at surfaces—the nanobubble puzzle,” *Soft Matter*, vol. 7, no. 1, pp. 40–48, 2011.
- [23] S.-T. Lou *et al.*, “Nanobubbles on solid surface imaged by atomic force microscopy,” *J. Vac. Sci. Technol. B Microelectron. Nanom. Struct.*, vol. 18, no. 5, pp. 2573–2575, 2000.
- [24] X. H. Zhang, A. Quinn, and W. A. Ducker, “Nanobubbles at the interface between water and a hydrophobic solid,” *Langmuir*, vol. 24, no. 9, pp. 4756–4764, 2008.
- [25] H. Liu and G. Cao, “Effectiveness of the Young-Laplace equation at nanoscale,” *Sci. Rep.*, vol. 6, no. 1, p. 23936, 2016.
- [26] L. Makkonen, “Young’s equation revisited,” *J. Phys. Condens. Matter*, vol. 28, no. 13, p. 135001, 2016.
- [27] Y. Liu, J. Wang, and X. Zhang, “Accurate determination of the vapor-liquid-solid contact line tension and the viability of Young equation,” *Sci. Rep.*, vol. 3, no. 1, p. 2008, 2013.
- [28] H. Jiang, F. Müller-Plathe, and A. Z. Panagiotopoulos, “Contact angles from Young’s equation in molecular dynamics simulations,” *J. Chem. Phys.*, vol. 147, no. 8, 2017.
- [29] Y. Liu and X. Zhang, “A unified mechanism for the stability of surface nanobubbles: Contact line pinning and supersaturation,” *J. Chem. Phys.*, vol. 141, no. 13, 2014.
- [30] I. Ibagon, M. Bier, and S. Dietrich, “Three-phase contact line and line tension of electrolyte solutions in contact with charged substrates,” *J. Phys. Condens. Matter*, vol. 28, no. 24, p. 244015, 2016.
- [31] X. Zhang, D. Y. C. Chan, D. Wang, and N. Maeda, “Stability of interfacial nanobubbles,” *Langmuir*, vol. 29, no. 4, pp. 1017–1023, 2013.
- [32] H. Teshima, T. Nishiyama, and K. Takahashi, “Nanoscale pinning effect evaluated from deformed nanobubbles,” *J. Chem. Phys.*, vol. 146, no. 1, 2017.
- [33] J. M. Grogan, N. M. Schneider, F. M. Ross, and H. H. Bau, “Bubble and pattern formation in liquid induced by an electron beam,” *Nano Lett.*, vol. 14, no. 1, pp. 359–364, 2014.

- [34] N. M. Schneider, M. M. Norton, B. J. Mendel, J. M. Grogan, F. M. Ross, and H. H. Bau, “Electron-Water interactions and implications for liquid cell electron microscopy,” *J. Phys. Chem. C*, vol. 118, no. 38, pp. 22373–22382, 2014.
- [35] E. R. White, M. Mecklenburg, S. B. Singer, S. Aloni, and B. C. Regan, “Imaging nanobubbles in water with scanning transmission electron microscopy,” *Appl. Phys. Express*, vol. 4, no. 5, 2011.
- [36] D. Shin *et al.*, “Growth dynamics and gas transport mechanism of nanobubbles in graphene liquid cells,” *Nat. Commun.*, vol. 6, p. 6068, 2015.
- [37] E. R. White, M. Mecklenburg, B. Shevitski, S. B. Singer, and B. C. Regan, “Charged nanoparticle dynamics in water induced by scanning transmission electron microscopy,” *Langmuir*, vol. 28, no. 8, pp. 3695–3698, 2012.
- [38] A. S. Powers, H. G. Liao, S. N. Raja, N. D. Bronstein, A. Paul Alivisatos, and H. Zheng, “Tracking Nanoparticle diffusion and interaction during self-assembly in a liquid cell,” *Nano Lett.*, vol. 17, no. 1, pp. 15–20, 2017.
- [39] A. Verch, M. Pfaff, and N. De Jonge, “Exceptionally Slow Movement of Gold Nanoparticles at a Solid/Liquid Interface Investigated by Scanning Transmission Electron Microscopy,” *Langmuir*, vol. 31, no. 25, pp. 6956–6964, 2015.
- [40] H. Zheng, S. a Claridge, a M. Minor, a P. Alivisatos, and U. Dahmen, “Nanocrystal diffusion in a liquid thin film observed by in situ transmission electron microscopy - Supporting Info,” *Nano Lett*, vol. 9, no. 6, pp. 2460–2465, 2009.
- [41] T. J. Woehl and T. Prozorov, “The Mechanisms for Nanoparticle Surface Diffusion and Chain Self-Assembly Determined from Real-Time Nanoscale Kinetics in Liquid,” *J. Phys. Chem. C*, vol. 119, no. 36, pp. 21261–21269, 2015.
- [42] Y. Cui, M. T. Björk, J. A. Liddle, C. Sönnichsen, B. Boussert, and A. P. Alivisatos, “Integration of colloidal nanocrystals into lithographically patterned devices,” *Nano Lett.*, vol. 4, no. 6, pp. 1093–1098, 2004.
- [43] T. A. Land, J. J. De Yoreo, and J. D. Lee, “An in-situ AFM investigation of canavalin crystallization kinetics,” *Surf. Sci.*, vol. 384, no. 1–3, pp. 136–155, 1997.
- [44] T. A. Land and J. J. De Yoreo, “The evolution of growth modes and activity of growth sources on canavalin investigated by in situ atomic force microscopy,” *J. Cryst. Growth*, vol. 208, no. 1–4, pp. 623–637, 2000.
- [45] H. H. Teng, “Thermodynamics of Calcite Growth: Baseline for Understanding Biomineral Formation,” *Science (80-.)*, vol. 282, no. 5389, pp. 724–727, 1998.
- [46] J. De Yoreo and G. Waychunas, “In situ investigations of carbonate nucleation on mineral and organic surfaces,” *Rev. ...*, vol. 77, pp. 229–257, 2013.
- [47] J. Desarnaud, H. Derluyn, J. Carmeliet, D. Bonn, and N. Shahidzadeh, “Metastability limit for the nucleation of NaCl crystals in confinement,” *J. Phys. Chem. Lett.*, vol. 5, no. 5, pp. 890–895, 2014.
- [48] S. Brenner and R. W. Horne, “A negative staining method for high resolution electron microscopy of viruses,” *Biochim. Biophys. Acta*, vol. 34, pp. 103–110, 1959.
- [49] K. T. Tokuyasu, “A study of positive staining of ultrathin frozen sections,” *J. Ultrastructure Res.*, vol. 63, no. 3, pp. 287–307, 1978.

- [50] S. M. da C. and Elizabeth F. Rangel and B. M. Carvalho, “Negative and Positive Staining in Transmission Electron Microscopy for Virus Diagnosis,” in *Microbiology in Agriculture and Human Health*, 2015, pp. 45–56.
- [51] J. Dubochet *et al.*, “Cryo-electron microscopy of vitrified specimens.,” *Q. Rev. Biophys.*, vol. 21, no. 2, pp. 129–228, 1988.
- [52] E. Zeitler, “Cryo Electron Microscopy,” *Ultramicroscopy*, vol. 10, pp. 1–6, 1982.
- [53] M. Adrian, J. Dubochet, J. Lepault, and a W. McDowell, “Cryo-electron microscopy of viruses,” *Nature*, vol. 308, pp. 32–36, 1984.
- [54] A. Bartesaghi *et al.*, “2.2 Å resolution cryo-EM structure of B-galactosidase in complex with a cell-permeant inhibitor,” *Electron Microsc. ICEM14, Mex. ...*, vol. 348, no. 6239, pp. 1147–1152, 2015.
- [55] N. de Jonge and F. M. Ross, “Electron microscopy of specimens in liquid,” *Nat. Nanotechnol.*, vol. 6, no. 11, pp. 695–704, 2011.
- [56] N. de Jonge, N. Poirier-Demers, H. Demers, D. B. Peckys, and D. Drouin, “Nanometer-resolution electron microscopy through micrometers-thick water layers,” *Ultramicroscopy*, vol. 110, no. 9, pp. 1114–1119, 2010.
- [57] T. J. Woehl *et al.*, “Correlative electron and fluorescence microscopy of magnetotactic bacteria in liquid: toward in vivo imaging.,” *Sci. Rep.*, vol. 4, p. 6854, 2014.
- [58] D. C. Joy and C. S. Joy, “Scanning electron microscope imaging in liquids – some data on,” *J. Microsc.*, vol. 221, no. July 2005, pp. 84–88, 2006.
- [59] J. Roth and M. Binder, “Colloidal gold, ferritin and peroxidase as markers for electron microscopic double labeling lectin techniques,” *J. Histochem. Cytochem.*, vol. 26, no. 3, pp. 163–169, 1978.
- [60] J. E. Evans *et al.*, “Visualizing macromolecular complexes with in situ liquid scanning transmission electron microscopy,” *Micron*, vol. 43, no. 11, pp. 1085–1090, 2012.
- [61] H. Rinderknecht, “Ultra-Rapid Fluorescent Labelling of Proteins,” *Nature*, vol. 193, pp. 167–168, 1962.
- [62] E. R. Goldman and H. Mattoussi, “Quantum dot bioconjugates for imaging , labelling and sensing,” p. 2005, 2005.
- [63] B. A. Griffin, S. R. Adams, and R. Y. Tsien, “Specific Covalent Labeling of Recombinant Protein Molecules Inside Live Cells,” vol. 281, no. July, pp. 269–273, 1998.
- [64] N. G. Anderson *et al.*, “The Fluorescent Toolbox for Assessing,” no. April, pp. 217–225, 2006.
- [65] D. B. Peckys and N. De Jonge, “Visualizing gold nanoparticle uptake in live cells with liquid scanning transmission electron microscopy,” *Nano Lett.*, vol. 11, no. 4, pp. 1733–1738, 2011.
- [66] E. S. Pohlmann, K. Patel, S. Guo, M. J. Dukes, Z. Sheng, and D. F. Kelly, “Real-Time Visualization of Nanoparticles Interacting with Glioblastoma Stem Cells,” *Nano Lett.*, vol. 15, no. 4, pp. 2329–2335, 2015.
- [67] D. B. Peckys and N. de Jonge, “Gold Nanoparticle Uptake in Whole Cells in Liquid Examined by Environmental Scanning Electron Microscopy,” *Microsc. Microanal.*, vol. 20, no. 1, pp. 189–197, 2014.

- [68] H. Sugi *et al.*, “Direct demonstration of the cross-bridge recovery stroke in muscle thick filaments in aqueous solution by using the hydration chamber,” *PNAS*, vol. 105, no. 45, pp. 17396–17401, 2008.
- [69] E. Kennedy, E. M. Nelson, T. Tanaka, J. Damiano, and G. Timp, “Live Bacterial Physiology Visualized with 5 nm Resolution Using Scanning Transmission Electron Microscopy,” *ACS Nano*, vol. 10, no. 2, pp. 2669–2677, 2016.
- [70] U. M. Mirsaidov, H. Zheng, Y. Casana, and P. Matsudaira, “Imaging protein structure in water at 2.7 nm resolution by transmission electron microscopy,” *Biophys J*, vol. 102, no. 4, pp. L15-7, 2012.
- [71] J. Hermannsdörfer, V. Tinnemann, D. B. Peckys, and N. de Jonge, “The Effect of Electron Beam Irradiation in Environmental Scanning Transmission Electron Microscopy of Whole Cells in Liquid,” *Microsc. Microanal.*, vol. 22, no. 3, pp. 656–665, 2016.
- [72] V. Crespi, N. Chopra, M. Cohen, a Zettl, and S. Louie, “Anisotropic electron-beam damage and the collapse of carbon nanotubes,” *Phys. Rev. B. Condens. Matter*, vol. 54, no. 8, pp. 5927–5931, Aug. 1996.
- [73] R. F. Egerton, P. Li, and M. Malac, “Radiation damage in the TEM and SEM,” *Micron*, vol. 35, no. 6, pp. 399–409, 2004.
- [74] J. Park *et al.*, “Direct Observation of Wet Biological Samples by Graphene Liquid Cell Transmission Electron Microscopy,” *Nano Lett.*, vol. 15, no. 7, pp. 4737–4744, 2015.
- [75] Q. Chen *et al.*, “3D motion of DNA-Au nanoconjugates in graphene liquid cell electron microscopy,” *Nano Lett.*, vol. 13, no. 9, pp. 4556–4561, 2013.
- [76] H. Cho, M. R. Jones, S. C. Nguyen, M. R. Hauwiller, A. Zettl, and A. P. Alivisatos, “The use of graphene and its derivatives for liquid-phase transmission electron microscopy of radiation-sensitive specimens,” *Nano Lett.*, vol. 17, no. 1, pp. 414–420, 2017.
- [77] H. Rasool, G. Dunn, A. Fathalizadeh, and A. Zettl, “Graphene-sealed Si/SiN cavities for high-resolution in situ electron microscopy of nano-confined solutions,” *Phys. Status Solidi Basic Res.*, vol. 253, no. 12, pp. 2351–2354, 2016.
- [78] S. Bhaviripudi, X. Jia, M. S. Dresselhaus, and J. Kong, “Role of kinetic factors in chemical vapor deposition synthesis of uniform large area graphene using copper catalyst,” *Nano Lett.*, vol. 10, no. 10, pp. 4128–4133, 2010.
- [79] F. J. Blanco *et al.*, “Novel three-dimensional embedded SU-8 microchannels fabricated using a low temperature full wafer adhesive bonding,” *J. Micromechanics Microengineering*, vol. 14, no. 7, pp. 1047–1056, 2004.
- [80] S. Li, C. B. Freidhoff, R. M. Young, and R. Ghodssi, “Fabrication of micronozzles using low-temperature wafer-level bonding with SU-8,” *J. Micromech. Microeng.*, vol. 13, no. 3, pp. 732–738, 2003.
- [81] S. Tuomikoski and S. Franssila, “Free-standing SU-8 microfluidic chips by adhesive bonding and release etching,” *Sensors Actuators, A Phys.*, vol. 120, no. 2, pp. 408–415, 2005.
- [82] M. Agirregabiria *et al.*, “Fabrication of SU-8 multilayer microstructures based on successive CMOS compatible adhesive bonding and releasing steps,” *Lab Chip*, vol. 5, no. 5, pp. 545–552, 2005.

- [83] L. Yu, F. E. H. Tay, G. Xu, B. Chen, M. Avram, and C. Iliescu, “Adhesive bonding with SU-8 at wafer level for microfluidic devices,” *J. Phys. Conf. Ser.*, vol. 34, no. 1, pp. 776–781, 2006.
- [84] P. Svasek, E. Svasek, B. Lendl, and M. Vellekoop, “Fabrication of miniaturized fluidic devices using SU-8 based lithography and low temperature wafer bonding,” *Sensors Actuators, A Phys.*, vol. 115, no. 2–3 SPEC. ISS., pp. 591–599, 2004.
- [85] I. Welch, W., J. C. J. Chae, S.-H. L. S.-H. Lee, N. Yazdi, and K. Najafi, “Transient liquid phase (TLP) bonding for microsystem packaging applications,” *Proc. 13th Int. Conf. Solid-State Sensors, Actuators Microsystems*, pp. 1350–1353, 2005.
- [86] R. Straessle, Y. Pétremand, D. Briand, and N. F. De Rooij, “Evaluation of thin film indium bonding at wafer level,” *Procedia Eng.*, vol. 25, pp. 1493–1496, 2011.
- [87] U. Hochuli and P. Haldemann, “Indium Sealing Techniques,” *Rev. Sci. Instrum.*, vol. 43, no. 8, pp. 1088–1089, 1972.
- [88] G. Pan *et al.*, “Nanobubbles at Hydrophilic Particle – Water Interfaces,” 2016.
- [89] J. W. Chang *et al.*, “Hybrid electron microscopy-FRET imaging localizes the dynamical C-terminus of Tfg2 in RNA polymerase II-TFIIF with nanometer precision,” *J. Struct. Biol.*, vol. 184, no. 1, pp. 52–62, 2013.
- [90] K. Ohgaki, N. Q. Khanh, Y. Joden, A. Tsuji, and T. Nakagawa, “Physicochemical approach to nanobubble solutions,” *Chem. Eng. Sci.*, vol. 65, no. 3, pp. 1296–1300, 2010.
- [91] J. Howatson, D. M. Grev, and B. Morosin, “Crystal and molecular structure of uranyl acetate dihydrate,” *J. Inorg. Nucl. Chem.*, vol. 37, no. 9, pp. 1933–1935, 1975.
- [92] S. A. Burgess, M. L. Walker, H. Sakakibara, P. J. Knight, and K. Oiwa, “Dynein structure and power stroke,” *Nature*, vol. 421, no. 6924, pp. 715–718, 2003.
- [93] A. J. Roberts *et al.*, “AAA+ Ring and Linker Swing Mechanism in the Dynein Motor,” *Cell*, vol. 136, no. 3, pp. 485–495, 2009.

Part II:

**Carbon Nanotube Neural
Probes**

Chapter 4

Background – Electrophysiology and Nanoprobes

4.1 Overview

Here we discuss our work towards a carbon nanotube (CNT) based neural probe. The idea behind the probe is straightforward – the CNT would act as an electrode, inserted into a neuron like a needle, where it is capable of recording changes in potential across the cell membrane. The CNT would need to be insulated except for an active sensing area at the inserted tip. In this chapter, we will cover the essentials of electrophysiology and evaluate CNTs as an electrode material. In the following chapter, we will first discuss the results of a single-unit CNT probe, followed by our scalable approach to fabricating a multi-unit CNT device.

4.2 Introduction

The scale of the questions neuroscientists ultimately seek to answer is enormous. The human brain consists of nearly 100 billion neurons, with each of those neurons making thousands of connections with other neurons, creating a vastly complex network. In order to fully understand this network and the emergent behavior born out of it, we need to be able to record from neurons at the single-unit level at scales that have yet to be even close to realized. With neural densities far exceeding 100,000 neurons/mm³, the need for miniaturization is clear.

Existing single-unit recording technology has allowed for a clearer understanding of the signaling mechanism of neurons. Ion pumps along the cell membrane create a resting potential inside the neuron of around -70mV relative to the cell's exterior. The input of other neurons trigger the opening or closing of ion channels which modulate the ionic potential of the cell. These small changes in potential are referred to as post-synaptic potentials (PSPs) and can be inhibitory or excitatory. The change in potential can vary greatly, and typically occurs at a characteristic frequency of around 100Hz. If these PSPs push the membrane potential past a critical threshold, around -55mV, additional voltage-gated ion channels begin to open as well. This creates a runaway process – an action potential – that causes a large spike in the membrane potential to +40mV, before the ion channels close and the cell returns to its resting state, with a characteristic frequency of 1kHz. This can be seen schematically in Figure 4.1.

Decoding the brain becomes an issue of intercepting these swings in ionic potential. Simply being able to identify and monitor all of the 100mV at 1kHz action potentials in a dense region would be enormously valuable and would mark a major step towards our understanding of the brain. Being able to detect the smaller PSPs to a level of 1mV at 100Hz for a large number of neurons in a network could revolutionize the study of systems neuroscience.

Unfortunately, existing techniques do not scale well to meet this challenge. Typical extracellular probes are now capable of recording action potentials from a large number of individual neurons, but they are incapable of registering PSPs and the necessary size of the probes sensing region makes it impossible to scale to high density recordings of every neuron within a region. Intracellular glass micropipette recording devices are capable of recording PSPs, but do so with a device geometry and preparation that do not allow for many unit recordings and are typically unsuitable for long-term recordings. Researchers have ultimately turned towards nanotechnology to allow for many-unit probes capable of entering the cell and capable of a probe density that can match neural densities. Nanotubes and nanowires have been obvious points of interest as their high aspect ratios allow for easy injection into a cell, while maintaining enough surface area for adequate sensing.

While a significant amount of work has been done in the last decade using silicon nanowires, there are a number of reasons to believe that Carbon Nanotubes (CNTs) may make an

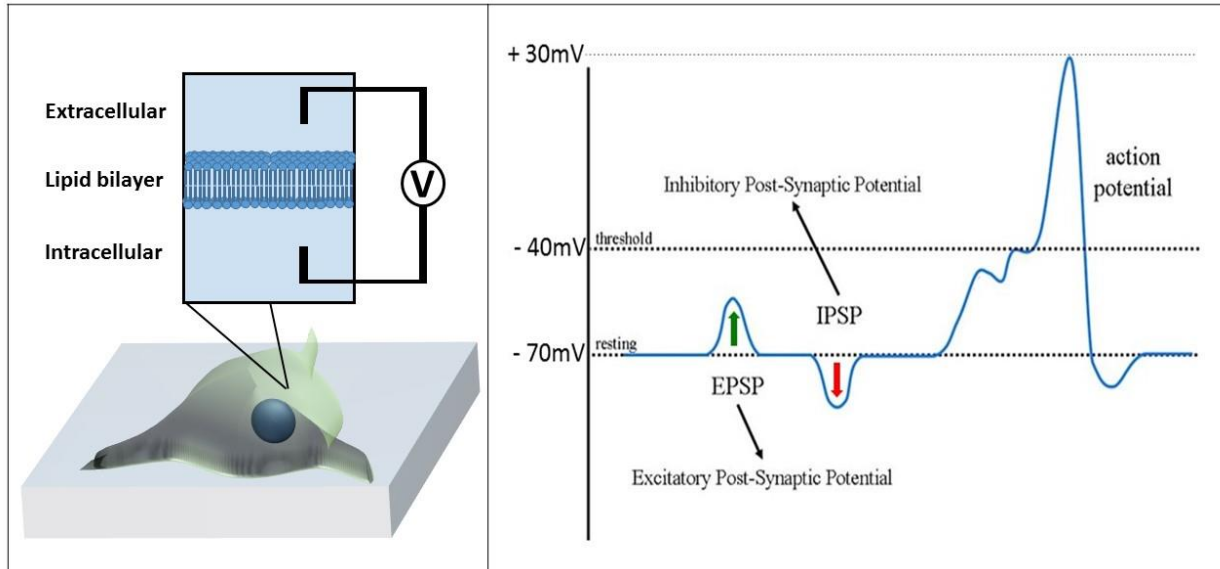


Figure 4.1: Electrophysiology of a neuron. Left shows a cartoon of a neuron, with the inset showing the lipid bilayer interface. If one were to perfectly measure the potential of the inside of the cell relative to the outside of the cell, it would have characteristics much like the cartoon plot on the right.

ideal nanoprobe material. Physically, they are capable of higher aspect ratios, have higher Young's moduli, and are more ductile. They are themselves metallic, and have uniquely rich and tunable electrochemical properties.

4.3 Electrophysiology

A neural recording devices needs to translate the changes in ionic potential within a cell to an electronic readout. Therefore, electrochemical impedance of the sensing area is a key measure of a probe's viability. Beyond this, the presence of the probes should have a minimal impact on the activity they hope to be measuring. Especially in the case of long-term implants, the biocompatibility of the probe is also essential. We will talk about both of these factors generally before discussing specific examples of neural probes.

Single-unit neural probes can be split into two groups: extracellular and intracellular. Where intracellular recording devices access the interior of a cell and the signals they are recording are the full potential between the interior and exterior of the cell, while extracellular probes sit outside of the target cells and measure dipole field of the action potential. As such, the characteristics of the signal and noise these two probes see is very different. For action potentials, the intracellular probe is seeing the full 100mV swing at 1kHz, while extracellular probes are typically seeing between 1-100 μ V depending on the probes distance from the target

cell. Because of the often dense packing of neurons, a significant source of noise for extracellular probes is the activity of surrounding neurons, or the local field potential (LFP), whereas intracellular probes are more shielded from this.

4.3.1 Electrochemical Impedance

The ability of a neural probe to measure action potentials or PSPs relies on the probe's electrochemical impedance. This depends on the exposed surface area of the device and the electrochemical impedance per area of the material. While the electrochemical impedance is critical in assessing a probe's capability, the signal-to-noise ratio will also depend on the amplitude of the signal being measured as well as noise. As such, we will also discuss expected signal sizes and noise sources and how they differ in extracellular and intracellular measurements.

The electrochemical impedance per unit area can be split into two components, non-Faradaic and Faradaic. The non-Faradaic component is capacitive and arises from the Helmholtz double-layer that forms at the interface of the electrode and ionic solution. For most materials, the double-layer thickness is comparable and hence the capacitance is similar. In this case, the net capacitance then scales with surface area. However, many nanomaterials have exhibited anomalously low non-Faradaic impedances [1]. The exact reason for this is unclear, but as classic derivations of the Helmholtz double-layer assume an effectively infinite plane, it is perhaps not surprising that nanoscopic features produce anomalous results.

The Faradaic component is a resistive component, in which some reaction is taking place at the interface of the electrode. This impedance can be seen as the cost of going from ionic charge carriers to electronic charge carriers. A polarizable electrode is one in which no charge transfer takes place, such is the case with Au or Pt. An ideal non-polarizable electrode is one in which charge transfer happens readily, such as Ag/AgCl electrodes. Typical extracellular probes use materials with no charge transfer and rely instead on high surface area capacitance [2]. It is worth noting that we have limited the discussion of electrode material properties to recording from neurons and not stimulation. By shrinking the electrode surface area substantially, as is the case with the CNT intracellular electrode, it is unlikely that enough charge can be injected into the cell to stimulate action potentials. Still, graphene and CNTs have demonstrated extremely high charge injection limits, so it may be worth revisiting their ability to stimulate neural action potentials, or at least contribute to the inhibition or excitation of PSPs [1], [3], [4].

When comparing probe materials, it is common to discuss the impedance per unit area at 1kHz, as this is the principle frequency in an action potential. This measurement is typically performed in 0.9% saline solution, similar to in-vivo concentrations [2]. Because we are not just interested in action potentials, but also the more sensitive PSPs, we are also interested in the impedance at lower frequencies and will refer to the impedance at 100Hz as well.

The extracellular probe is at a tremendous disadvantage in terms of signal. Immediately outside of a cell, signal from an action potential is reduced to $\sim 1\text{mV}$. Due to encapsulation of the electrode and cell damage, probes are typically much further from the surface of the neuron. As one travels away from the neuron, the intensity of the signal drops exponentially. Typical extracellular probes only see signals on the order of $1\text{-}100\mu\text{V}$, or 3-5 orders of magnitude lower than the full 120mV signal.

In contrast, the intracellular probe is capable of seeing the full 120mV signal. The primary limitation in signal for an intracellular probe is leakage through the entry site of the probe in the cell or through an exposed area of the electrode not fully in the cell.

Noise sources differ for extracellular and intracellular probes as well. The dominant noise source for extracellular probes is the activity of surrounding neurons, or local field potential (LFP). As regions of neurons often fire in concert, this noise source can be quite large. While the magnitude of this noise can often be many times the signal, this noise can be greatly reduced in post-processing, where voltage spikes can be attributed to their source neuron. While effective, this can be computationally very demanding.

In comparison, an intracellular probe is significantly less effected by noise from surrounding neurons. For the nanoelectrodes we will be considering, the more significant source of noise is Johnson noise, resulting from the high impedance of the electrochemical interface. The RMS magnitude of the Johnson noise is given by:

$$V_{RMS} = \sqrt{4k_B T R \Delta f}$$

Where k_B is the Boltzmann constant, T is the temperature, R is the resistance, and Δf is the recording bandwidth. This noise source is inherent to the system, and there is no means of separating it from the signal. For glass micropipettes, the surface area of the voltage probe wire is not limited as it lies outside of the cell, so the impedance and hence the Johnson noise are negligible.

4.3.2 Biocompatibility

The immune response to neural implants is complex but vital to the success of a neural probe. The body uses multiple different inputs to identify a foreign body, contributing to this complexity. Once a foreign body is recognized, the body will work to wall the probe off and expel it from the body. This response creates a layer of cells between the sensing area and the cells of interest, and can cause movement in your probe further affecting measurements.

The initial insertion of a neural probe can be, by all accounts, a violent one. As the electrode enters the cortex, it likely ruptures capillaries and neural cells, and extracellular tissue is compressed and disturbed. In response to this, the brain mounts an immune response. A variety of immunoresponsive cells, such as astrocytes and microglia, are redirected to the area, edema (fluid build-up in the area) quickly sets in, and the pressure in the area can increase further [5]–[8]. Hemorrhaging and increased pressure in the area, as well as signaling molecules

from lysed cells, may lead to cell death of nearby neurons, killing the very cells one hopes to record.

Over the following days, the immune response continues. Glial cells begin to encapsulate the foreign body and aim to expel it. In addition to the glial encapsulation, cell death is common amongst neurons in the immediate area. For longer term implants, these glial cells form a scar tissue layer around the foreign electrode, as shown in Figure 4.2. This encapsulating layer can create a number of problems for recording units. The encapsulating layer serves to insulate the active sites of the probe. The encapsulating layer can also wedge itself between the electrode and the healthy neural tissue, increasing the distance between the recording sites and the active neurons. And finally, this encapsulation can cause a drift in the position of the electrode, making it more difficult to stably record from individual units over a long period of time reliably [5], [9]–[12]

The methods which the immune system uses to recognize foreign bodies, and how this immune system is signaled in the first place is essential in coming up with strategies to reduce the response. Beyond the byproducts of insertion site trauma, the scale of the immune response can depend on the size of the foreign body, the material makeup of the foreign body, and the elastic properties of the foreign body.

Kipke et al. first clearly demonstrated the probe size dependence of glial scar formation. They used a novel parylene probe in which a microscale lateral edge was supported by a larger shank, as can be seen in Figure 4.3a. For various lateral edge dimensions, they measured the immune response. As can be seen in Figure 4.3, the immune response for the smaller lateral

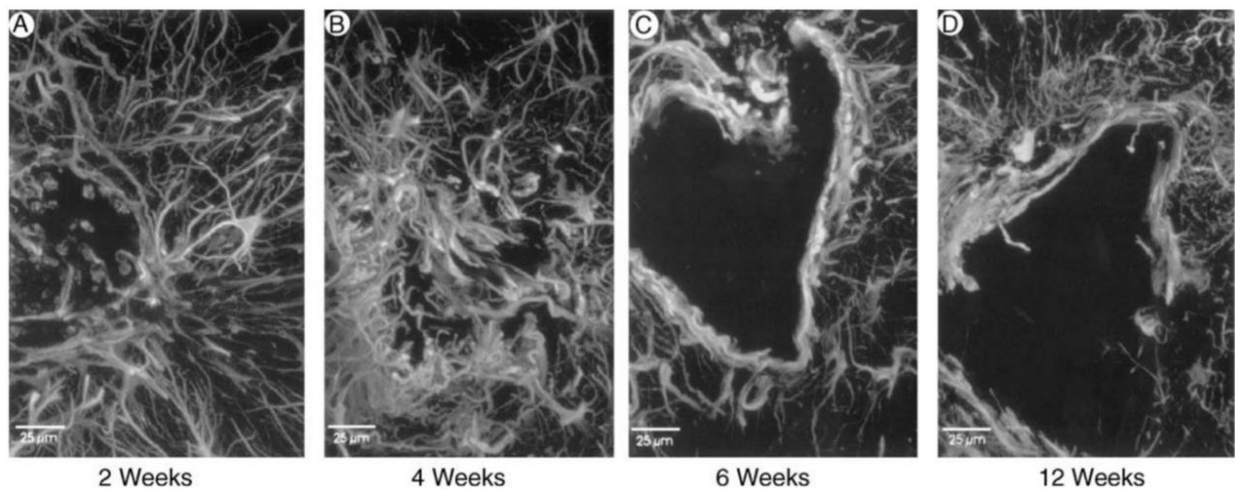


Figure 4.2: Glial scar formation after probe removal. Fluorescent images taken with glial cell and astrocyte marker stain. A)-B) In first 4 weeks, astrocytes are activated and recruited into the region the probe left behind. C)-D) A glial sheath forms around the implant site. Adapted from Ref [5]

edges was significantly diminished compared to the larger shank, and the smaller the later edge, the smaller the immune response [10].

The material makeup of the probe is also of importance in considering the immune system's ability to recognize the probe as foreign and treat it as a threat. A range of metals and polymers have been identified as biocompatible in that they are not in and of themselves toxic. Of particular note for our work is the polymer Parylene C, which has demonstrated excellent biocompatibility and is an often used substrate for medical devices [13]. This does not preclude these materials from triggering an immune reaction in response to a foreign body. The engineering of advances materials which demonstrate reduced immune responses is an entire field of its own [14]. Beyond biocompatibility, a great deal of work has also been done in developing bioactive materials, in which biological material is incorporated into the probe design [15]–[21]. Kennedy et al. demonstrated that a glass cone electrode with a section of sciatic nerve placed into the cone before insertion caused neurons to grow into the implanted nerve, better facilitating long-term chronic recording [22].

Elastic modulus can also be critical in reducing the immune response. Flexible electrodes are capable of providing strain relief against micromotions of the electrode within the neural tissue [23]. These micromotions can increase local pressure regions and can lead to an increase in inflammation at the insertion site. Immune cells may use this mismatch in elastic modulus as a means of recognizing a foreign body, exacerbating the immune response [24], [25]. Finally, these micromotions can pull the recording sites away from the target neuron, hampering long-term single-unit recordings. While attempting to better match the elastic modulus of the neural tissue is appealing, the probe must have a high enough buckling strength to enter the tissue in the first place.

While we have discussed how this immune response leads to diminished signal amplitudes and potentially increased noise, this says nothing about how severely we may be altering the very system we hope to observe. Improving biocompatibility of neural probes is more than just an issue of improving recordings, but ensuring that the recordings we gather are representative of a normally functioning brain.

4.4 Standard Neural Probes

Extracellular electrodes have seen major advances in the last thirty years due in large part to advances in planar silicon fabrication processes for microelectronics. Early extracellular electrodes consisted of sharpened insulated rods with the tips exposed. These early electrodes were used in the first recordings of neural activity in the central nervous system.

In the early 80's researchers began developing silicon based microelectrode arrays (MEAs). Two devices of particular note were the Michigan and Utah arrays shown in Figure 4.4, named after the institutions in which they were developed. The Michigan array, originally developed by Wise et al., consists of multiple metallic electrodes patterned along a silicon shank using typical silicon planar processing techniques [26]. This allows for a tremendous density of

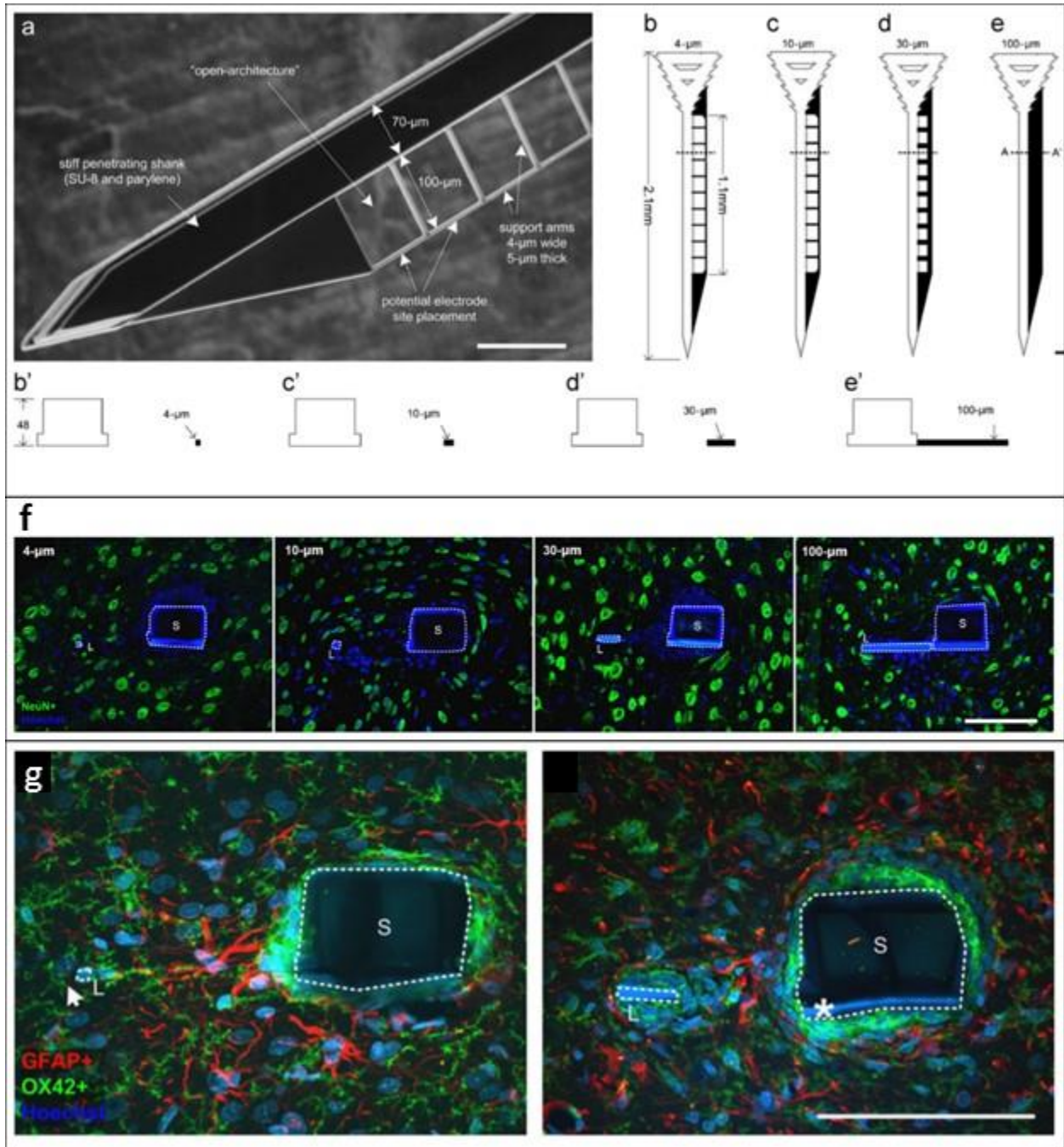


Figure 4.3: Probe size dependence of immune response. a)-e) Probe design. Silicon shanks with smaller lateral edges were coated in parylene. 4µm, 10µm, 30µm, and 100µm lateral fins were compared. f) Fluorescent images of neuron viability. Neurons are shown in green and the parylene in blue. While there were clear areas of cell death surrounding the shank, the smaller lateral edges do not illustrate this. g) Fluorescent images of immune reaction. Each color represents distinct immunoreactive cell types. Once more, the smaller lateral edge sites show a significantly diminished immunoresponse. Scale bar is 100µm. Adapted from Ref [10].

recording sites along the length of the silicon shank. These probes continued to be developed by Wise and other researchers, and eventually became commercially available under the company name, NeuroNexus [27]–[32].

In the Utah array, a grid of silicon needles is coated in platinum, and a parylene insulation layer is then selectively removed with an oxygen plasma at the tip to create the probes seen in Figure 4.4B [33]–[36]. While still used and further improved today, most of the next-generation single-unit recording MEAs being developed are more similar to the Michigan array. While each silicon needle represents an individual recording unit in the Utah array, the Michigan array can support a densely packed array of recording sites. Modern Michigan arrays have also begun to incorporate CMOS electronics directly onto the probe and some have even started to incorporate optical waveguides as well [32].

Meanwhile, intracellular electrodes have been slow to advance until the last decade. Intracellular recording has been dominated by glass microelectrodes since their development in 1949 by Gerard and Ling [37]–[40]. Glass microelectrodes are formed by locally heating a glass capillary tube to its melting point and pulled to a fine point. Remarkably, these tips can be drawn down to outer diameters as small as 50nm and maintain an open capillary. The pipette is then

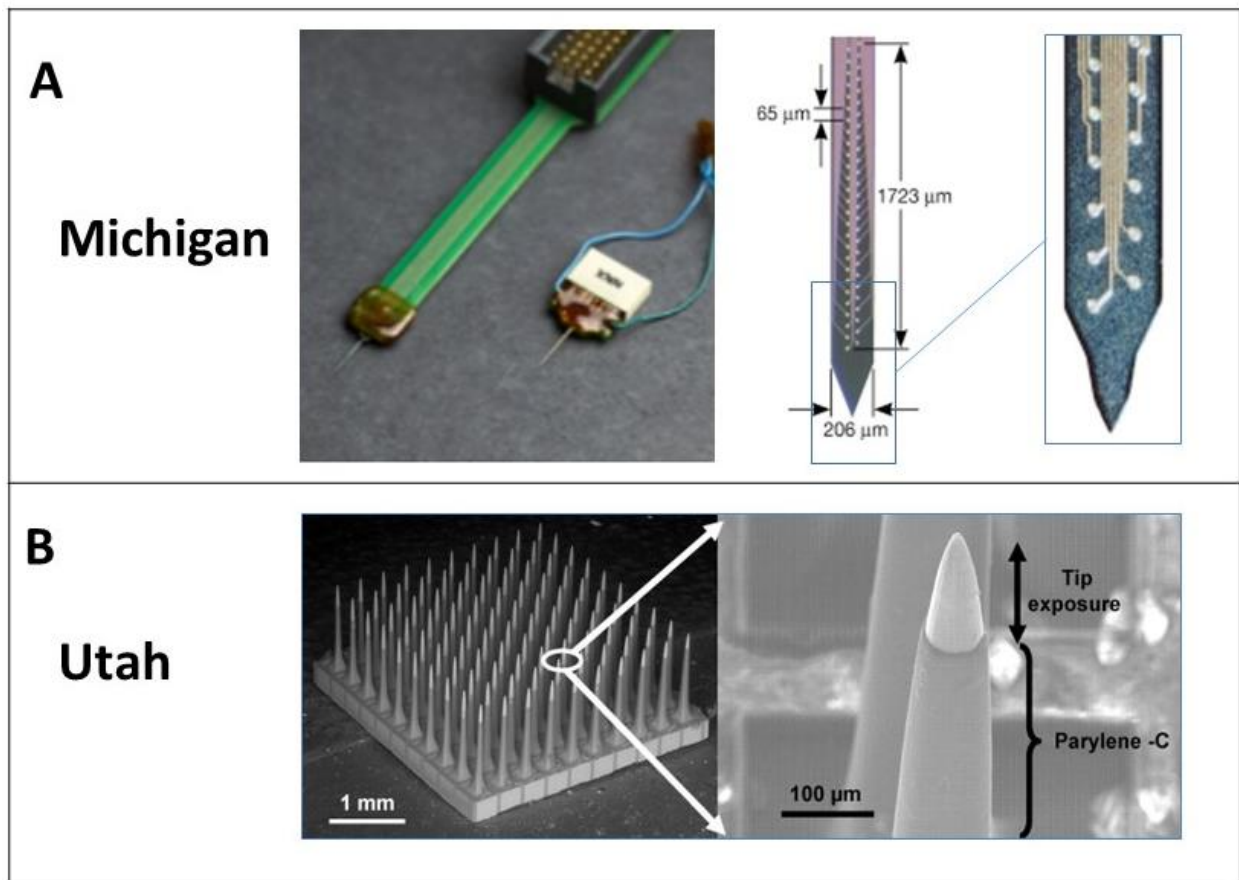


Figure 4.4: Multi-electrode array extracellular probes. A) Optical images of a typical Michigan electrode. Adapted from Ref [26]. B) SEM images of Utah array. Adapted from Ref [35]

filled with an electrolyte solution and a conducting wire is inserted. The pipette can be used to suction on to and rupture a cell membrane, putting the conducting wire and electrolyte solution in contact with the interior of the cell [41]. Whole cell recording, as it is called, can be seen in Figure 4.5.

The membrane potential resolution for whole cell recording far exceeds that of extracellular recording for a number of reasons. By accessing the interior of the neuron, the glass electrode is seeing the full action potential voltage swing. Additionally, the LFP noise from nearby neurons is greatly reduced. And finally, because the solution in the barrel of the pipette is now in ionic contact with the inside of the cell, the internal electrode can be made arbitrarily large, making the electrochemical impedance a non-issue. Due to these factors, whole cell recordings are easily capable of picking up post-synaptic potentials (PSPs), the sub-threshold changes in membrane potential. These PSPs represent an incredibly important and rich data source in understanding the behavior of the brain.

Despite their tremendous value, intracellular recording technology has been extremely slow to progress and glass microelectrodes as we know them have a number of drawbacks. The tapered geometry of the pipette means it has a significant footprint in the cortex, causing damage on insertion. Whole cell recording is a famously difficult technique which requires a great deal of skill to utilize. Multi-unit in-vivo glass microelectrode recording is extremely difficult and has only been demonstrated a handful of times and even then with at most two neurons [41]. Finally, because of the bulk and rigidity of the glass electrode and its sensitivity to small displacement, its use has been primarily limited to cultured neurons, neurons in a slice of cortical tissue, or in anesthetized animals and not awake animals, with few exceptions. While the glass microelectrode has led to great advances in our understanding of neural communication, if the

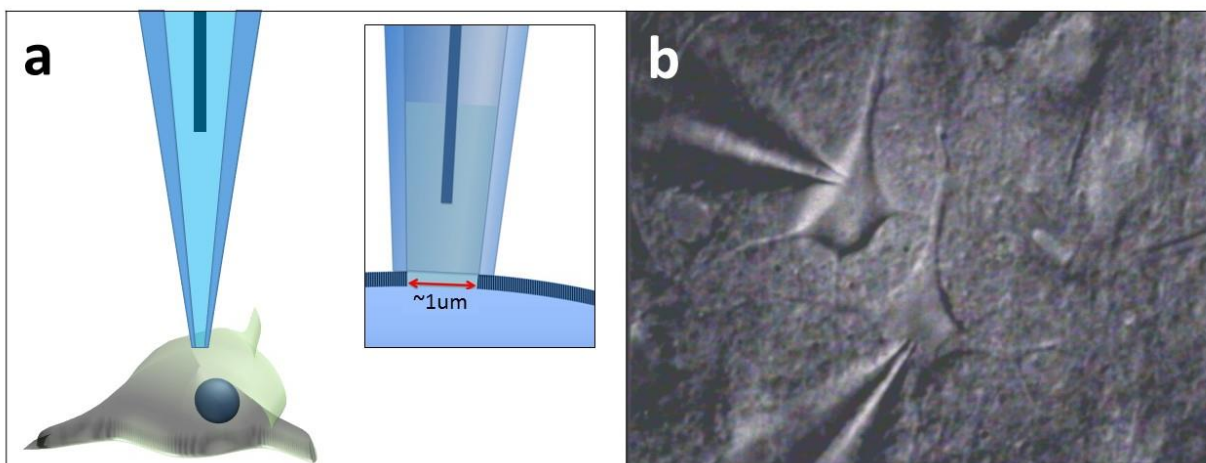


Figure 4.5: Whole Cell Recording. a) Cartoon of whole cell recording with a glass micropipette. B) Differential Interference Contrast image of a two-unit whole cell recording [41].

goal is to understand the behavior of a complex network of neurons in an awake and freely behaving animal, it falls well short.

4.5 Nanowire Electrophysiology

With the advent of nanoscience, probes with sensing areas small enough to enter an individual cell became a possibility. Over the past decade, nanowires in particular have emerged as a promising candidate to realize large scale intracellular recording. While many have focused on passive multi-electrode arrays similar to the microscale examples discussed above, other groups, like the Lieber group, have focused on active transistor devices.

Park et al. demonstrated a vertical nanowire electrode array (VNEA) as shown in Figure 4.6. Neurons were interfaced with vertically grown silicon nanowires. A thermally grown SiO_2 layer was used to insulate the bulk of the SiNWs, while the tips were exposed using buffered hydrofluoric acid (BHF) to remove the SiO_2 insulation. These NEAs proved too thick to spontaneously penetrate the cell, and instead the cell membrane would bend around them. Park et al found that a technique borrowed from micropipette recording, electroporation, would gain them temporary access to the interior of the cell. Voltage pulses were used which introduced pores into the cell membrane immediately surrounding the electrodes. While the nanowires still don't fully enter the cell, it did put them in contact with the internal milieu of the cell. While greatly increasing the signal amplitude, this method still suffered from a great deal of leakage

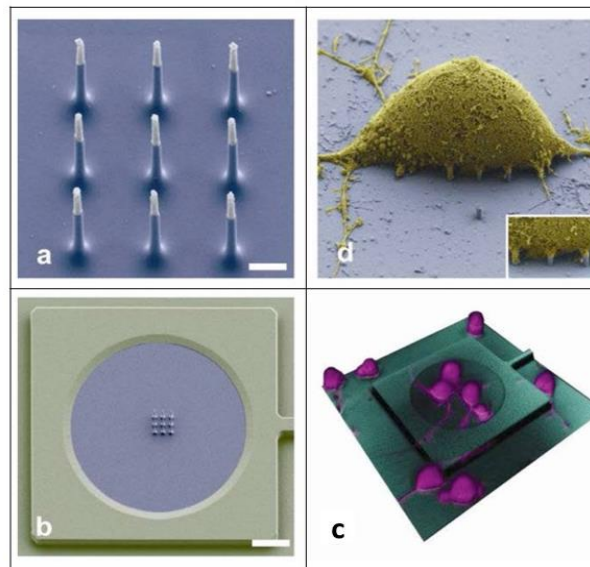


Figure 4.6: Vertical Nanowire Electrode Array (VNEA). a) SEM image of VNEA. Scale bar is $1\mu\text{m}$. b) Zoomed out SEM image of VNEA from (a). Scale bar is $10\mu\text{m}$. c) Confocal microscope image of rat cortical neurons cultured on a VNEA pad. Scale bar is $40\mu\text{m}$. d) SEM image of a neuron placed on top of the 9-unit VNEA. Adapted from Ref [42]

current. It also allowed for only temporary signal boosts as the cell membrane would heal and the SiNW would remain on the outside [42].

The Lieber group out of Harvard has focused its attention on actively driven SiNW field effect transistor (SiNW FET) devices. Their first demonstration of SiNW FETs for electrophysiology is shown in Figure 4.7. An array of contacted nanowires have a neural axon stretching over them. As the neuron fires, the action potential can be detected by the SiNW FETs as it propagates along the axon and acts to modulate the gate voltage of the FETs [43]–[47]. While the core concept remained the same, Lieber et al. have developed two additional probe geometries which greatly improve the applicability of these probes for intracellular electrodes, shown in Figure 4.8. The first was a kinked nanowire electrode. In this case, the sensing region is isolated to a small area near the tip of the kink, and the kink is capable of penetrating the cell membrane, as shown in Figures 4.8a-d [48]–[51]. The second uses a branched nanowire device shown in Figures 4.8e-g. In this case, a SiO₂ nanotube with a hollow core is branched off of the SiNW FET device and is used to penetrate the cell. The SiO₂ nanotube fills with and is in

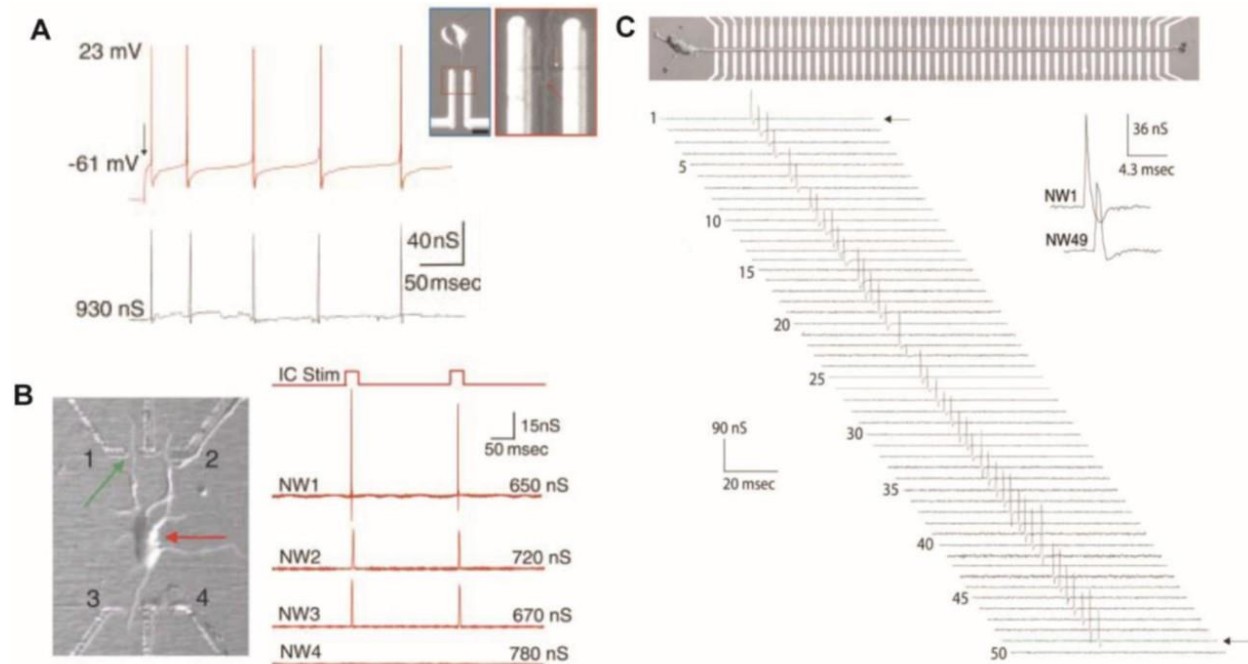


Figure 4.7: Extracellular nanowire FETs (NW-FETs) for action potential detection. A) Top plot shows the intracellular potential as measured by a glass micropipette. Bottom plot shows the change in conductance of the nanowire device caused by gating from the action potential. Inset shows an optical image of the axon crossing the NW-FET. B) NW-FET recordings for various axonal branches. C) Action potential propagation along the axon as measured by a series of NW-FETs. The top is an optical image of the axon stretching from the cell body across an array of NW-FETs. Adapted from Ref [43].

contact with the intracellular environment. This fluid is then in contact with the gate region of the SiNW FET, allowing for active intracellular recording [52]–[54].

The SiNW FETs highlight a key distinction in nanowire probes, active versus passive. Active probes such as SiNW FETs require some power source in amplifying signals. While such probes can achieve remarkable low-noise recordings, this power requirement may represent a hurdle to scaling. Similar to transistors in a computer, this active amplifying will generate heat. While CPUs are designed to handle and dissipate this heat, the brain is incredibly sensitive to even small temperature changes. A temperature change of $>10^{\circ}\text{C}$ will ultimately be fatal, and below this may still cause neural dysfunction, interfering with the very phenomena you are trying to measure. If the ultimate goal is to create high-density single-neuron probes, heating will likely be critical in determining the applicability of active devices.

Beyond just probe development, the Lieber group has dedicated a significant amount of effort to demonstrating how these devices could be delivered in-vivo at large scale. Initially, they use strain engineering to lift the SiNW FET devices from the fabrication substrate, as shown in Figure 4.9. They also demonstrated that lengthy nanowires could be incorporated into biological tissue with little to no immune response [47], [55]–[58]. From here, they began developing embeddable polymer meshes [58]–[62]. By incorporating the strain engineered devices, they now had a probe device that would be capable of innervating the cortex and potentially provide long-term in-vivo intracellular recordings. In order to inject these devices, they used capillary forces to collapse the strain engineered cantilevers by dipping the device in water, then freezing it in liquid nitrogen, fixing the probes in a collapsed state. The probe could then enter the brain, at which point it would thaw and the probes would be released, moving into the surrounding tissue. As shown in Figure 4.9, such devices have demonstrated stable single-unit extracellular recordings for more than 8 months without repositioning the electrode [63], [64]. While they have not managed to demonstrate a chronic in-vivo intracellular recording, this is clearly a direction they are working towards and they have developed many of the elements necessary to achieve it.

The work being done in silicon nanowire bioelectronics is currently poised to define the future of bioelectronics. The need for better neural interfaces with smaller footprints is clear. The tremendous advantage SiNWs hold over other materials is a relative ease of fabrication. However, as we shall discuss, carbon nanotubes hold a number of advantages over SiNWs which may make them ideal electrophysiological probes, and makes it worthwhile to overcome the associated fabrication challenges.

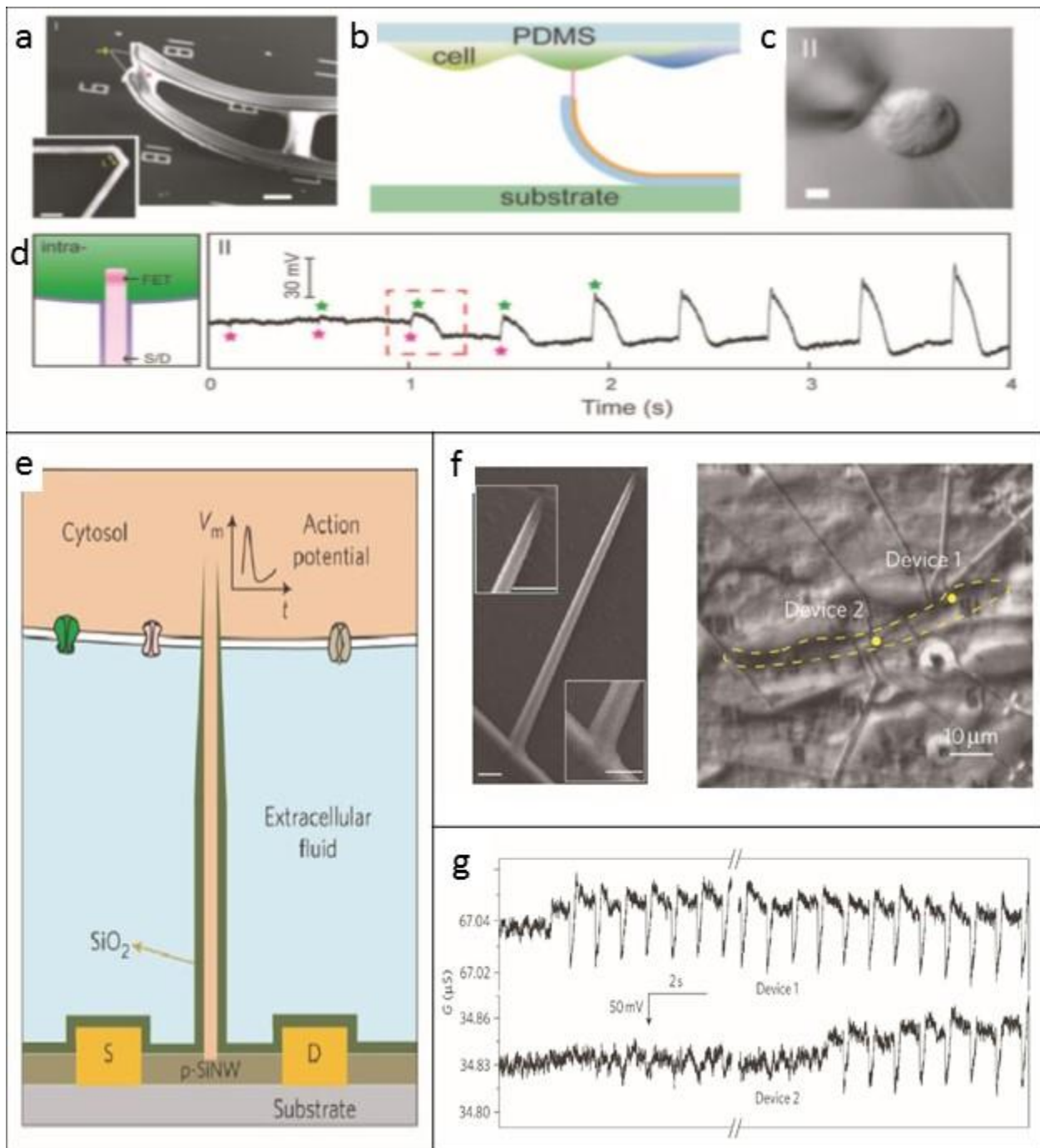


Figure 4.8: Intracellular NW-FETs. a) SEM image of kinked NW-FET device on strained SU8. b) Cartoon of experiment design. c) Optical image of neuronal body being penetrated by kinked NW-FET. d) Left is a cartoon of the intracellular recording. Right is a voltage trace of the probe as it enters the cell and begins to detect intracellular signals. a-d were adapted from Ref [48]. e) Cartoon of branched NW-FET device. f) Left is SEM image of branched NW-FET. Right is an optical image of the device interfacing with a neuron in slice. g) Intracellular recordings as the cell enters the cell. e-g were adapted from Ref [52].

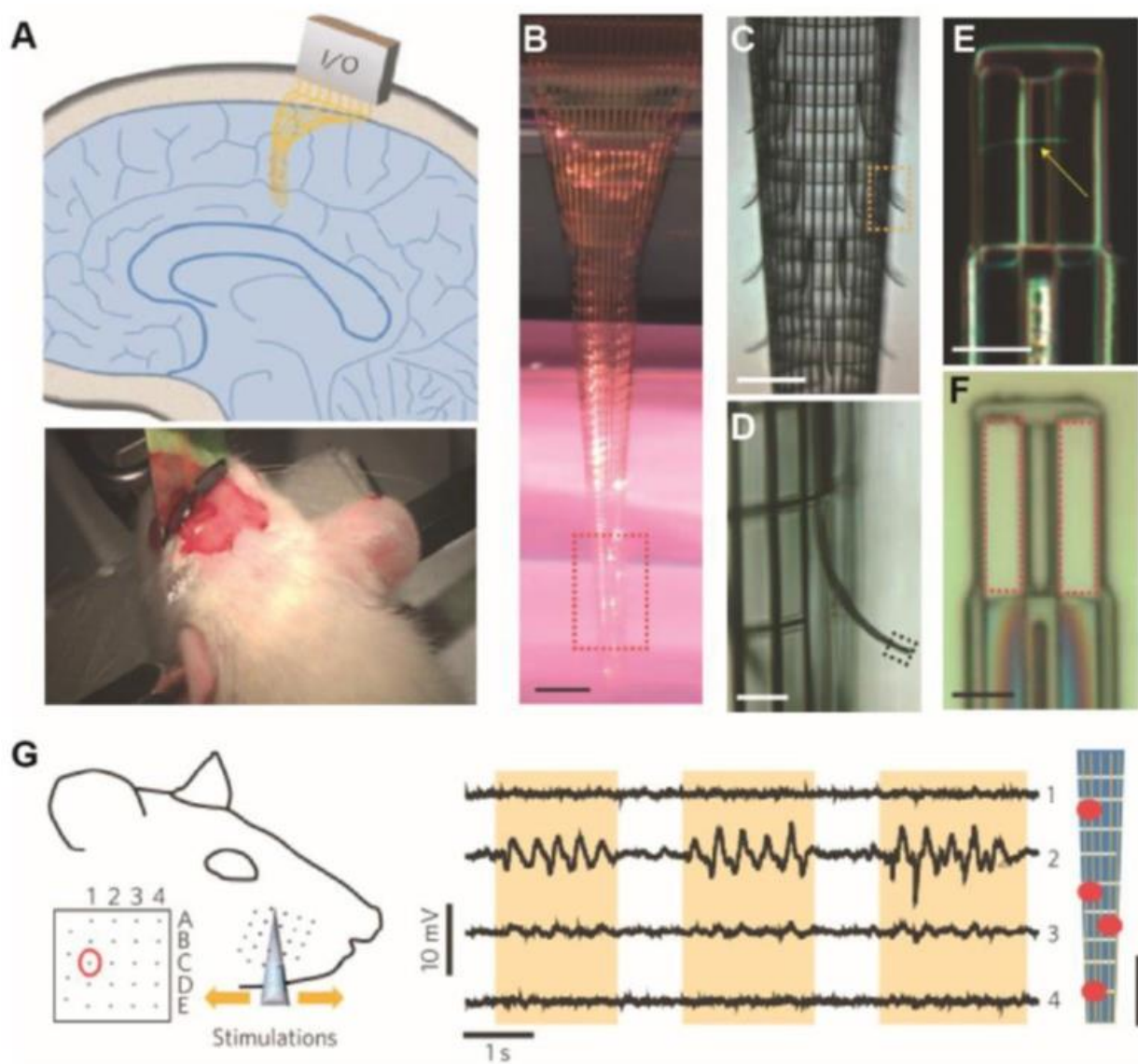


Figure 4.9: Vertical Nanowire Electrode Array (VNEA). a) SEM image of VNEA. Scale bar is $1\mu\text{m}$. b) Zoomed out SEM image of VNEA from (a). Scale bar is $10\mu\text{m}$. c) Confocal microscope image of rat cortical neurons cultured on a VNEA pad. Scale bar is $40\mu\text{m}$. d) SEM image of a neuron placed on top of the 9-unit VNEA. Adapted from Ref [42]

4.6 Carbon Nanotube Properties

When considering the potential of a novel neural probe, a number of factors must be considered. Is the probe robust enough to survive implantation? Will it be capable of recording an action potential or possibly post-synaptic potentials? What kind of immune response will the probe elicit? The answers to these questions for carbon nanotube based neural probes highlights what makes them particularly appealing candidates for neural nanoelectrodes.

4.6.1 Mechanical Properties

In terms of robustness, CNTs are, in a number of ways, the strongest known 1D material. They have the highest known and predicted tensile strength and elastic modulus. As we shall see, this means that CNTs are capable of withstanding buckling at much higher insertion forces or alternatively with much higher aspect ratios. In addition to this, CNTs have been shown to be extremely ductile. When buckling does occur, rather than breaking or becoming permanently deformed, CNTs kink and are then capable of fully returning to their original form [65], [66].

For insertion into a cell, we would want to consider what maximum length of CNT would withstand buckling. The Euler buckling force is given by

$$F_B = \frac{3\pi^2}{2} \cdot \frac{EI}{L^2}$$

Where E is the elastic modulus of the material, I is the moment of inertia, and L is the length of the column. The elastic modulus times the moment of inertia of a CNT is given by

$$EI = \frac{\pi}{4} E_{CNT} R^4 = \frac{\pi}{4} \cdot 0.5TPa \cdot R^4$$

Where the elastic modulus for CNTs has been taken from Ref [67]. Hence, the buckling force can now be written as

$$F_B = \frac{3\pi^3}{16} TPa \cdot \frac{R^4}{L^2}$$

The insertion force necessary for the nanotube to enter the cell is dependent on the tip radius. From previous work, we have found that the insertion force for a 20nm diameter tube is approximately 0.1nN, as shown in Figure 4.10 [68]. This would correspond to a maximum length of only 30 μ m. However, this does not take into account the insulating layer we would coat the tube in. As we shall discuss shortly, we have chosen the polymer, Parylene C as an insulating material. While the elastic modulus of Parylene C is well below that of the CNT (3.2GPa), the R^4 dependence of the moment of inertia means the increase in probe thickness can have a profound effect. With a 100nm thick coating of parylene, the maximum probe length becomes 3mm, long

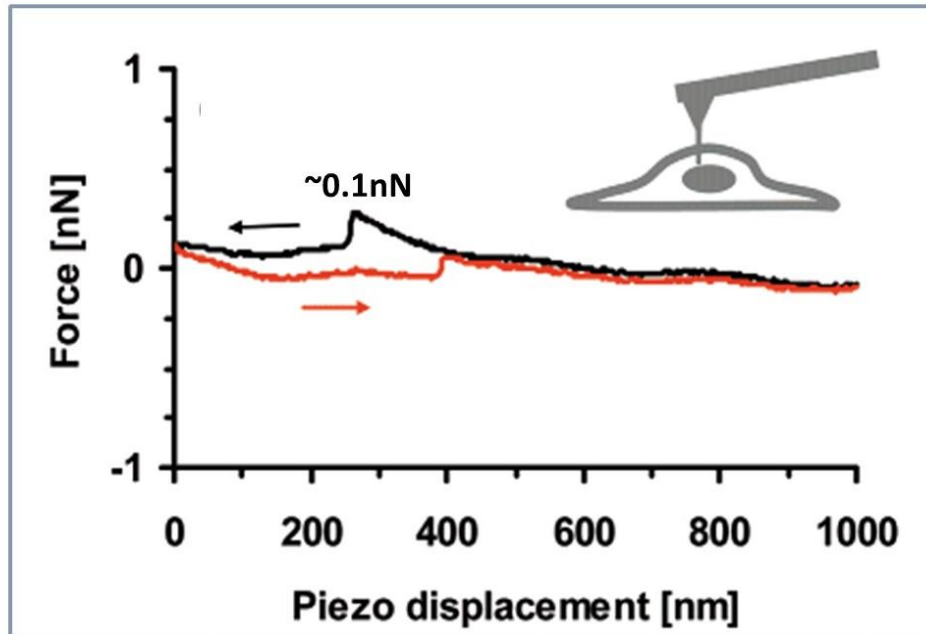


Figure 4.10: Intracellular insertion force for a CNT. Force plot for a CNT attached to the tip of an AFM cantilever as it is guided into and out of a cell. As can be seen, the insertion force is slightly less than the force required for removal and is less than 0.1nN. Adapted from Ref [68]

enough to reach deep into the cortex even without supporting structures. This R^4 dependence also means that were thicker CNTs to be used, their buckling force would be greatly increased.

The ability for CNTs to be stable and capable of cellular penetration at such small diameters is key to their potential as neural probes. While SiNWs have been able to penetrate cells, often they require functionalization to do so, or they are limited to relatively short lengths. While the nanowire itself may not trigger a substantial immune reaction, the supporting structure will, which makes the potential for longer probe lengths critical for envisioning a large-scale implementation of nanowire probes.

4.6.2 Biocompatibility

As discussed above, the CNS's immune response to foreign bodies is complex, and CNTs are no exception. A significant body of work has explored the effects of CNTs in solution on biological tissue, and has been met with varying results. Cytotoxicity of CNTs appears to be dependent on tube diameter, length, synthesis, impurities and defects. Despite this volume of work, very little has been done to determine the long-term cytotoxicity of a tethered nanotube probe.

Early reports suggested CNTs were highly cytotoxic, leading to cell death and changes in cell morphology as well as accelerated oxidative stress over the course of only 18 hours [69]. However, it was later determined that this was primarily due to the presence of transition metal catalysts used for nanotube growth, and not the CNTs themselves. When this work was repeated with CNTs synthesized without transition metals present, the adverse effects were no longer seen [70].

The effects of nanotube length and aspect ratio on cytotoxicity have also been extensively studied, with varying results. Adding to the complexity of this work is controlling for factors like aggregation of tubes, which can vary for tube diameters and defect ratios, as well as impurities. In one study, researchers found that larger diameters led to increased cytotoxicity, while a follow-up study found the opposite to be true [69]. The mechanism of immune response to CNT nanomaterials was typically the envelopment of CNTs by macrophages. As the tethered CNT probes we are proposing will not be floating freely, it is unlikely that the same immune response cycle is as relevant. Other proposed mechanisms involve short CNT fragments behaving akin to asbestos and interfering with cellular functioning [8]. Once more, we believe this immune reaction pathway to not be relevant for an individual tethered CNT.

While considerably more work needs to be done to establish the biocompatibility of CNT probes, given the chemical structure, small footprint and previous results, we have reason to be optimistic. While CNTs in solution have demonstrated variable cytotoxicity, the loading per cell is significantly higher than what we're proposing. In applications in which cells are in contact with fixed nanotubes, in which free floating nanotubes are not present, toxicity has generally not been observed [71]–[74]. In addition to this, one of the advantages of CNTs is the numerous pathways for functionalization to improve its inherent qualities.

4.6.3 Electrochemical Properties

The electrochemical properties of CNTs can vary considerably and rely on synthesis method, quality, functionalization and diameter. Highly order pyrolytic graphite (HOPG) – very pristine bulk graphite – demonstrates the source of this variation. The basal plane of HOPG, consisting of a nearly perfect graphene sheet, is extremely inert in saline, shows no Faradaic current and has a very low double layer capacitance ($3\mu\text{F}/\text{cm}^2$ vs. $20\mu\text{F}/\text{cm}^2$ for most metals). However, the edge plane of HOPG, consisting of a variety of functional groups, is extremely electrochemically active and has a capacitance of $50\text{--}100\mu\text{F}/\text{cm}^2$ [3], [4]. While pristine carbon nanotubes may likely behave much like the basal plane of HOPG, straightforward functionalization steps, such as light oxidation of the outer most shell, will drastically alter that behavior. In bulk CNTs, functionalization increased the capacitance from $5\mu\text{F}/\text{cm}^2$ to $1600\mu\text{F}/\text{cm}^2$ [75]. Similar electrochemical characterization of the edge plane of graphene reveals an anomalously large capacitance of $100,000\mu\text{F}/\text{cm}^2$, orders of magnitude larger than any other reported material [1]. This suggests that the nanoscale aspect ratios of individual CNTs will also have a profound effect on their electrochemical properties compared to those in bulk.

If we consider our intracellular electrode to consist of a 20nm diameter nanotube with 1 μ m of exposed length at its tip, we have an active sensing area of $\sim 60,000\text{nm}^2$. Because the resistance of the CNT and ionic solution are negligible compared to the electrochemical impedance, the signal amplitude can be approximated by considering the Faradaic and non-Faradaic elements of the electrochemical impedance in parallel with one another. As discussed above, the non-Faradaic element could be as low as 3-5 $\mu\text{F}/\text{cm}^2$ if left untreated, to anywhere from 1,600 $\mu\text{F}/\text{cm}^2$ -100,000 $\mu\text{F}/\text{cm}^2$ if properly functionalized. For a surface capacitance of 25,000 $\mu\text{F}/\text{cm}^2$, this corresponds to an impedance of 10M Ω and 100G Ω at 1kHz and 100Hz respectively. While inside the cell, assuming the nanotube makes a tight seal with the cellular membrane, the probe should see the entire 100mV action potential and 1-10mV PSPs. For action potentials, this means a current signal of $\sim 10\text{nA}$, with only $\sim 1\text{pA}$ of thermal noise. This should be easily detectable by a decent amplifier. For PSPs, the current signal will be 10 -100pA, with around 0.3pA of thermal noise. Given that this is the absolute noise floor and doesn't take into account other noise sources, and that a signal-to-noise ratio of 5 is optimal, detecting PSPs may be considerably more difficult.

First, even if an intracellular CNT probe proves incapable of measuring PSPs, it would still be capable of measuring action potentials with a smaller footprint than any extracellular probe is capable of, without the need for complex data analysis and spike-sorting in post-processing. As discussed above, extracellular probes appear to be incapable of scaling down to high-density single-unit levels.

Second, the values discussed above only consider the non-Faradaic contribution. The Faradaic contribution can vary widely, and if properly utilized, may be enough to push PSPs within the capability of the probe. Little work has been done on the Faradaic activity of individual CNTs in saline, and much of the work done on using bulk CNTs for neural electrodes have aimed to minimize these surface reactions [75]–[77]. Wang et al. demonstrated that electrodes formed from a CNT paste had largely different electrochemical behaviors in saline depending on the CNT source, as shown in Figure 4.11. Similar to the case of the basal and edge planes of HOPG, this is likely due to variation in the number and nature of chemically reactive defect sites along the tube [78], [79]. While it is unclear what kind of effect these Faradaic reactions at the CNT surface will have on cell viability, it is an area well worth exploring. Reactions at an individual CNT surface may be limited enough for cells to tolerate.

It is also possible that with more complex recording schemes we could improve the signal as well. By bringing the voltage of the probe to the onset of an electrochemical reaction, we would see a nonlinear response when there are changes in membrane potential from an action potential or PSP. Pulsing the probe could limit the effects of reaction byproducts on the cell. I believe such a method would be particularly useful for identifying action potentials, or simply the presence and sign of PSPs, but may have difficulty giving reliable information on the magnitude of such potentials.

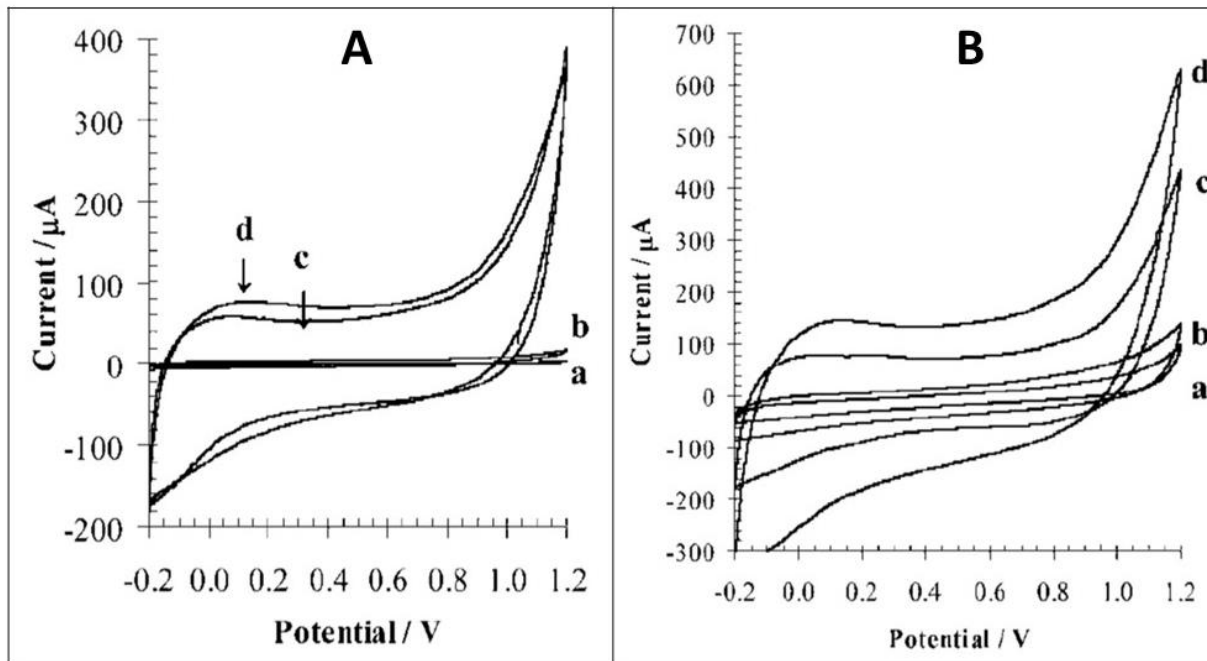


Figure 4.11: Variations in Faradaic reactions of CNTs in PBS. A) Cyclic Voltammetry (CV) curves of CNT films attained from 4 different commercial sources. B) CV curves after treatment in HNO_3 . HNO_3 introduces active functional groups along the tube that increase its electrochemical reactivity. Adapted from Ref [79]

4.6.5 CNTs as Neural Probe Examples

CNTs have attracted a great deal of attention as neural probes due to the properties described above. While there have been a number of experiments using nanotube forests as high surface area extracellular electrodes, there has been very limited work done towards using CNTs as intracellular probes. It is still worth reviewing what has been done in this vein.

Initial work using CNTs as neural interfaces used bulk collections of nanotubes and took advantage of their increased effective surface area. Gross et al. showed that coating electrodes with CNT films would decrease the electrode's impedance [80]. Similarly, Harris et al. showed that CNT pillars demonstrated high charge transfer and could be used as neural stimulators. In addition to these, a great deal of work has been done developing CNT polymer composites to act as flexible electrodes [76], [81], [82]. This work has helped demonstrate the biocompatibility of tethered CNTs, and helped establish some of the baseline electrochemical properties of CNT films.

Independently, work has been done to demonstrate that individual CNTs are capable of entering cells, either spontaneously [83], through functionalization [84], or by applied force [68]. Zettl and Bertozzi et al. demonstrated that an individual CNT attached to an AFM tip could be used as a nanoinjector, piercing a cell membrane. Furthermore, they demonstrated that by

utilizing disulfide bonds which are reduced within the cell's cytosol, they could use this injector to insert cargo – in this case a quantum dot – into the cell [68]. This is just one example of how functionalization can be used to enhance CNT neural probes.

Donald et al. demonstrated the first intracellular recording with a CNT electrode. As shown in Figure 4.12A, a self-tangled bundle of CNTs was formed into a needle, which was then coated in parylene. The tip was then defined by focused ion beam (FIB), exposing the very tips of the nanotubes. With this probe they were able to accurately measure PSPs as shown in Figure 4.12D as well as action potentials[85].

Gogotsi et al. used a large diameter (100nm) carbon nanotube grown in a porous alumina template as an intracellular fluidic probe. They attached the open ended nanotube to the tip of a glass micropipette and then sealed it with epoxy. The device was shown to penetrate cells, kink and reform without damage, and could inject attoliter volumes into the cell. They also showed that the CNT tip could be used as a SERS enhanced Raman probe [86]. While they demonstrated that electrochemical analysis could be performed by a wire electrode placed in the micropipette, this was just an improvement on existing micropipette experiments.

Other researchers have attempted to make an individual CNT neural probe, but stopped short of an intracellular measurement. Patil et al. worked towards an individual nanotube nanoelectrochemistry probe, but stopped short of applying it. Similar to the nanoinjector work of Zettl et al., they used a MWCNT mounted onto an AFM tip. In order to insulate the tube, they used Parylene C, which they then removed from the tip using laser ablation. They discuss a number of technical challenges in fabrication of these devices, which resulted in extremely low yields and unpredictable device performance, which is likely why the device was never applied [87]–[89]. Kawano et al. developed a MEMS based design for CNT neural probe fabrication. In this case, tubes were grown on the device chip by CVD, coated in parylene, and then the parylene was removed using a MEMS heater [90]. Still, this device was never used, and the goal of an individual CNT intracellular neural probe has remained elusive.

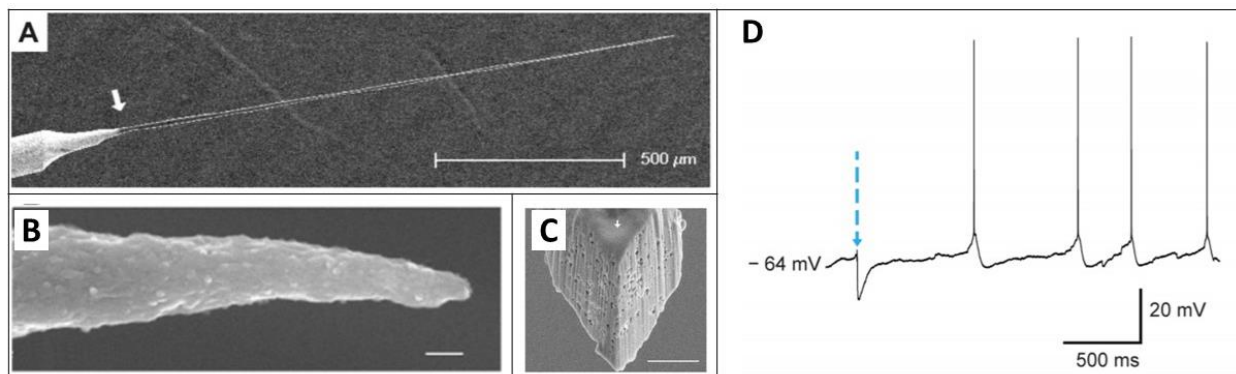


Figure 4.12: Intracellular CNT Bundle Probe. A) SEM image of a CNT bundle needle formed through dielectrophoresis. B) SEM image of tip after coating in Parylene C. C) SEM of tip after cutting with FIB. Scale bars are 500um, 1um and 1um respectively. D) Voltage recording from intracellular probe. Blue arrow points to a PSP being recorded, while the other spikes all correspond to action potentials. Adapted from Ref [85].

Chapter 5

Carbon Nanotube Neural Probes – Fabrication and Scientific Results

5.1 Overview

We first sought to characterize and demonstrate the promise of CNT probes with single-unit probes. By directly attaching CNTs to sharpened tungsten wires, coating in an insulating polymer, and selectively removing that polymer with electron beam irradiation, we had a straight forward means for fabricating a CNT probe.

Next, we turned our attention to demonstrating that this method is scalable. The design of a scalable carbon nanotube electrode had three central challenges that needed to be overcome: 1) the controlled placement of the CNTs; 2) the selective insulation of all but the tip of the CNT; 3) a means of freely cantilevering the nanotube probe or having a macroscopic handle on a nanoscale interface. Our initial plan was to grow the nanotubes on an array of silicon wires, with a device geometry similar to the Utah array discussed previously. However, growing single or few nanotubes on nanowires proved difficult.

We ended up abandoning the tip growth approach and instead focused on a planar approach of nanotube fabrication. Here, we worked on further developing the precise placement and alignment of CNTs, a method of selective insulation of the CNT with parylene, and a method of cantilevering the device.

Beyond the tethered probes we worked on, I will also outline an idea of wirelessly interfacing CNTs with neurons. A heterostructure of a CNT and plasmonic nanoparticle would allow for a neural interface which would shift the plasmonic response of the nanoparticle with

changing ionic potential of the cell. This could prove a substantial improvement over existing voltage sensitive dyes.

This work was done in collaboration with Professor Mike DeWeese, along with Graduate Student Konlin Shen from Professor Michel Maharbiz's group. Graduate students Aidin Fathalizadeh and Badr Albanna contributed to the ideation of this project along. Undergraduates Emil Barkovich and Jason Belling contributed to the direct-growth of CNTs on tungsten wire, while undergraduates Kyle Chism, Tran Nguyen and Jason Belling all contributed to the beam activated adhesion of CNTs for a scalable probe. Postdoctoral researchers Hamid Barzegar and Aiming Yan performed the microscopy and TEM removal of parylene, while postdoctoral researcher Wu Shi performed the wire bonding. All fabrication work was performed by myself in the Zettl Lab and Marvell Nanolab.

5.2 Direct Attachment

Simultaneously with developing the tip growth method described above, we also worked on directly attaching CNTs to tungsten wires. While this process does not lend itself to scaling in the same manner than tip growth does, its aim was to provide a quick straightforward means to characterize the performance of CNT neural probe.

In this case, tungsten wires are sharpened to a fine point by an electrochemical etch. The tungsten wire is biased against a counter electrode in an NaOH solution. The etch rate at the air/liquid interface is significantly faster, leading to point sharpened down to 10's of nanometers. The wire etches faster at the liquid-air interface, creating an extremely precise point (this is the method often employed for creating STM tips). The tungsten tip is loaded into a 3-axis Attocube nanotranslation stage. This stage has been outfitted to be loaded into the SEM.

Opposite the tungsten tip, a chip with overhanging nanotubes is attached to a fixed point on the Attocube stage. In order to fabricate this chip, arc-grown MWCNTs are sonicated in IPA until well dispersed. A few (typically 5-10) droplets of the dispersion are immediately spun onto a silicon chip, leaving nanotubes randomly placed and oriented along the chip. The chip is then cleaved in half. Due to the lattice plane of the underlying Si, one chip will have an acute angle at the top, while the other obtuse. The chip with the acute angle is affixed to the translation stage.

Inside the SEM, the tungsten tip can be brought into contact with an overhanging nanotube. This can be done by using the Attocube control box for large scale movements. This uses a slip-stick mechanism to push the stage along and can cover around 3mm of translation on each axis. Bringing the tungsten tip to the correct height can be difficult and requires you to focus on both the nanotube and the tip in order to tell the relative height difference. As you get closer to the nanotube, you can switch to the nanomanipulator LabView VI on the EDAX computer. This allows you to use the joystick, and as opposed to the slipstick motion, this biases

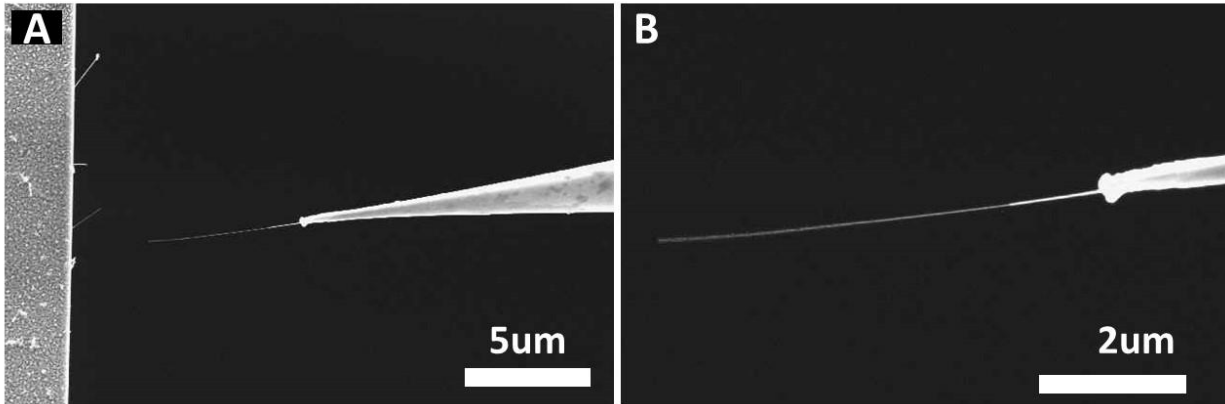


Figure 5.1: Direct attachment of CNT to tungsten tip. A) SEM image of CNT attachment. Tungsten wire is nanomanipulated into contact with a CNT overhanging a substrate. The tube is connected to the tungsten wire by an e-beam deposited Pt joint. B) SEM image of a close up of the 7 μ m MWCNT attached.

the piezo, creating smoother nanoscale movement. The travel distance for this is extremely short, so this should only be done when sufficiently close to a nanotube.

Once the nanotube has been contacted, the CNT needs to be fixed to the tungsten wire. This can be accomplished in a number of ways. The most straightforward and reliable was to use a Pt soldered joint. This is accomplished by using the Gas Injection System (GIS) in the SEM to inject an e-beam sensitive Pt precursor gas. By doing a small-area scan of the CNT-tungsten joint, you deposit Pt which will bond the CNT to the wire. Something similar can be accomplished without the use of Pt, but instead simply scanning over a small region of the joint will deposit enough carbon to bond the CNT. Finally, a bias can be applied between the tip and CNT substrate, which can cause the CNT to fuse to the tungsten wire.

After the tube is attached, the tip is slowly pulled away from the substrate and the CNT is released. The result can be seen in Figure 5.1. The tungsten wire is then backed away back to its starting point and the system can be vented. In handling the CNT-tipped tungsten wire, one needs to pay particular attention to electrostatic discharge. Grounded tweezers should be used for all handling, and the tip should be held in a static free box.

5.3 Insulation

Parylene C was a clear choice for insulating material. Parylene C is an insulating polymer which has demonstrated high biocompatibility, conformal room temperature coating, flexibility and a number of other favorable mechanical factors [13], [35], [91], [92]. As shown in Figure 5.2, parylene coats CNTs without pinholes or defects. In addition to this, parylene is extremely inert, making it compatible with further fabrication steps. However, because of this, it is also

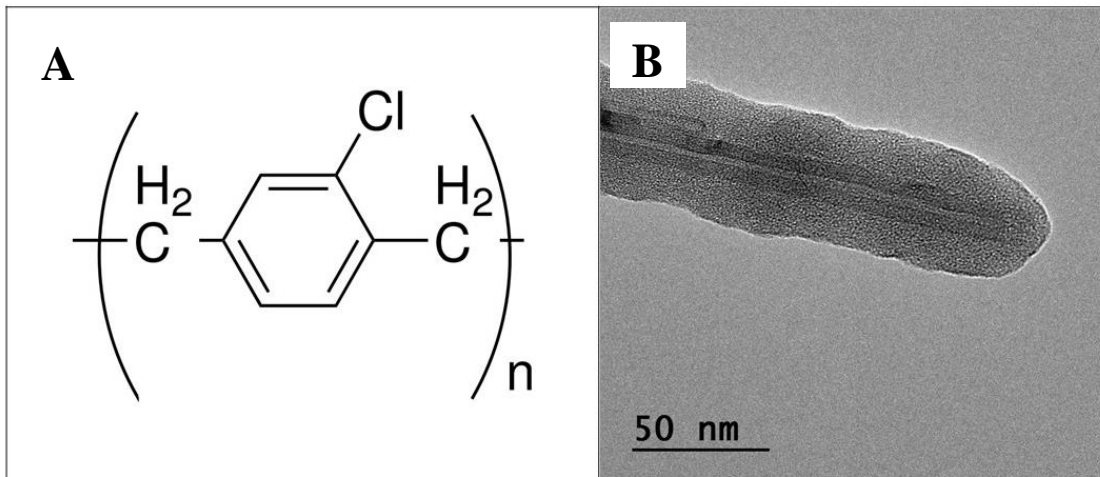


Figure 5.2: Parylene for CNT Insulation. A) Chemical structure of Parylene-C. B) TEM image of conformal coating of parylene on a MWCNT.

difficult to selectively remove. In order to expose the tip of the CNT, we have found that electron beam irradiation causes the Parylene film to pull back from the CNT tip. Rather than a sputtering effect from knock-on damage from the beam, it would appear as if the electron beam irradiation produces a strain in the Parylene film. This is evidenced by the fact that the rate of tip exposure appeared much faster than the rate of parylene thinning. This can be explained by an isotropically strained cylinder of parylene, which would shrink more in the axial than radial dimension. After approximately 5min of electron beam irradiation, the rate of CNT exposure had slowed considerably and around 25nm of CNT had been left exposed, as shown in Figure 5.3.

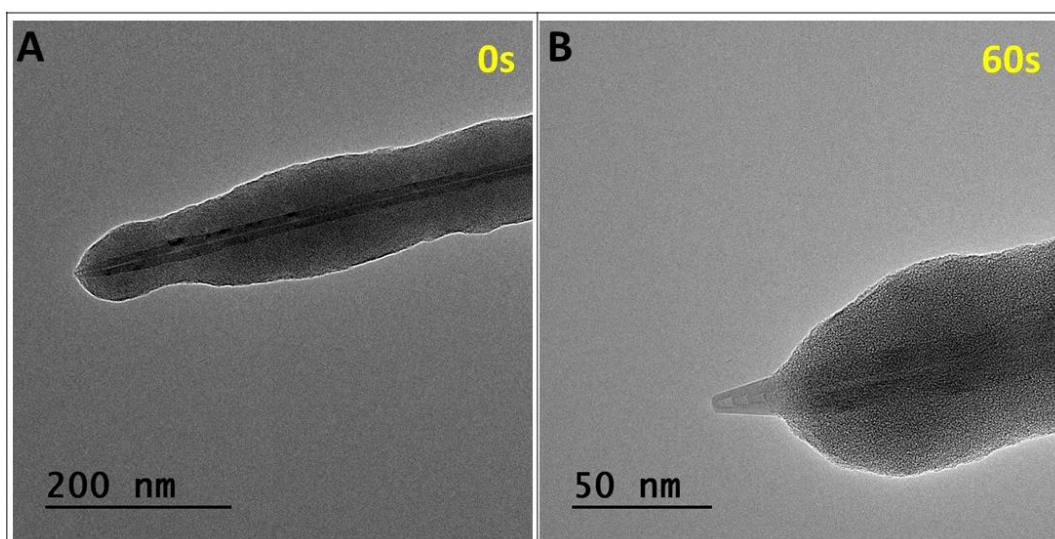


Figure 5.3: E-Beam Exposure of Parylene Coated CNT. A) TEM image of parylene coated CNT at 0s. B) TEM image of parylene coated CNT at 60s. Parylene has begun to pull back, leaving the CNT tip exposed.

While the Parylene C is an ideal choice for insulating the CNT, the thin films we were depositing (~30nm thick) would be unsuitable for insulation of the entire tungsten wire. Given that we expect the CNT probe to have impedances upwards of 100M Ω , it's important that the impedance from the tungsten wire be significantly higher. In order to insulate the bulk of the CNT probe, it was dipped in an ethyl lactate based nail polish. This is similar to the sharpened wire preparations used by Hubel and Weisel in the original intracellular electrode measurements. This insulation could likely be performed before attaching the nanotube, but the outgassing of the nail polish in the SEM and TEM was a concern. Given that the drying of the nail polish never produced enough force on the tungsten tip to bend it, we felt confident that the soldered and parylene coated tube would withstand it.

5.4 Electrochemical Impedance Spectroscopy

In order to characterize these probes and their insulations, we used a Gamry Potentiostat to perform Electrochemical Impedance Spectroscopy (EIS). EIS measures the impedance and phase shift of a circuit at various frequencies. The sweeps we performed measured from 10Hz-10kHz. The impedance at 1kHz was of particular concern as this is the characteristic impedance

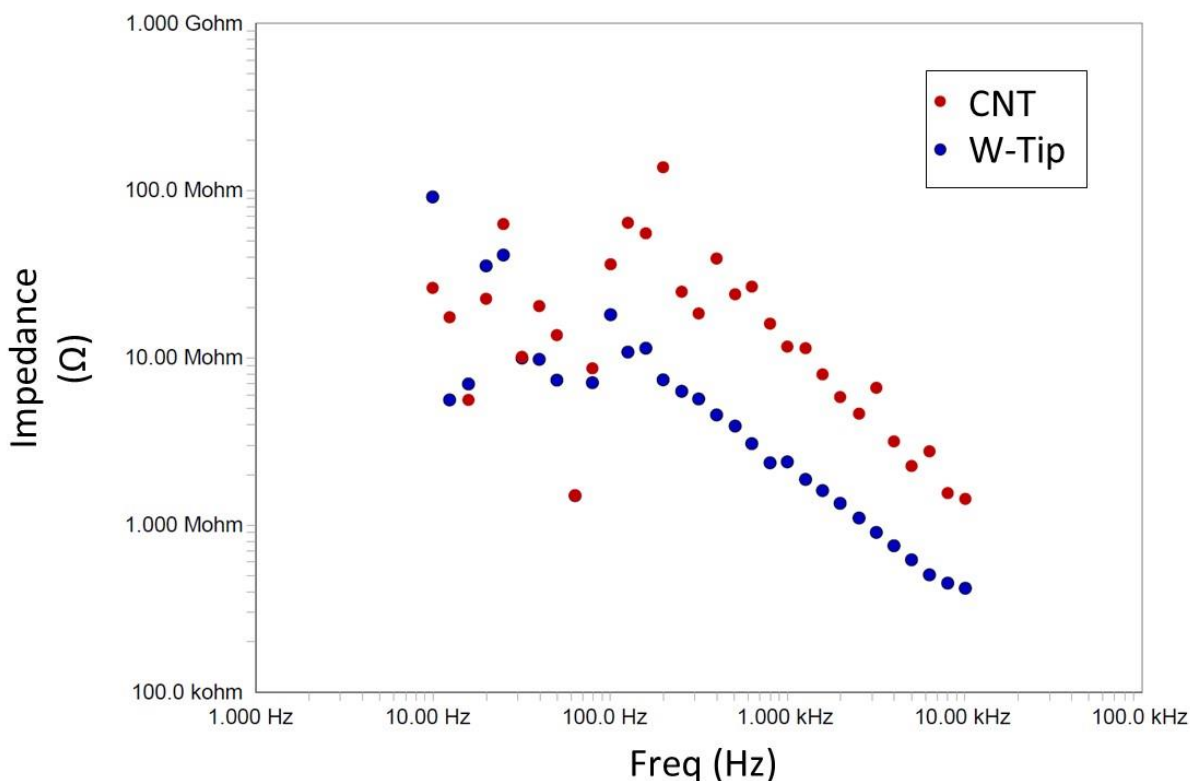


Figure 5.4: Electrochemical Impedance Spectroscopy (EIS). Impedance versus frequency log-log plot for the exposed CNT tip and a sharpened tungsten wire insulated in nail polish as a control. The impedance for the sharpened tungsten wire is shown in blue, and was on the order of 1M Ω at 1kHz. The CNT tip are the red data points and correspond to an impedance of around 10M Ω at 1kHz. The CNT has been refluxed in HNO₃ prior to measurement.

of action potentials and is what is often quoted as the impedance of a neural probe. Due to internal capacitance of the potentiostat, impedances above 100 M Ω cannot be measured.

For control, we measured a nail polish insulated tungsten wire with its tip exposed and no parylene deposited, and found an impedance of around 1M Ω at 1kHz. Without any functionalization, the exposed CNT tip had an impedance >100M Ω as measured by our potentiostat. However, we found that an extended nitric acid treatment substantially reduced this impedance. After 1hr of 60% HNO₃ exposure, the impedance of the probe was ~10M Ω at 1kHz, as shown in Figure 5.4. As discussed previously, this is expected, as the nitric acid treatment improves hydrophilicity of the nanotube and can allow for limited Faradaic interactions.

5.5 Visualization

In order to guide the nanotube into the cell, we needed a means of imaging the cell and tip during insertion. A few imaging methods would be useful for this. Differential Interference Contrast (DIC) microscopy would be particularly useful for guiding the probe into the cell. DIC is similar to phase contrast microscopy, but limits halo effects and has better defined edges. As shown in Figure 5.5, cell membranes are particularly well resolved with DIC compared to standard optical techniques. Fluorescent imaging would also be useful if we are interested in subcellular structures as well as potentially monitoring immune response factors. In order to achieve super-resolution imaging, we chose to use confocal fluorescent microscopy as it was the simplest to outfit given our system. Other super-resolution techniques could also have been used.

We outfitted a Nikon TE2000 inverted microscope that was previously being used for integrated AFM and optical microscopy. We added a DIC objective and lens set, as well as a retrofitted stage for our intended use. We also updated the lamp and replaced some of the missing filters for epi-fluorescent imaging as well as confocal fluorescent imaging. The optical setup is shown in Figure 5.5A.

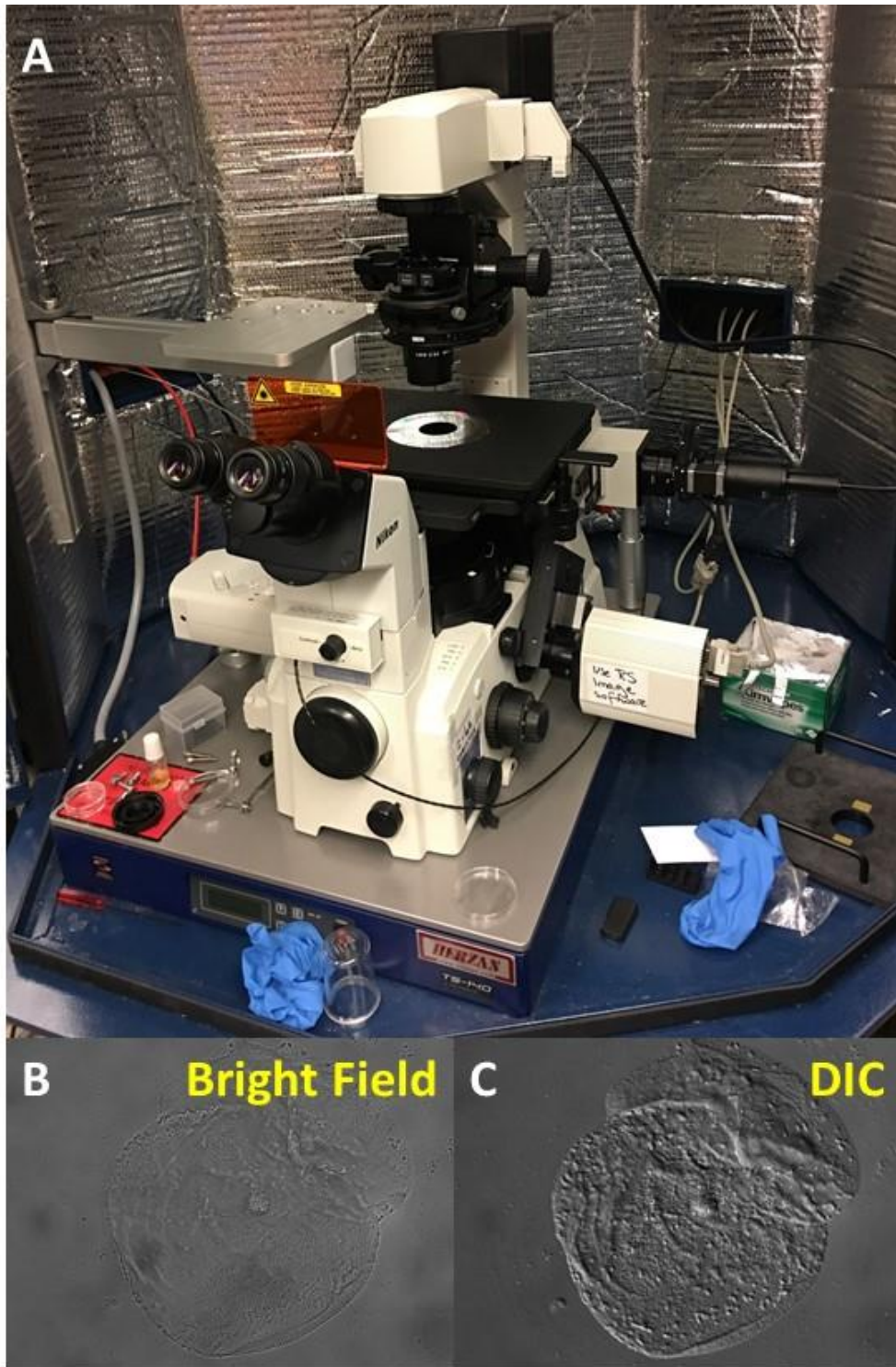


Figure 5.5: Microscope setup. A) Nikon TE2000 inverted microscope on a vibrational noise isolation table. The entire microscope is in a metal enclosure to isolate from electronic noise sources. All stages and focus can be controlled remotely. DIC and confocal epifluorescent lenses and equipment have been added. B) Bright Field (BF) image of cheek cell. C) DIC image of same cell. Significantly better contrast than in (B).

5.6 Precision Stage Movement

In order to actually interface the cantilevered chip with the cell, we needed a means of guiding the probe precisely through the cell membrane. Substantial movements or vibration during the process could result in damage to the probe. In order to accomplish this, we chose to use a 3-axis piezo driven translation stage. The piezo motors used were three ECSx3030 linear translation stages purchased from Attocube Systems and feature a slip-stick driven motion for long travel lengths. The slip stick movement pulses the piezo to create small steps of the stage along an inertial friction plate, allowing it to travel macroscopic distances – in the case of the ECSx3030, 20mm – as shown in Figure 5.6. While the step resolution is quoted as optimally 1nm/step, in previous applications of the Attocube translation stages, we have found it more useful to use the slip stick motion to position stage close to the desired range, and then use traditional piezo biasing to move the stage at the nanoscale for smooth continuous motion.

The translation stages are controlled by an ECC100 motion controller. The ECC100 itself is controlled by computer. While there is proprietary software offered by Attocube, this only accommodates for slip-stick motion, and not the smooth piezo-driven motion discussed above. For this, we use a LabView program previously developed in our lab for use with an Attocube system in our SEM. Beyond being able to directly bias the piezos, the program allows for a joystick interface, making positioning easier.

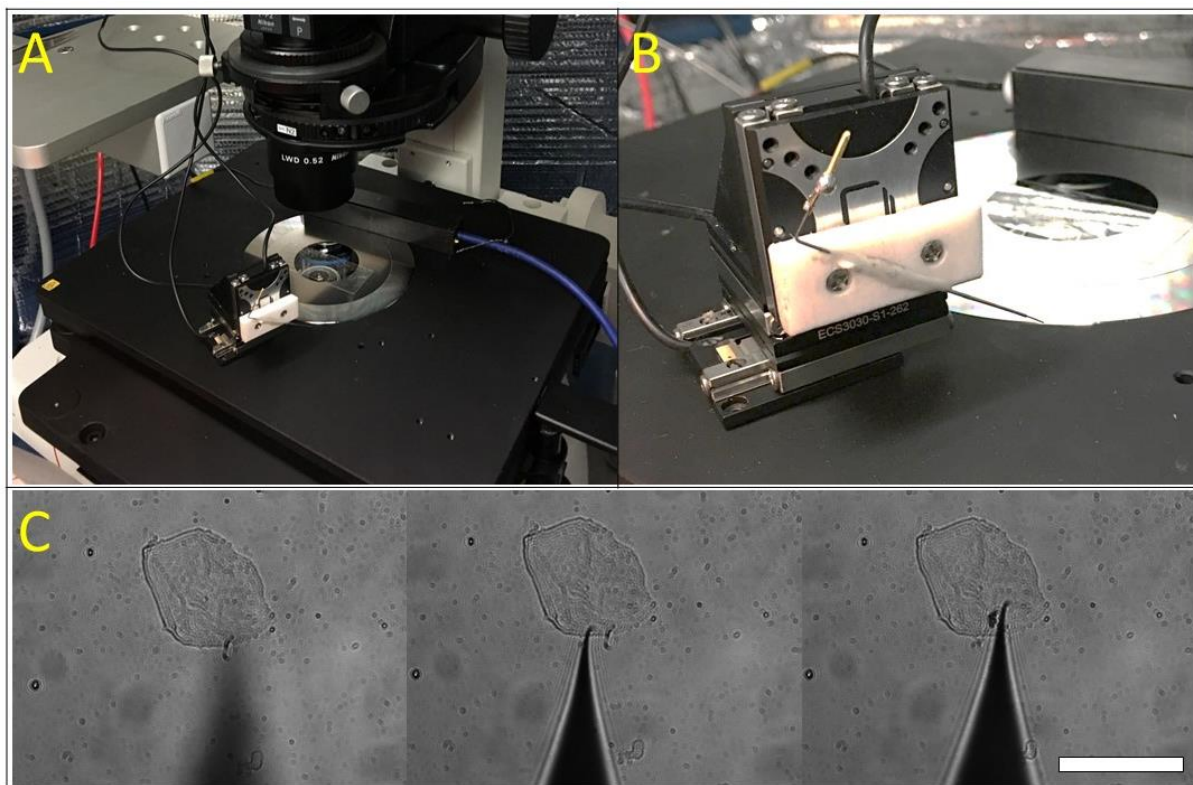


Figure 5.6: Precision Stage Movement. A-B) Attocube nanomanipulation stage with a holder for a sharpened tungsten wire. C) Bright-Field images of a tungsten tip being guided into a cheek cell. Scale bar is 20 μ m.

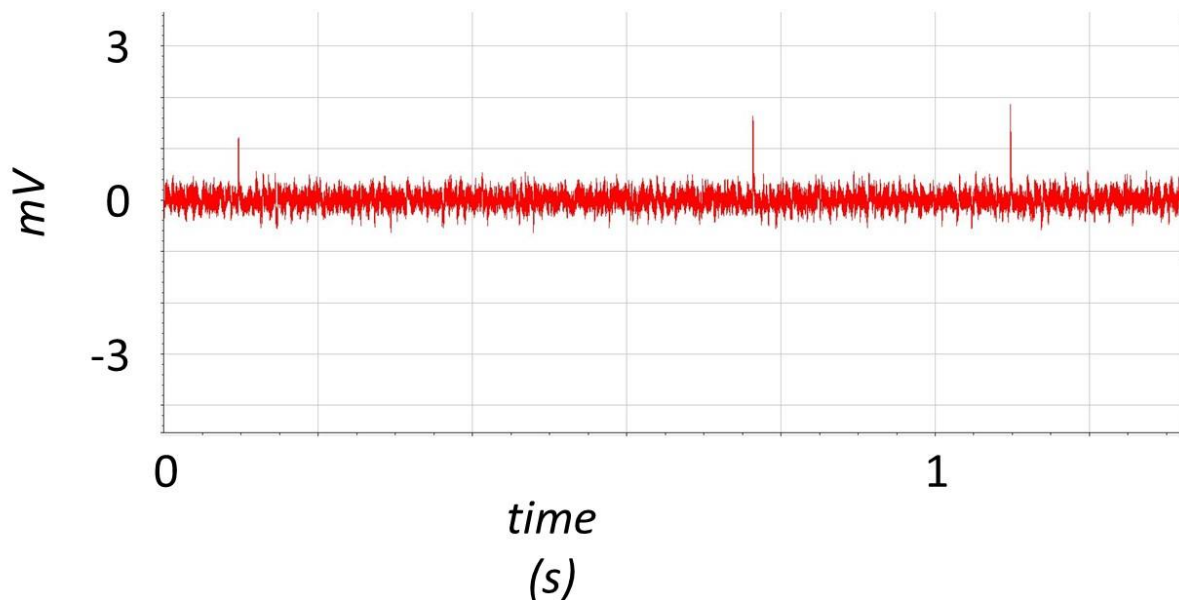


Figure 5.7: Action Potentials. Measured with a sharpened tungsten wire coated with nail polish, with an impedance of around $100\text{k}\Omega - 1\text{M}\Omega$. Axopatch 200B amplifier was used in conjunction with a DigiData 1550A digitizer.

5.7 Neurons

The neurons we used for recording were cultured by graduate student Konlin Shen in Michel Maharbiz's lab. The neurons are immortalized hypothalamic (GT1-7) which exhibit spontaneous action potentials [93]. Rather than initiating neural spiking with glutamate puffs, or inducing action potentials by simultaneous patch clamp recording, the spontaneous action potentials of these neurons allows for a simple means of cellular recording. The cells were cultured in a petri dish with a thin glass bottom. The thin bottom is necessary due to the small working distance of our 40x DIC objective.

We began with a test electrode consisting of a nail polish insulated sharpened tungsten tip. With this probe, action potentials could be recorded, as shown in Figure 5.7. This confirmed that the cells were in fact active.

5.8 CNT Probe Results

With the CNT probe, the impedance is too high to reliably detect extracellular action potentials. The probe is lowered under the 60x DIC objective until it is near the neural substrate. Small steps in z-height are performed in order to enter the cell. The amplifier is operated in current-clamped mode. Once inside of a cell, action potentials are seen which fall just above our noise levels, as shown in Figure 5.8.

These spikes had amplitudes of around $\sim 3\text{-}6\text{mV}$. Lower than this, and they would not be distinguishable from noise. While these signals were detectable, they were significantly lower than the $\sim 100\text{mV}$ action potential signals we would hope to see. This suggests that the probe is not making a good seal with the lipid bilayer. This is likely due to the conical shape of the tungsten wire, and the tip being inserted further into the neuron than necessary. With these signal amplitudes, while action potentials were detectable, PSPs would be too small to detect.

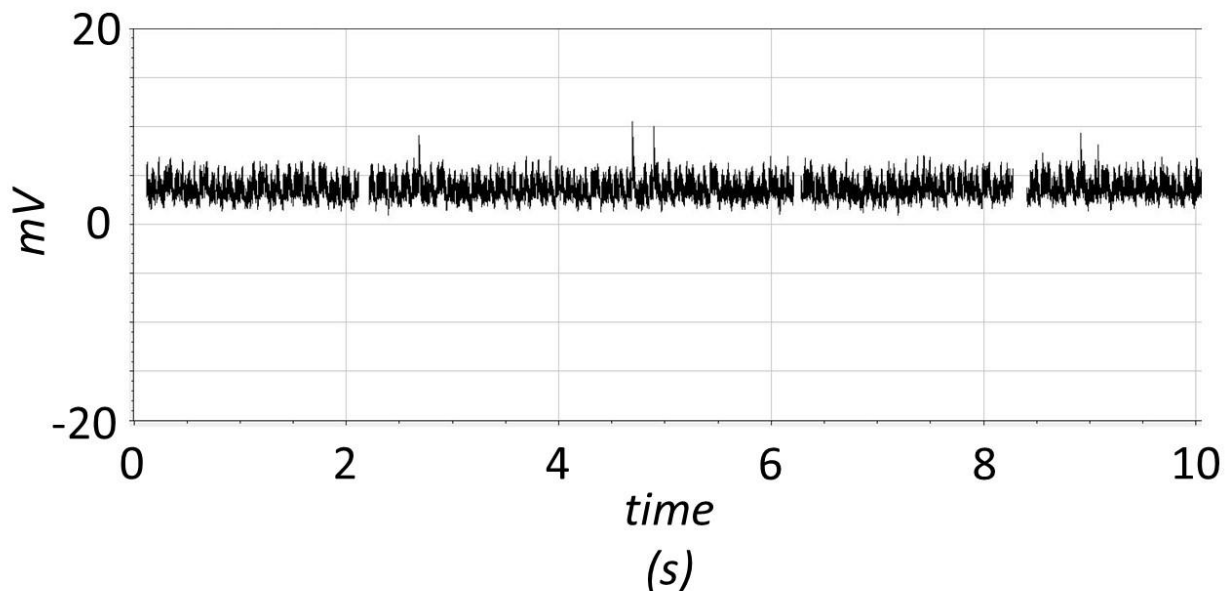


Figure 5.8: Intracellular Action Potentials measured with CNT probe. Axopatch 200B amplifier was used in conjunction with a DigiData 1550A digitizer. The action potentials are $\sim 3\text{-}6\text{mV}$ in amplitude, suggesting there is some leakage – likely due to the conical tungsten tip being inserted too far into the cell.

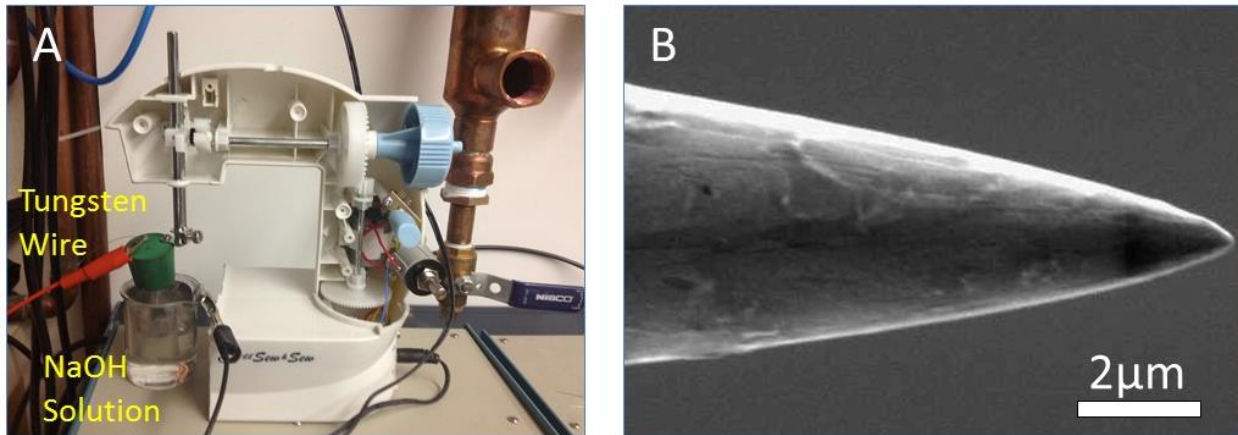


Figure 5.9: Tungsten wire preparation. A) The wire was fed into NaOH solution with an electrode attached to the wire and a counter electrode in the solution. The wire was connected to an altered sewing machine which allowed it to be dipped during the electrochemical etching process. B) The resulting wire tips came to a sharp tapered point.

5.9 Tip Growth of CNTs

Having demonstrated the potential of CNT probes, we aimed to further demonstrate that this technology was scalable. As described above, our initial aim was to directly grow CNTs off an array of sharpened silicon needles. Towards this initial aim, we first set out to demonstrate CNT tip growth sharpened tungsten wire by electrochemically depositing a copper catalyst at the tip, followed by a chemical vapor deposition growth of CNTs. In order to get a more tapered tungsten wire geometry, we used a sewing machine to dip the wire into the solution during etching, as shown in Figure 5.9.

In order to deposit catalyst at the tip of the electrode, we wished to take advantage of field enhancement at the tip of the electrode during electroplating of Fe with an FeCl solution. The tip was placed in a solution of FeCl. The Fe plating results in a net charge being added to the electrode for each reaction. In order to attempt to control and keep constant the amount of charge transfer, we used a charged capacitor that would then be discharged into the electrode tip. The higher the capacitance, the more charge transferred, and the more Fe deposited on the tip.

The tungsten wires were then loaded into a tube furnace. CNTs were grown by Chemical Vapor Deposition (CVD) process. Briefly, the wire was annealed in 200:50sccm::Ar:H₂ at 750°C, followed by CNT growth in 200:375sccm::Ar:CH₄ at 925°C. As shown in Figure 5.10, the higher capacitance trials resulted in tungsten wires that were well covered in nanotubes, while for properly low capacitances, it was possible to get fewer nanotubes concentrated near the tip.

This process proved to still be highly variable and difficult to reliably repeat. In addition, the tubes we were able to grow were typically between 0.5-2μm and rarely much longer. As a result, this work was abandoned in favor of a different method.

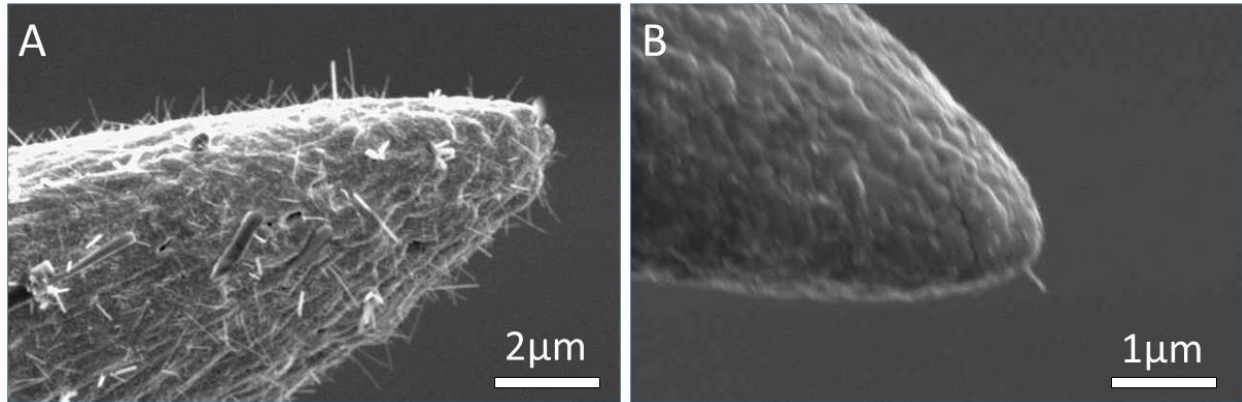


Figure 5.10: Electrochemical plating of iron CNT catalyst. A) $1\mu\text{F}$ capacitor used to deposit iron on tungsten wire. Many tubes grew along the length of the wire. B) 10pF capacitor used to deposit iron. Individual tube was grown at the tip.

5.10 Planar Process

We turned our focus to a planar method of producing nanowire probe arrays, more akin to the Michigan electrode. There were three key challenges in producing arrays of cantilevered CNT probes. The first was to control the placement and orientation of CNTs. Second was a method for selectively insulating the CNTs while leaving the tip exposed. Finally, we needed to release the CNTs from the substrate to allow for a freely cantilevered nanotube probe. Below, we provide an overview of the chip fabrication and discuss these three challenges and the approaches that we took to address them.

5.10.1 Microfabrication

The fabrication process consists of microfabrication steps performed at the wafer scale, primarily at the Marvell nanolab, and nanofabrication steps performed on a chip-by-chip basis primarily in the Zettl lab. The entire process is shown in Figure 5.11.

Wafer fabrication was performed on 6" Si wafers, typically Silicon-On-Insulator (SOI) wafers. A 150nm thick layer of low-stress SiN was first deposited by PECVD. Contacts were then patterned in three distinct die types shown in Figure 5.12. The dies with closely spaced electrodes were meant for interfacing multiple CNTs with a single cell, while the dies with greater spacing were meant for interfacing multiple CNTs with distinct neurons. The contacts are then insulated with a 5 μm layer of SU8, a photo-patternable epoxy. The probe shape is defined

by etching the SiN and a deep reactive ion etch (DRIE) down to the SOI oxide layer. A 3D profile of the probe after SU8 deposition and DRIE is shown in Figure 5.13.

As we will discuss, the backside of the wafer was handled differently for different approaches of releasing the CNT cantilevers from the substrate. In our initial efforts, we used a shallow cut with a dicing saw along the backside to provide a scribe line which we could use to break the handle wafer off when appropriate. In future iterations, we instead did a backside KOH etch to remove the handle wafer before processing. An example of a finished wafer is seen in Figure 5.12. Finally, we coat the wafer in a protective layer of photoresist and dice it into individual dies.

The remaining steps were all done on a chip-by-chip basis. These nanofabrication steps can be broken into the three main tasks mentioned above, controllably placing the CNTs, selectively insulating the CNTs, and cantilevering the CNTs.

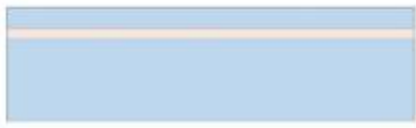

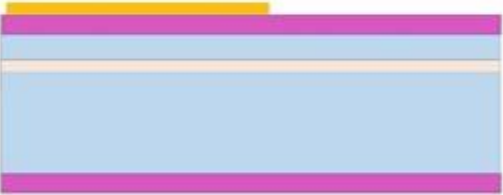
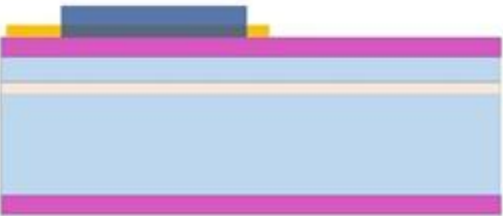
| | |
|---|--|
|  <div data-bbox="673 262 771 514" style="display: inline-block; vertical-align: top;"> <ul style="list-style-type: none"> Si SiO₂ Si₃N₄ Au SU8 CNT Fe Parylene C </div> | <p>6" SOI wafers were used. Material legend shown on right.</p> |
|  | <p>100-200nm of low stress nitride was deposited in the tystar17 furnace. Low stress nitride was chosen to reduce stress on the cantilevered device after release.</p> |
|  | <p>16 gold contact pads and alignment markers were patterned onto the chip.</p> |
|  | <p>SU8 was patterned on top of the chip to insulate the bulk of the contact lines. The bonding pads and the ends of the contacts were left exposed.</p> <p>Not shown: SiN etch in lam6 and DRIE in sts2 at the nanolab to shape probe.</p> |

Figure 5.11: Schematic of planar fabrication process.





| | |
|---|--|
|  <p>A cross-sectional schematic of a wafer. The wafer has a pink bottom layer, a light blue middle layer, and a thin orange layer. On top, there are yellow and blue layers. A white rectangular cutout is shown on the backside of the wafer.</p> | <p>Option 1: We used the disco wafer dicing saw to make a shallow cut along the backside of the wafer. This is to allow for the chip to be easily cleaved later in a precise spot to cantilever nanotube.</p> |
|  <p>A cross-sectional schematic of a wafer, similar to the first one, but with a tapered backside etch that has been performed, creating a wider base.</p> | <p>Option 2: Eventually we moved on to using a backside KOH etch. For this, we designed a Teflon chuck to keep the KOH contained to the backside of the wafer.</p> <p>Not shown: The wafer was then diced using the disco wafer saw in the nanolab into individual dies.</p> |
|  <p>A cross-sectional schematic of a wafer with a tapered backside etch. A small black rectangular feature, representing a carbon nanotube, is now placed on top of the blue layer of the chip.</p> | <p>Carbon nanotubes are placed onto the chip using the electron beam activated adhesion process described later.</p> |
|  <p>A cross-sectional schematic of a wafer with a tapered backside etch. The chip now has several thin black lines on its top surface, representing patterned electrodes.</p> | <p>Electrodes contacting the initial electrodes and the nanotubes are patterned by e-beam lithography followed by Cr/Au evaporation.</p> |

Figure 5.11: (cont.) Schematic of planar fabrication process.


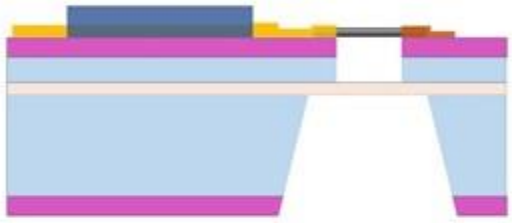


| | |
|---|--|
|  | <p>Iron pads are patterned by e-beam lithography and deposited in an electron beam metal evaporator. This iron will inhibit parylene deposition on the</p> |
|  | <p>An etch mask is patterned in PMMA and a XeF₂ etch is used to remove the SiN and the underlying Si using the nanolab's xetch tool.</p> |
|  | <p>A thin film of parylene was deposited using the parylene tool in the nanolab. Typically a single pellet of parylene dimer was enough to coat with ~20-30nm of parylene.</p> |
|  | <p>The Fe was etched away in a 20% nitric acid solution for 5min. The parylene on the Fe will lift off with it if it has not formed a network.</p> |

Figure 5.11: (cont.) Schematic of planar fabrication process.

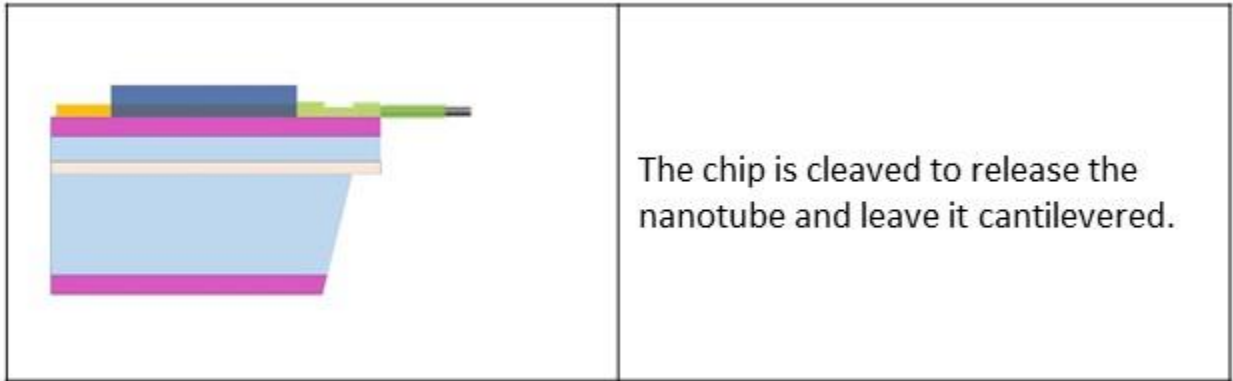


Figure 5.11: (cont.) Schematic of planar fabrication process.

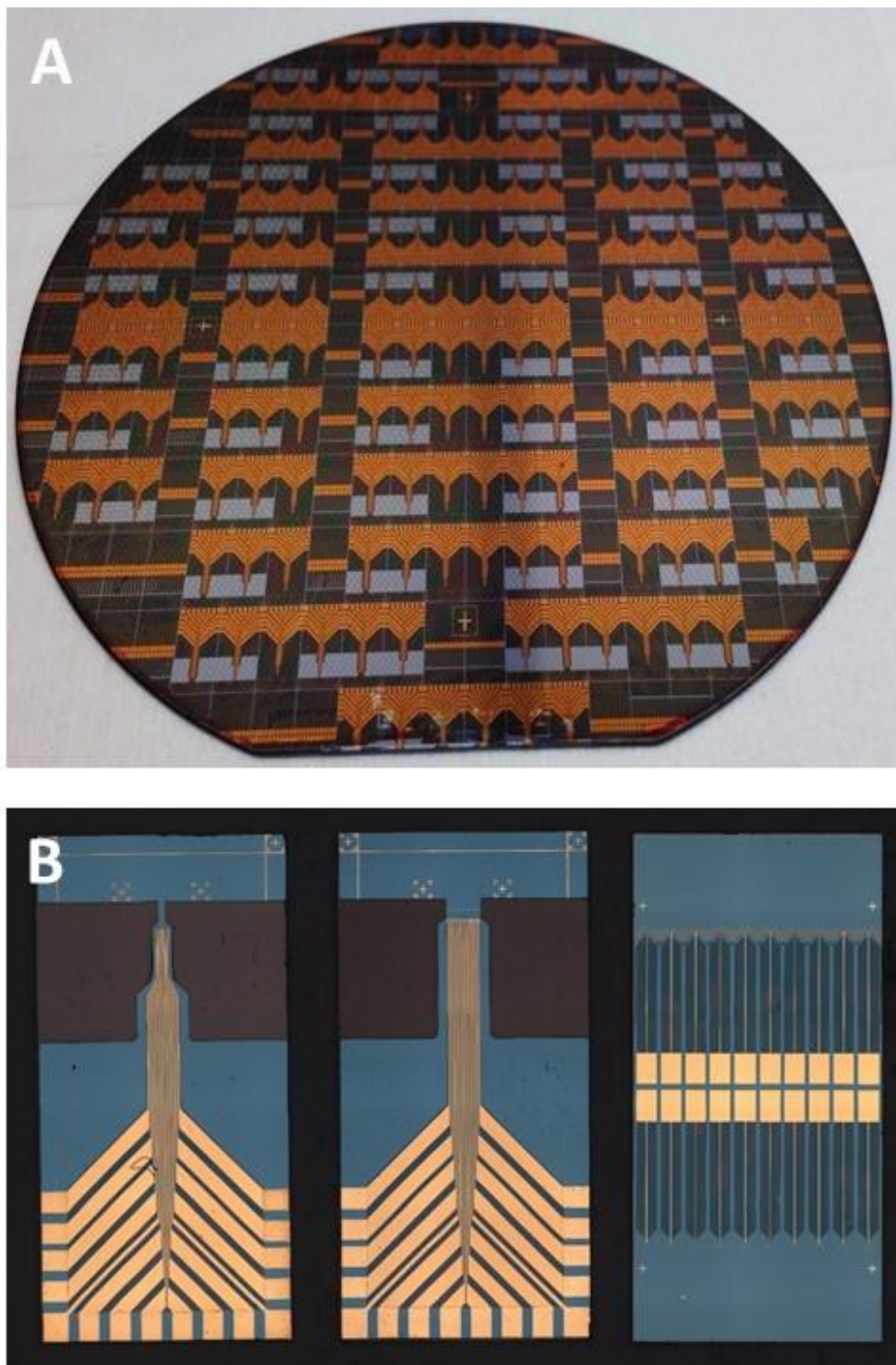


Figure 5.12: Wafer fabrication. A) Completed wafer before dicing. B) (i)-(iii) Three distinct die types. i) Narrow spaces electrodes for multiple CNTs in a single cell. ii) Larger spacing for individual electrodes in multiple cells. iii) Test chip not designed to be a probe, but instead useful for electrochemical characterization of the probes.

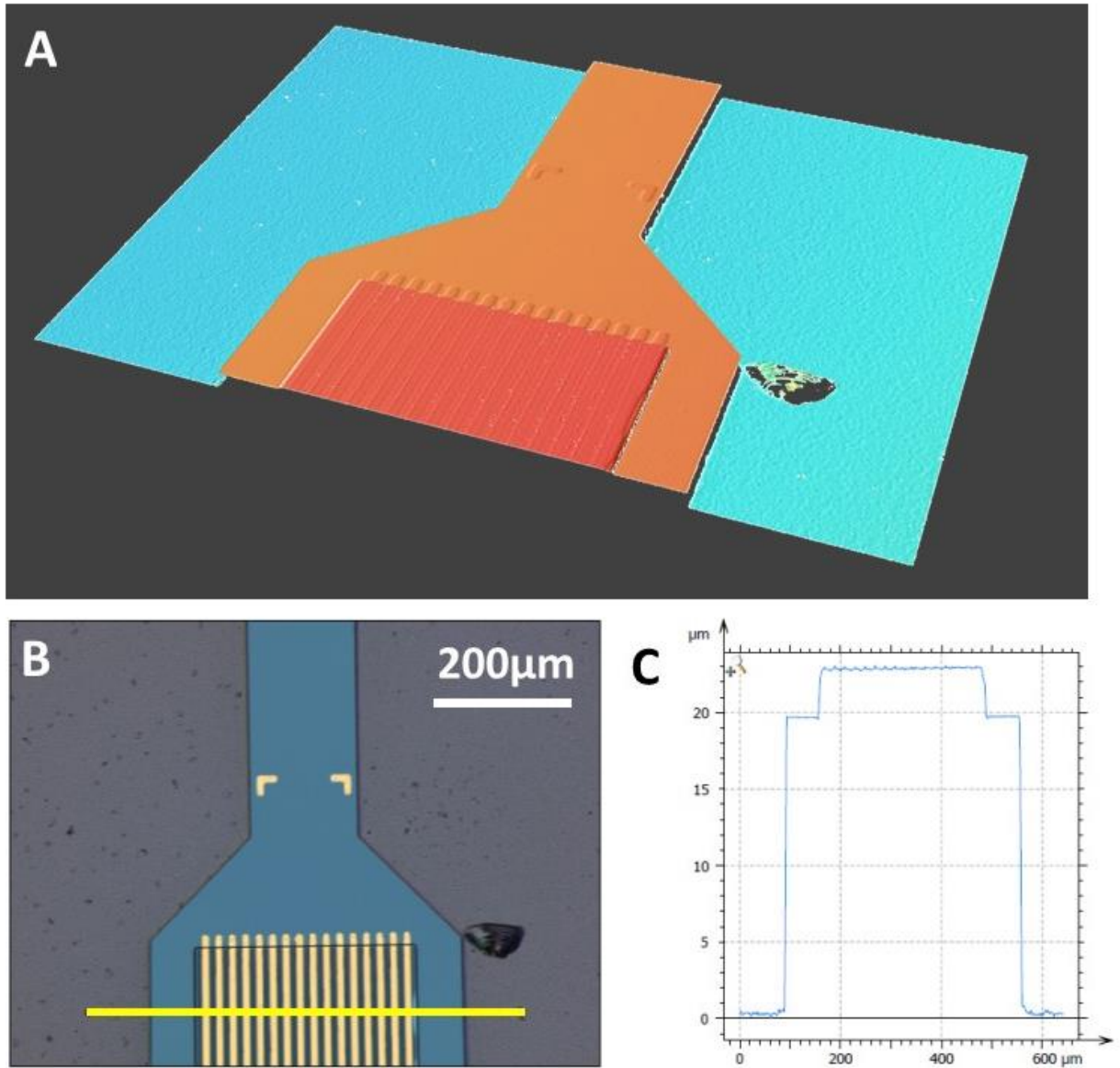


Figure 5.13: 3D Morphology of Chips. A) 3D map of the tip of one of the probes. B) 2D image of same chip as in (A). C) Height trace of yellow line in (B). The device layer is 20μm thick formed by DRIE, while the SU8 layer on top of the gold electrodes is around 5μm thick.

5.10.2 Controllable Placement of CNTs

One of the principal challenges of working with CNT arrays is how to place and orient them in a desired area. Because this is a challenge for realizing large-scale arrays of CNT transistors, a great deal of work has been done in this area. As one of the primary challenges of working with CNTs, we tried a number of different approaches for CNT placement. Haensch et al. reported a method of selective adhesion through ionic exchange (IBM), which we attempted to use towards developing our own ion exchange paradigm to directly attach CNTs to Au contacts [94]. We also tried using PDMS trenches to align and stamp nanotubes. We also used electrophoresis to align tubes across two electrodes [95], [96]. We also worked on directly transferring aligned CNTs grown on mis-cut quartz. Ultimately, what worked the best for us was an electron beam patterned selective adhesive region that we will describe first.

The placement of CNTs relies on a selective adhesion layer that was developed by Yuzvinsky et al., while the orientation of the CNTs are directed by fluidic alignment during dropcasting [97]. A layer of PMMA EL6 or A4, a common electron beam sensitive resist, is spin-coated onto the target chip, and after baking at 200°C for 4min, the chip is soaked in acetone for 60s. The acetone removes all but a residual layer of the PMMA. The chip is then loaded into an SEM, where the adhesion sites are exposed with a 1kV beam for a dose of at least 1,000C/cm². It is worth noting the typical dose for PMMA patterning is 300uC/cm² is being far exceeded.

CNTs are prepared by sonication in ODCB. Typically between 5-10min was necessary at power level 9 in a bath ultrasonicator. Undispersed particulates could be seen in the solution if not sonicated for long enough. The use of ODCB is critical for the adhesion of the CNTs to the activated region, and other common dispersal solutions such as SDS will not work. The reason for this, as well as the adhesion mechanism is still unclear.

The chip is then placed on a spin coater and spun at 5000rpm. Individual drops of CNT:ODCB solution are dropped onto the chip at 30s intervals. The time between droplets proved to be important in getting proper tube alignment. 10-20 droplets were typically enough to saturate the adhesion regions.

The resulting aligned CNTs can be seen in Figure 5.14. The darker areas in the SEM image are the beam activated regions which serve to anchor the CNTs. CNT solution purity proved to be critical as impurities would also stick to the adhesion region, blocking CNTs from adhering. For multi-wall CNT samples, this was particularly an issue. While we attempted to purify our own MWCNT samples through ultracentrifugation, chemical treatment and annealing, we never did manage to get pure enough samples to avoid this problem. Instead, we switched to using high-purity commercial single- and double-walled CNT samples.

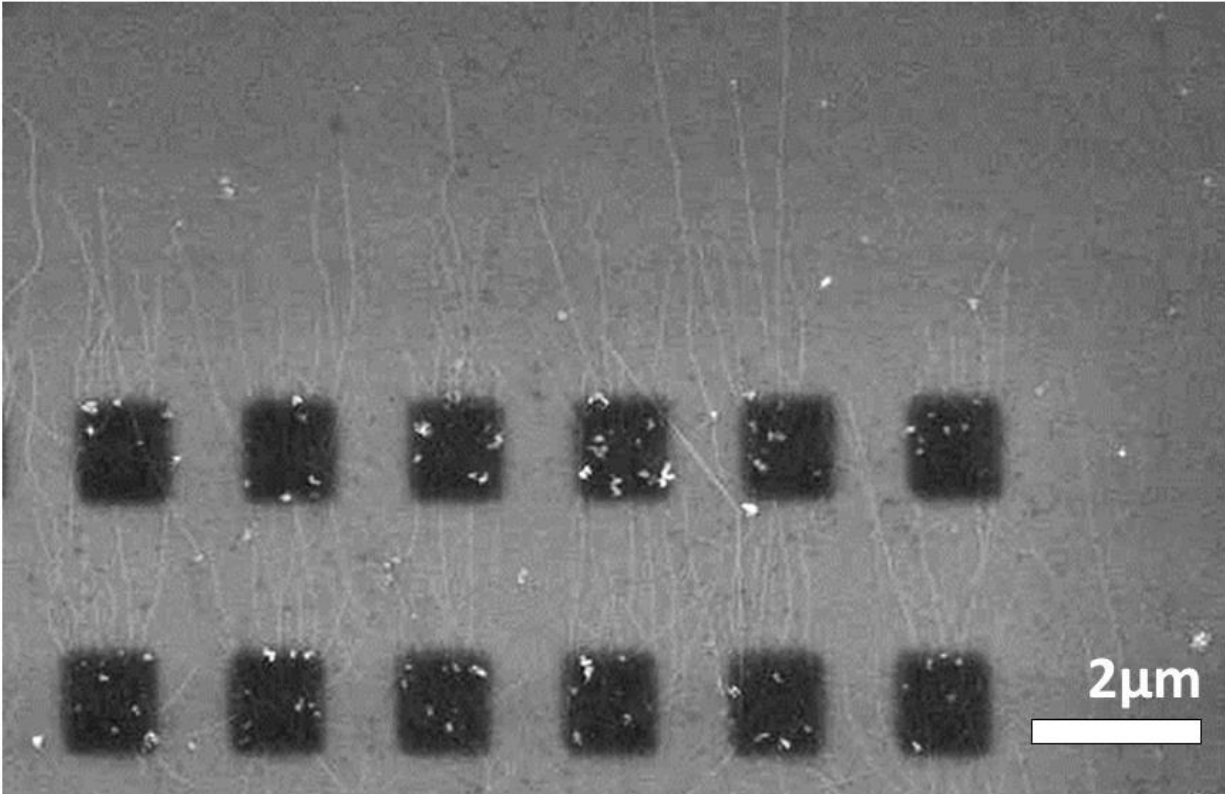


Figure 5.14: Beam Activated Adhesion for CNT Placement. Areas of dark contrast were hyper-exposed areas of residual PMMA EL6. These serve as adhesion sites for functionalized CNTs. Few-wall CNTS were sonicated in ODCB and drop-cast onto the chip at 5000rpm.

5.10.3 Insulation and Exposure of CNT Tip

As discussed earlier, Parylene C is an ideal insulating material. While the e-beam exposure method of pulling parylene from the tips of CNTs was effective for individual probes it did not lend itself to scaling. First, it requires chips compatible with a TEM holder. Second, the length of CNT that can be exposed is limited. Previously reported methods of parylene removal also have little to no control over exposure length, have extremely low yields, and proved to be difficult to implement.

One of the earliest methods mentioned was laser ablation to melt the parylene away from the nanotube tip [87], [104]. In this case, the laser power needed to be carefully controlled to find a regime in which the parylene was ablated, but the nanotube was left intact. Other work showed that a microheater could be used to similarly melt away the parylene [90]. Others demonstrated that mechanical stress could separate nanotubes from parylene encapsulation [105].

While we did work on laser ablation as well as using a Focused Ion Beam (FIB) to selectively remove parylene, as shown in Figure 5.15, both of these methods had significant problems. For the laser ablation, the device yield was extremely low and there was no way to control the length of exposed tube with any precision. In the case of the FIB, while it appeared to be doing a good job of selectively etching the parylene, closer examination revealed the tube was often either etched entirely through or was left partially encapsulated. Instead, we developed a novel method which lends itself to planar processing and allows for precise control over exposure length without damage to the underlying nanotube.

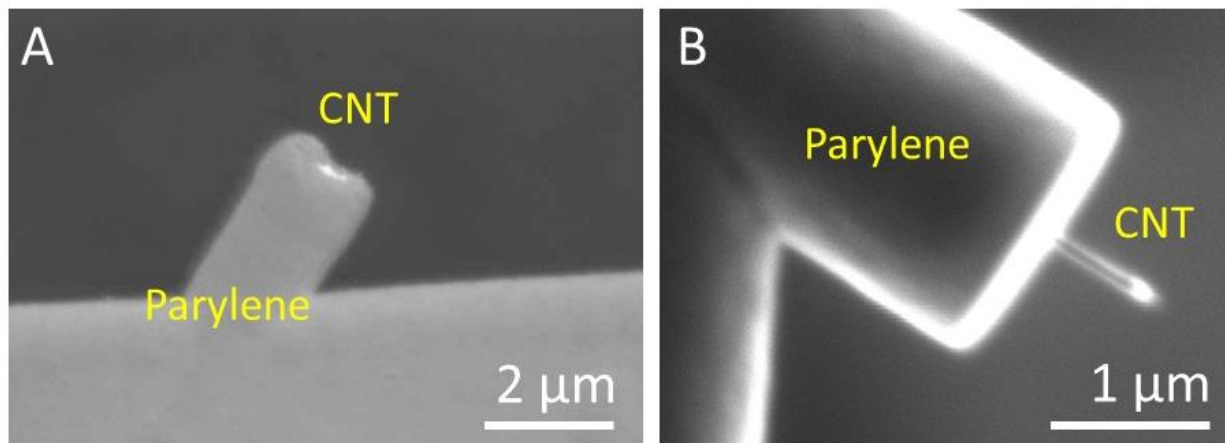


Figure 5.15: Parylene removal. A) SEM image after attempted laser ablation parylene encapsulated CNT. B) SEM image of FIB exposure of CNT tip. While results looked promising, often the nanotube would etch away before the parylene was completely removed. This technique would only be possible for large diameter multiwall tubes.

5.10.3.1 Selective Parylene Deposition

While parylene deposition can be very uniform, it has been observed that deposition on transition metals typically results in highly non-uniform films. As described by Vaeth and Jensen, the transition metal serves to limit both the initiation and propagation of parylene growth. Parylene molecules more readily desorb from the transition metal substrate, and when adsorbed are often deactivated and fail to form polymer chains [106]. Over time, active parylene molecules will adsorb onto the metal, serving as nucleation sites that grow with further deposition. After sufficient deposition, the nucleation sites will grow together to create a continuous film. If we limit the amount of parylene deposited so that the nucleation sites are not able to form a continuous film, when the transition metal is removed, the disjoint parylene islands will lift-off as well, as shown in the schematic in Figure 5.16.

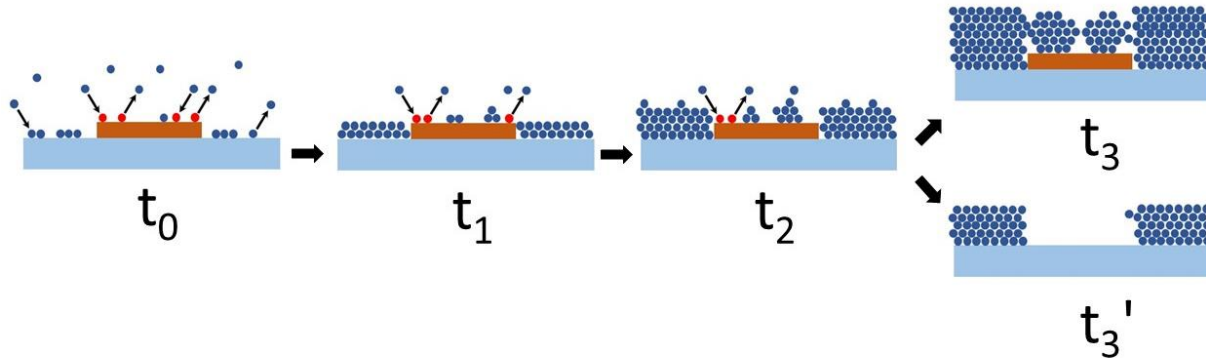


Figure 5.16: Schematic of selective parylene deposition on iron film. At times t_0 - t_2 , parylene deposits uniformly on substrate, but readily desorbs and is often deactivated (shown in red) on the Fe film. Nucleation sites eventually form and grow on Fe. At t_3 , the nucleation sites have grown together to create a continuous film (upper arrow). Alternatively, if the iron is removed before the nucleated areas have grown together, the incomplete parylene islands are lifted off as well (lower arrow).

To first demonstrate that this method is effective in the selective removal of parylene films, parafilm was used as a shadow mask to deposit 50nm of Fe by electron beam evaporation onto half of a Si chip. A 60nm thick film of Parylene C was then deposited using a Specialty Coating Systems Parylene Deposition System 2010 Labcoater 2. The chip is then placed in a 20% nitric acid etch at room temperature for 1min to remove the iron and the parylene islands that had been forming. Figure 5.17 shows SEM and AFM images of the Si chip. The border between the Fe-free area where parylene is present, and the area which had been coated in Fe and is now parylene-free, can be clearly seen in the SEM. The conductive bare Si substrate shows up as a brighter contrast region in the SEM compared to the insulating parylene coated area. The AFM image in Figure 5.17b shows a chip with 60nm of parylene deposited before the Fe has been removed by the HNO₃ etch. Very small – on the order of 10's of nanometers – particles can be seen on the iron-coated side, which are likely small areas of parylene nucleation. It is worth noting that the larger parylene particles at the border are likely due to patchy iron deposition as a shadow mask was used. The AFM image in Figure 5.17c was taken after the nitric acid etch. As can be seen, the parylene remains unaffected by the etch, and the small parylene nucleation sites are now gone.

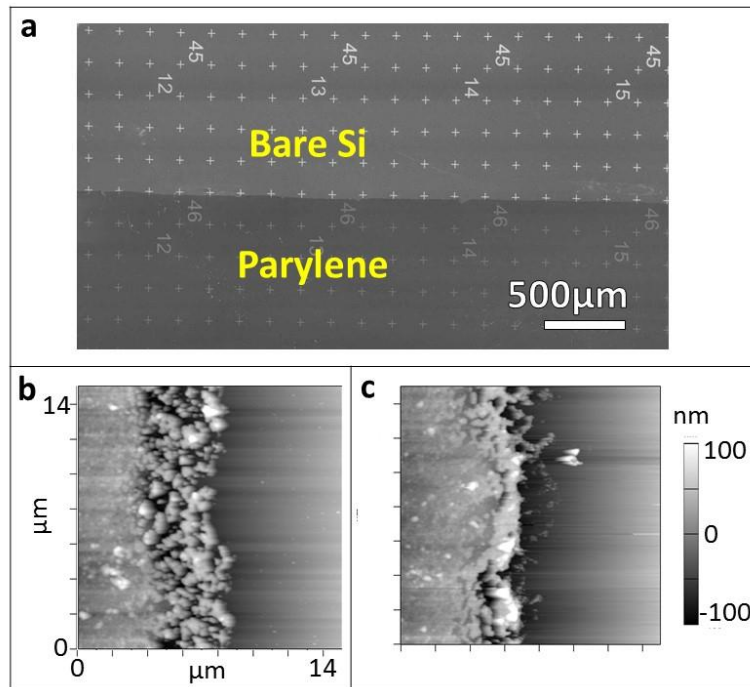


Figure 5.17: Parylene removal on Si chip. (a) SEM image of Si chip in which Fe has been deposited and removed on the top half, leaving bare Si, whereas parylene readily coated the bottom, Fe-free region. (b) AFM image of parylene border after 60nm deposition, but before Fe-etch. Very small parylene nucleation sites can be seen on the right-hand side. (c) AFM image of border after Fe-etch in 20% HNO₃ for 1min. No parylene nucleation sites can be seen on the right.

This method of selective thin film parylene deposition and removal lends itself to the selective encapsulation of carbon nanotubes, in which other methods of parylene removal, such as oxygen plasma or ion milling, may damage the underlying nanotube. To verify that this method results in fully exposed nanotubes, a multi-walled CNT (Sigma Aldrich) IPA solution was dropcast onto a TEM grid. A glass slide was placed on top of half of the grid to serve as a shadow mask, while 50nm of Fe was evaporated onto the grid. Parylene was then deposited onto the grid as described earlier. The grid was then floated on a 20% nitric acid solution for 20s to remove the Fe, then transferred to two sequential water baths to remove any excess nitric acid. The grid was then imaged under TEM to verify the absence of parylene in regions which had been coated in iron and the presence of parylene in the uncoated regions. Figure 5.18a shows the resulting TEM grid, and TEM images taken from both sides of the grid after the Fe-etch are shown in Figure 5.18b. CNTs on the side of the grid that had not been coated in iron are uniformly coated in a layer of parylene around 30nm thick. In contrast, CNTs on the Fe-coated side are parylene free, as shown in Figure 5.18c. The CNTs on the parylene-free side of the chip show no significant indications of tube wall damage, confirming that the brief dilute nitric acid etch does not damage the CNT. There is also very little indication of residual Fe after the etch. This may be critical in using the CNT as an intracellular probe, as Fe has been shown to be cytotoxic [107].

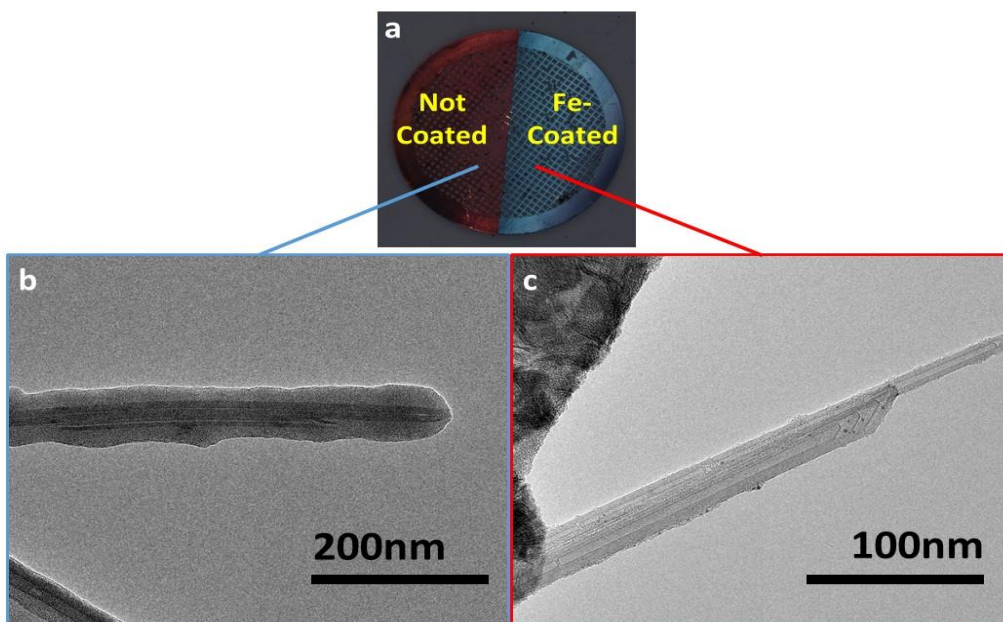


Figure 5.18: Parylene coverage and inhibition on CNTs. (a) Optical image of a CNT-covered TEM grid with half coated in Fe and the other half uncoated, after a 30nm parylene deposition. (b) TEM image of parylene encapsulated nanotube on the Fe-free side of the grid. (c) TEM image of a parylene-free bundle of two CNTs which had been on the Fe-coated side of the grid, after the iron was etched by floating on HNO₃ for 20s.

Finally, we demonstrated that this method can also be applied to individual nanotubes in order to leave an exposed region of controllable length, while leaving the rest of the tube encapsulated. CNTs are controllably placed on a substrate as described in the previous chapter. Chrome/gold (2nm/75nm) contacts are patterned by electron beam lithography and electron beam evaporation at the base of the tube, serving as an electrical contact, an anchor point, and an etch mask. Similarly, a pad of Fe (75nm) is patterned by electron beam lithography and electron beam evaporation at the tip of the tube. In order to encapsulate the full circumference of the nanotube, the underlying Si_3N_4 and Si are etched using a XeF_2 vapor phase etch (20 x 30s cycles at 3.0Torr), leaving the tube suspended. The etch area is defined by an electron beam patterned layer of PMMA, where the Fe and Au layers serve as an etch mask at either end of the tube. A thin film of Parylene C is then deposited. The chip is then placed in a 20% nitric acid solution for ~5min. It is worth noting that while the etchant rapidly dissolves iron, the graphitic nanotube layers are etch resistant at this concentration. After the chemical etch, the chip is rinsed in DI water and IPA and dried in a critical point dryer to avoid damaging the suspended tube. Another XeF_2 vapor phase etch is used to etch the now parylene-free iron pad sites, releasing the nanotube (10x30s cycles at 3.0Torr). The complete fabrication process is shown in Figure 5.19.

Figure 5.20a-h shows the resulting chips from the fabrication steps described above. The chip shows an array of individual nanotube sites, demonstrating that this method lends itself to large-scale, multi-unit probe fabrication. As can be seen from the SEM images in Figure 5.20, the tip of the CNT is exposed, while the rest is uniformly coated in parylene. The length of exposed tip can be controlled by the length of the nanotube initially coated in Fe, and in this instance is $1.25\mu\text{m}$.

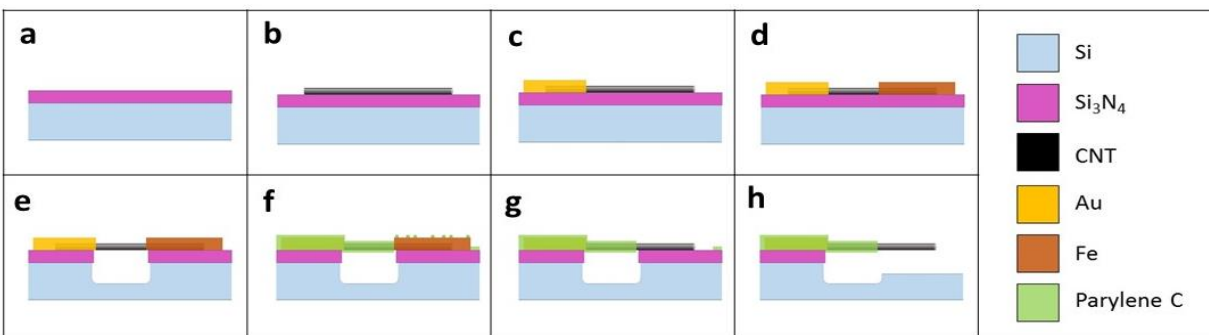


Figure 5.19: Schematic of selective parylene encapsulation of individual CNT process. (a) Si_3N_4 is deposited by CVD onto a silicon wafer, which is then diced. (b) CNTs are controllably placed on the substrate. (c)-(d) Au and Fe pads are patterned onto the base of the CNT by e-beam lithography and e-beam evaporator. (e) A XeF_2 vapor etch is used to undercut the tube to allow it to be fully coated in parylene. (f) Parylene C is deposited by CVD. (g) Fe and Parylene are removed in 20% HNO_3 wet etch for 5min. (h) A second XeF_2 etch is used to release the CNT.

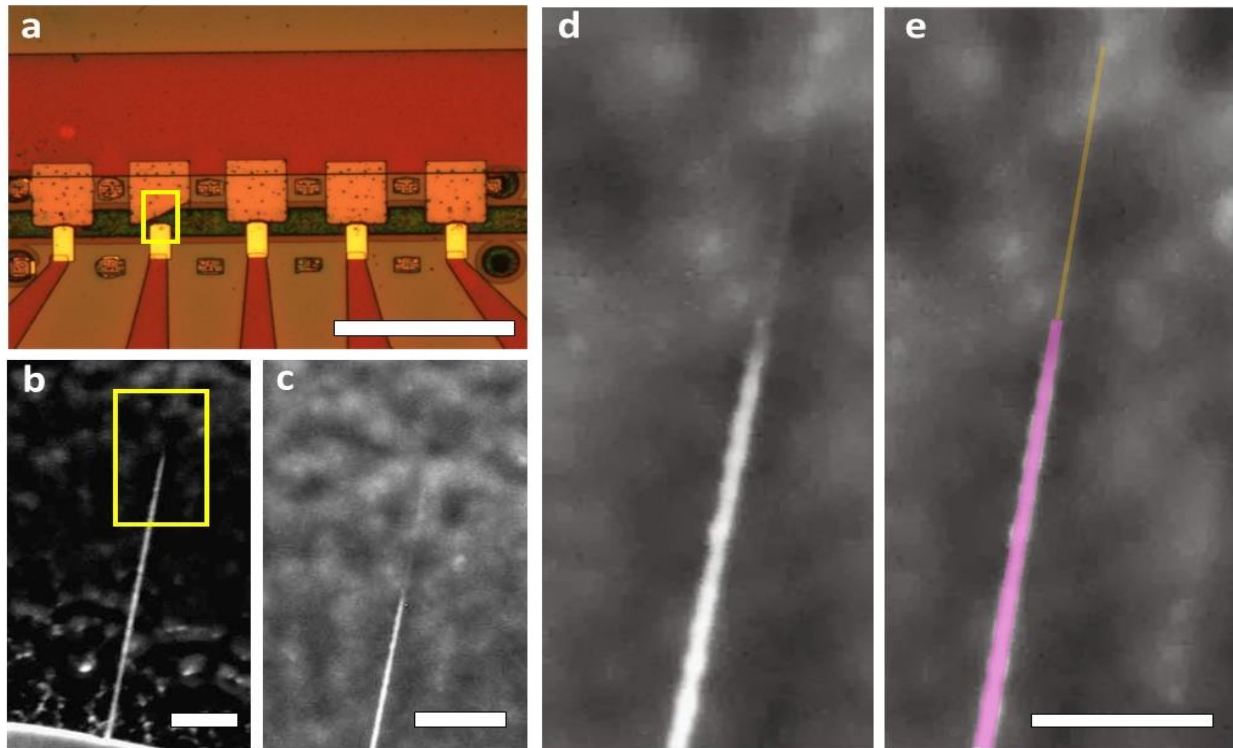


Figure 5.20: Selective parylene encapsulation of individual CNT. (a) Optical image of multi-unit CNT probe chip. Scale bar is 500 μ m. (b)-(d) SEM images of encapsulated CNT with tip exposed. The parylene thickness in this image is 30nm, and the CNT appears well encapsulated. Scale bars are 1 μ m, 1 μ m and 500nm respectively. (e) A false-color version of (d) to highlight the parylene-coated (purple) and exposed (yellow) regions of the CNT. The exposed length of the tube is 1.25 μ m.

5.10.4. Electrochemical Impedance Spectroscopy

In order to establish if the CNT probe would be suitable for neural recording, we performed EIS using the Gamry setup described earlier, as shown in Figure 5.21. In order to release the CNTs from the substrate, an additional XeF_2 etch was used after the parylene deposition. While these CNTs were fully cantilevered, the support substrate was still present a few microns beneath them. We will talk about how this support substrate can be fully removed shortly.

A printed circuit board for the electronic readout is shown in Figure 5.22. The chips were wire bonded to a custom designed printed circuit board (PCB) made to leave the chip extended over the edge of the board. The PCB with attached chip can be seen in Figure 5.22A. The backplane of the chip is connected to a ground connection beneath the chip. The backside of the chip is scratched to ensure good contact, and then a silver epoxy is used to bond the chip to the PCB and contact the ground. If the chips are on an SOI substrate, we also put a small drop of silver epoxy at the corner of the chip to ensure the device layer of the wafer was grounded as well as the handle layer.

The PCB was fitted with a 20 pin molex connector. The first 16 pins are connected to each of the CNT chip's pads. Pin 17, 18 and 19 are left open with pinouts on the PCB and pin 20 is connected to ground. 20 wire interconnects bridge from the chip carrier PCB to a PCB outfitted with a 16 position + ground rotary dial. The rotary dial board reduces the output to a



Figure 5.21: Electrochemical Test Setup for Multi-Unit Array. EIS was performed using a platinum counter electrode. The backplane of the Si-chip and PCB were at a common ground with the counter electrode. Dulbecco phosphate buffer solution (DPBS) – a biological buffer solution – was used as the solution.

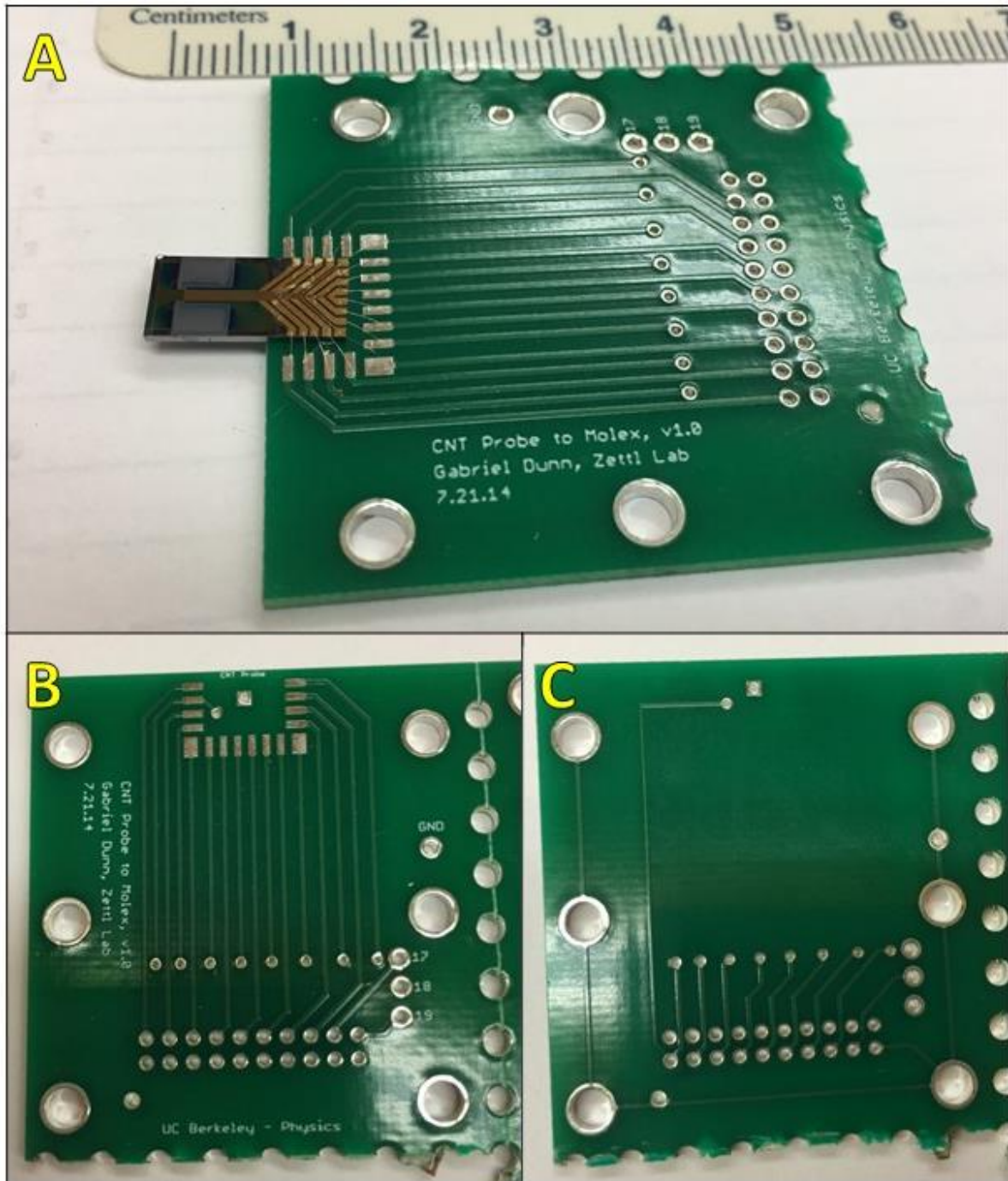


Figure 5.22: Printed Circuit Boards (PCBs). A) Optical image of chip wire bonded to PCB. Chip is left overhanging and screw holes mount to a nanomanipulator stage for cell interrogation. B) PCB wiring, front-side. C) PCB wiring, back-side. 20 pins are made to accommodate a Molex™ interconnect system.

single channel, so each CNT pad can be looked at individually. This is only necessary because our recording and characterization devices only accept individual input lines.

The probes used had multiple exposed CNTs for any given pad. Each pad contacted a $1\mu\text{m}$ wide area of CNTs. The parylene was patterned to expose $1\mu\text{m}$ of the tube ends. Once again, functionalization in HNO_3 was necessary in order to lower the impedance of the probe. The EIS results are shown in Figure 5.23. The impedance of the probes at 1kHz was on the order of $100\text{k}\Omega$ for each channel with CNTs present. For pads in which no nanotubes were contacted, the impedance was considerably higher, around $100\text{M}\Omega$.

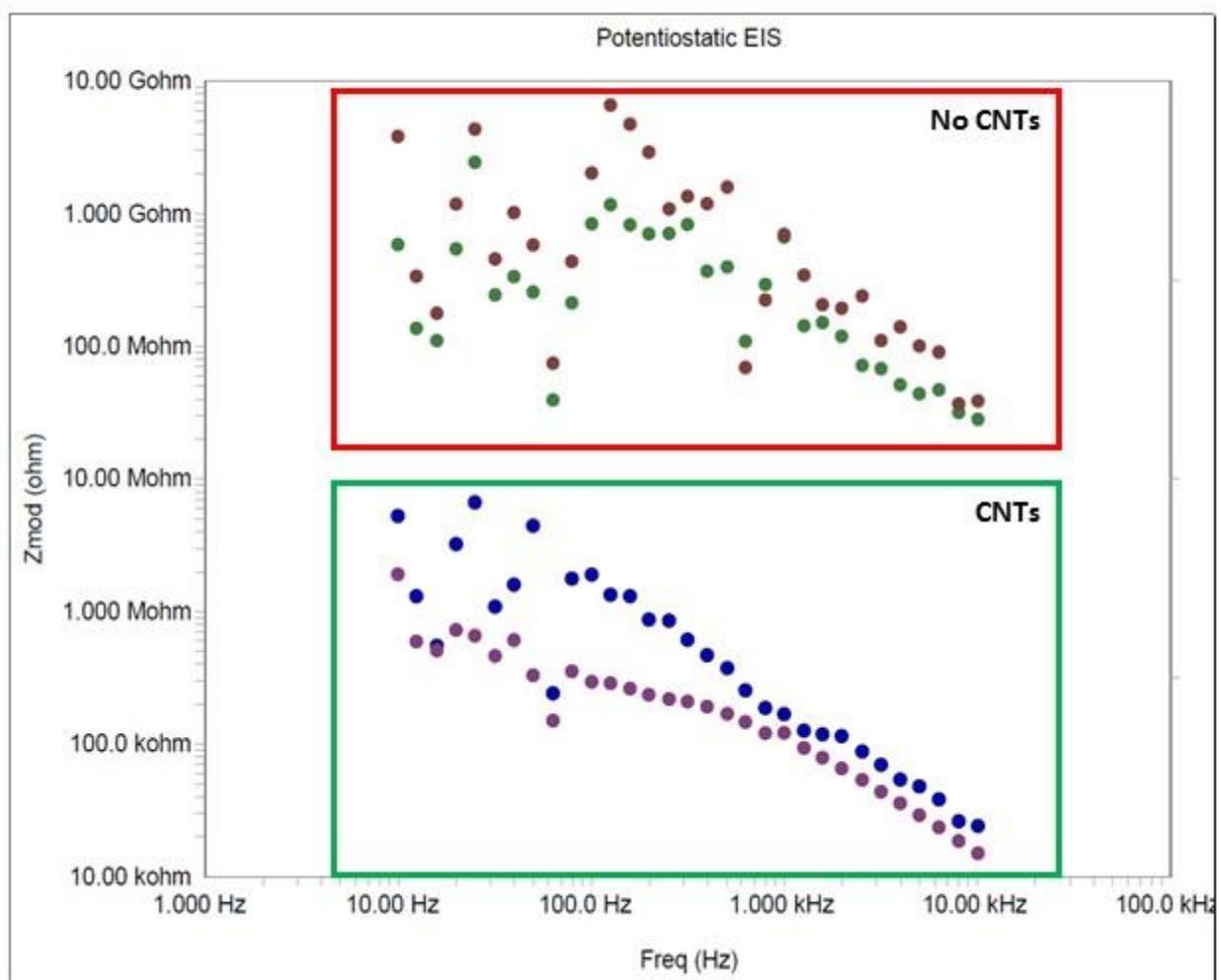


Figure 5.23: Multi-Unit Array Electrochemical Impedance Spectroscopy. EIS was performed with a sweep from 10Hz - 10kHz . The top two traces show the impedance for pads which were not contacts CNTs. The bottom two traces show to samples from which CNTs had been placed and contacted.

5.10.5 Cantilevered Probe

The final remaining difficulty was in releasing the CNTs to make a fully cantilevered probe. Alternatively, this difficulty could be seen as having a macroscopic handle on a nanoscopic probe. While approaches like the nanotube growth off of a sharpened wire or direct attachment incorporate this effortlessly, this was a major hurdle with the planar process outlined above.

Our initial work relied on using a silicon-on-insulator (SOI) wafer. SOI wafers are commercially available and consist of a thin device-layer of Si bonded to a thicker handle wafer with a thin layer of oxide in between them. The device-layer can then be released from the handle wafer by HF removal of the oxide layer. As shown in Figure 5.24, we intended to use this undercut to release the Si cantilever from the handle wafer, and cleave the edges of the chip, leaving a cantilevered nanotube probe. However, we found that the length of HF dip needed to accomplish this caused a number of difficulties. Primarily, while parylene is said to be highly resistant to HF, over long periods of time (~18hrs) the parylene would swell and crack. The SU8 would experience something similar. The HF would also begin to peel up the exposed gold contact pads.

In order to shorten the amount of time that the chip would be exposed to HF, we decided to include a KOH back-etch step, so that the oxide layer could be etched from the backside. Here we encountered two issues: strain from the SU8 and Au contacts caused the silicon beams to be

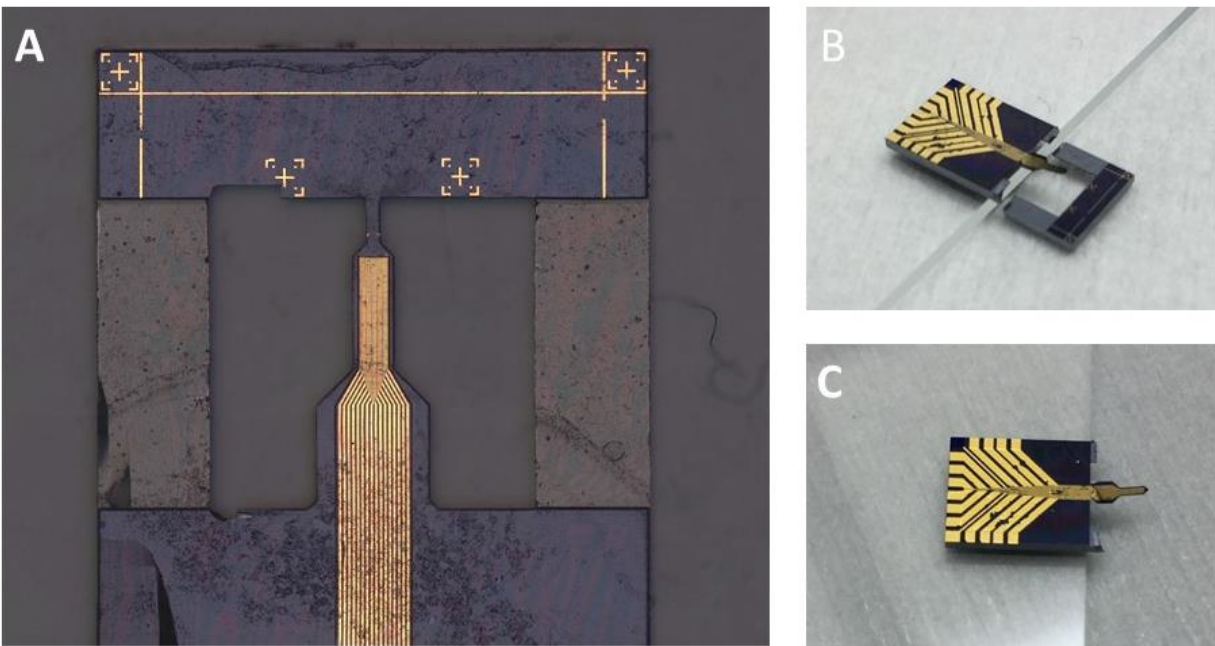


Figure 5.24: Selective parylene insulation of CNTs. A) Optical image of device after iron removal. B) SEM of parylene insulated nanotube. C) SEM close up of CNT and exposed tip. D) False-color image of C) to highlight insulation and tip.

unstable, as should in Figure 5.25. Often times, the Si bridges would curl up during chip processing. The other issue we had was with the stability of the nanotubes after they had been left suspended. While we did not have these issues with the SOI wafers without the back-etch, small movements would seemingly dislodge or break the suspended nanotubes.

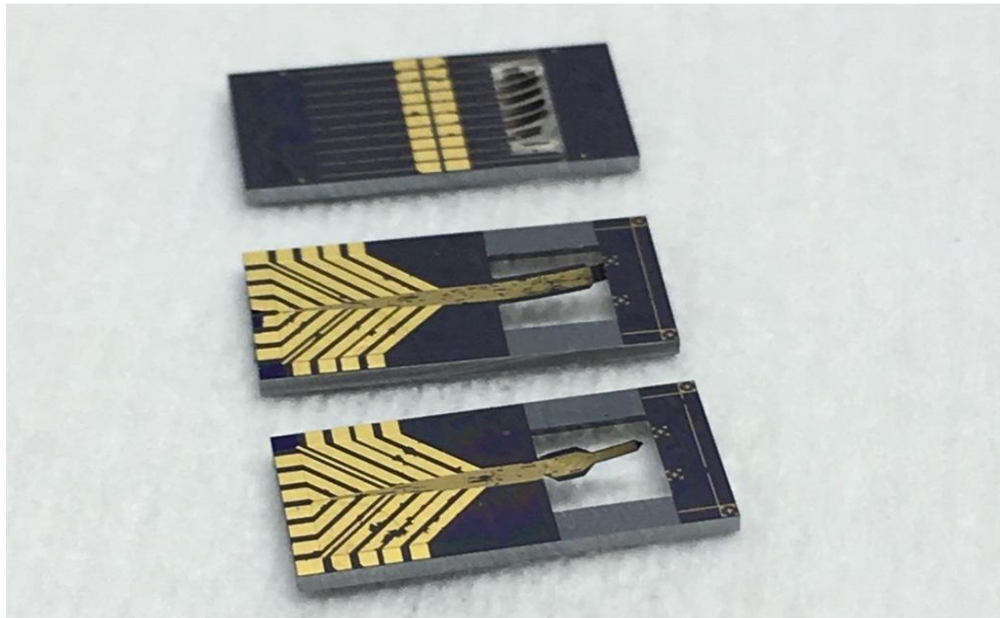


Figure 5.25: Selective parylene insulation of CNTs. A) Optical image of device after iron removal. B) SEM of parylene insulated nanotube. C) SEM close up of CNT and exposed tip. D) False-color image of C) to highlight insulation and tip.

5.11 CNT Plasmonic Push Pin

The properties of CNTs described at the beginning of this chapter make a strong case for them being ideal electrophysiological interfaces with cells, and this need not be limited to tethered probes. I will describe an approach we considered using a gold nanoparticle (Au-NP) terminated CNT heterostructure as an optical probe. We will henceforth refer to this heterostructure as a CNT Push-pin due to its resemblance to the commercial product. The device consists of a sensing end, the CNT tip, and a scattering end, the Au-NP, as shown in Figure 5.26A. I envision two potential setups for this probe as shown in Figure 5.26: the first being a microfluidic assay, and the second a transmembrane voltage indicator.

The extended length of the CNT allows the sensing region and scattering region to be in distinct environments, in particular this allows for a potential to be placed between the two. In such a case, the voltage modulates the peak scattering wavelength of the Au-NP local surface plasmon resonance (LSPR). This device could also hold promise as a surface enhanced Raman spectroscopy (SERS) probe. Both of these possibilities will be discussed, followed by a proposal for how to fabricate such a device.

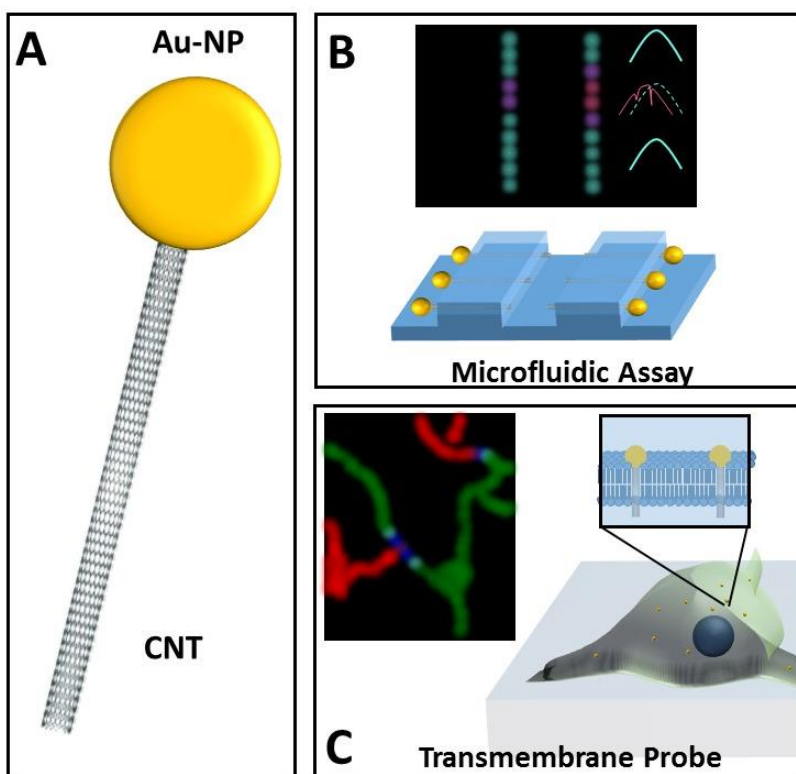


Figure 5.26: CNT Pushpin. A) Cartoon schematic of the device. B) Setup for use as a microfluidic assay and for probe characterization. C) Cartoon of probe being used as a transmembrane voltage indicator.

Plasmonic NPs could be ideal optical probes compared to standard fluorescent probes. While fluorescent probes readily photobleach and become unusable, NPs will continue to scatter. In addition to this, the scattering of light off a plasmonic NP is significantly more efficient than the stimulated emission of a fluorescent marker. For neural recording, this is significant as a main limitation is the amount of heat produced by imaging with enough luminosity to garner a significant signal.

Zhang and Nurmikko et al. demonstrated a plasmonic NP based neural probe that relied on the change of the dielectric function of the medium surrounding the NP surface caused by the change in ionic potential during an action potential. Because the probe is relying on a local ionic change, it does not benefit from the full 120mV signal of an action potential, but is only seeing the equivalent of $\sim 300\mu\text{V}$. In addition to this, the shift in plasmonic resonance is very slight, only 0.00125nm/mV , meaning the expected shift in wavelength is 0.000375nm for an action potential [108]. The CNT plasmonic push pin would be capable of performing significantly better in both aspects, leading to a significantly larger signal.

While most LSP probes rely on changes of dielectric constant in the surrounding medium for detection, in the CNT Push-pin voltages across the probe would result in a change in the dielectric constant of the NP itself. The polarizability of a NP under an external field is given by:

$$\alpha = 4\pi a^3 \frac{\epsilon - \epsilon_m}{\epsilon + 2\epsilon_m}$$

where ϵ and ϵ_m are the dielectric coefficients of the NP and the medium respectively and a is the radius of the NP. This leads to the resonance condition $\text{Re}[\epsilon(\omega)] = -2\epsilon_m$, where

$$\text{Re}[\epsilon(\omega)] = 1 - \frac{\omega_p^2 \tau^2}{1 + \omega^2 \tau^2}$$

and the plasma frequency is given by

$$\omega_p^2 = \frac{ne^2}{\epsilon_0 m}$$

where n is the electron density of the NP [109]. In a typical LSP probe, binding events cause the dielectric constant of the medium to shift, and in turn alter the resonant scattering frequency. In the case of the plasmonic push-pin, a voltage difference between the AuNP and the CNT directly shifts the dielectric constant of the Au-NP instead.

When the CNT pushpin is placed across some electrochemical barrier with a voltage across it, Faradaic charge from the CNT will result in a capacitive charging of the Au-NP and a shift in its electron density, either donating or removing electrons from the free electron gas. The added charge spreads evenly on the surface of the Au-NP. The surface plasmon interaction is isolated to the surface as well, with the relevant length scale being the Thomas-Fermi screening length ($\sim 1\text{-}2\text{\AA}$). Because of this, otherwise modest changes in the bulk electron density result in

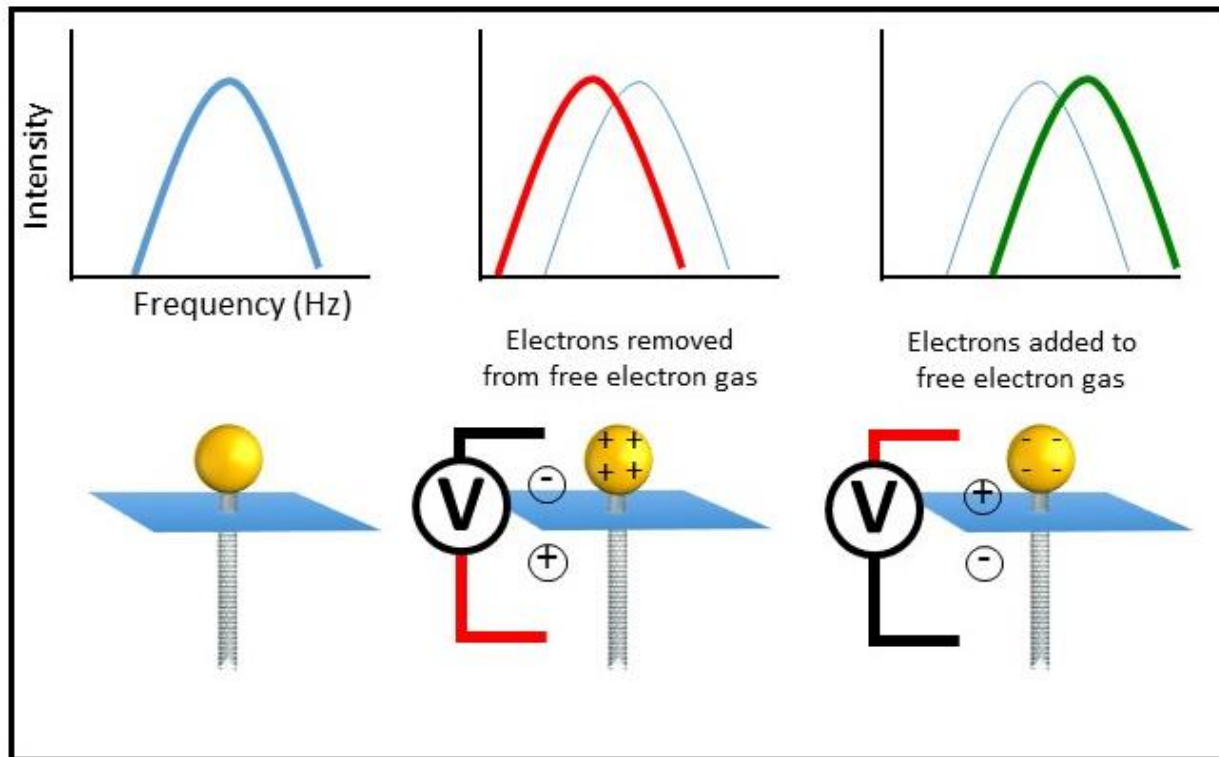


Figure 5.27: Voltage dependence frequency shift of Plasmonic Push Pin. As a bias is applied across the push pin, electrons are either added to or removed from the electron gas in the AuNP. This causes a shift in the peak scattering intensity.

relatively significant shifts in the peak scattering wavelength. This results in a shift in plasma frequency, which in turn modulates the resonant frequency by the resonance condition mentioned above, as shown in Figure 5.27.

For the model described above, and with a AuNP, the expected shift in peak wavelength should be 0.04-0.08nm/mV, nearly 50 times larger than for a AuNP alone. For an action potential, this should mean a scattering wavelength shift of 4.8-9.6nm, or nearly 20,000 times better than the AuNP alone.

Through functionalization, the CNT push pin may naturally insert itself across the cell membrane. As discussed previously, sufficiently small diameter CNTs should be capable of spontaneously entering a cell membrane without an applied force, without the need for any functionalization. By functionalizing the AuNP to be hydrophilic, they will be resistant to crossing the cell membrane. This can be achieved by a simple thiol functionalization with 1-dodecanethiol. Alternatively, an integrin or glycoprotein functionalization could be used to ensure stronger and more selective tethering to the cell surface, as well as allowing the targeting of specific cell lines.

In addition to a sensitive voltage probe, the CNT push pin may be useful as SERS probe as well due to a large tip-enhancement of signals because of its high aspect ratio. The geometric

field enhancement, β , of a cylindrical rod is approximately proportional to its aspect ratio (L/r) [110]. As CNTs are capable of larger stable aspect ratios than any other material, they are in turn capable of larger geometric field enhancement, with enhancement factors of nearly 20,000 having been demonstrated [111]. In Tip-Enhanced Raman Spectroscopy (TERS), the Raman signal is enhanced by $(E/E_0)^4$, where E is the geometrically enhanced electric field, and E_0 is the un-enhanced field [112]. For a CNT Pushpin probe with an aspect ratio of 1000:1, the Raman signal is enhanced by a factor of 10^{12} . In addition to the massive increase in signal strength, the CNT pushpin is reducing the sensing volume to a small localized area at its tip (1-2nmR).

5.11.1 Proposed Experimental Methods

The proposed fabrication and experimental steps are outlined in Figure 5.28. Briefly, horizontally aligned CNTs are placed on a polycrystalline quartz substrate and metal contacts are patterned on top. A further photolithography step defines the Au-NP growth region. A reactive ion etch (RIE) is used to open the CNT ends and create a trench in the substrate. The photoresist etch-mask is used as a passivation layer for the electrochemical growth of Au-NP on the exposed CNT tips. The procedure for this growth follows the electrochemical addition of Au-NP to CNT sidewalls performed previously [113]. The photoresist etch mask is then re-exposed to define the second microfluidic trench at the sensing end of the probe and expose the metallic contact. The metallic contacts are chemically etched and then a second RIE step etches the substrate and exposed the CNT tip.

This synthesis method lends itself to an intermediary experiment studying these probes in a microfluidic chamber. This will allow one to characterize the wavelength shift versus an applied potential. While I believe this same process could be used to synthesize CNT pushpins which would ultimately be suspended in solution and injected into an extracellular region, achieving high concentrations with a 2D synthesis method such as this may be arduous. There is likely a solution based method of synthesis that can be explored.

A microfluidic chip is formed by bonding the chip to a PDMS substrate. The photoresist acts as a barrier between the CNT sensing end of the chip and the Au-NP optical scattering end. To characterize the voltage modulation of the peak scattering frequency and the integrity of the photoresist barrier, a bias can be placed between the two channels

Alternatively, the photoresist layer can be removed and the CNT pushpins can be lifted off the substrate by a light sonication in an appropriate solvent, for use as a transmembrane probe. Where optical economy will be important for in-vitro and in-vivo studies, rather than using a white light probe and taking a full spectrum, a single frequency can be monitored. It is best to pick something off-resonance in the highest sloped area of the spectrum, to maximize signal.
















| | | |
|--|--|---|
| <p>i</p> <p>Top View</p>  <p>Side View</p>  | <p>Close-up</p>  | <p>Begin with a Si, pyrex, or miscut quartz wafer or chips (if you are planning on doing the aligned growth directly on the device substrate)</p> |
| <p>ii</p>  <p>Side View</p>  |  | <p>Either transfer aligned nanotubes as discussed earlier, or grow directly on quartz substrate</p> |
| <p>iii</p>  <p>Side View</p>  |  | <p>Deposit a comb pattern of metallic electrodes. Metal choice is unimportant, something easily etchable.</p> |
| <p>iv</p>  <p>Side View</p>  |  | <p>Deposit a photoresist for insulation like PMMA, i-line or g-line. Needs to be re-patternable for future steps.</p> |
| <p>v</p>  <p>Side View</p>  |  | <p>Etch the CNT and the underlying substrate. SF_6 plasma followed by an O_2 plasma should work.</p> |

Figure 5.28: Potential Fabrication for Push Pin Probe.

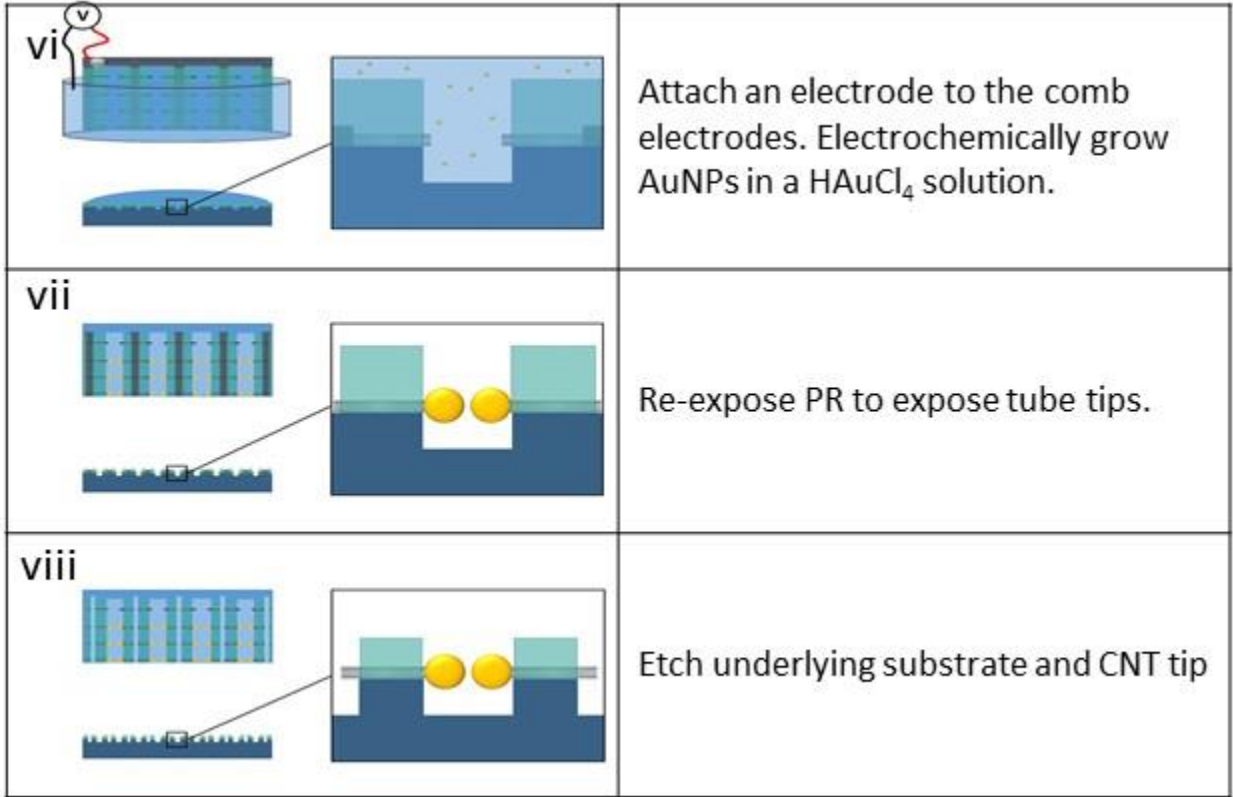


Figure 5.28 (cont.): Potential Fabrication for Push Pin Probe.

- [1] W. Yuan *et al.*, “The edge- and basal-plane-specific electrochemistry of a single-layer graphene sheet,” *Sci. Rep.*, vol. 3, no. Cvd, p. 2248, 2013.
- [2] K. W. Horch and G. S. Dhillon, *Neuroprosthetics: Theory and Practice*. 2004.
- [3] T. Kuo and R. L. McCreery, “Surface Chemistry and Electron-Transfer Kinetics of Hydrogen-Modified Glassy Carbon Electrodes,” *Electroanalysis*, vol. 71, no. 8, pp. 1553–1560, 1999.
- [4] R. L. McCreery and K. K. Cline, “Carbon Electrodes,” in *Laboratory Techniques in Electroanalytical Chemistry*, 1996.
- [5] V. S. Polikov, P. A. Tresco, and W. M. Reichert, “Response of brain tissue to chronically implanted neural electrodes,” *J. Neurosci. Methods*, vol. 148, no. 1, pp. 1–18, Oct. 2005.
- [6] J. N. Turner *et al.*, “Cerebral astrocyte response to micromachined silicon implants,” *Exp. Neurol.*, vol. 156, no. 1, pp. 33–49, 1999.
- [7] H. Szarowski *et al.*, “Brain responses to micro-machined silicon devices,” *Brain Res.*, vol. 983, pp. 23–35, 2003.
- [8] N. A. Kotov *et al.*, “Nanomaterials for Neural Interfaces,” *Adv. Mater.*, vol. 21, no. 40, pp. 3970–4004, Oct. 2009.
- [9] R. Biran, D. C. Martin, and P. A. Tresco, “Neuronal cell loss accompanies the brain tissue response to chronically implanted silicon microelectrode arrays,” *Exp. Neurol.*, vol. 195, no. 1, pp. 115–126, 2005.
- [10] J. P. Seymour and D. R. Kipke, “Neural probe design for reduced tissue encapsulation in CNS,” *Biomaterials*, vol. 28, no. 25, pp. 3594–607, Sep. 2007.
- [11] Y. T. Kim, R. W. Hitchcock, M. J. Bridge, and P. A. Tresco, “Chronic response of adult rat brain tissue to implants anchored to the skull,” *Biomaterials*, vol. 25, no. 12, pp. 2229–2237, 2004.
- [12] N. A. Kotov *et al.*, “Nanomaterials for neural interfaces,” *Adv. Mater.*, vol. 21, no. 40, pp. 3970–4004, 2009.
- [13] C. Hassler, R. P. Von Metzen, P. Ruther, and T. Stieglitz, “Characterization of parylene C as an encapsulation material for implanted neural prostheses,” *J. Biomed. Mater. Res. - Part B Appl. Biomater.*, vol. 93, no. 1, pp. 266–274, 2010.
- [14] S. P. Nichols, A. Koh, W. L. Storm, J. H. Shin, and M. H. Schoenfisch, “Biocompatible materials for continuous glucose monitoring devices,” *Chem. Rev.*, vol. 113, pp. 2528–2549, 2013.
- [15] T. D. Yoshida Kozai *et al.*, “Ultrasmall implantable composite microelectrodes with bioactive surfaces for chronic neural interfaces,” *Nat. Mater.*, vol. 11, no. 11, pp. 1–9, Nov. 2012.
- [16] X. Cui *et al.*, “Surface modification of neural recording electrodes with conducting polymer / biomolecule blends,” 2001.

- [17] Y. Kato, I. Saito, T. Hoshino, T. Suzuki, and K. Mabuchi, "Preliminary Study of Multichannel Flexible Neural Probes Coated with Hybrid Biodegradable Polymer 1," pp. 660–663, 2006.
- [18] X. Cui, J. Wiler, M. Dzaman, R. A. Altschuler, and D. C. Martin, "In vivo studies of polypyrrole / peptide coated neural probes," vol. 24, pp. 777–787, 2003.
- [19] R. A. Green, N. H. Lovell, G. G. Wallace, and L. A. Poole-warren, "Conducting polymers for neural interfaces : Challenges in developing an effective long-term implant q," *Biomaterials*, vol. 29, pp. 3393–3399, 2008.
- [20] N. Gomez and C. E. Schmidt, "Nerve growth factor-immobilized polypyrrole : Bioactive electrically conducting polymer for enhanced neurite extension," pp. 4–9, 2006.
- [21] M. Jorfi, J. L. Skousen, C. Weder, J. C. Williams, M. M. H. Ii, and S. P. Massia, "Multi-site incorporation of bioactive matrices into MEMS-based neural probes."
- [22] P. R. Kennedy, "The cone electrode: a long-term electrode that records from neurites grown onto its recording surface," *J. Neurosci. Methods*, vol. 29, no. 3, pp. 181–193, 1989.
- [23] P. J. Rousche, D. S. Pellinen, D. P. Pivin, J. C. Williams, R. J. Vetter, and D. R. Kipke, "Flexible polyimide-based intracortical electrode arrays with bioactive capability," *IEEE Trans. Biomed. Eng.*, vol. 48, no. 3, pp. 361–370, 2001.
- [24] A. J. Engler, S. Sen, H. L. Sweeney, and D. E. Discher, "Matrix Elasticity Directs Stem Cell Lineage Specification," *Cell*, vol. 126, no. 4, pp. 677–689, 2006.
- [25] D. E. Discher, "Tissue Cells Feel and Respon to the Stiffness of Their Substrate," *Science (80-.)*, vol. 310, no. 5751, pp. 1139–1143, 2005.
- [26] S. L. BeMent, K. D. Wise, D. J. Anderson, K. Najafi, and K. L. Drake, "Solid-State Electrodes for Multichannel Multiplexed Intracortical Neuronal Recording," *IEEE Trans. Biomed. Eng.*, vol. BME-33, no. 2, pp. 230–241, 1986.
- [27] K. L. Drake, K. D. Wise, J. Farraye, D. J. Anderson, and S. L. BeMent, "Performance of Planar Multisite Microprobes in Recording Extracellular Single-Unit Intracortical Activity," *IEEE Trans. Biomed. Eng.*, vol. 35, no. 9, pp. 719–732, 1988.
- [28] S. J. Tanghe, K. Najafi, and K. D. Wise, "A planar IrO multichannel stimulating electrode for use in neural prostheses," *Sensors Actuators B. Chem.*, vol. 1, no. 1–6, pp. 464–467, 1990.
- [29] K. Najafi and K. D. Wise, "An implantable multielectrode array with on-chip signal processing," *IEEE J. Solid-State Circuits*, vol. 21, no. 6, pp. 1035–1044, 1986.
- [30] K. D. Wise, D. J. Anderson, J. F. Hetke, D. R. Kipke, and K. Najafi, "Wireless Implantable Microsystems: High-Density Electronic Interfaces to the Nervous System," *Proc. IEEE*, vol. 92, no. 1, pp. 76–97, Jan. 2004.
- [31] D. J. Anderson *et al.*, "Batch-Fabricated Thin-Film Electrodes for Stimulation of the Central Auditory System," *IEEE Trans. Biomed. Eng.*, vol. 36, no. 7, pp. 693–704, 1989.

- [32] G. Buzsáki *et al.*, “Tools for probing local circuits: High-density silicon probes combined with optogenetics,” *Neuron*, vol. 86, no. 1, pp. 92–105, 2015.
- [33] E. M. Maynard, C. T. Nordhausen, and R. a Normann, “The Utah intracortical Electrode Array: a recording structure for potential brain-computer interfaces.,” *Electroencephalogr. Clin. Neurophysiol.*, vol. 102, no. 3, pp. 228–39, Mar. 1997.
- [34] K. E. Jones, P. K. Campbell, and R. a Normann, “A glass/silicon composite intracortical electrode array.,” *Ann. Biomed. Eng.*, vol. 20, no. 4, pp. 423–37, Jan. 1992.
- [35] J. Hsu, L. Rieth, R. A. Normann, P. Tathireddy, and F. Solzbacher, “Encapsulation of an Integrated Neural Interface Device With Parylene C,” vol. 56, no. 1, pp. 23–29, 2009.
- [36] P. J. Rousche and R. a Normann, “Chronic recording capability of the Utah Intracortical Electrode Array in cat sensory cortex.,” *J. Neurosci. Methods*, vol. 82, no. 1, pp. 1–15, Jul. 1998.
- [37] G. Ling and R. W. Gerard, “The normal membrane potential of frog sartorius fibers.,” *J. Cell. Physiol.*, vol. 34, pp. 383–396, 1949.
- [38] G. Ling and J. W. Woodbury, “Effect of temperature on the membrane potential of frog muscle fibers,” *J. Cell. Physiol.*, vol. 34, no. 3, pp. 97–98, 1949.
- [39] G. Ling and R. W. Gerard, “The membrane potential and metabolism of muscle fibers,” *J. Cell. Physiol.*, vol. 34, no. 3, pp. 413–438, 1949.
- [40] G. Ling and R. W. Gerard, “The influence of stretch on the membrane potential of the striated muscle fiber,” *J. Cell. Physiol.*, vol. 34, no. 3, pp. 383–396, 1949.
- [41] I. C. Kleppe and H. P. C. Robinson, “Correlation entropy of synaptic input-output dynamics,” *Phys. Rev. E - Stat. Nonlinear, Soft Matter Phys.*, vol. 74, no. 4, pp. 1–6, 2006.
- [42] J. T. Robinson, M. Jorgolli, A. K. Shalek, M.-H. Yoon, R. S. Gertner, and H. Park, “Vertical nanowire electrode arrays as a scalable platform for intracellular interfacing to neuronal circuits,” *Nat. Nanotechnol.*, vol. 7, no. 3, pp. 180–184, 2012.
- [43] F. Patolsky *et al.*, “Detection, stimulation, and inhibition of neuronal signals with high-density nanowire transistor arrays,” *Science (80-.)*, vol. 313, pp. 1100–1104, 2006.
- [44] B. P. Timko, T. Cohen-Karni, G. Yu, Q. Qing, B. Tian, and C. M. Lieber, “Electrical recording from hearts with flexible nanowire device arrays,” *Nano Lett.*, vol. 9, no. 2, pp. 914–918, 2009.
- [45] T. Cohen-Karni, B. P. Timko, L. E. Weiss, and C. M. Lieber, “Flexible electrical recording from cells using nanowire transistor arrays,” *Proc Natl Acad Sci U S A*, vol. 106, no. 18, pp. 7309–7313, 2009.
- [46] B. P. Timko, T. Cohen-Karni, Q. Qing, B. Tian, and C. M. Lieber, “Design and implementation of functional nanoelectronic interfaces with biomolecules, cells, and tissue using nanowire device arrays,” *IEEE Trans. Nanotechnol.*, vol. 9, no. 3, pp. 269–280, 2010.
- [47] Q. Qing *et al.*, “Nanowire transistor arrays for mapping neural circuits in acute brain

- slices.,” *Proc. Natl. Acad. Sci. U. S. A.*, vol. 107, no. 5, pp. 1882–7, 2010.
- [48] B. Tian *et al.*, “Three-dimensional, flexible nanoscale field-effect transistors as localized bioprobes.,” *Science*, vol. 329, no. 5993, pp. 830–4, 2010.
- [49] Z. Jiang, Q. Qing, P. Xie, R. Gao, and C. M. Lieber, “Kinked p–n Junction Nanowire Probes for High Spatial Resolution Sensing and Intracellular Recording,” no. Cvd, 2012.
- [50] L. Xu, Z. Jiang, Q. Qing, L. Mai, Q. Zhang, and C. M. Lieber, “Design and synthesis of diverse functional kinked nanowire structures for nanoelectronic bioprobes,” *Nano Lett.*, vol. 13, no. 2, pp. 746–751, 2013.
- [51] Q. Qing, Z. Jiang, L. Xu, R. Gao, L. Mai, and C. M. Lieber, “Free-standing kinked nanowire transistor probes for targeted intracellular recording in three dimensions.,” *Nat. Nanotechnol.*, vol. 9, no. 2, pp. 142–7, 2014.
- [52] X. Duan *et al.*, “Intracellular recordings of action potentials by an extracellular nanoscale field-effect transistor.,” *Nat. Nanotechnol.*, vol. 7, no. 3, pp. 174–9, Mar. 2012.
- [53] R. Gao *et al.*, “Outside Looking In : Nanotube Transistor Intracellular Sensors,” 2012.
- [54] T.-M. Fu *et al.*, “Sub-10-nm intracellular bioelectronic probes from nanowire-nanotube heterostructures.,” *Proc. Natl. Acad. Sci. U. S. A.*, vol. 111, no. 4, pp. 1259–64, 2014.
- [55] W. Zhou, X. Dai, T. M. Fu, C. Xie, J. Liu, and C. M. Lieber, “Long term stability of nanowire nanoelectronics in physiological environments,” *Nano Lett.*, vol. 14, no. 3, pp. 1614–1619, 2014.
- [56] J. Liu, C. Xie, X. Dai, L. Jin, W. Zhou, and C. M. Lieber, “Multifunctional three-dimensional macroporous nanoelectronic networks for smart materials.,” *Proc. Natl. Acad. Sci. U. S. A.*, vol. 110, no. 17, pp. 6694–9, 2013.
- [57] B. Tian *et al.*, “Macroporous nanowire nanoelectronic scaffolds for synthetic tissues,” *Nat. Mater.*, vol. 11, no. 10, pp. 872–876, 2012.
- [58] T. Zhou *et al.*, “Syringe-injectable mesh electronics integrate seamlessly with minimal chronic immune response in the brain.,” *Proc. Natl. Acad. Sci. U. S. A.*, vol. 114, no. 23, p. 201705509, 2017.
- [59] G. Hong, T. M. Fu, T. Zhou, T. G. Schuhmann, J. Huang, and C. M. Lieber, “Syringe Injectable Electronics: Precise Targeted Delivery with Quantitative Input/Output Connectivity,” *Nano Lett.*, vol. 15, no. 10, pp. 6979–6984, 2015.
- [60] J. Liu *et al.*, “Syringe-injectable electronics,” *Nat. Nanotechnol.*, vol. 10, no. 7, pp. 629–636, 2015.
- [61] X. Dai, W. Zhou, T. Gao, J. Liu, and C. M. Lieber, “Three-dimensional mapping and regulation of action potential propagation in nanoelectronics-innervated tissues,” *Nat. Nanotechnol.*, vol. 11, no. 9, pp. 776–782, 2016.
- [62] T. G. Schuhmann, J. Yao, G. Hong, T.-M. Fu, and C. M. Lieber, “Syringe-Injectable Electronics with a Plug-and-Play Input/Output Interface,” *Nano Lett.*, p. acs.nanolett.7b03081, 2017.

- [63] C. Xie, J. Liu, T.-M. Fu, X. Dai, W. Zhou, and C. M. Lieber, “Three-dimensional macroporous nanoelectronic networks as minimally invasive brain probes,” *Nat. Mater.*, vol. 14, no. 12, pp. 1286–1292, 2015.
- [64] T.-M. Fu, G. Hong, T. Zhou, T. G. Schuhmann, R. D. Viveros, and C. M. Lieber, “Stable long-term chronic brain mapping at the single-neuron level,” *Nat. Methods*, vol. 13, no. 10, pp. 875–82, 2016.
- [65] J. N. Coleman, U. Khan, W. J. Blau, and Y. K. Gun’ko, “Small but strong: A review of the mechanical properties of carbon nanotube-polymer composites,” *Carbon N. Y.*, vol. 44, no. 9, pp. 1624–1652, 2006.
- [66] M. Nardelli, B. Yakobson, and J. Bernholc, “Brittle and Ductile Behavior in Carbon Nanotubes,” *Phys. Rev. Lett.*, vol. 81, no. 21, pp. 4656–4659, 1998.
- [67] B. G. Demczyk *et al.*, “Direct mechanical measurement of the tensile strength and elastic modulus of multiwalled carbon nanotubes,” *Mater. Sci. Eng. A*, vol. 334, no. 1–2, pp. 173–178, 2002.
- [68] X. Chen, A. Kis, a Zettl, and C. R. Bertozzi, “A cell nanoinjector based on carbon nanotubes,” *Proc. Natl. Acad. Sci. U. S. A.*, vol. 104, no. 20, pp. 8218–22, May 2007.
- [69] Y. Zhu and W. Li, “Cytotoxicity of carbon nanotubes,” *Sci. China Ser. B Chem.*, vol. 51, no. 11, pp. 1021–1029, Oct. 2008.
- [70] H. Isobe *et al.*, “Preparation, purification, characterization, and cytotoxicity assessment of water-soluble, transition-metal-free carbon nanotube aggregates,” *Angew. Chemie - Int. Ed.*, vol. 45, no. 40, pp. 6676–6680, 2006.
- [71] M. K. Gheith, V. A. Sinani, J. P. Wicksted, R. L. Matts, and N. A. Kotov, “Single-walled carbon nanotube polyelectrolyte multilayers and freestanding films as a biocompatible platform for neuroprosthetic implants,” *Adv. Mater.*, vol. 17, no. 22, pp. 2663–2670, 2005.
- [72] M. P. Mattson, R. C. Haddon, and a M. Rao, “Molecular functionalization of carbon nanotubes and use as substrates for neuronal growth,” *J. Mol. Neurosci.*, vol. 14, pp. 175–182, 2000.
- [73] V. Lovat *et al.*, “Carbon nanotube substrates boost neuronal electrical signaling,” *Nano Lett.*, vol. 5, no. 6, pp. 1107–1110, 2005.
- [74] M. A. Correa-Duarte, N. Wagner, J. Rojas-Chapana, C. Morscheck, M. Thie, and M. Giersig, “Fabrication and biocompatibility of carbon nanotube-based 3D networks as scaffolds for cell seeding and growth,” *Nano Lett.*, vol. 4, no. 11, pp. 2233–2236, 2004.
- [75] K. Wang, H. A. H. a Fishman, H. Dai, and J. S. J. S. Harris, “Neural stimulation with a carbon nanotube microelectrode array,” *Nano Lett.*, vol. 6, no. 9, pp. 2043–8, 2006.
- [76] Y. Lu *et al.*, “Electrodeposited polypyrrole/carbon nanotubes composite films electrodes for neural interfaces,” *Biomaterials*, vol. 31, no. 19, pp. 5169–5181, 2010.
- [77] S. Minnikanti, P. Skeath, and N. Peixoto, “Electrochemical characterization of multi-walled carbon nanotube coated electrodes for biological applications,” *Carbon N. Y.*, vol.

- 47, no. 3, pp. 884–893, Mar. 2009.
- [78] J. Wang, “Carbon-Nanotube Based Electrochemical Biosensors: A Review,” *Electroanalysis*, vol. 17, no. 1, pp. 7–14, 2005.
- [79] N. S. Lawrence, R. P. Deo, and J. Wang, “Comparison of the electrochemical reactivity of electrodes modified with carbon nanotubes from different sources,” *Electroanalysis*, vol. 17, no. 1, pp. 65–72, 2005.
- [80] E. W. Keefer, B. R. Botterman, M. I. Romero, A. F. Rossi, and G. W. Gross, “Carbon nanotube coating improves neuronal recordings,” *Nat. Nanotechnol.*, vol. 3, no. 7, pp. 434–9, Jul. 2008.
- [81] L. Bareket-Keren and Y. Hanein, “Carbon nanotube-based multi electrode arrays for neuronal interfacing: progress and prospects,” *Front. Neural Circuits*, vol. 6, no. January, p. 122, 2012.
- [82] X. Luo, C. L. Weaver, D. D. Zhou, R. Greenberg, and X. T. Cui, “Highly stable carbon nanotube doped poly(3,4-ethylenedioxythiophene) for chronic neural stimulation,” *Biomaterials*, vol. 32, no. 24, pp. 5551–5557, 2011.
- [83] N. W. S. Kam, Z. Liu, and H. Dai, “Carbon nanotubes as intracellular transporters for proteins and DNA: An investigation of the uptake mechanism and pathway,” *Angew. Chemie - Int. Ed.*, vol. 45, no. 4, pp. 577–581, 2006.
- [84] D. Pantarotto *et al.*, “Functionalized carbon nanotubes for plasmid DNA gene delivery,” *Angew. Chemie-International Ed.*, vol. 43, no. 39, pp. 5242–5246, 2004.
- [85] I. Yoon, K. Hamaguchi, I. V. Borzenets, G. Finkelstein, R. Mooney, and B. R. Donald, “Intracellular Neural Recording with Pure Carbon Nanotube Probes,” *PLoS One*, vol. 8, no. 6, pp. 6–11, 2013.
- [86] R. Singhal *et al.*, “Multifunctional carbon-nanotube cellular endoscopes,” *Nat. Nanotechnol.*, vol. 6, no. 1, pp. 57–64, Jan. 2011.
- [87] A. Patil, J. Sippel, G. W. Martin, and A. G. Rinzler, “Enhanced Functionality of Nanotube Atomic Force Microscopy Tips by Polymer Coating,” *Nano Lett.*, vol. 4, no. 2, pp. 303–308, Feb. 2004.
- [88] A. V Patil *et al.*, “Fabrication and characterization of polymer insulated carbon nanotube modified electrochemical nanopores,” *Nanoscale*, vol. 2, no. 5, pp. 734–8, May 2010.
- [89] D. Barrow, A. Patil, and A. G. Rinzler, “Investigation of Multi-Walled Carbon Nanotubes as Electrochemical Electrodes,” *Nano Lett.*, pp. 1–8, 2004.
- [90] T. Kawano, M. Ieee, C. Y. Cho, and L. Lin, “Carbon Nanotube-based Nanoprobe Electrode,” *Image (Rochester, N.Y.)*, pp. 895–898, 2007.
- [91] C. Pang, “Parylene Technology for Neural Probes Applications,” vol. 2008, 2008.
- [92] J. P. Seymour, Y. M. Elkasabi, H.-Y. Chen, J. Lahann, and D. R. Kipke, “The insulation performance of reactive parylene films in implantable electronic devices,” *Biomaterials*, vol. 30, no. 31, pp. 6158–67, Oct. 2009.

- [93] A. C. Charles and T. G. Hales, "Mechanisms of Spontaneous Calcium Oscillations and Action Potentials in Immortalized Hypothalamic (GT1-7) Neurons," *Journal of Neurophysiol.*, vol. 73, no. 1, pp. 56–64, 1995.
- [94] H. Park *et al.*, "High-density integration of carbon nanotubes via chemical self-assembly," *Nat. Nanotechnol.*, vol. 7, no. 12, pp. 787–791, 2012.
- [95] T. Nagasaka *et al.*, "Orientation of Carbon Nanotubes Using Electrophoresis," *J. Appl. Phys.*, vol. 35, pp. 917–918, 1996.
- [96] W. B. Choi *et al.*, "Electrophoresis deposition of carbon nanotubes for triode-type field emission display," *Appl. Phys. Lett.*, vol. 78, no. 11, pp. 1547–1549, 2001.
- [97] T. D. Yuzvinsky, a M. Fennimore, a Kis, and a Zettl, "Controlled placement of highly aligned carbon nanotubes for the manufacture of arrays of nanoscale torsional actuators," *Nanotechnology*, vol. 17, no. 2, pp. 434–438, Jan. 2006.
- [98] C. Kocabas, S. H. Hur, A. Gaur, M. A. Meitl, M. Shim, and J. A. Rogers, "Guided growth of large-scale, horizontally aligned arrays of single-walled carbon nanotubes and their use in thin-film transistors," *Small*, vol. 1, no. 11, pp. 1110–1116, 2005.
- [99] J. L. Xiao *et al.*, "Alignment Controlled Growth of Single-Walled Carbon Nanotubes on Quartz Substrates," *Nano Lett.*, vol. 9, no. 12, pp. 4311–4319, 2009.
- [100] L. Ding, D. Yuan, and J. Liu, "Growth of high-density parallel arrays of long single-walled carbon nanotubes on quartz substrates," *J. Am. Chem. Soc.*, vol. 130, no. 16, pp. 5428–5429, 2008.
- [101] D. Yuan, L. Ding, H. Chu, Y. Feng, T. P. McNicholas, and J. Liu, "Horizontally Aligned Single-Walled Carbon Nanotube on Quartz from a Large Variety of Metal Catalysts," *Nano Lett.*, vol. 8, no. 8, pp. 2576–2579, 2008.
- [102] N. Patil *et al.*, "Wafer-scale growth and transfer of aligned single-walled carbon nanotubes," *IEEE Trans. Nanotechnol.*, vol. 8, no. 4, pp. 498–504, 2009.
- [103] S. J. Kang *et al.*, "High Performance Electronics Based on Dense, Perfectly Aligned Arrays of Single Walled Carbon Nanotubes," *Nat. Nanotechnol.*, vol. 2, no. April, pp. 230–236, 2007.
- [104] J. D. Weiland, D. J. Anderson, C. C. Pogatchnik, and J. J. Boogaard, "Recessed Electrodes Formed by Laser Ablation of Parylene Coated, Micromachined Silicon Probes," vol. 2273, no. C, pp. 2273–2276, 1997.
- [105] a. Inaba, Y. Takei, T. Kan, K. Matsumoto, and I. Shimoyama, "Nanoprobe electrodes cut by physical stretch of Parylene-insulated carbon nanotube bridges," *2011 16th Int. Solid-State Sensors, Actuators Microsystems Conf.*, vol. 2, no. v, pp. 2586–2589, Jun. 2011.
- [106] K. M. Vaeth and K. F. Jensen, "Transition metals for selective chemical vapor deposition of parylene-based polymers," *Chem. Mater.*, vol. 12, no. 5, pp. 1305–1313, 2000.
- [107] J. W. Eaton and M. Qian, "Molecular bases of cellular iron toxicity" ¹Guest Editor: Mario Comporti ²This article is part of a series of reviews on 'Iron and Cellular Redox

- Status.’ The full list of papers may be found on the homepage of the journal.,” *Free Radic. Biol. Med.*, vol. 32, no. 9, pp. 833–840, 2002.
- [108] J. Zhang, T. Atay, and A. V Nurmikko, “Optical Detection of Brain Cell Activity Using Plasmonic Gold Nanoparticles 2009,” *Nano Lett.*, vol. 9, no. 2, pp. 1–6, 2009.
- [109] S. A. Maier, *Plasmonics: Fundamentals and Applications*. 2007.
- [110] X. Q. Wang, M. Wang, P. M. He, Y. B. Xu, and Z. H. Li, “Model calculation for the field enhancement factor of carbon nanotube,” *J. Appl. Phys.*, vol. 96, no. 11, pp. 6752–6755, 2004.
- [111] J. Y. Huang, K. Kempa, S. H. Jo, S. Chen, and Z. F. Ren, “Giant field enhancement at carbon nanotube tips induced by multistage effect,” *Appl. Phys. Lett.*, vol. 87, no. 5311, 2005.
- [112] E. Bailo and V. Deckert, “Tip-enhanced Raman scattering,” *Chem. Soc. Rev.*, vol. 37, no. 5, p. 921, 2008.
- [113] T. M. Day, P. R. Unwin, N. R. Wilson, and J. V. Macpherson, “Electrochemical templating of metal nanoparticles and nanowires on single-walled carbon nanotube networks,” *J. Am. Chem. Soc.*, vol. 127, no. 30, pp. 10639–10647, 2005.

Part III:

Boron Nitride Nanopores for DNA Sequencing

Chapter 6

Background: Boron Nitride Nanopores for DNA Sequencing

6.1 Overview

Here we discuss the application of nanopores engineered in hexagonal boron nitride (hBN) for solid-state nanopore DNA sequencing. In this chapter, we will briefly discuss DNA sequencing, specifically the development of biological and solid-state nanopore sequencing. Finally, we will discuss the promise of hBN nanopores and why they may very well represent the future of nanopore sequencing. In the following chapter, we will discuss the ongoing work we are doing towards realizing this. Critical to this effort, we have developed a means of fabricating an individual nanopore of atomically precise size, and the necessary equipment to measure the translocation of DNA across a nanopore.

6.2 DNA Sequencing

It is difficult to overstate the role DNA sequencing will play in the future of healthcare and scientific study. Readily available whole genome sequencing will allow for the identification of genetic diseases, as well as a genetically personalized approach to medicine [1], [2]. DNA sequencing is already being used to study anthropology, the migration of humans and their evolution [3]. It is also invaluable in the genetic modification and screening of crops and livestock. It is because of these wide-reaching consequences that there has been such an enormous interest in developing ever cheaper means of DNA sequencing, with the past two decades witnessing tremendous advances.

The traditional Sanger method of sequencing has been all but replaced by next-generation sequencing technology, capable of sequencing at a fraction of the time and cost. A range of commercial next-generation sequencing technology now exists, each competing to outdo one another on accuracy, speed and cost. But on the horizon, nanopore sequencing holds the potential to disrupt the entire field. Commercial nanopore devices are just now becoming available and are already competing with next-generation technologies on a number of fronts. It appears that by overcoming the remaining difficulties facing nanopore sequencing, it may rapidly begin to render them obsolete.

6.3 Nanopore Sequencing

The idea behind nanopore sequencing is straightforward: A nanopore channel separates two reservoirs filled with an ionic solution. When a bias is placed between the two reservoirs, an ionic current flows through the nanopore. Through electrophoretic forces, the ionic current drives the negatively charged DNA through the pore, as shown in Figure 6.1. As a strand of DNA passes through, it blocks the channel, causing a decrease in ionic current. As the molecular size of guanine, adenine, thymine and cytosine – the four nucleotide bases – differ slightly, each blocks the current to a different degree. By monitoring the current, one can then back out the sequence of a DNA chain as it passes through the pore [4].

Despite the simplicity of the technique, the promise of nanopore sequencing is significant. It requires no labelling or PCR amplification of DNA in order to sequence, reducing both the time and cost compared to current sequencing tools. While the read time for other cutting edge sequencing technologies is on the order of hours to days, nanopore sequencing can

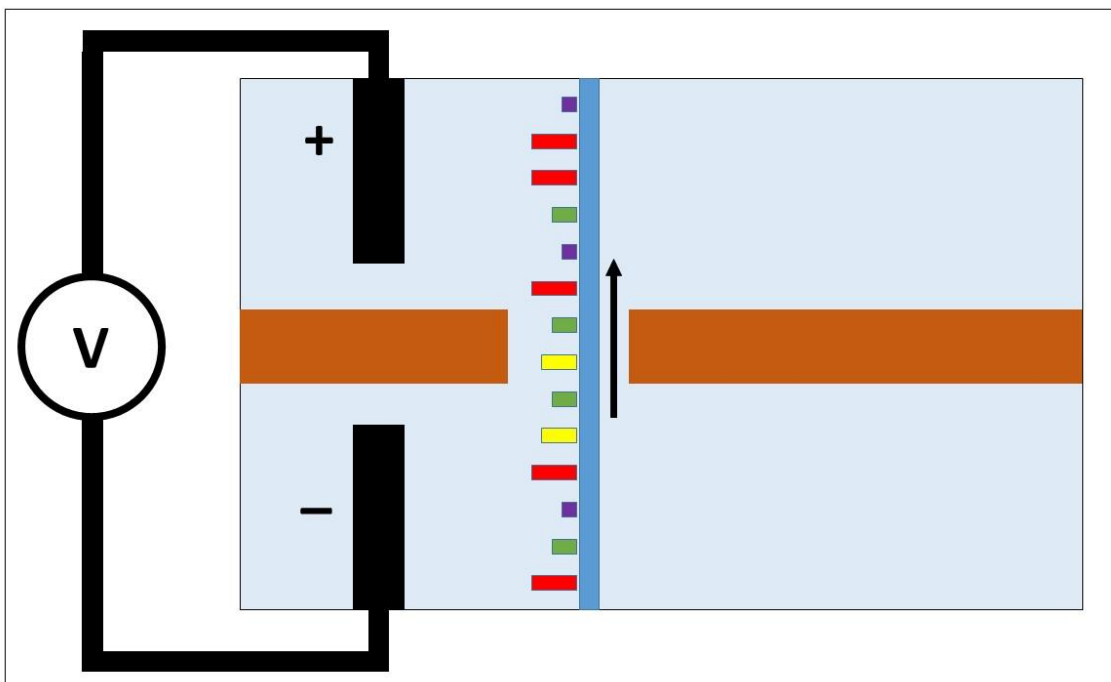


Figure 6.1: Schematic of DNA Nanopore Sequencing. A nanopore separates two reservoirs. A bias is applied between the two reservoirs which drives DNA through the pore. The nucleotides block the flow of current to varying degrees, allowing one to electronically read out the DNA sequence.

offer real-time readout. Nanopores also hold the potential for sequencing extremely long chains

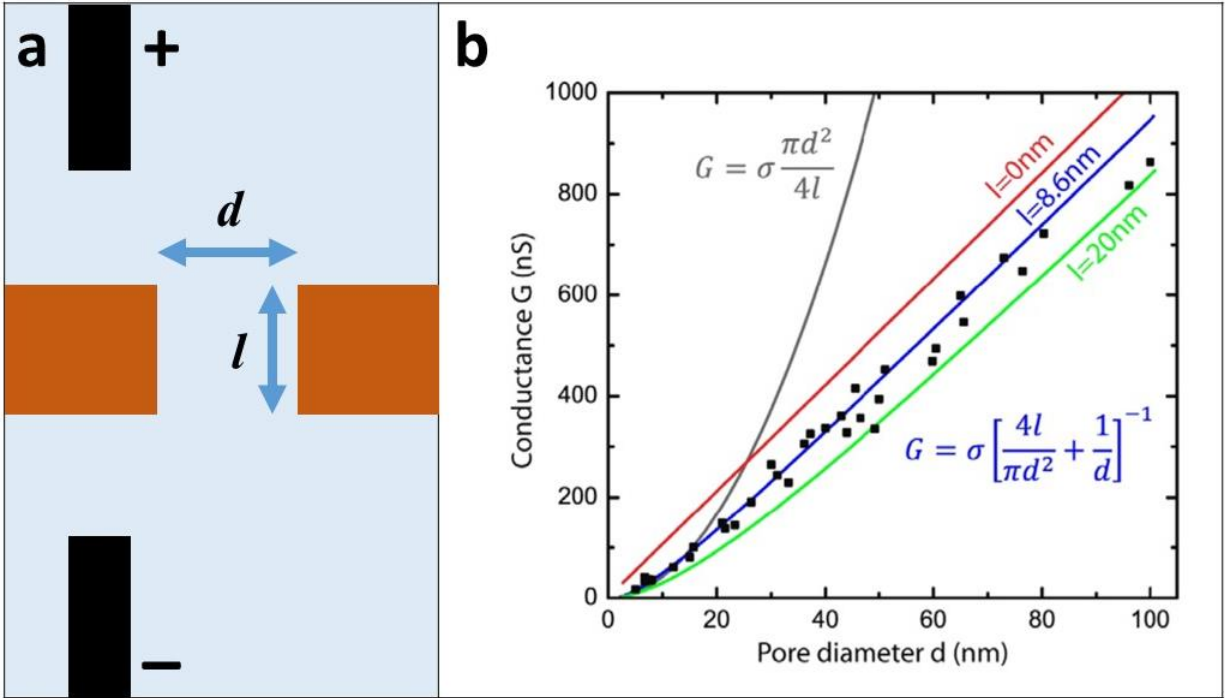


Figure 6.2: Nanopore conductance. a) A schematic of a nanopore, with pore width and length shown as d and l respectively. b) Plot of conductance as a function of pore diameter for different channel lengths. Black dots are experimental results for SiN nanopores. Adapted from Ref [5].

of DNA, whereas other techniques fragment larger strands into manageable lengths. This is particularly essential for whole genome sequencing, where the human genome is over 3 billion base pairs long, split amongst only 23 chromosomes. Finally, nanopore technology can be integrated into small units, allowing for desktop or even portable devices.

Before considering specific approaches to nanopore sequencing, we will explore the concept more generally. If two reservoirs of an electrolyte are separated by a narrow channel, this channel serves as an ionic equivalent of a resistor, reducing the ease at which charge carriers can pass from one reservoir to another. The conductance of the channel is given by:

$$G = \sigma \cdot \left[\frac{4l}{\pi d^2} + \frac{1}{d} \right]^{-1} \quad (1)$$

where σ is the bulk conductance of the solution, l is the length of the channel, and d is the diameter of the pore, as shown in Figure 6.2a. As can be seen in Figure 6.2b, this agrees well with experiment [5]. The bulk conductance of the solution is dependent on the electrolyte and its concentration, and at higher concentrations, the conductance scales linearly with salt concentration [6]. Typically, a 1M KCl electrolyte solution is used.

As DNA passes through the pore, it blocks the channel, effectively reducing the pore size. Therefore, for a DNA translocation event, the drop in conductance is given by:

$$\Delta G = \frac{\sigma A}{l} \quad (2)$$

where A is the hydrodynamic cross-section of the DNA molecule. For a double-strand of DNA the diameter is 2.2nm, the cross-sectional area is approximately 3.8nm^2 . Such a derivation is instructive in thinking about the dynamics of nanopore sequencing, but only holds for pore diameters significantly larger than the diameter of the DNA. At smaller pore diameters, which are typical for nanopore sequencing, interactions between the DNA and the sidewalls of the pore become important, as well as ionic confinement effects and double-layers [7].

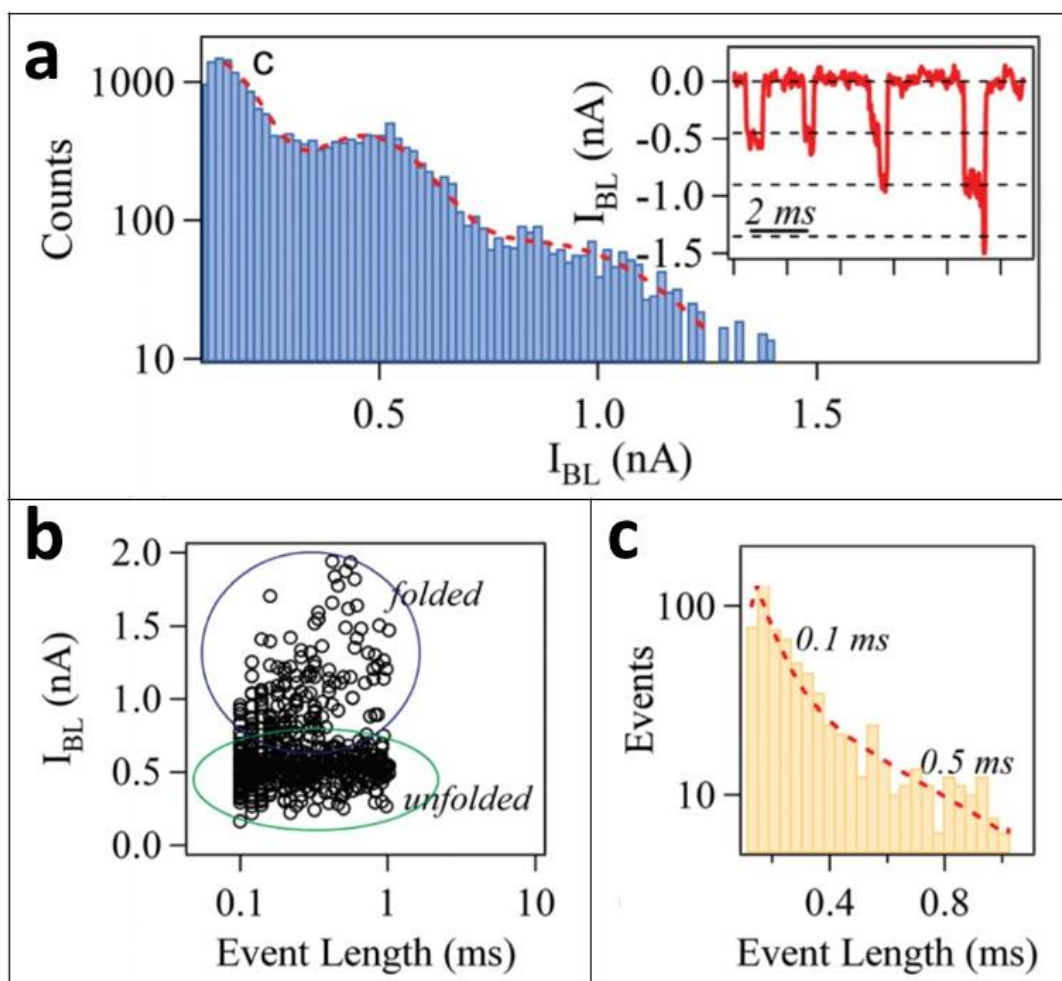


Figure 6.3: DNA folding. a) A histogram of current blockade amplitude for various DNA translocation events. Shows quantized peaks around 0.5 and 1.0 corresponding to unfolded and folded translocations. Inset shows example current traces from folded and unfolded events. b) Current blockade amplitude as a function of event length, separated into folded and unfolded events. c) Histogram of event lengths. Adapted from Ref [8]

As expected, if the DNA enters the pore folded, this will effectively double the change in pore conductance and in turn the blockage current. Figure 6.3 shows an examples of current traces from a dsDNA passing through a pore unfolded, folded over once, and folded over twice or more [8].

For single-strand DNA passing through the nanopore, the individual nucleotides have unique hydrodynamic cross-sectional areas. Modelling the blocking current of the individual nucleotides for small nanopores can be quite complex. The effects of the nanopore edge and the nucleotide end groups on the ionic charge carriers needs to be considered, as well as the double-layer and hydration shells of both. Figure 6.4 shows the sizes of the four nucleotide molecules as well as their regions of affinity or repulsion for K^+ and Cl^- [9].

The speed at which the DNA travels through the nanopore is critical as well. When solely driven by electrophoresis, translocation events of entire strands of DNA take place on the order of 1-10 μ s. In order to get the signal-to-noise ratios necessary to sequence individual bases, each nucleotide needs to spend \sim 100 μ s in the pore [4]. While it may be tempting to reduce the bias voltage to reduce the transport speed, the issue is actually more fundamental than this. Reducing the bias reduces the ion flux through the pore, reducing the signal. It is also beyond being an issue of improving sampling rate. The crux of the problem is that at the typical translocation speeds seen, during the time in which an individual nucleotide is in a pore, only around 100 ions

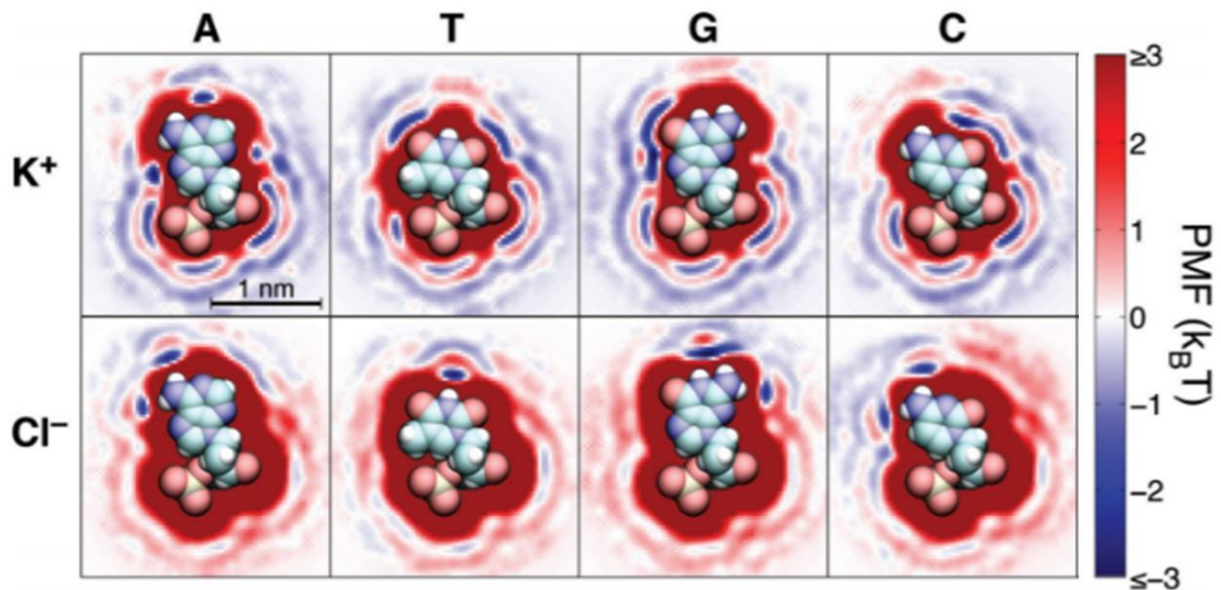


Figure 6.4: Hydrodynamic cross0section of nucleotide bases. Each of the four constituents of DNA are shown in each column, superimposed on a heat map of the relative attraction or repulsion of K^+ and Cl^- [9].

pass through the pore. As slowing the passage of DNA is an unavoidable hurdle, a number of manners of overcoming it have been explored, which we will discuss shortly.

6.4 Biological Nanopores

Nanopores are abundant in cellular biology. There are a variety of intramembrane proteins that allow for the passage of ionic currents or other cargo. Utilizing these naturally produced nanopores by immobilizing them on artificial lipid bilayers, biologists were first able to demonstrate the potential of nanopores for DNA sequencing.

Deamer and Branton et al. published a series of seminal papers using the biological nanopore protein α -hemolysin to detect DNA translocation events. Using long chains of single-nucleotide DNA, they further demonstrated that the blocking current for each of the four nucleotide bases were distinguishable [10]–[12]. The α -hemolysin nanopores used had diameters ranging from 1.4nm-2.8nm. More recently, mycobacterial porin (MspA), another pore forming intramembrane protein, has demonstrated improved performance due to the channels reduced effective length, as shown in Figure 6.5 [4], [13].

Next, researchers demonstrated that individual nucleotides could be distinguished. To do so, the DNA strand needed to be immobilized in the nanopore for long enough to generate an adequate signal-to-noise ratio. Either a hairpin at the terminal end of the DNA or a streptavidin-biotin complex were used to stop it from fully travelling through the pore [14]–[16]. This would leave a single DNA segment blocking the pore for an extended period of time. While a significant step towards demonstrating true sequencing, these results still relied on engineering

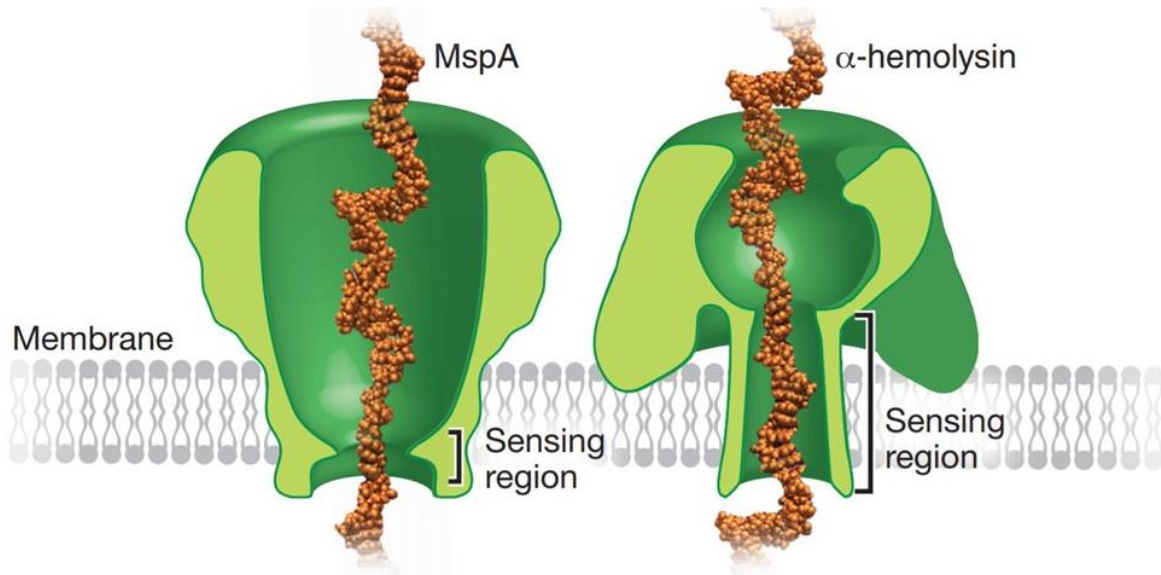


Figure 6.5: Difference between α -hemolysin and MspA. MspA has become the preferred nanopore protein to use due to its smaller sensing region. Adapted from Ref [4].

the DNA strand to slow it down enough to get a stable recording and was only reading a single nucleotide on the DNA chain.

The breakthrough that allowed for the first sequencing of DNA through a biopore was the incorporation of a polymerase, a protein involved in the duplication of DNA. Groups out of UC Santa Cruz and the University of Washington independently demonstrated single-base resolution sequencing using α -hemolysin and MspA pores respectively and phi29 DNA polymerase [17], [18]. The DNA double strand is passed through the nanopore by the polymerase at a controllable speed, slowing translocation to the point at which individual nucleotides may be read, as shown in Figure 6.6. This is a significant step on the way to realizing the full promise of biological nanopore sequencing.

These advances have led to additional progress in bioengineered nanopore sequencing devices, with a commercial device (MinION, Oxford Nanopore) recently released. Even in their infancy, these nanopores are capable of faster readouts than any other sequencing technology, are more mobile, and require no reagents. These devices have received considerable excitement and investment from the biopharmaceutical industry.

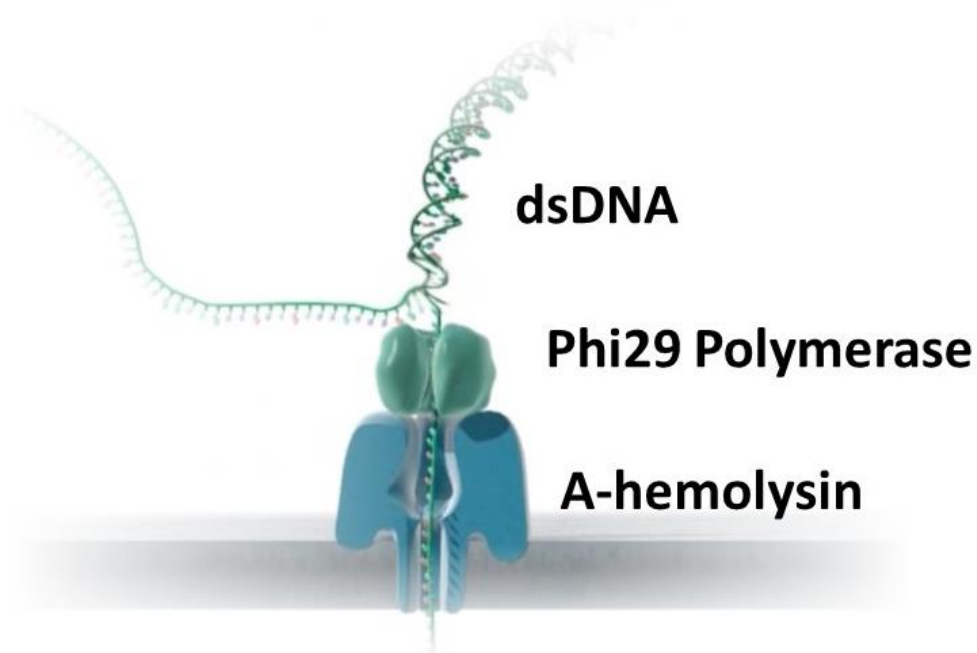


Figure 6.6: Phi29 DNA Polymerase for Nanopore Sequencing. The Phi29 polymerase unzips a double-strand of DNA and passes it through the nanopore. The rate of translocation depends on the concentration of ATP. Image courtesy of Oxford Nanopore.

However, biological nanopores are not without their disadvantages. Lipid bilayers and DNA polymerase are sensitive to pH, thermal and mechanical stresses, and a variety of chemistries, making device stability an issue. In addition to this, while the MspA channel length is only around 0.6nm, molecular dynamics (MD) simulations suggest that due to pore geometry, up to five nucleotides effect the blocking current [19]. This means current signals must be matched to multiplets of possible nucleotides, greatly complicating the sequencing operation, and reducing accuracy. Finally, the operation of DNA polymerase is a stochastic process. Small intervals between ratcheting to the next base can mean individual nucleotides can be missed, while large intervals between ratcheting can be confused as duplicate sequential nucleotides [4]. This is perhaps the most critical of the issues facing nanopore sequencing, as the current reported accuracy for the MinIon (96%) is well below that of other next-gen sequencing techniques (>99%). New methods of greatly reducing the speed of DNA translocation through a nanopore without sacrificing read accuracy are clearly needed.

6.5 Solid-State Nanopore Sequencing

Despite the successes of biological nanopores, the drawbacks mentioned above have driven continued interest in solid-state nanopores for DNA sequencing. In addition to their stability relative to biopores, solid-state nanopores have additional advantages. Established nanofabrication procedures could dramatically lower the cost of devices, and solid-state nanopores could be integrated with electronics or optics for secondary forms of readout. While challenges still remain which we will discuss shortly, the initial hurdle to solid-state nanopore sequencing was the fabrication of pores at the nanometer scale. A number of approaches have since been developed.

Golovchenko et al. demonstrated the first solid-state nanopore for DNA detection. In order to form the nanopore, they used a novel method of ion beam sculpting shown in Figure 6.7. The ions were incident on the top of a SiN membrane, while a sensitive ion detector was placed beneath the surface. By monitoring and detecting the moment that ions were able to pass through the membrane, they could terminate the etch as soon as it had formed a pore. With this method, they were able to form nanopores with diameters as small as 1.8nm [20].

Shortly thereafter, it was shown that a transmission electron microscope (TEM) beam could be focused to mill away SiN. This allowed one to monitor the progress of the milling by eye and terminate the process when the pore had reached its desired size [21]. This approach created even better pore size control than the Golovhenko technique described above.

Dekker et al. demonstrated a new method of pore formation, using SiO₂. First, a pore was formed by standard electron beam lithography and etching techniques, creating a larger nanopore (10-20nm). It was then found that under high-intensity electron beam irradiation under the TEM, smaller nanopores (less than the thickness of the SiO₂ film) would shrink, allowing them to tune the size of the pore precisely while imaging [22]. Additional methods of pore formation are continually being explored [23]–[26]. A method of controlled dielectric breakdown of the SiN

membrane has been developed which allows for an ionic feedback to terminate the process when the nanopore has formed [27].

In addition to the relative stability of solid-state nanopores compared to biological nanopores, solid-state nanopores can better incorporate additional forms of readout. This second source of readout can provide a secondary signal improving the read accuracy, or it can be used to better identify clogging or stalled DNA translation. A number of different modes of readout have been proposed or realized. A variety of transistor-based schemes that rely on the DNA to gate a transistor, locally modulating the charge carrier density, have been demonstrated [28]–[30]. Figure 6.8 shows a graphene nanoribbon transistor with an incorporated nanopore [29]. Tunneling-based schemes have also been suggested, in which DNA passing between a narrow gap between two electrodes modulates the tunneling current between them [31], [32]. In addition to transistor-based mechanisms, optical readouts incorporating plasmonics have also been proposed [33]–[35].

Despite the successes of early solid-state nanopores, they are still not competing with biopores in performance. The biggest unaddressed issue was that the translocation speed

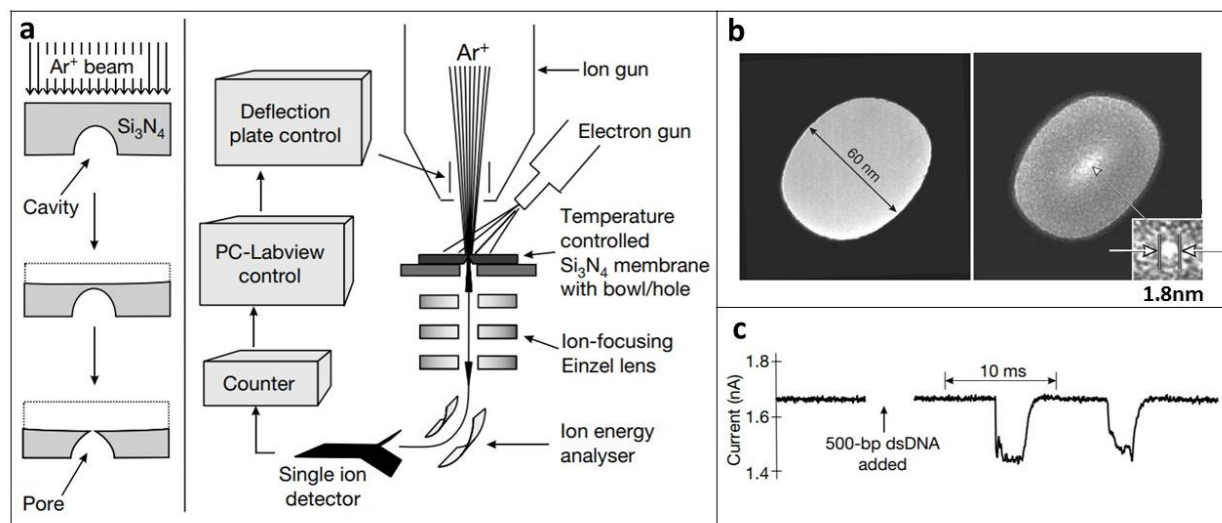


Figure 6.7: Golevchenko et al.'s nanopore fabrication. a) Schematic of ion milling process. SiN is milled away by focused ion beam (FIB), with an ion detector behind the membrane. As soon as the SiN is breached, the ion beam can be turned off. b) TEM of example pore. Left side is before ion milling, right is after. Inset shows a 1.8nm pore produced by this means. c) Current blockades produced by dsDNA translocation events [20].

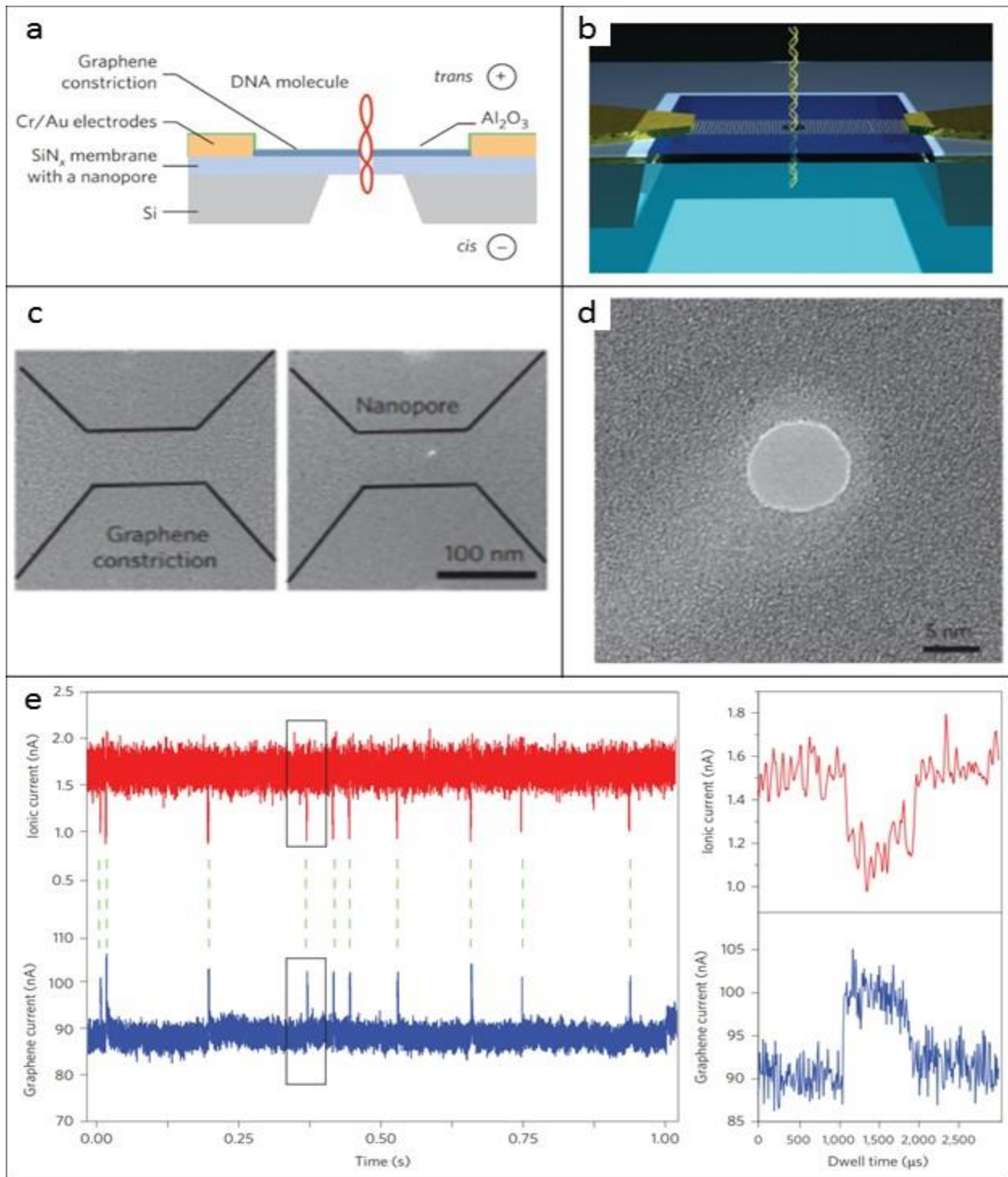


Figure 6.8: Co-detection with graphene nanoribbon transistor. a) Schematic of design. b) Cartoon of DNA translocation through GNR transistor. c) TEM image of nanopore in graphene constriction. d) TEM close-up of produced nanopore. e) Readouts of ionic current blockades (red) and GNR current (blue) shows translocation events recorded by both modalities. The right side shows zoom in on individual translocation event [29].

discussed above has yet to be sufficiently addressed for solid-state nanopores. As integrating polymerase is not a straightforward option and would suffer the same issues with stochastic ratcheting as discussed above, other means of slowing DNA translocation became necessary. Progress has been made in this front [35]–[38]. For starters, as shown in Figure 6.9, the size of the pore does effect the translocation speed, with smaller pore sizes lowering the speed [39]. In addition to this, Wanunu et al found that by using different electrolyte solutions on either reservoir, an osmotic current force could be used to actually slow the translocation [36], [40], [41]. Despite these successes, to date no one has been able to demonstrate a slow enough translocation speed to facilitate individual nucleotide sequencing.

Finally, the early solid-state nanopore channels were long compared to biopores. Nitride membranes thinner than 5nm become increasingly unstable and difficult to suspend over any appreciable length. Growth of even thinner membranes is plagued by non-uniformity and pinhole defects. This however, was an area where solid-state nanopores could eventually surpass biopores. By switching from conventional nitride and oxide membranes to 2D materials, capable of channel lengths of single-atoms, the channel length could be reduced to its logical minimum. While biopores are reliant on a quartet library of often times extremely similar blocking currents, sufficiently thin solid-state nanopores could be sensitive to individual nucleotides and thus improve accuracy.

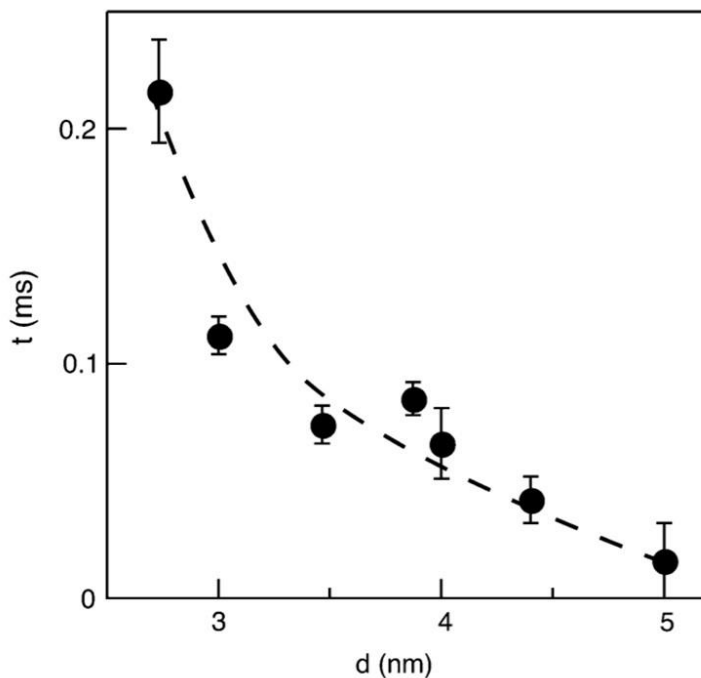


Figure 6.9: Nanopore size dependence of DNA translocation speed. A plot of average translocation time for various nanopore diameters. Translocation time increases as the nanopore diameter approaches the size of the DNA.

6.5.1 2D Materials for Nanopore Sequencing

Graphene was the first 2D material to be used for nanopore sequencing. Golovchenko, Dekker and Drndic et al. independently demonstrated DNA translocation through graphene nanopores [8], [42], [43]. In each case, the graphene nanopore was formed through condensing a transmission electron microscope's electron beam to a point, and milling away material.

Other methods of graphene nanopore fabrication have since been developed, but milling with a condensed TEM beam is still most commonly employed. Using a similar method as the dielectric breakdown approach employed for SiN nanopores, Golovchenko et al. demonstrated that voltage pulses could be used to generate nanopores in graphene. The graphene membrane separated two ionic solutions with Ag/AgCl electrodes in both. The electrodes would be used to introduce 5-7V spikes and monitor the current between the two reservoirs[44]. Beyond this, groups have demonstrated that focused ion beams and helium ion beams can be used to generate sub-5nm nanopores [45], [46]. While these results and the control over pore size they offer is impressive, none of them have demonstrated atomic-scale control over the pore forming process.

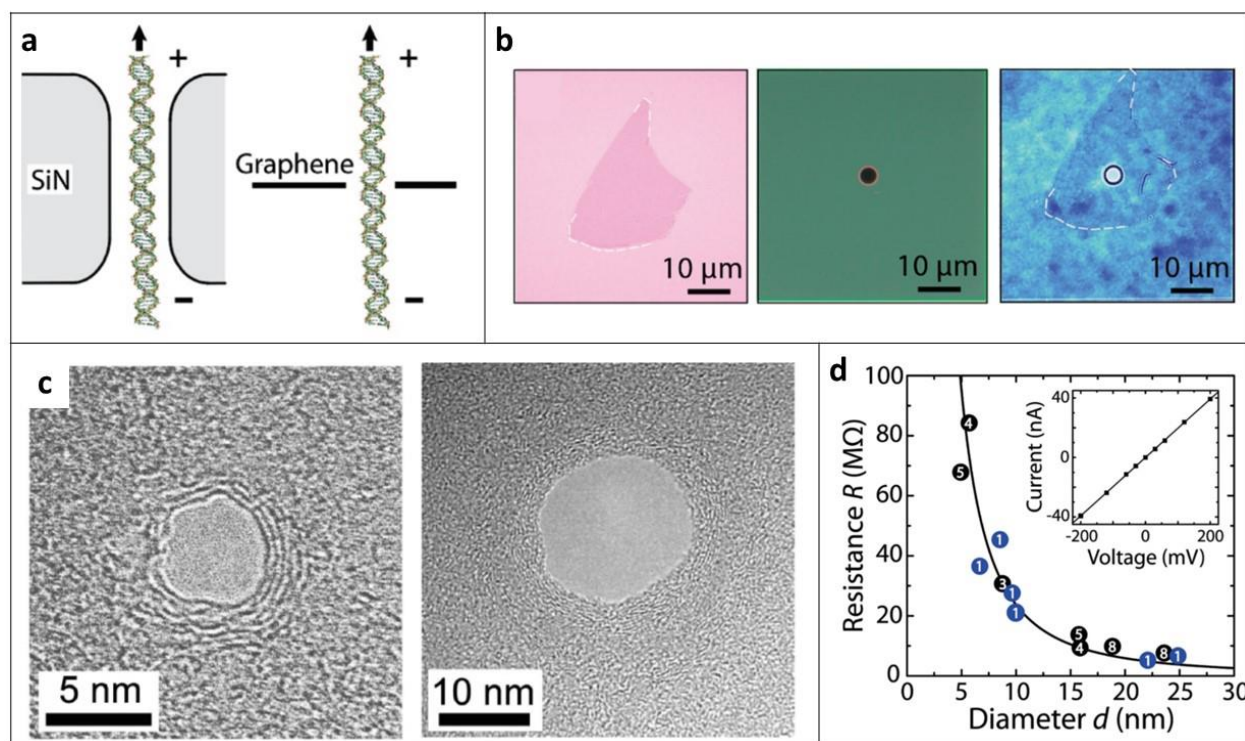


Figure 6.10: Graphene Nanopores. a) To scale schematic comparing a typical SiN device to graphene device. Note the number of nucleotides present in the nanopore channel for SiN versus graphene. b) Optical images of graphene transfer process. Exfoliated graphite flake was transferred on top of a SiN micropore. c) TEM images of two different sized nanopores. Image on left is a hole in multilayer graphene, while the image on the right is single layer. d) Pore impedance as a function of pore diameter. Inset shows a sample IV trace. Adapted from Ref [42].

One difficulty in working with graphene instead of SiN is the hydrophobicity of the material. Hydrophobic interactions will cause DNA to bind to the surface and interfere with sensing as the strand will interact with the substrate material as it passes through the pore. This can cause unreliable recordings, as well as nanopores that quickly clog and become unusable. It can also make it difficult to wet the nanopore chips, and air bubbles will easily block the nanopore. For this reason, a number of surface treatment methods have been developed to improve the hydrophilicity. The most straightforward is an oxygen plasma. While many groups have done so, graphene is very sensitive to oxygen plasma, and it is unclear what this is doing to the size and shape of the original pore as well as whether it is creating more pores in the process. Other groups have found an atomic layer deposition (ALD) coating of TiO₂ improves hydrophilicity, but this does so at the expense of increasing the nanopore's channel length [8]. More recently, Dekker et al. demonstrated that a self-assembled monolayer (SAM) of pyrene ethylene glycol will pi-pi stack on the graphene, rendering it hydrophilic [42]. While the increase in channel length is less than that which is achieved with ALD, for DNA sequencing the effect is still not negligible. As we shall discuss later, hBN offers a clearer route towards rendering the substrate hydrophilic.

While the majority of work performed to date has been with graphene, other 2D materials have begun to be explored. Radenovic et al. developed MoS₂ nanopores using similar TEM milling as was used for graphene. Unlike the graphene nanopores, no special surface treatment was needed to render the material hydrophilic. In addition to this, it was argued that the MoS₂ may make a better probe for secondary transverse conductance measurements [47]. Drndic et al. demonstrated that WS₂ nanopores grow under laser illumination allowing for precise pore size control. They also suggest that the unique optical properties of the transition metal dichalcogenides could be exploited as a means of additional readout [48].

6.5.2 hBN for Nanopore Sequencing

There are a number of qualities of hBN that may make it an ideal 2D material for nanopore sequencing. Perhaps the most significant is the manner in which pores form in hBN under electron beam irradiation. Triangular vacancies grow in a quantized manner, yielding metastable triangular pores [49]. This allows us to tune the size of the nanopore with atomic precision. In addition to this, as an insulator, hBN is less subject to the capacitive noise effects that plague graphene solid-state nanopores and wouldn't require further passivation. Also due to it being an insulator, hBN nanopores could be integrated with additional electronics, allowing for multimodal sensing. Finally, hBN is extremely inert and even stable under light oxygen plasma, allowing for a clear method of making the substrate hydrophobic without damaging or altering the nanopore, and making cleaning the pores significantly easier.

Using the same condensed beam milling method which was used for graphene, Liu et al. and Zhou et al. independently measured DNA translocation events across an hBN pore [50], [51]. Liu went on to demonstrate that the hBN hydrophilicity can be improved in a straightforward manner. Unlike graphene, hBN is resistant to oxidation and can withstand a light

oxygen plasma, improving hydrophilicity without increasing the diameter of the nanopore channel. However, by utilizing the traditional TEM milling techniques, they have failed to take advantage of the metastable quantized growth of nanopore defects with regular geometries.

The defect formation and growth of hBN under electron beam irradiation has been studied in depth by our group and others. Due to the preferential ejection of boron, attributed either to electron knock-on effects or selective chemical etching by atomic species present in the TEM, metastable nitrogen terminated zig-zag edges form and preserve a triangular shape under the electron beam. As these undercoordinated nitrogen atoms are ejected, a new nitrogen zig-zag edge is exposed allowing for the precise quantized growth of the triangle defects [49]. By taking advantage of this quantized pore growth, we are now capable of creating nanopores with atomic precision. Figure 6.11 shows this quantized growth process for an individual nanopore. As shown in Figure 6.12, the triangular nanopore's edge length would need to be between 1.75nm and 2.5nm, or $N=7-9$ for ssDNA to just narrowly fit through the pore, depending on the ability of the DNA's hydration shell to rearrange as well as interactions with the nanopore edge.

Atomic precision in nanopore size would confer a number of benefits in sequencing. The strength of the ionic blocking signal depends on how much of the pore is being blocked by the DNA. Comer et al. have theoretically surmised that for an ultra-small nanopore – 1.6x1.1nm – the change in blockage current for different nucleotide bases could be as high as 25% [9]. As has been seen with small graphene nanopores (~3nm), nanopores closing in on the size of the polymer they are trying to detect see unusually high sensitivities to changes in the polymer shape [7]. The work done with graphene has still been with imprecise pore size and geometry, whereas hBN nanopores have the potential to demonstrate even higher sensitivities. In addition to this, the spatial confinement and geometry of a triangular hBN nanopore may act to slow down the DNA translocation. As discussed previously, at sizes close to the cross section of the DNA, translocation speeds rapidly decrease. In terms of geometric effects, while DNA has been modeled as a cylinder for much of the work described above, in a triangular nanopore of precisely tuned size, the helical DNA would need to corkscrew in order to fit through the pore. As emphasized earlier, the primary hurdle standing in the way of solid-state nanopore sequencing is the speed of translocation, so any possibility of slowing it represents a major potential opportunity.

While we have primarily considered triangular hBN nanopores, previous work from our lab has demonstrated alternative pore geometries. Pham et al. demonstrated that at higher temperatures (>700°C) parallelogram and hexagon-shaped defects begin to form. Interestingly, these are no longer solely nitrogen terminated as is the case for the triangular defects. Instead, some facets will be boron-terminated, while others will remain nitrogen terminated, as shown in Figure 6.13 [52]. As the boron-terminated end-groups are more reactive, this presents an interesting approach for selective functionalization along the pore edges.

In addition to the benefits of precise pore size control, hBN may also be a useful nanopore substrate simply because it is insulating. Electronics or other elements can be patterned on top of the hBN to allow for multimode detection schemes like those described above. In addition to those already discussed, theorists have recently proposed that a nanopore in a

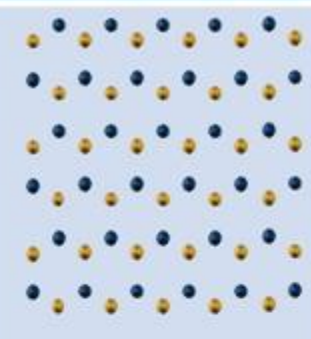
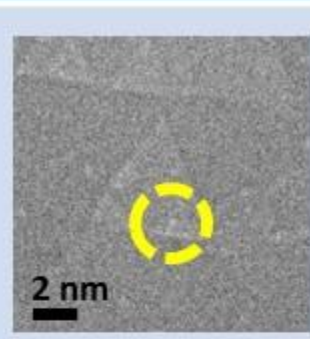
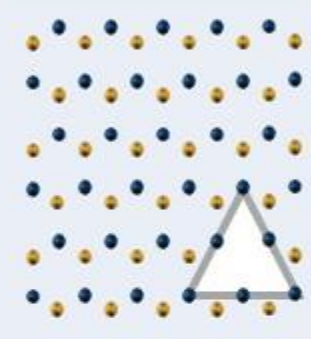

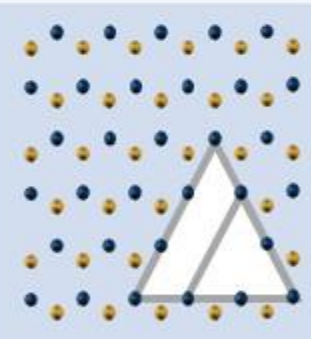
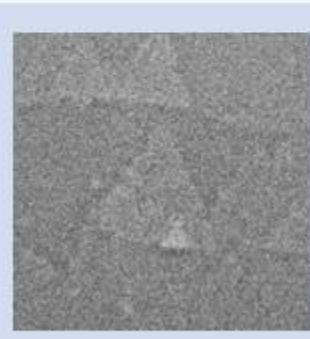
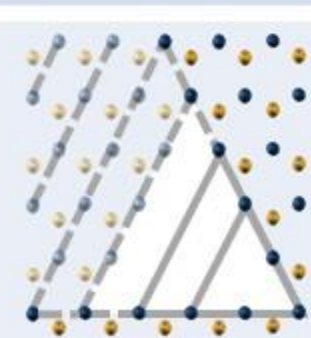
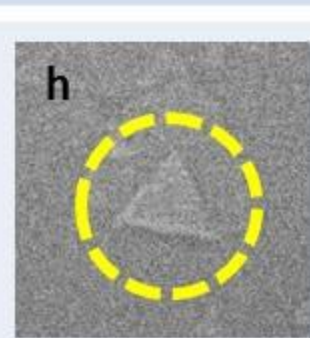
| Index | Schematic | TEM Image | Pore Area |
|-------|---|---|--|
| N = 0 |  |  | $A = 0$ |
| N = 1 |  |  | $A = (2a_o)^2 \frac{3\sqrt{3}}{4}$ $= 0.11nm^2$ |
| N = 2 |  |  | $A = (3a_o)^2 \frac{3\sqrt{3}}{4}$ $= 0.25nm^2$ |
| N = n |  |  | $A = ((n + 1)a_o)^2 \frac{\sqrt{3}}{4}$ $= (n + 1)^2 * 0.027nm^2$ |

Figure 6.11: hBN metastable quantized pore growth. For each quantized value, a schematic as well as a representative TEM image are shown. The pore area is then calculated on the right.

graphene/hBN/graphene sandwich may serve as a particularly sensitive nanopore detection device. The two graphene layers would be separated by the hBN, and the translocation of DNA would enhance the transmission through the hBN by quantum interference [53].

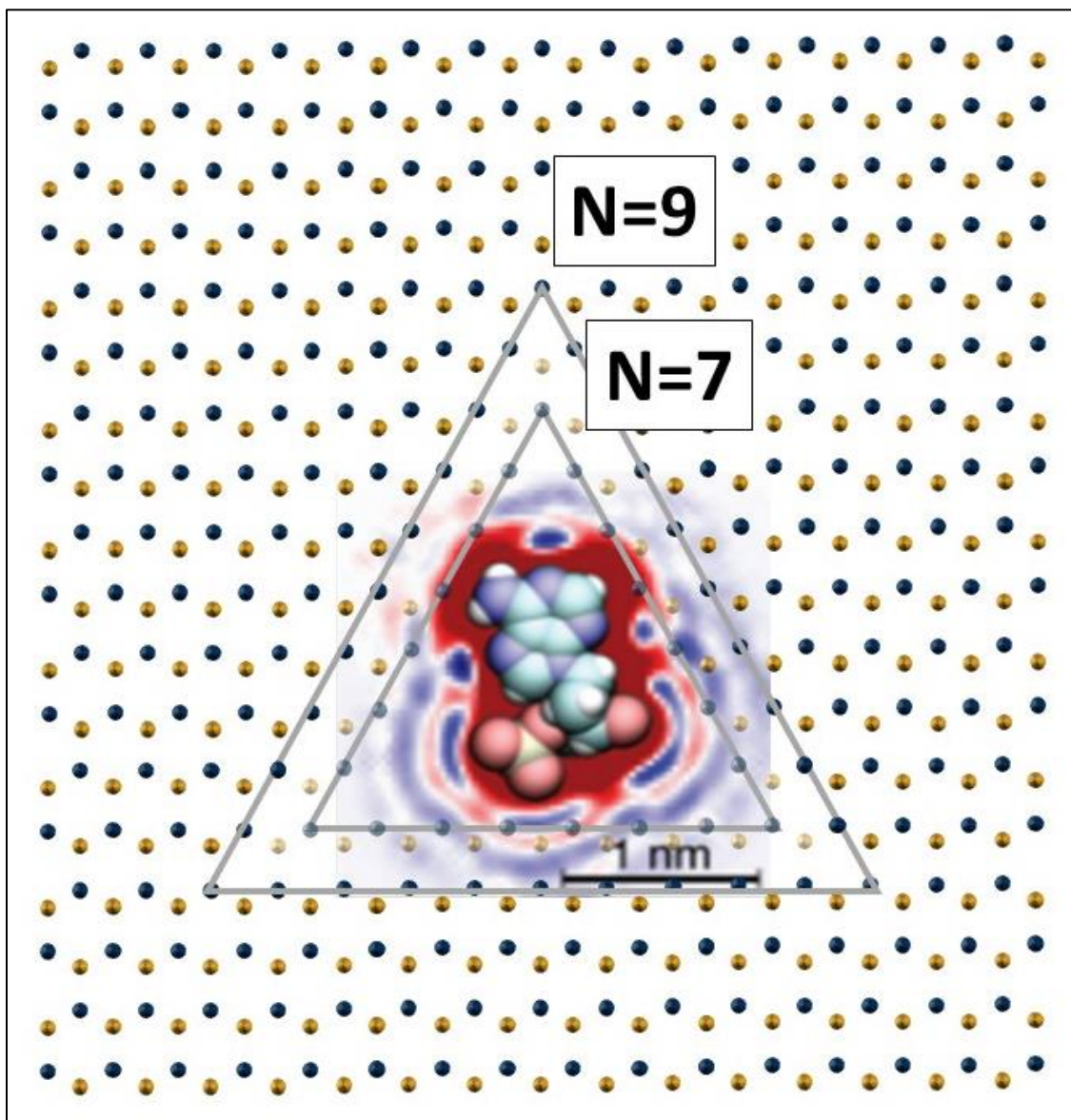


Figure 6.12: Ultraprecise nanopores for nucleotide confinement. The molecule shown inside the BN nanopore is adenosine triphosphate. The inner triangular pore is an $N=7$ pore, while the outer is $N=10$. The reason for the range of pore sizes is it is unclear what role the hydration shell of the molecule, as well as interactions with the Nitrogen terminated end groups, will play. A formal Molecular Dynamics (MD) simulation will be necessary to determine the proper pore size. As in Figure 6.11, Boron is shown in yellow, and nitrogen in blue.

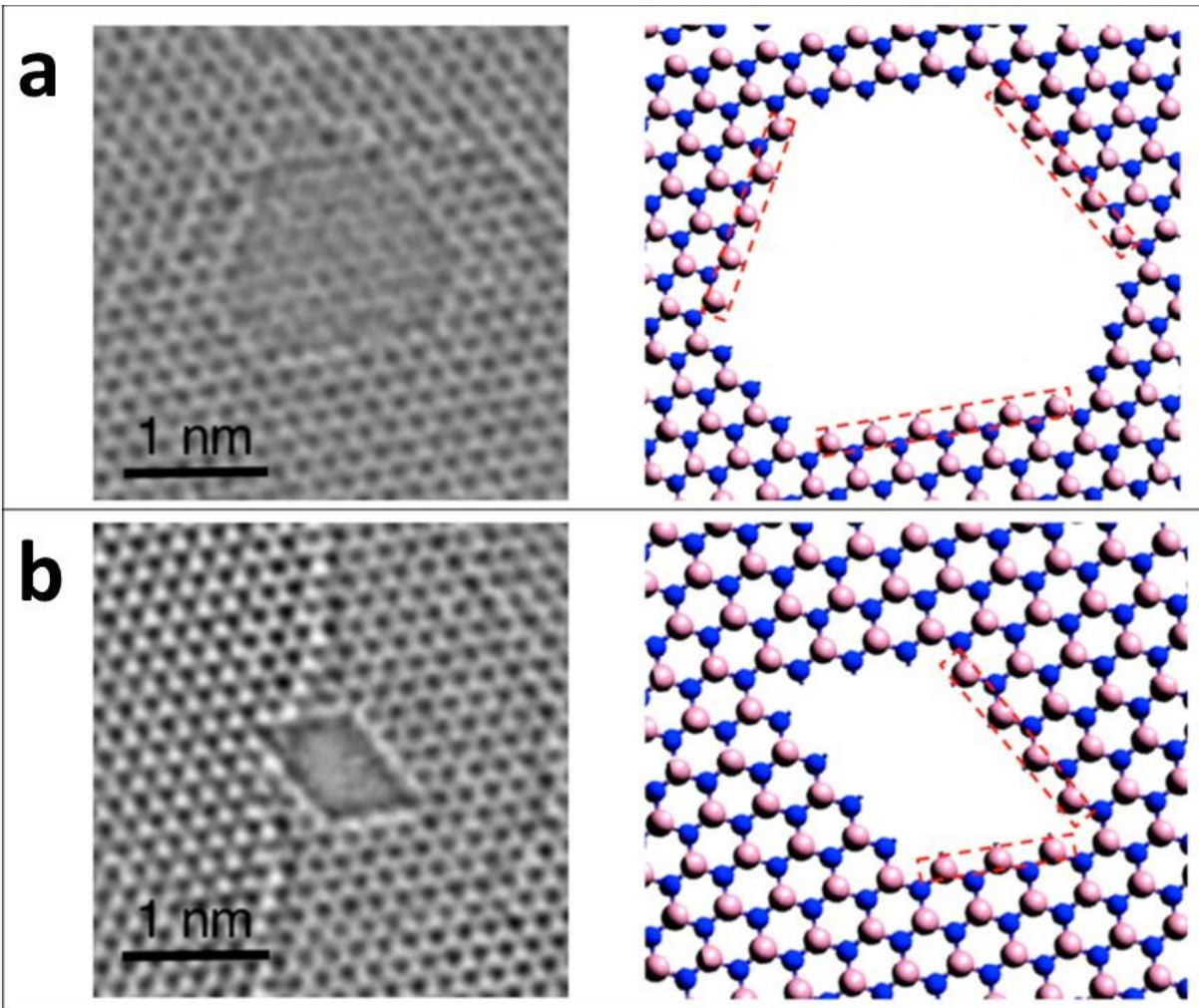


Figure 6.13: HRTEM images of hexagonal and parallelogram-shaped defects at 900°C. In model on the right, boron atoms are represented in pink and nitrogen in blue. Adapted from [52]

6.5.3 Edge Functionalization

The chemical functionalities of the nanopore edge-groups can greatly influence DNA sequencing. Interactions with the edge-plane can cause the DNA to stochastically bind to the pore, stalling sequencing, or coulombic forces can slow the translocation of the negatively charged DNA. Additionally, the charge density distribution inside the nanopore can aid orienting the DNA strand as it passes through. This can help limit fluctuations in the ionic blocking current due to differing DNA orientations. The charge density along the nanopore edge will not only influence interactions with DNA, but also ion transport. As we move to atomically precise nanopores, these effects become more pronounced. As such, it is important that we consider the edge functionalization when evaluating hBN nanopores for DNA sequencing.

There has been limited research on the effect of edge-group functionalization on graphene nanopores for DNA translocation, however, much of this has been focused on the effect on transverse tunneling measurements. In this case, a graphene gap is considered, and DNA passing between the two sides of the gap would create or alter a tunneling current between the two electrodes. In this case, hydrogen and nitrogen functionalization has been theoretically explored as a means of increasing tunneling response [54].

As discussed previously, the edge-termination of triangular defects from electron beam irradiated hBN is consistently nitrogen terminated. While these nitrogen terminated end-groups will provide a coulombic attraction/repulsion as we will discuss, they should be inert, limiting binding interactions with the passing DNA strand. This is critical in that binding events with translocating ssDNA would cause stalling and introduce artifacts into the sequencing.

Based on Density Functional Theory (DFT) calculations, the simulated charge density of a small nitrogen terminated nanopore is shown in Figures 6.14(a)-(b). As would be expected given the iconicity of the Nitrogen in the BN covalent bonds, the nitrogen edge-groups carry a negative charge. These DFT calculations also predict that the repulsive forces between these nitrogen terminations allows the N-N bonding seen at the vertex [55]. While it may be expected that for DNA sequencing, this negative charge will exert a repulsive force on the negatively

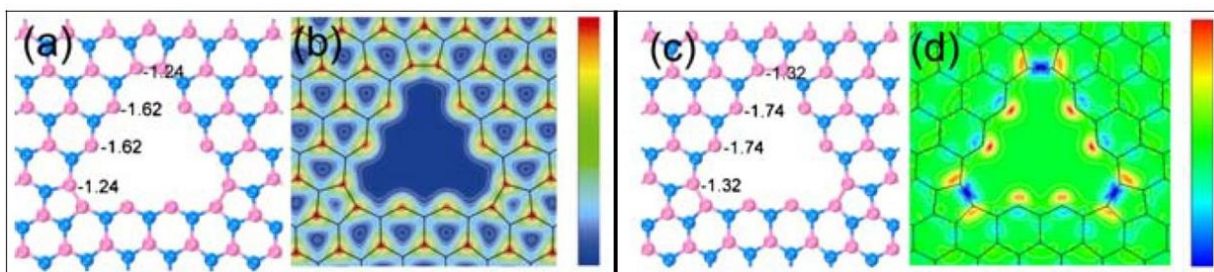


Figure 6.14: N-terminated nanopore edge-charges – DFT simulation. a) Charge population of a 4 unit wide nitrogen terminated nanopore. b) Charge density map of nanopore. c) Charge population of same nanopore negatively charged by $2e^-$. d) Difference in charge density from (b) when nanopore is negatively charged ($2e^-$). Adapted from Ref [55].

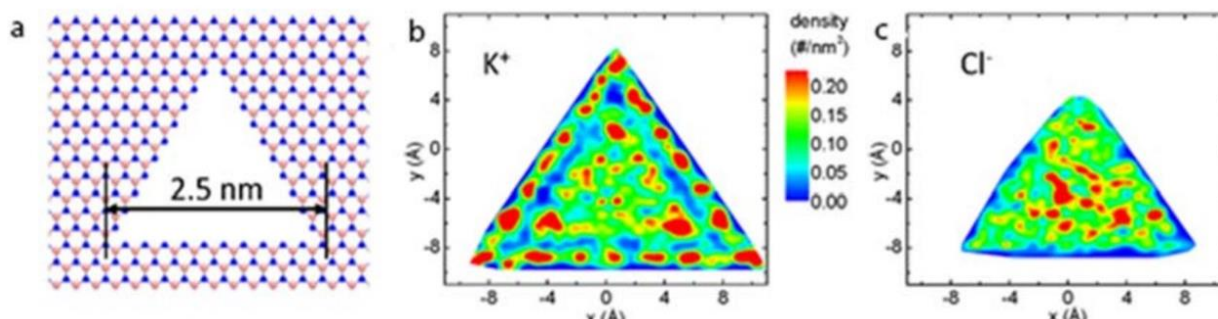


Figure 6.15: Ion concentrations – MD simulations. a) N-terminated nanopore used for MD simulation. b) Ion density map for K^+ . c) Ion density map for Cl^- . Cl^- is confined to a smaller region due to the negatively charged nitrogen endgroups. Adapted from Ref [56]

charged DNA backbone, thus increasing the translocation speed, this may not necessarily be the case. The negatively charged end-groups will attract positively charged potassium ions, which will agglomerate around the pore. Figure 6.15 shows an MD simulation of the ion concentrations inside of a nanopore. Note that the charge density for Cl^- ions is significantly smaller [56]. This suggests that the negatively charged DNA will be similarly confined, and will likely be slowed by interactions with the K^+ ions surrounding the nitrogen end-groups.

In addition to this, the triangular nature of the nanopore and charge densities will affect the conformation of the DNA as it passes through the nanopore. This should serve two purposes in sequencing: As discussed earlier, due to the triangular nature of the nanopore and the accompanying charge density, the DNA will have preferred conformations which will require it to corkscrew as it translocates, slowing the translocation speed; Second, the consistent conformation will decrease noise associated with geometrical effects of the ionic current. As shown earlier, the local charge distribution of the DNA nucleotides themselves will affect passage of ions near the molecule, an effect that is of particular importance for very small nanopores. The local charge densities of the nanopore edge will have a similar effect.

If the hBN substrate holds additional charge, this will change these charge densities, as shown in Figure 6.14(c). When the nitrogen terminated pore is negatively charged, this additional charge has an outsized impact on the charge density in the nanopore. Figure 6.14(d) shows a heatmap of the difference in charge densities from the uncharged nanopore. This charge can be controlled by a gate electrode, something that may become important were we to consider hybridized devices. It is also predicted that a gate field could be used during the nanopore creation process to favor Boron-terminated edges over the typical nitrogen termination.

As was discussed previously, in addition to the nitrogen terminated triangular hBN defects, we are capable of producing additional geometries at higher temperatures or beam currents. These pores have been shown to have alternating boron and nitrogen terminated pore edges. While the nitrogen are expected to be inert, the boron can be additionally functionalized. As expected, the B-terminated edges would be positively charged, as shown in Figure 6.16.

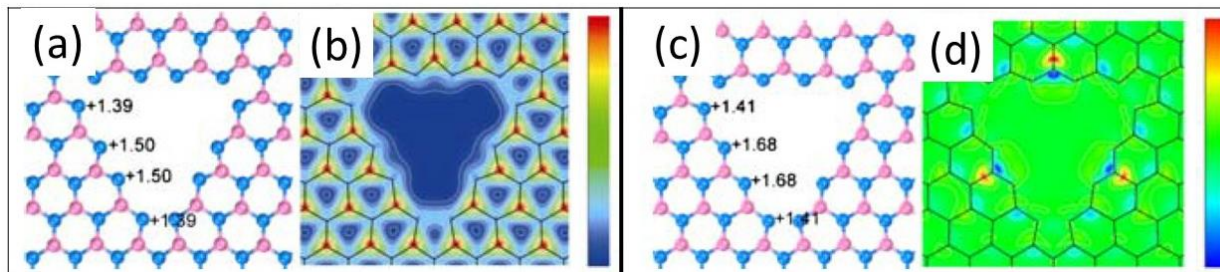


Figure 6.16: B-terminated hBN nanopore edge-charges – DFT simulation. a) Charge population of a 4 unit wide nitrogen terminated nanopore. b) Charge density map of nanopore. c) Charge population of same nanopore negatively charged by $2e^-$. d) Difference in charge density from (b) when nanopore is negatively charged ($2e^-$). Adapted from Ref [55].

Chapter 7

Experimental: Boron Nitride Nanopores for DNA Sequencing

7.1 Overview

The experimental work in this project can be split into two parts: the nanoscale pore fabrication, and the macroscopic experimental design. The nanopore fabrication was guided by previous work on defect formation in hBN under electron beam irradiation. The major outstanding challenge was how to controllably form an isolated nanopore in a specific region. While the defect formation we had seen previously was somewhat random and diffuse, causing defects to nucleate and grow over the entire irradiated area, we have shown that by controlling beam conditions, this process could be controlled.

The macroscopic experimental details were guided by the work of other solid-state nanopore experiments utilizing 2D materials. The body of research on solid-state nanopores is comprehensive. Nanopore experiments require a fluidic chuck which contains two reservoirs separated by the nanopore channel. This chuck needs to take trapped air bubbles into consideration, and needs to have an access point for electrodes. Towards this purpose, we adapted designs found in the literature for our specific TEM grid size. Beyond the chuck, the electrodes and electronic readout needed to be addressed. We found these to be increasingly standardized across nanopore research groups.

This work was done in collaboration with graduate student Matt Gilbert, who performed the BN nanopore fabrication with assistance from graduate students Thang Pham, Brian Shevitski, and postdoctoral researcher Amin Azizi. Graduate students Ashley Gibb and Thang Pham previously performed much of the work surrounding the geometric growth of BN defects. The macroscopic experimental details were guided by myself and undergraduates Jonathan Adam Jackson and Samuel Johnson, and will be continued by Matt Gilbert.

7.2 Pore Fabrication

Pore fabrication was one of the first major challenges faced in this project. While work out of our lab has demonstrated the growth of triangular defects in hBN under electron beam irradiation, this was done under a diffuse beam in which defects formed at random across the entire illuminated area, as shown in Figure 7.1. Trying to instead isolate a single pore proved considerably more difficult. By limiting the area in which a monolayer of hBN was suspended, and developing a novel process for single-pore formation by carefully tailoring beam conditions, we were able to do just that [57].

As a first step in limiting the area over which hBN is supported, we start by milling a small hole in a commercial SiN TEM chip. The chip is loaded into the TEM where the beam is condensed and left to mill away material. Using this method, we were able to get SiN pores as small as 6nm in diameter, but more typically around 20nm. Multi-layer hBN was then transferred on top of the SiN pore. Both CVD grown and exfoliated hBN were used. In the case of CVD grown, the hBN is grown on a copper foil in a tube furnace (see Ref. [57] for recipe details). PMMA is then spun onto the topside of the copper foil, and the hBN on the backside is etched in an extended oxygen plasma. The Cu foil is then etched in a sodium persulfate bath, leaving the PMMA covered hBN floating on the top. This is then transferred to a water bath, where it is scooped onto the TEM grid. In the case of the exfoliated hBN, hBN is exfoliated by the standard scotch tape method [58] and transferred to a SiO₂ substrate. Sufficiently thin regions are

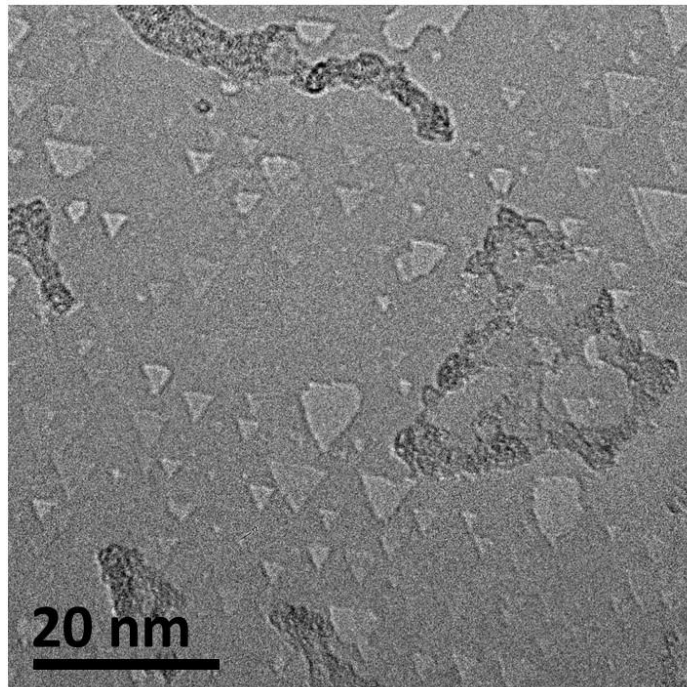


Figure 7.1: TEM image of hBN defects introduced with a diffuse beam. While the geometries are highly regular, pores are introduced at random throughout the entire exposed area.

identified by optical microscope. These flakes can then be transferred and positioned over the SiN pore.

As shown schematically in Figure 7.2, by careful control of beam intensity and width, we are capable of preferentially introducing monovacancy defects, stripping away hBN layers, or growing nanopores. For individual nanopores in multilayer hBN, we first strip away layers in a localized region by milling with a condensed electron beam in our JEOL 2010 TEM operated at 80kV. As shown in figures 7.3(a)-(f), by using a beam condensed to a diameter of 10-20 nm at a current density of 37 A/cm², vacancies are readily formed in each layer sequentially and steadily grow with dose (Figures 7.3(g) and 7.3(h)), effectively stripping away layer by layer. Under

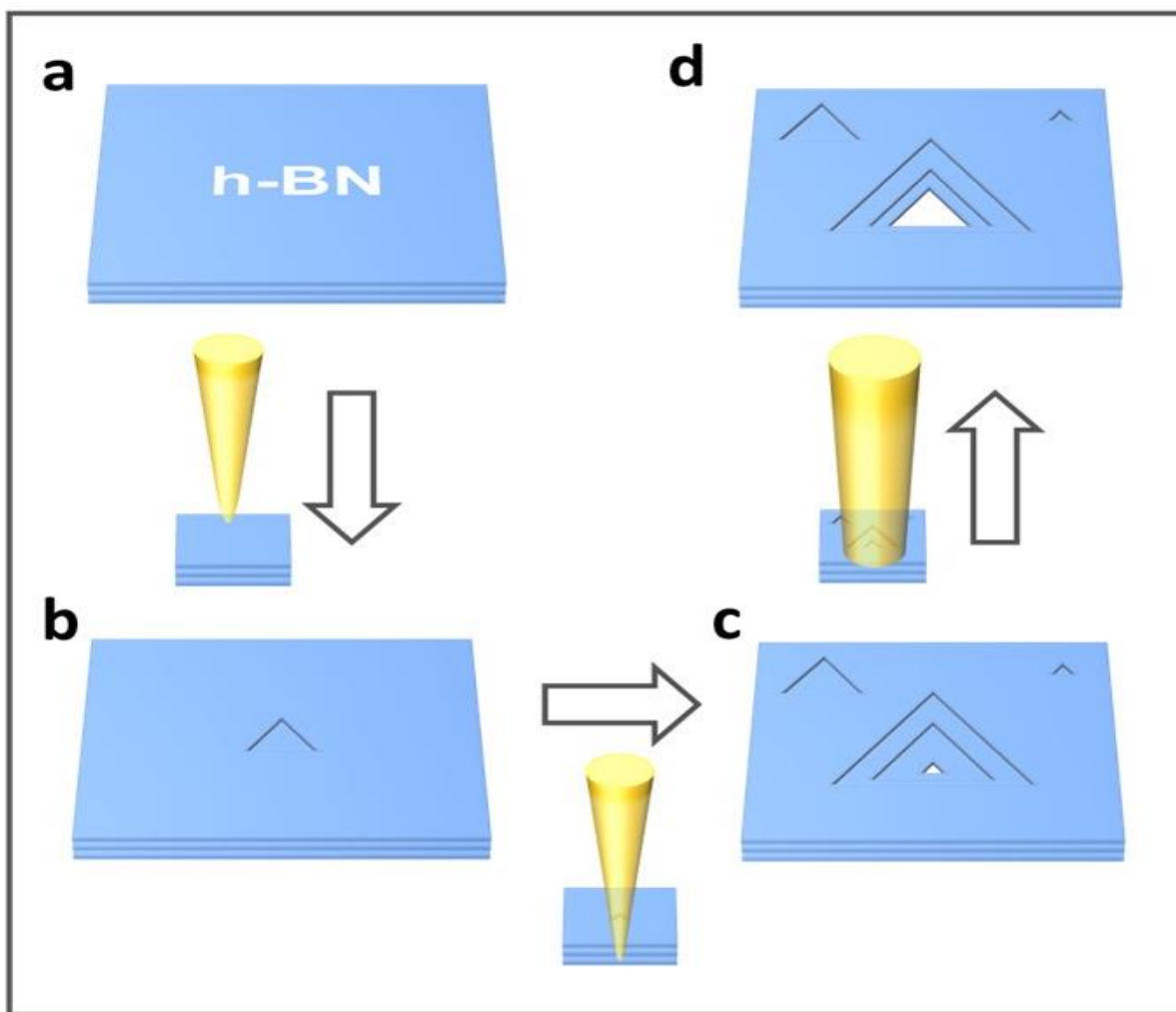


Figure 7.2: Schematic of our nanopore fabrication method. a) Starting from pristine h-BN a TEM electron beam is condensed to 10-20 nm area. b) Triangular defects form under the condensed beam, mostly near the center, allowing for the stripping of the h-BN layer by layer. c) After the formation of a single few-atom vacancy in the final layer, the beam is spread. d) Under a lower beam energy density, the pore is grown to the desired size.

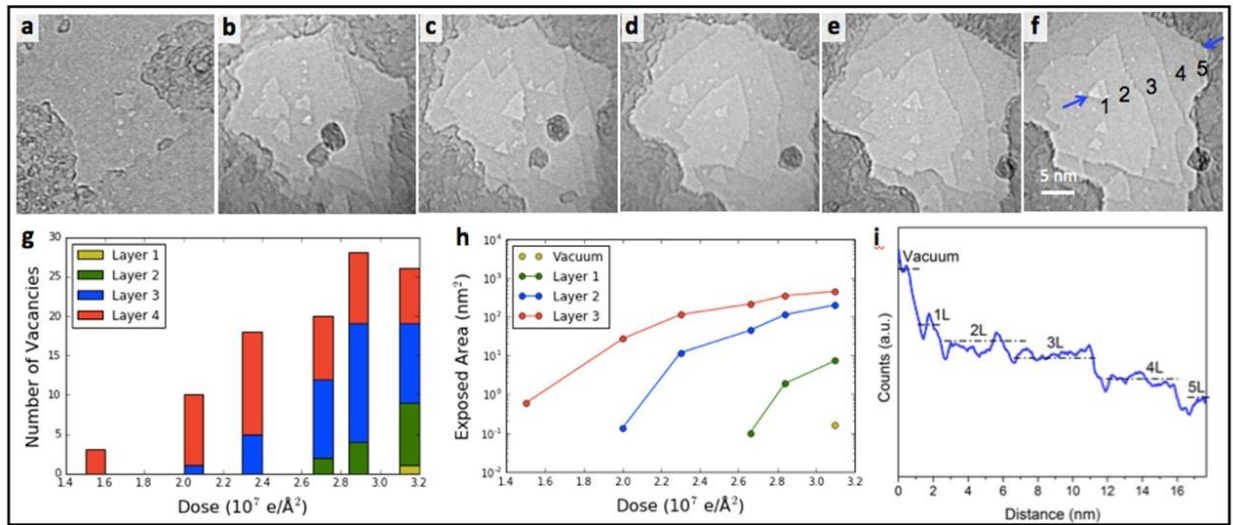


Figure 7.3: Layer by layer stripping of multilayer h-BN. a-f.) TEM time series showing the formation of defects and stripping of layers at doses of a.) 0, b.) $2.0 \times 10^7 \text{ e}/\text{\AA}^2$, c.) $2.3 \times 10^7 \text{ e}/\text{\AA}^2$ (11 min), d.) $2.8 \times 10^7 \text{ e}/\text{\AA}^2$ (15 min), and e.) $3.1 \times 10^7 \text{ e}/\text{\AA}^2$ (18.5 min) under a 10-20 nm condensed electron beam with a current density of $37 \text{ A}/\text{cm}^2$. After frame e), the beam is expanded with a current density of $3 \text{ A}/\text{cm}^2$ to produce the single nanopore shown in f.). In f.) the layer numbers are denoted. g.) The number of continuous vacancies present in each layer of the sample as a function of dose. h.) A graph depicting the amount of area exposed of a given layer or below, note that the area exposed of each layer or below goes asymptotically towards probe size. i.) Grayscale count profile along the path between the two arrows in f.). The difference between layer 1 and vacuum is larger than between other layers. All scale bars are 10 nm.

these beam conditions, this process proceeds fairly slowly, giving a good deal of control; Figure 7.3(h) shows the area of the sample exposed for a given layer or below. In this experiment, it requires a dose of approximately $6 \times 10^6 \text{ e}/\text{\AA}^2$ or 4.5 minutes to strip to each successive layer under the condensed beam. Vacancies in the final single-layer region of the hBN can be identified by a larger contrast difference (Figure 7.3(i)), allowing us to stop the milling after an isolated vacancy has been introduced in the single-layer region.

Once we have reached a sufficient area of exposed single-layer hBN and have introduced an individual defect, we now wish to only grow this defect and not nucleate additional vacancies. Compared to the higher energy density beam used to strip away layers and introduce vacancies, a lower energy density beam allows us to grow the nanopore in quantized triangles of precise size, while new vacancy formation is inhibited. As the nanopore grows, it favors a triangular geometry and is metastable at each quantized triangle size, allowing for easily reproducible, highly regular pore geometry. Figures 7.4(a)-(h) show an example of the growth of a single nanopore from a few-atom vacancy to 8 nm^2 with the beam current density reduced to $6 \text{ A}/\text{cm}^2$, where the pore growth as a function of dose can be seen in Figure 7.4(i). As has been described previously,

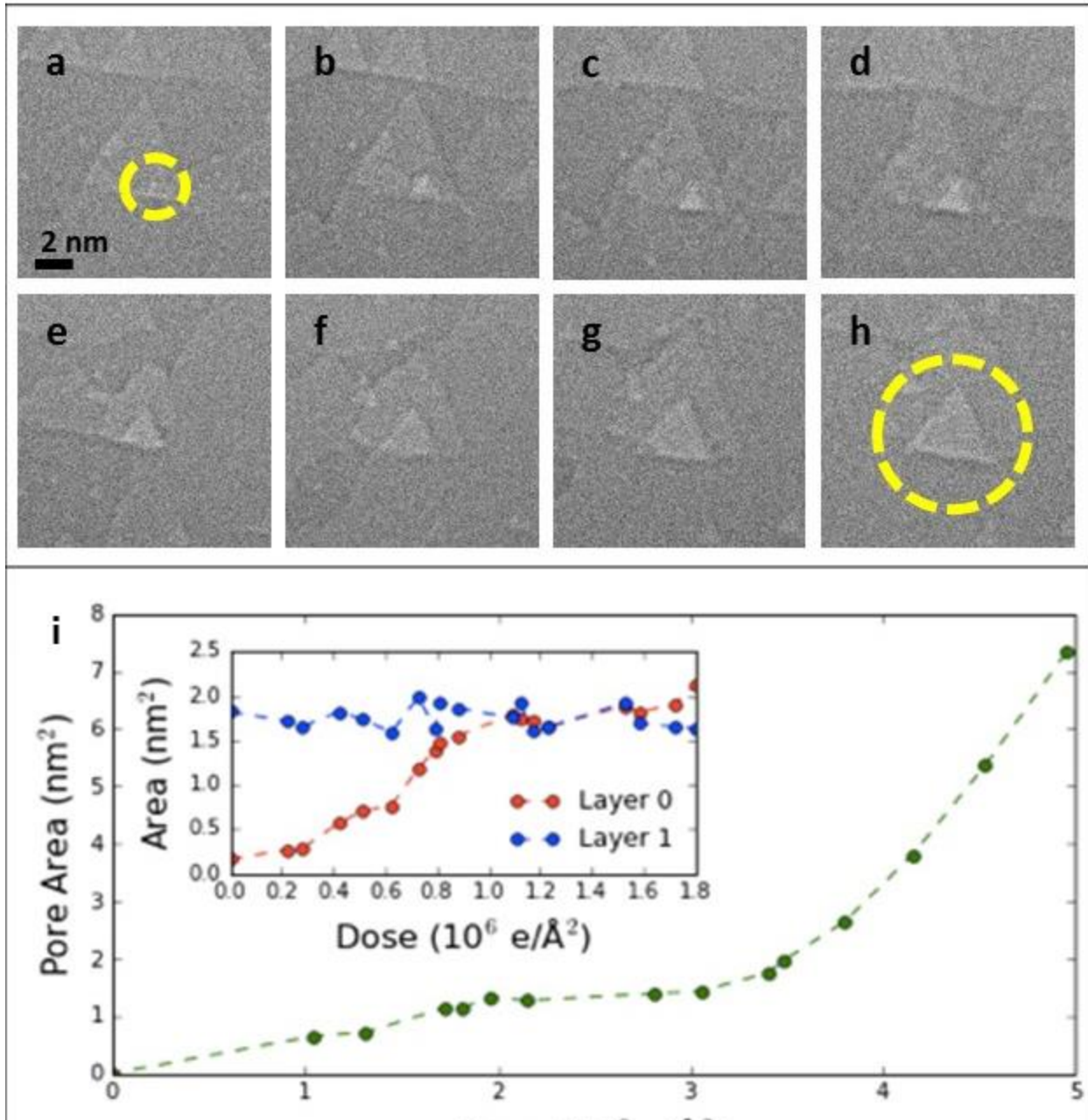


Figure 7.4: Metastable quantized growth of triangular nanopores. a-h) A time series showing the quantized growth of a triangular nanopore in h-BN from a few-atom vacancy to approximately 8 nm² under a beam current of 6 A/cm². Images are taken at roughly 2 minute intervals. j.) A plot of pore area versus dose for the images shown in (a-h). The inset shows a similar growth of pore area versus dose for the nanopore shown in figure (a)-(f) and a neighboring vacancy of similar size in the second layer under a beam current of 3 A/cm². Unlike the pore that spans the full thickness of the h-BN, the vacancy that sits on top of another layer of h-BN does not grow at an appreciable rate.

electron knock-on effects and/or selective chemical etching due to gases present in the TEM column preferentially eject boron atoms and preserves nitrogen zig-zag edge termination. Hence, each of the triangular pores created is reliably nitrogen terminated, desirable for many nanopore applications where controlling end-group chemistry is critical. When the nanopore has reached its desired size, the beam can be fully expanded or blanked to cease pore growth.

By further lowering the beam current density, the nanopore in the single-layer region can be preferentially grown while similar defects in the multilayer region remain static. This is possible because vacancies in multi-layer regions appear to be stabilized, with inhibited further evolution, by the supporting h-BN layers. This is shown in the inset in Figure 7.4(i), where over the course of exposing the sample with a total electron dose of $1.8 \times 10^6 \text{ e}/\text{\AA}^2$ over 16 minutes at beam current of $3 \text{ A}/\text{cm}^2$, the pore that spans the bottom layer grows by 10-fold while the similar vacancy in the second layer remains constant in size.

While we have restricted ourselves to considering triangular nanopores, as mentioned above, additional pore geometries are possible. In addition to heating the substrate, we found that tuning the beam properties could alternatively produce hexagonal pores, as shown in Figure 7.5. Higher current densities allowed for the production of the hexagonal pores which we had seen with higher temperatures. While it is unclear how stable these pores are when exposed to air, because these additional geometries could confer some potential advantages, as well as utilizing the active boron end-groups for functionalization, this area warrants further study. In addition to the potential instability in air, it is more difficult to create individual nanopores given the high beam energy density requirement, so it may be necessary to try at higher temperatures as described above.

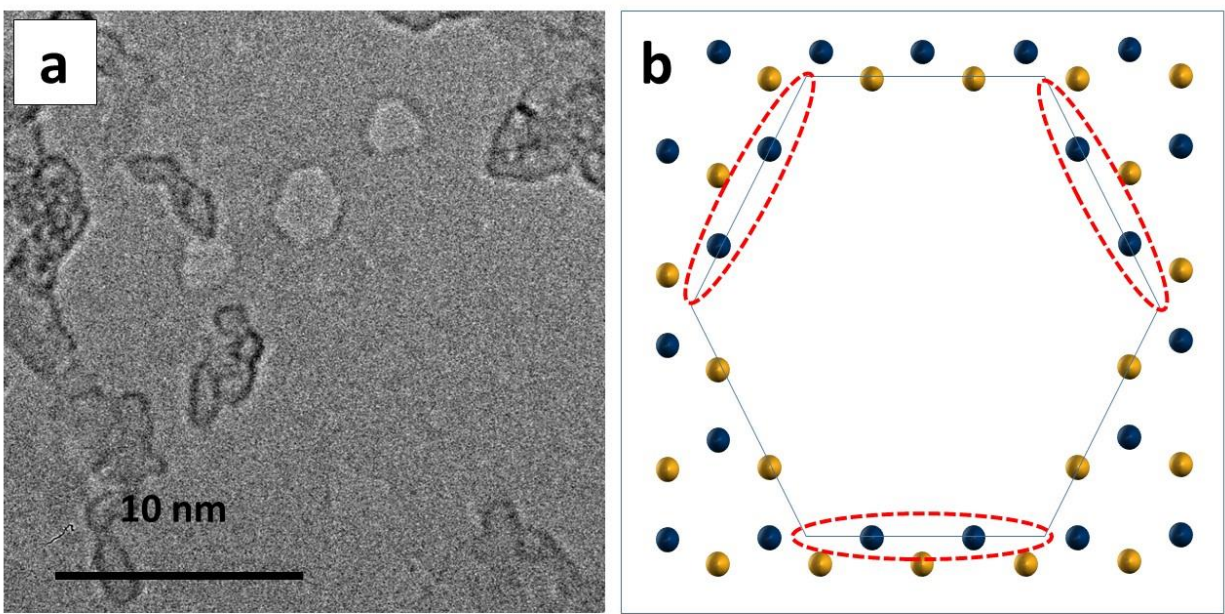


Figure 7.5: Hexagonal nanopores in hBN. a) TEM image of hexagonal h-BN pore created by condensing the beam at higher spot sizes to achieve higher current density. b) Alternating boron and nitrogen facets as demonstrated in Ref [52]. Boron and Nitrogen represented in blue and gold respectively. Boron terminated facets are circled in red.

7.3 Experimental Design

7.3.1 Reservoir Chuck Design

There were two iterations on the chuck we used to create the two reservoirs separated by the TEM grid. The first is shown in Figure 7.6. It was designed to have as little dead volume as possible to limit the volumes of DNA necessary. The chuck was machined in the Berkeley Physics Machine Shop out of PMMA, because the clear plastic would allow us to better see liquid filling and bubbles. The two sides of the chuck screw together with a pocket for a TEM chip, and two recessed areas for viton o-rings. The o-rings ensure a liquid tight seal around the chip. The o-ring groove depth is made to allow for 15% compression of the o-ring. On the top of the two chuck halves is a channel leading to a threaded Omnifit™ connector. This connector attaches to PEEK tubing which can attach to a Luer lock syringe. This allows for liquid to be injected into the reservoir with very minimal dead volume from the tubing to the machined PMMA channel. A side channel serves as both a flow outlet and an entry point for the electrodes.

The primary issue with this device was the small channel diameter leading up to the TEM grid which allowed for bubbles to be easily trapped. We shall discuss many of the steps taken to reduce bubble formation, such as using an ethanol mixture to initially wet the channels, sonication and pumping down on the liquids, and pumping down on the filled reservoirs; however, even with these steps this chuck design often showed signs of being blocked.

We moved to a second chuck design, shown in Figure 7.7. This chuck used a shorter, slightly wider channel leading directly to the nanopore chip. Rather than the syringe connected inlet port, two open reservoirs were used on either side of the TEM grid. Both of these changes helped reduce the presence of bubbles and allow for pumping down on the fluid filled chuck itself. With this setup, we were able to consistently record reasonable currents across the pores. The primary issue with this chuck that may be resolved in future versions is the amount of dead volume at the base of each of the reservoirs. Because the TEM grid channel is about halfway from the bottom of the reservoir, were we to nearly empty the reservoir we would risk de-wetting the nanopore, something we try to avoid to prevent bubbles, contamination and membrane collapse. Instead, we must empty the reservoir down to just above the channel. This means that in order to completely switch solutions, a number of cycles of half emptying and filling must be done. Fixing this would be as simple as reducing the depth of the reservoir. This would help with another issue with this chuck design, the amount of dead space means a significant volume of DNA is required for experiments.

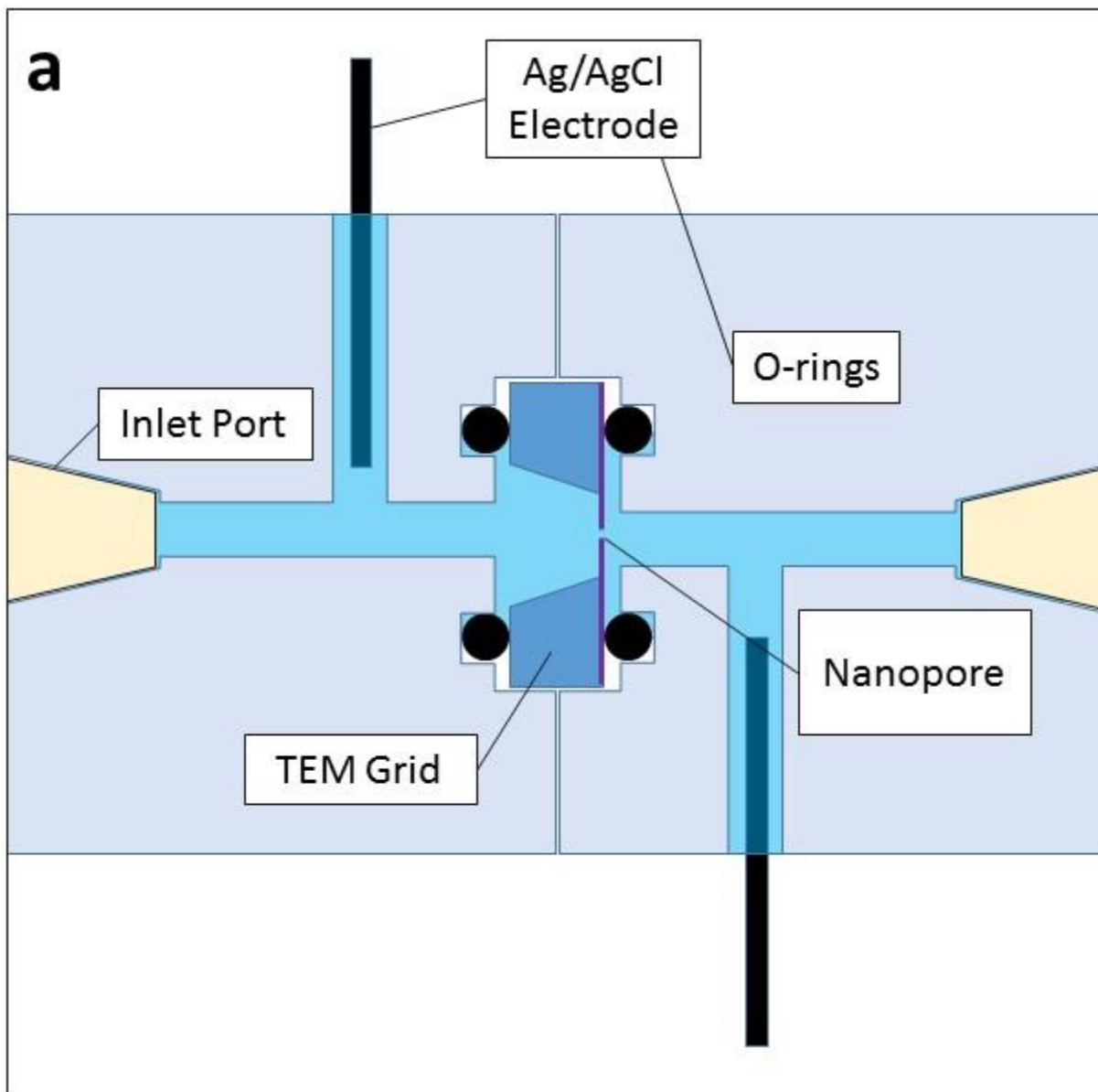


Figure 7.6: Nanopore Fluidic Chuck Version 1 design (continued on next page). a) Cartoon of design. The two halves of the chuck screw together to isolate a TEM grid with an integrated nanopore. Solutions are injected via Omnifit™ syringe inlet ports. The solution can exit through a side outlet port which also serves as an insertion site for a Ag/AgCl electrode.

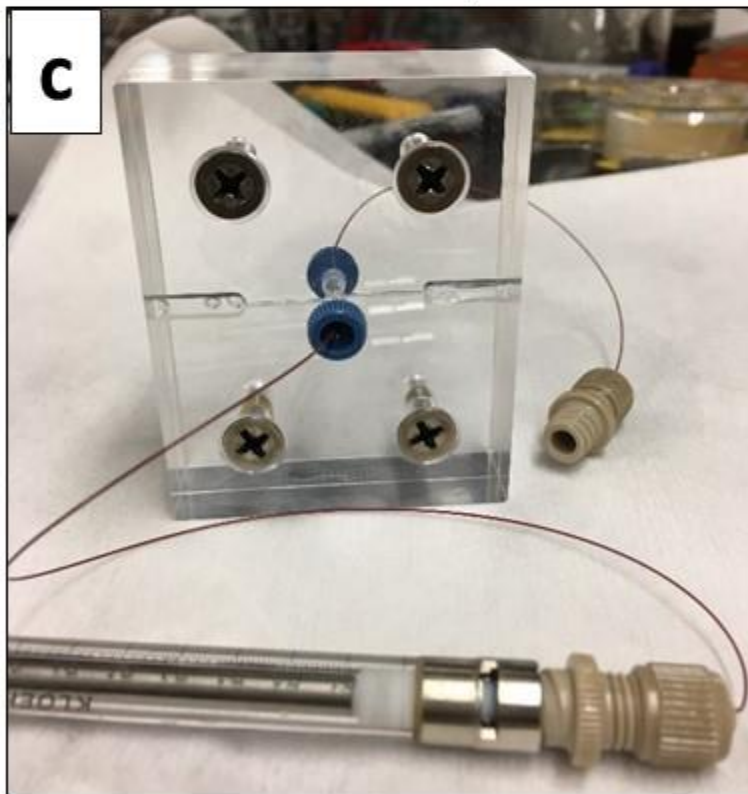
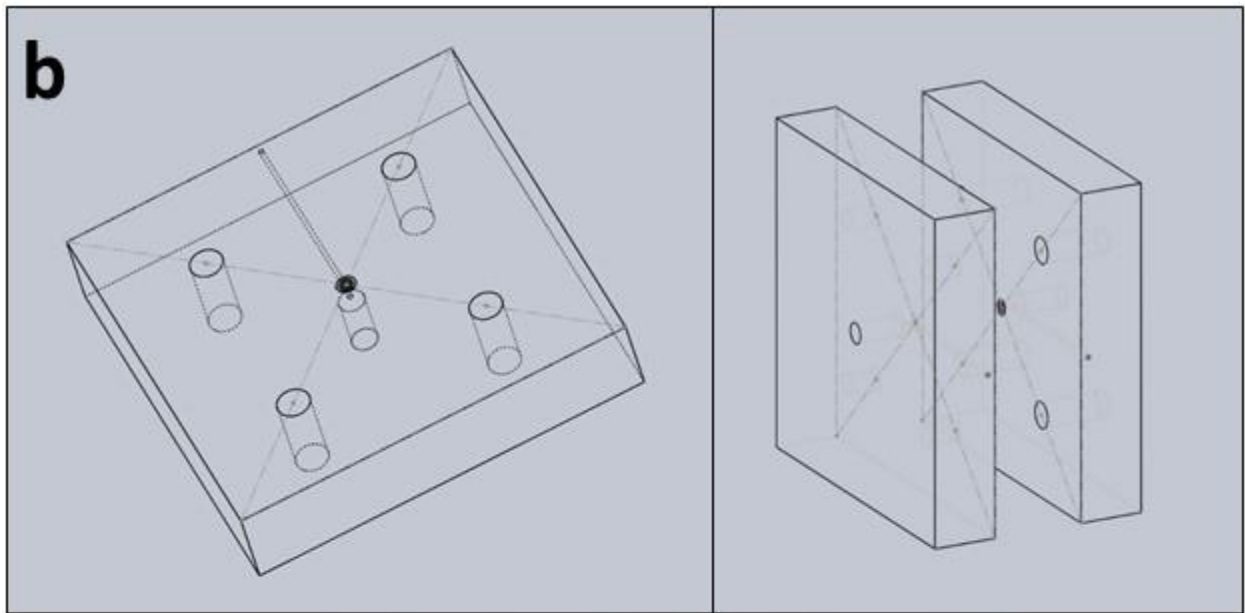


Figure 7.6 (cont): Nanopore Fluidic Chuck Version 1 design. b) Schematic drawings of chuck assembly. c) Optical image of completed fluidic chuck, with syringe injected inlet ports.

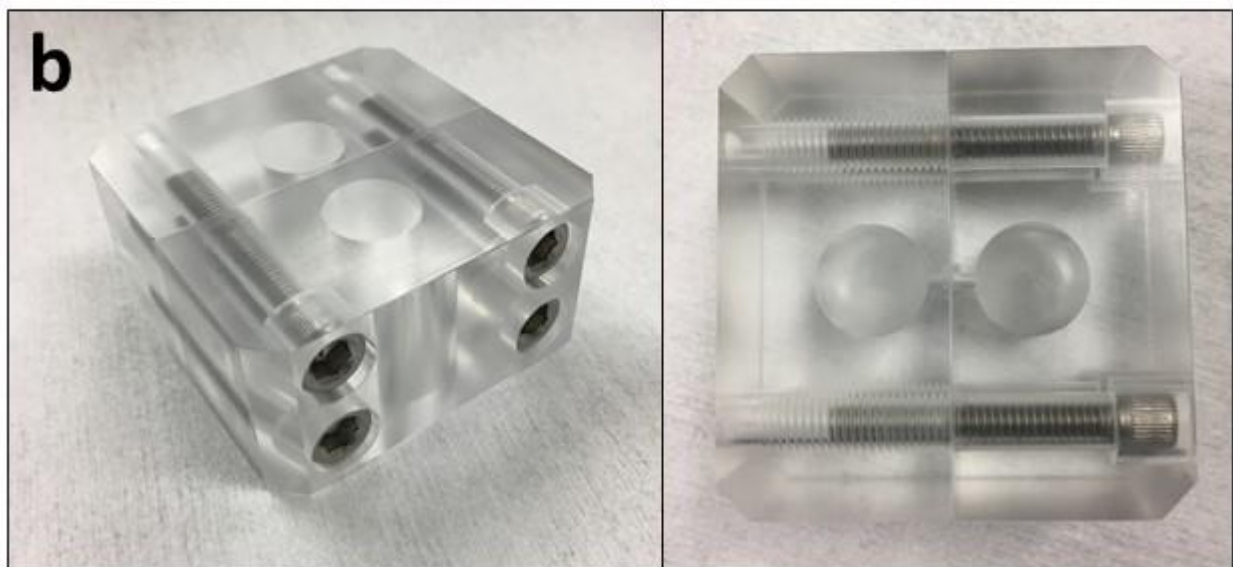
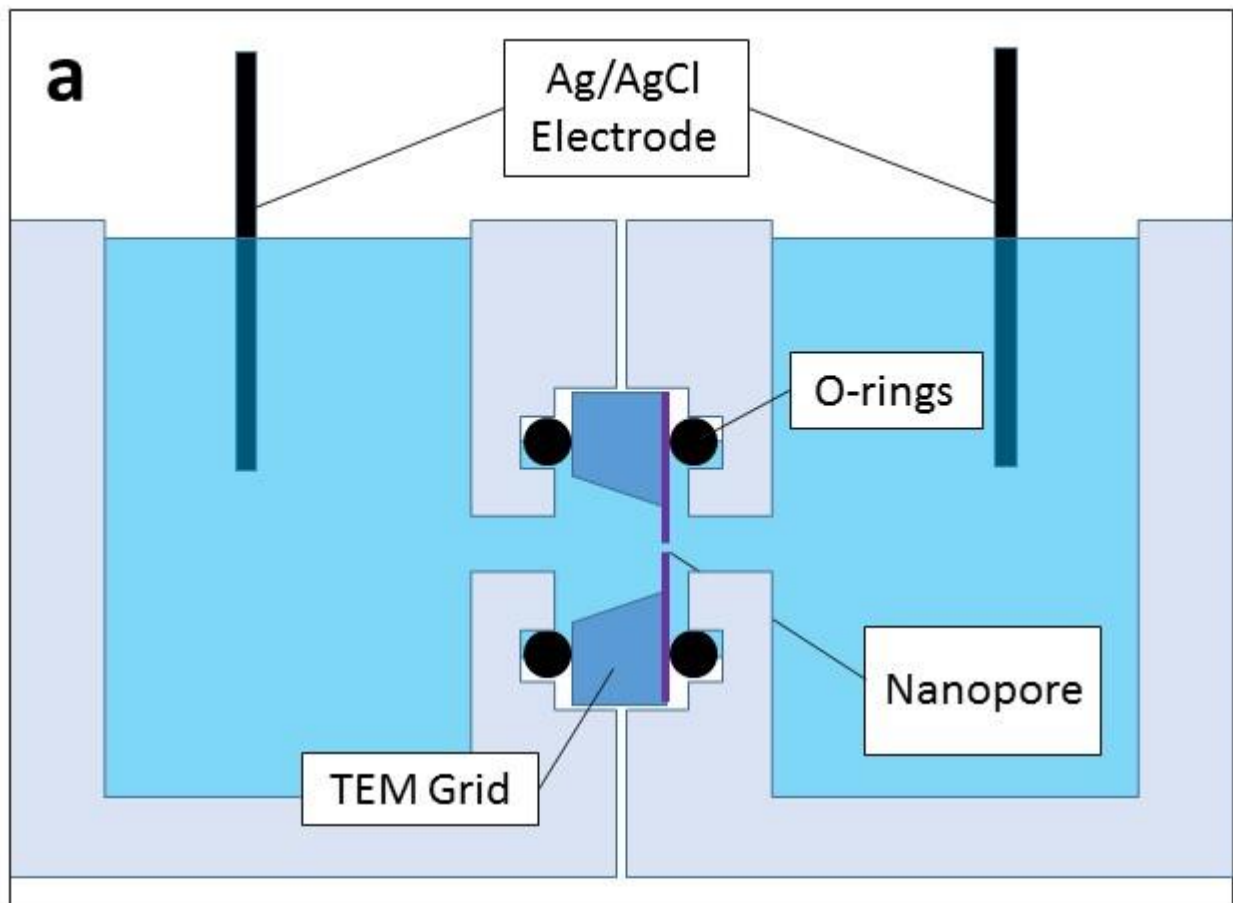


Figure 7.8: Nanopore Fluidic Chuck Version 2 design. b) Schematic drawings of chuck assembly. c) Optical image of completed fluidic chuck, with two reservoirs on either side of the press-sealed TEM grid.

7.3.2 Electronics

The electronics setup consists of homemade Ag/AgCl electrodes, a low-noise amplifier, a digitizer, and computer readout. The Ag/AgCl electrodes are formed by dipping Ag wire in bleach for at least 30min (Note: the wire should be made long enough to reach from the headstage into the reservoirs). The wire will quickly turn a brownish black while in the bleach, indicating that the surface of the wire is in fact being converted to AgCl. The wire is then removed from the bleach and placed in DI water baths in order to remove all residual bleach. After drying the wire, a pin is soldered onto the end of the wire to connect to the amplifier headstage. The rest of the wire is then covered in heatshrink to limit the potential for shorting and noise. An image of a finished electrode is shown in Figure 7.9. When the wire isn't being used, we found storing in IPA was the best way to ensure a decent lifetime of the electrode.

The amplifier, digitizer and computer readout used are all commercially available from Molecular Devices. The amplifier is an Axopatch 200B low-noise amplifier. This amplifier has been designed for the study of cell membrane channels, making it particularly well suited for nanopore measurements. The amplifier features an actively cooled headstage to reduce thermal noise and a 4-pole Bessel filter. The Amplifier is shown in Figure 7.10 along with some of the important adjustment knobs and parameters. This device has become commonplace for research groups doing nanopore sequencing.

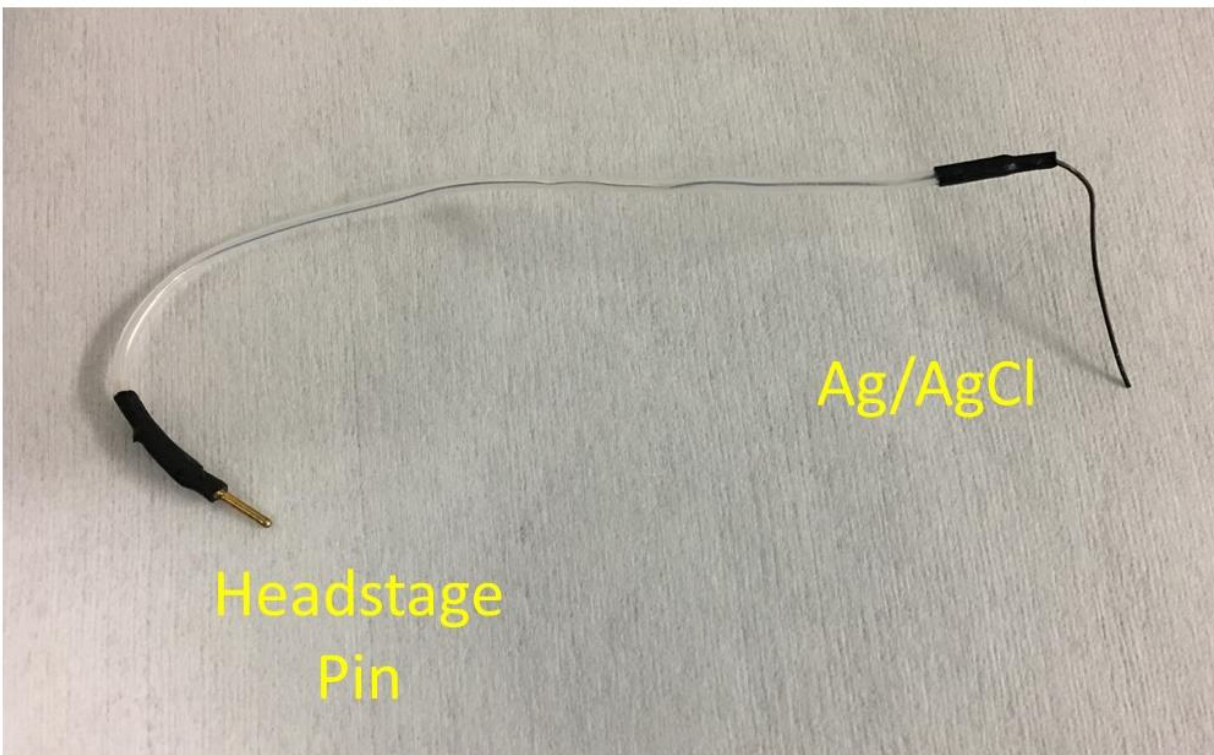


Figure 7.9: Ag/AgCl electrode. The silver wire is insulated with plastic tubing and sealed on both ends with heatshrink. One end is soldered to a pin which fits into the Axopatch headstage. The other end is converted to Ag/AgCl by soaking in bleach.



| Number | Function | Description |
|--------|----------------------|---|
| 1 | Power | On/Off |
| 2 | DC Offset | Used to balance any DC offsets that may be present. Before turning on bias, you should aim to balance out any zero voltage current. This should happen near a dial position of 5.0. Outside ± 0.5 suggests an issue (see Troubleshooting) |
| 3 | Zap | Provides short bipolar burst. Can be useful for dislodging contaminants in pore. |
| 4 | Bias Voltage Control | Positive or negative DC voltage bias can be applied. 50-200mV are typical. |
| 5 | Low-pass filter | 1kHz-2kHz was typically used. |
| 6 | Output Gain | Actual gain is determined by this parameter as well as the mode (patch vs. whole cell) which it is in. |
| 7 | Headstage | Cooled headstage. Signal terminal in front, ground in back. |
| 8 | DigiData 1550A | Digitizer with 60Hz noise cancellation. |

Figure 7.10: Data Acquisition Electronics. Key elements and their functions have been highlighted. Top box is the Axopatch 200B, bottom is DigiData 1550A

The digitizer is a DigiData 1500B low-noise data acquisition system. It has a maximum sampling rate of 500kHz. The digitizer is also shown in Figure 7.10. The digitizer operation is straightforward and requires little to no modification or adjustments from the user.

The initial software used for data acquisition was the pCLAMP software included with the Axon digitizer. The software interface is very basic and monitors and records current values with a sampling rate as high as 50kHz. We have since moved to using an interface adapted from OpenNanopore, an open source MatLab package designed by the Radenovic group particularly for nanopore sequencing research. The program utilizes a cumulative sums algorithm (CUSUM algorithm) that fits current blockages caused by molecules passing through our nanopore by looking for sharp changes in current. This method allows one to easily gain statistics on the amplitude and time length of each translocation event. The software then highlights the fitted events and allows the user to cycle through each individually and cut out the data that are not useful for molecule identification [59]. Figure 7.11 shows a screenshot of the OpenNanopore software.

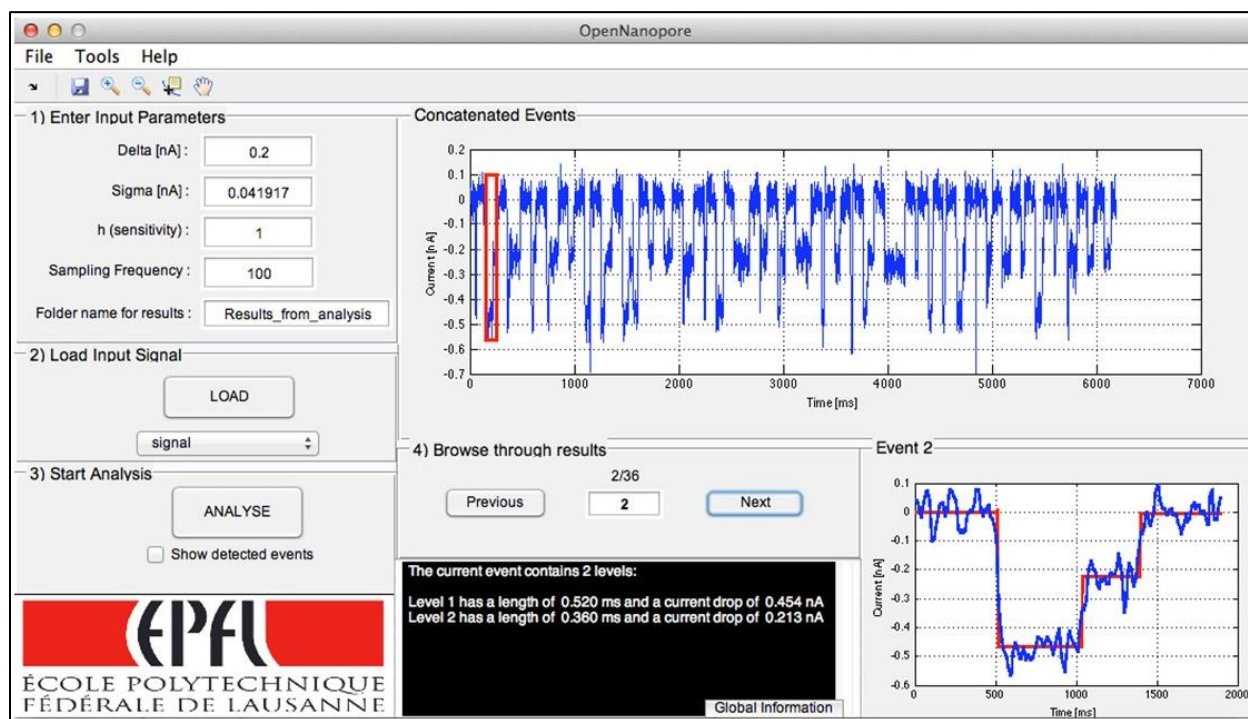


Figure 7.11: OpenNanopore GUI Screenshot. OpenNanopore interface allows for the fast and automated interpretation of nanopore blockade events and was particularly developed for solid-state nanopores [59].

7.3.3 Setup Procedure

A number of procedural steps need to be taken to ensure bubbles or contaminants do not block the pore. Everything must be kept as clean and contained as reasonably possible given the lab environment.

Before each use, the chuck is first sonicated in DI water for 5min. Then, it is submersed in a 20% HNO₃ acid bath at 80°C for at least 30 min. It is then rinsed in copious amount of DI water, and blown dry with nitrogen. Only woven techwipes should be used to handle it to avoid lint from other paper towel materials. It is very important that the chuck be left completely dry, or leftover liquid can cause a shorting path. The o-rings are cleaned separately by sonication in a 1:1 DI:Ethanol mixture. They are placed on a techwipe to dry.

While this is happening, all liquids to enter the chuck are to be degassed. In our case, this is primarily a 1:1 DI:Ethanol mixture, pure DI water, and a 1M KCl solution. Each liquid is first sonicated in a bath sonicator for at least 5min. The liquids are then left in a vacuum jar for at least 1hr, although overnight is best. This process may be repeated to ensure there is no air left in the solution.

The chips are best transferred to the chuck directly from being milled in the TEM. If there is a substantial delay or a chip is being reused, it must be cleaned. A 20% HNO₃ bath can be used again, or a heated piranha bath can be used. Afterwards, the chip is soaked in multiple DI baths, followed by IPA, and gently blown dry.

The chuck is carefully fitted with the o-rings, and the chip is gently placed on top of the bottom portion of the chuck. The top part is then held above the chip as the screws are inserted to ensure the two parts of the chuck properly align with one another. The screws are tightened in a cross-hatch fashion until tight, while taking care not to strip the screws.

In order to promote wetting of the chip, the entire chuck with the chip is placed in a light N₂ plasma. The N₂ plasma is struck at 20W with 20sccm of N₂ for only 2s. Incredibly, even this short of a plasma time seems to have a dramatic effect on the wettability of the channel.

The reservoirs are then filled with a 1:1 DI:Ethanol mixture, and the entire chuck is pumped down on in an evacuated bell jar to attempt to dislodge any remaining bubbles. The DI:Ethanol mixture is then gradually subbed out by removing the mixture down to the channel level, and topping off with DI water. This process is repeated at least 6 times in order to remove a good fraction of the ethanol. The chuck is then placed back in the vacuum bell jar overnight. The DI is then substituted for the KCl solution in the same manner. It is possible to directly introduce the KCl from the DI:Ethanol mixture, however, we were concerned about crystallization of the KCl as well as changes in the concentration of the solution when left under mild vacuum overnight.

After the chip is loaded, the reservoirs are filled, and you are confident there are no bubbles, the next steps in the procedure are aimed to limit noise. The chuck is held in a double-Faraday cage consisting of a machined aluminum block and a standard metal electronics box shown in Figure 7.12. A wire is wrapped around the chuck and it is lowered into a machined

aluminum box (the wire will allow you to easily lift it back out of the box when finished). The Ag/AgCl electrodes are removed from being stored in IPA, connected to the Axopatch headstage, and placed in each reservoir. The top of the aluminum box is screwed on. A ground wire is wrapped around one of the screws to ground this box. This box and the headstage are held in a larger metallic box. The Axopatch wires run through a hole cut in the side of the box, and the ground wire is fed through a different hole. The ground wire is then connected to the Axopatch ground as well as the outer box by an alligator clip.

The Axopatch amplifier and the DigiData digitizer are then turned on to collect data in the pCLAMP software interface. For typical resistances, the amplifier gain is set to only x1 or x2 as any higher will cause it to rail. The amplifier is used in patch clamp mode. In order to account for any potential offsets, the pipette offset dial is turned to zero the current. This typically requires very minor adjustments, and anything more significant than a few ticks on the dial indicates a problem (see troubleshooting at the end of the chapter). After zeroing, the voltage can be controlled by the bias control dial. Typically, we would use 50-200mV.

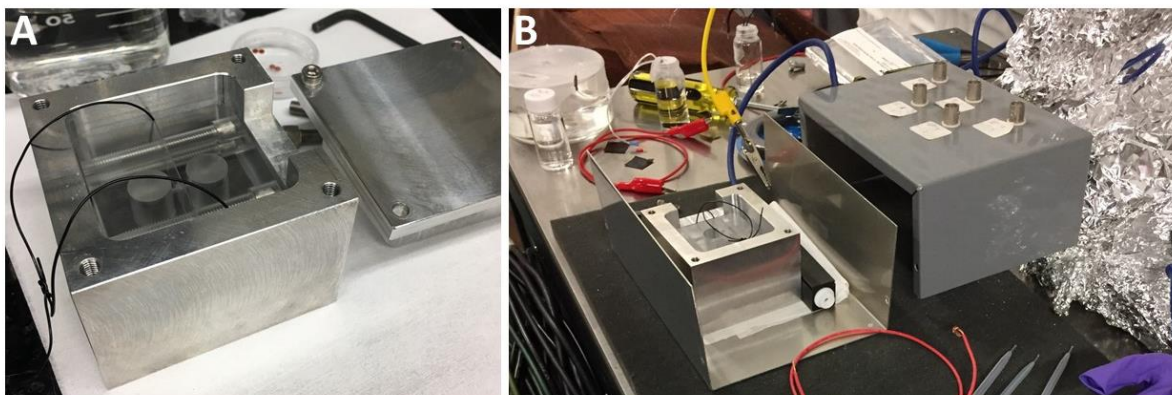


Figure 7.12: Faraday cages. A) The chuck is lowered into a machined aluminum box. B) This setup is then placed inside a larger Faraday cage along with the Axopatch headstage. Both boxes are grounded.

7.4 Preliminary Results

7.4.1 Noise

We first aimed to confirm that our experimental setup was functioning and set a baseline for noise and performance. The noise spectrum of the headstage at open circuit, and the headstage hooked up to the fluidic cell with a nanopore at 0V can be seen in Figure 7.13 for control. As can be seen, the noise levels we are experiencing are on par with or better than what is typically reported.

There is consistently a 60Hz noise peak for the fluidic setup which is not present in the headstage alone. This suggests that the ionic liquid filled channels of the chuck are serving as antennas that are picking up 60Hz noise, even with the double Faraday cage. The digitizer is equipped with a HumSilencer™ feature which analyzes and subtracts 60Hz noise. For these noise measurements, this feature was disabled, but with the feature enabled, the noise is greatly reduced.

In addition to the baseline noise at 0V bias, we also see a current dependent noise. This is characteristic of $1/f$ noise which is commonly seen in solid-state nanopores, as shown in Figure 7.13C. The precise origins of this noise is unclear, however it is worth noting that it is dependent on channel length, and both graphene and hBN have been shown to have higher $1/f$ noise levels [60]. For comparison, Figure 7.13 shows a comparable measurement for silicon nitride and graphene nanopores with a 10kHz low-pass filter.

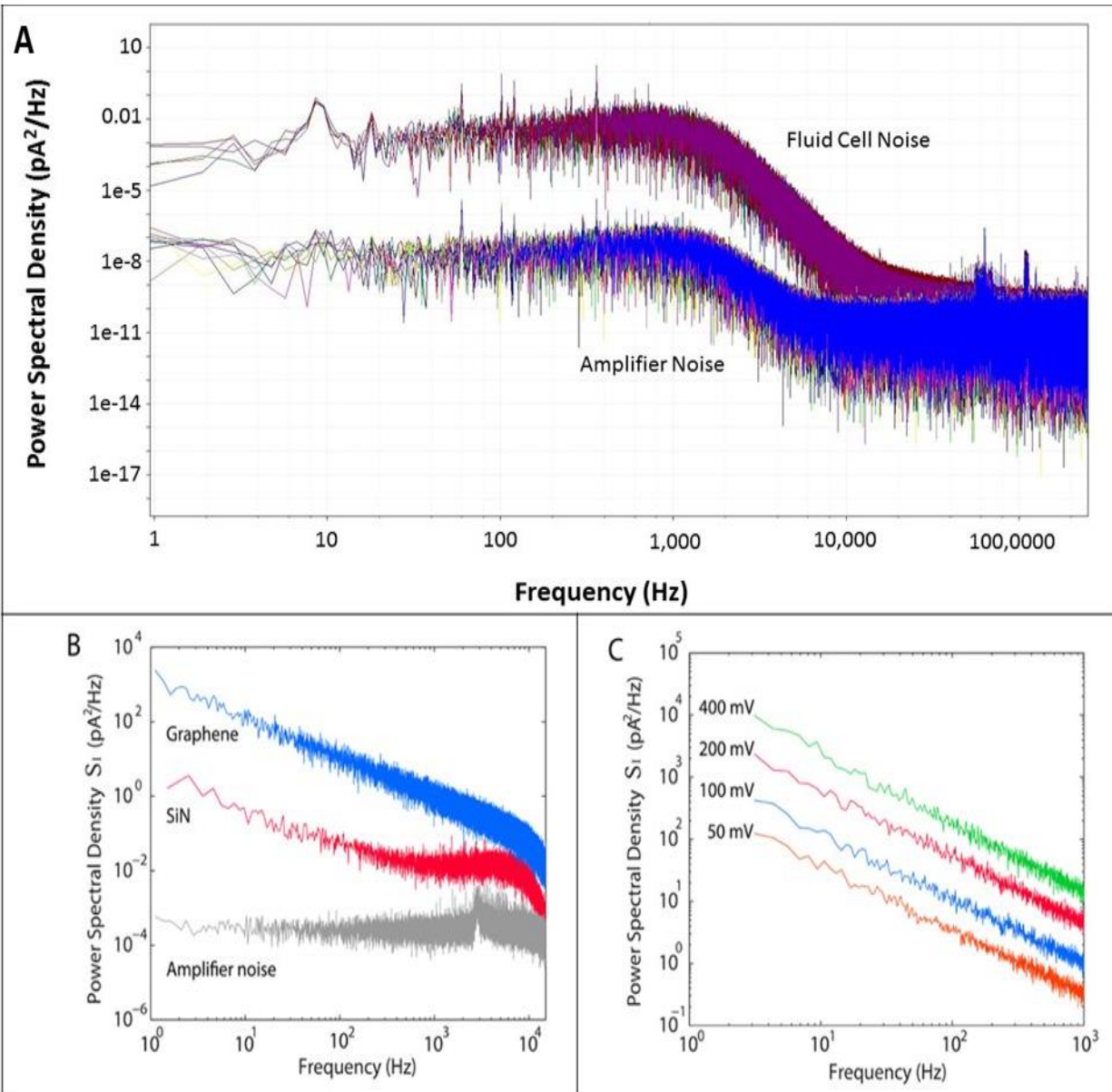


Figure 7.13: Noise Spectra. A) Noise spectrum from our setup with 1kHz low-pass filter. Top plot shows the noise spectrum for the fluid cell with a SiN nanopore, the bottom for the headstage at open circuit. B) Comparison noise spectra from Ref [60]. C) Current dependent noise for a graphene nanopore. Adapted from Ref [60]

7.4.2 Ionic Current

We also wanted to confirm that our experimental setup was functioning properly and that we were capable of measuring an ionic current across a pore. For this, we worked with nanopores drilled into SiN membranes by helium ion beam or a condensed electron beam. Following the procedures outlined above, we were able to reliably wet the chip without bubbles or contamination blocking it. As can be seen in Figure 7.14, the IV plots show the clear linear dependence we are expecting. Working with a number of SiN nanopores, we have been able to confirm that this ionic current matches roughly what we would expect given the pore geometry and previous experiments. Typical values range from 1-50M Ω . Significantly lower than this suggests a short or broken membrane. Significantly higher than this suggests a blockage in the channel, such as an air bubble.

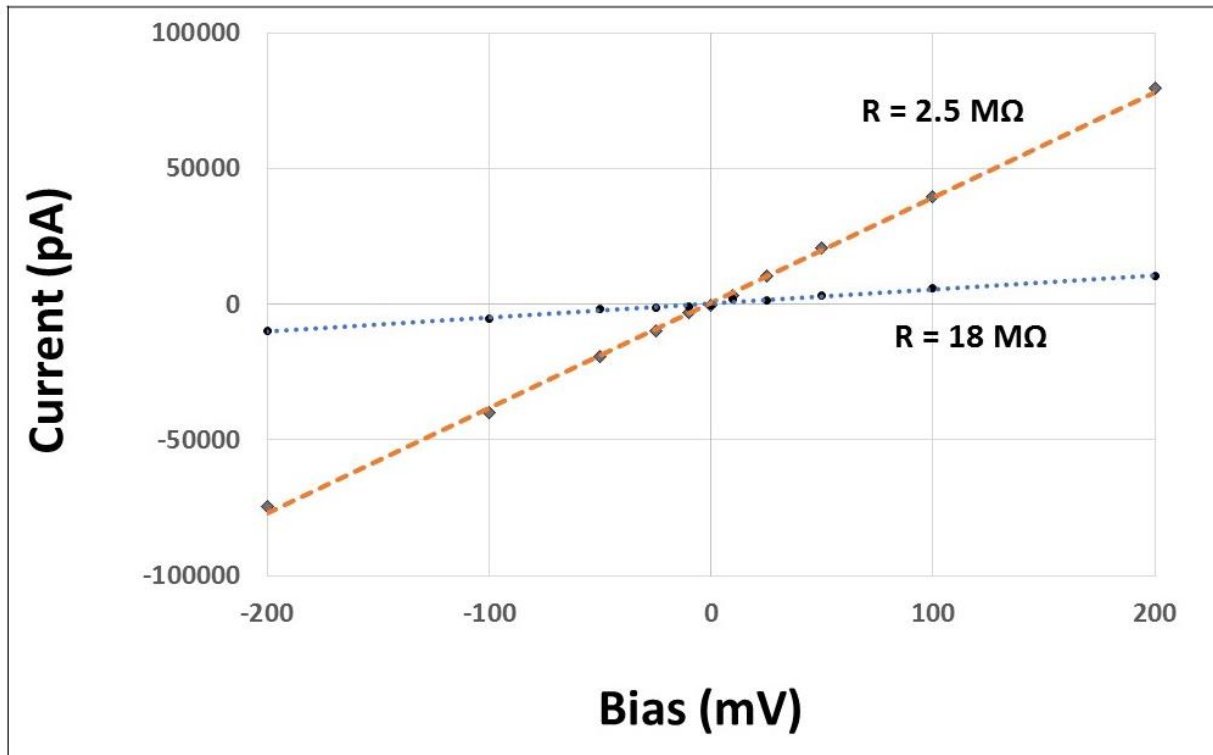


Figure 7.14: SiN Nanopore Ionic Current. Current vs. Voltage plots of two nanopores in SiN. Data shows a clear linear relation as expected and are in the expected range (1-50M Ω) for nanopore currents.

7.4.3 DNA Translocation Events

Next, we demonstrated that DNA current blockages could be seen for translocation events. For this we used double-stranded λ -DNA, a viral DNA commonly used due to its length, 48,502 base pairs or 16.5 μm . These were purchased from New England BioLabs and were at a concentration of 500 $\mu\text{g}/\text{mL}$. We diluted this 10-fold with TE buffer solution.

Before loading into one of the reservoirs, the reservoir liquid level was reduced to just above the channel. This was in order to maximize the DNA concentration while minimizing the amount of stock λ -DNA solution that was used. The DNA was then loaded into the remaining reservoir solution. DNA was loaded only into a single reservoir as this would help confirm that the translocation events we are seeing are really due to DNA, as they should only occur when applied bias will act to push the negatively charged DNA through the pore.

Figure 7.15 shows the translocation events we saw for a $\sim 6\text{nm}$ pore in SiN. Given the diameter of the pore was $\sim 6\text{nm}$, the approximate area is 113nm^2 . DNA has a cross-sectional area of around 3nm^2 , meaning we would expect a blocking current of 3% ($3\text{nm}^2/113\text{nm}^2=0.03$). For the 6000pA current we saw at 100mVmV, this would mean a blocking current of 180pA. This is very close to the roughly 200pA peak-to-peak behavior we saw.

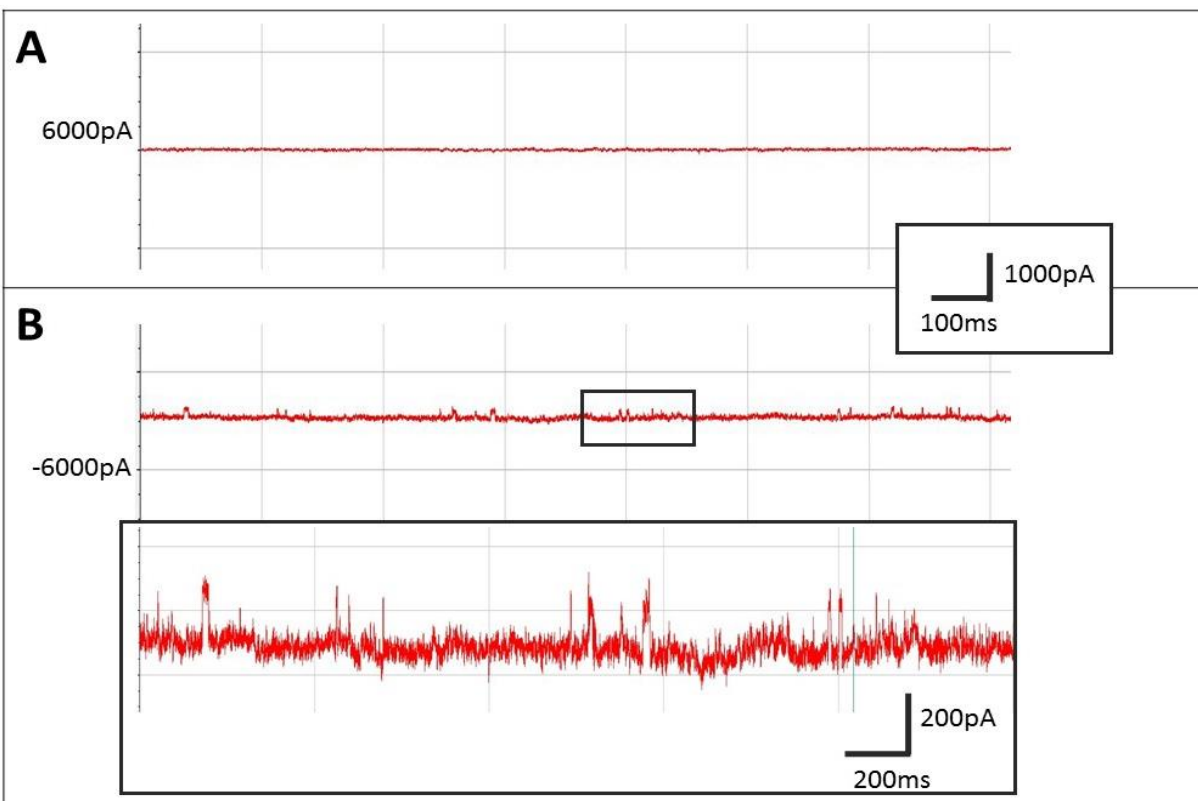


Figure 7.15: DNA Translocation in SiN Nanopores. A) Current vs. time plot with +100mV bias. No events detected as expected. B) Current vs. time plot with -100mV bias shows translocation events. Bottom plot shows a closer view of some of the events. Given the size of the pore, the amplitude of the current blockades is consistent with DNA.

7.4.4 BN Nanopore Impedance Measurement (ongoing)

This marks as far as this project has progressed to date. While we have demonstrated isolated nanopore fabrication, these have been done on quantifoil TEM grids where there are many areas of suspended BN and large areas that are torn or missing. This work is now being repeated on commercial SiN grids in which a small hole has been milled in the SiN. This ensures that the isolated BN nanopore is the only channel between the two reservoirs.

When this work is completed, the first measurement we will want to get is the ionic impedance of the pore. Similarly to what was done for the SiN nanopore characterization, we will manually sweep the voltage and measure the current at each to back out the impedance. Ideally, we would be able to do this for a range of hBN nanopore sizes and compare these to the predicted values. The hBN pore geometry may have interesting effects on pore impedance.

We will also want to test the stability of this impedance. It will be important to know if there is any continued etching or widening of the hole under an ionic potential, such as what has been observed in SiN pores. We are expecting the hBN nanopore to be nitrogen terminated and very stable, so we are not expecting the impedance to decrease. However, we may see contamination begin to block the channel, and start to see discrete increases in impedance.

7.4.5 BN Nanopore Double-Stranded DNA Translocation Events (ongoing)

We would first want to record DNA translocation events using double-stranded DNA. Single-stranded DNA can introduce additional complications as the single-strand can readily stall out on surfaces or charged functional groups. We would like to see the translocation for a number of quantized hBN nanopore sizes near the limits where DNA would no longer pass through.

After translocation events have been registered, we would want to first look at the magnitude of the current blockades. For nanopores atomically tailored to barely allow DNA to pass, we expect a large blocking magnitude. Directly below this level, we would expect to see either no current spikes, or large current spikes with extremely long durations suggesting that the DNA is blocking the pore but not passing through it.

The average translocation time would be another important metric to look at. By virtue of being the smallest possible pore size, we would already expect the translocation times to be longer. However, as mentioned previously, it is possible that the triangular pore geometry will cause the helical DNA to need to corkscrew through the pore in order to fit, further slowing down the translocation. By comparing the translocation times at various pore diameters to the expected translocation times based on pore size alone, we can see if we are seeing further slowing effects. The speed of translocation events is one of the primary barriers to effective solid-state nanopore sequencing, so any demonstration of slower translocation events would be critical.

7.4.6 BN Nanopore Single-Stranded DNA Translocation Events (ongoing)

The obvious next step is moving on to single-stranded DNA detection. Single-stranded λ -DNA is commercially available, or double-stranded DNA can be separated at 95°C, or in an alkali solution [61]. For the actual sequencing of DNA, moving to single-strand DNA will be necessary. The interaction of the single-stranded DNA with the nitrogen-terminated end-groups of the hBN nanopore will be of particular interest. Ideally, the inert nitrogen termination will limit binding with the DNA, but this is yet to be seen.

7.5 Troubleshooting

The nanoscale nature of this work means that you are often troubleshooting in the dark. Many issues are only present at the nanoscale and cannot be seen or addressed under optical microscope. Here, we detail a number of common problems we encountered, what we believe to likely be responsible, and how to remedy them.

7.5.1 No Voltage Response (or only transients)

This typically occurs when the channel is blocked, usually by an air bubble or by some contaminant. Using the zap function on the amplifier passes a short bipolar voltage burst which can occasionally dislodge a blockage. This is most likely to be successful when the pore has been showing a normal current, but then the current drops some time later, suggesting a blockage. If this doesn't work (most often it does not), you can next try pumping down on the chuck in a vacuum chamber for longer to dislodge any remaining bubbles.

If this does not work, there is likely some kind of contaminant in the chip. You will then need to remove the chip from the chuck. This can be done under water to limit damage to the membrane. The chip and chuck can then be cleaned as described earlier.

7.5.2 Extremely High Pore Impedance

Similar to the case of “No Voltage Response,” this is typically caused by some blockage of the channel. Once again, this can occasionally be solved by zapping the channel. What constitutes “extremely high” will depend on the pore being used. It is not uncommon for particularly narrow and long channels to have impedances above $100\text{M}\Omega$, while thinner chips with wider pores can be closer to $1\text{M}\Omega$.

7.5.3 Extremely Low Pore Impedance

This can either mean that the membrane has blown out, or that there is some kind of shorting path between the electrodes. The most typical shorting path is liquid that has been spilled while loading the two reservoirs that gets into the seam between the two pieces of the chuck. This is why there is a rubber pad underneath the chuck, to ensure that if a liquid path is present it cannot directly short to the grounded aluminum holder. Still, there can be a liquid path between both reservoirs which leads to a short.

7.5.4 High Current Offset

Similarly, this can have a number of possible causes. The likely source of the offset is an electrochemical overpotential, but there are a few potential sources for this overpotential. The most likely is that the Ag/AgCl electrode is beginning to fail, giving you an overpotential as you go from a Ag/AgCl electrode to just a Ag electrode. The easiest way to remedy this is regenerating the electrode by dipping the active region back in chlorine bleach for 30min. If this fails, the electrodes may need to be replaced entirely (this is not something we have encountered yet, but I imagine it could happen)

The offset may also occur if there is some kind of liquid shorting path to the aluminum holder. This is something we have hypothesized could happen, but it is not clear that we have actually seen this ever occur.

There is one more potential source of offset that, while we have not directly encountered, could be a problem. The ground inside of the padded XSTM room in B219 is separate from the ground located in the rest of B219. The room itself is meant to be grounded to the internal ground, which is supposed to be directly coupled to the earth ground. There is a nearly 0.7V offset between the ground inside and outside of the room. In the end, we found that the common ground outside the room was easier to use and had comparable noise levels (which is in itself surprising). If anything is grounded to the table, or the room, it could be experiencing the offset between the two grounds.

7.5.5 High Noise Levels

Noise is especially difficult to diagnose. Saving a recording of the noise, then taking the Fourier transform to get the power spectrum of the noise can be instructive in isolating sources. Taking additional data at different bias levels will also give you an idea of whether or not this noise is voltage/current dependent.

The most typical source of noise is 60Hz noise and is because of improper grounding. Ensure that the ground is well connected on both the inner Faraday cage, and the outer grounded electronics box.

In the manual for the Axopatch amplifier, there are checks that you can do on the baseline noise level of the headstage. This is worth doing to rule out any problems with the headstage or electronics. The noise levels when in actual use are typically worse than the test setup because the ionic channels and reservoirs serve as antennas and pick up 60Hz noise.

7.6 Conclusion

hBN nanopores at their core represent one of the most exciting areas I had the chance to work on during graduate school. Nanopore sequencing may very well be a significant disruptor, and hBN nanopores have a real possibility of playing a vital role in that disruption. However, it is not just its potential for sequencing that makes hBN nanopores so exciting. hBN nanopores represent nanofabrication at its very limit, down to the single atom. Beyond nanopore sequencing, these nanopores could find application in water desalination or act as molecular sieves. Similar to their role in sequencing, they could be used to identify any number of target molecules based on blocking current. The ability to pattern materials with atomic precision will surely find additional applications which never occurred to us.

- [1] D. A. Wheeler *et al.*, “The complete genome of an individual by massively parallel DNA sequencing,” *Nature*, vol. 452, no. 7189, pp. 872–6, 2008.
- [2] L. Chin, J. N. Andersen, and P. A. Futreal, “Cancer genomics: from discovery science to personalized medicine,” *Nat. Med.*, vol. 17, no. 3, pp. 297–303, 2011.
- [3] M. Stoneking, “The human genome project and molecular anthropology33,” *Genome Res.*, vol. 7, no. 2, pp. 87–91, 1997.
- [4] D. Deamer, M. Akeson, and D. Branton, “Three decades of nanopore sequencing,” *Nat. Biotechnol.*, vol. 34, no. 5, pp. 518–524, 2016.
- [5] S. W. Kowalczyk, A. Y. Grosberg, Y. Rabin, and C. Dekker, “Modeling the conductance and DNA blockade of solid-state nanopores,” *Nanotechnology*, vol. 22, no. 31, p. 315101, 2011.
- [6] R. M. M. R. M. M. Smeets *et al.*, “Salt-dependence of ion transport and DNA translocation through solid-state nanopores,” *Nano Lett.*, vol. 6, no. 1, pp. 89–95, 2006.
- [7] S. Garaj, S. Liu, J. a Golovchenko, and D. Branton, “Molecule-hugging graphene nanopores,” *Proc. Natl. Acad. Sci. U. S. A.*, vol. 110, no. 30, pp. 12192–6, 2013.
- [8] C. A. Merchant *et al.*, “DNA translocation through graphene nanopores,” *Nano Lett.*, vol. 10, no. 8, pp. 2915–2921, 2010.
- [9] J. Comer and A. Aksimentiev, “DNA sequence-dependent ionic currents in ultra-small solid-state nanopores,” *Nanoscale*, vol. 8, no. 18, pp. 9600–9613, 2016.
- [10] M. Akeson, D. Branton, J. J. Kasianowicz, E. Brandin, and D. W. Deamer, “Microsecond time-scale discrimination among polycytidylic acid, polyadenylic acid, and polyuridylic acid as homopolymers or as segments within single RNA molecules,” *Biophys. J.*, vol. 77, no. 6, pp. 3227–33, 1999.
- [11] D. D. W. D., “Characterization of individual polynucleotide molecules using a membrane channel,” *Proc. Natl. Acad. Sci. U.S.A.*, vol. 93, no. November, p. 13770, 1996.
- [12] A. Meller and D. Branton, “Single molecule measurement of DNA transport through a nanopore,” *Electrophoresis*, vol. 23, pp. 2583–2591, 2002.
- [13] T. Z. Butler, M. Pavlenok, I. M. Derrington, M. Niederweis, and J. H. Gundlach, “Single-molecule DNA detection with an engineered MspA protein nanopore,” *Proc. Natl. Acad. Sci.*, vol. 105, no. 52, pp. 20647–20652, 2008.
- [14] D. Stoddart, A. J. Heron, J. Klingelhoefer, E. Mikhailova, G. Maglia, and H. Bayley, “Nucleobase recognition in ssDNA at the central constriction of the ??-hemolysin pore,” *Nano Lett.*, vol. 10, no. 9, pp. 3633–3637, 2010.
- [15] D. Stoddart, A. J. Heron, E. Mikhailova, G. Maglia, and H. Bayley, “Single-nucleotide discrimination in immobilized DNA oligonucleotides with a biological nanopore,” *Proc. Natl. Acad. Sci. U. S. A.*, vol. 106, no. 19, pp. 7702–7, 2009.
- [16] N. Ashkenasy, J. Sánchez-Quesada, H. Bayley, and M. R. Ghadiri, “Recognizing a single base in an individual DNA strand: A step toward DNA sequencing in nanopores,” *Angew. Chemie - Int. Ed.*, vol. 44, no. 9, pp. 1401–1404, 2005.
- [17] E. A. Manrao *et al.*, “Reading DNA at single-nucleotide resolution with a mutant MspA nanopore and phi29 DNA polymerase,” *Nat Biotechnol.*, vol. 30, no. 4, pp. 349–353, 2012.

- [18] G. M. Cherf, K. R. Lieberman, H. Rashid, C. E. Lam, K. Karplus, and M. Akeson, “Automated forward and reverse ratcheting of DNA in a nanopore at 5-Å precision.,” *Nat. Biotechnol.*, vol. 30, no. 4, pp. 344–8, 2012.
- [19] S. Bhattacharya, I. M. Derrington, M. Pavlenok, M. Niederweis, J. H. Gundlach, and A. Aksimentiev, “Molecular dynamics study of MspA arginine mutants predicts slow DNA translocations and ion current blockades indicative of DNA sequence,” *ACS Nano*, vol. 6, no. 8, pp. 6960–6968, 2012.
- [20] J. Li, D. Stein, C. McMullan, D. Branton, M. J. Aziz, and J. a Golovchenko, “Ion-beam sculpting at nanometre length scales,” *Nature*, vol. 412, no. 6843, pp. 166–169, 2001.
- [21] A. J. Storm, J. H. Chen, X. S. Ling, H. W. Zandbergen, and C. Dekker, “Fabrication of solid-state nanopores with single-nanometre precision.,” *Nat. Mater.*, vol. 2, pp. 537–540, 2003.
- [22] A. J. Storm, J. H. Chen, X. S. Ling, H. W. Zandbergen, and C. Dekker, “Electron-beam-induced deformations of SiO₂ nanostructures,” *J. Appl. Phys.*, vol. 98, no. 1, 2005.
- [23] S. R. Park, H. Peng, and X. S. Ling, “Fabrication of nanopores in silicon chips using feedback chemical etching,” *Small*, vol. 3, no. 1, pp. 116–119, 2007.
- [24] M. Wu *et al.*, “Control of Shape and Material Composition of Solid-State Nanopores 2009,” 2009.
- [25] P. S. Spinney, D. G. Howitt, R. L. Smith, and S. D. Collins, “Nanopore formation by low-energy focused electron beam machining,” *Nanotechnology*, vol. 21, pp. 1–7, 2010.
- [26] M. J. Kim, B. McNally, K. Murata, and A. Meller, “Characteristics of solid-state nanometre pores fabricated using a transmission electron microscope,” *Nanotechnology*, vol. 18, pp. 1–5, 2007.
- [27] H. Kwok, K. Briggs, and V. Tabard-Cossa, “Nanopore fabrication by controlled dielectric breakdown,” *PLoS One*, vol. 9, no. 3, 2014.
- [28] P. Xie, Q. Xiong, Y. Fang, Q. Qing, and C. M. Lieber, “Local electrical potential detection of {DNA} by nanowire-nanopore sensors,” *Nat. Nanotechnol.*, vol. 7, no. 2, pp. 119–125, 2012.
- [29] F. Traversi *et al.*, “Detecting the translocation of DNA through a nanopore using graphene nanoribbons,” *Nat Nanotechnol*, vol. 8, no. 12, pp. 939–945, 2013.
- [30] S. J. Heerema and C. Dekker, “Graphene nanodevices for {DNA} sequencing,” *Nat. Nanotechnol.*, vol. 11, no. 2, pp. 127–136, 2016.
- [31] B. C. Gierhart *et al.*, “Nanopore with transverse nanoelectrodes for electrical characterization and sequencing of DNA,” *TRANSDUCERS EUROSENSORS '07 - 4th Int. Conf. Solid-State Sensors, Actuators Microsystems*, vol. 132, pp. 399–402, 2007.
- [32] J. Lagerqvist, M. Zwolak, and M. Di Ventra, “Fast {DNA} sequencing via transverse electronic transport,” 2006.
- [33] S. Pud, D. Verschueren, N. Vukovic, C. Plesa, M. P. Jonsson, and C. Dekker, “Self-Aligned Plasmonic Nanopores by Optically Controlled Dielectric Breakdown,” *Nano Lett.*, vol. 15, no. 10, pp. 7112–7117, 2015.
- [34] S. Nam *et al.*, “Graphene Nanopore with a Self-Integrated Optical Antenna,” 2014.
- [35] M. Belkin, S. Chao, M. P. Jonsson, C. Dekker, and A. Aksimentiev, “Plasmonic Nanopores for Trapping , Controlling Displacement , and Sequencing of DNA,” no. 11, pp. 10598–10611, 2015.

- [36] S. W. Kowalczyk, D. B. Wells, A. Aksimentiev, and C. Dekker, “Slowing down DNA translocation through a nanopore in lithium chloride . Slowing down DNA translocation through a nanopore in lithium chloride,” *Nano Lett.*, pp. 1–5, 2012.
- [37] S. Pud *et al.*, “Mechanical Trapping of DNA in a Double-Nanopore System,” *Nano Lett.*, vol. 16, no. 12, pp. 8021–8028, 2016.
- [38] C. Plesa, N. Van Loo, P. Ketterer, H. Dietz, and C. Dekker, “Velocity of DNA during translocation through a solid-state nanopore,” *Nano Lett.*, vol. 15, no. 1, pp. 732–737, 2015.
- [39] M. Wanunu, J. Sutin, B. McNally, A. Chow, and A. Meller, “DNA translocation governed by interactions with solid-state nanopores,” *Biophys. J.*, vol. 95, no. 10, pp. 4716–25, 2008.
- [40] M. Wanunu, W. Morrison, Y. Rabin, A. Y. Grosberg, and A. Meller, “Electrostatic focusing of unlabelled DNA into nanoscale pores using a salt gradient,” *Nat. Nanotechnol.*, vol. 5, no. 2, pp. 160–5, 2010.
- [41] C. Plesa, N. van Loo, and C. Dekker, “DNA nanopore translocation in glutamate solutions,” *Nanoscale*, vol. 7, no. 32, pp. 13605–9, 2015.
- [42] G. F. Schneider *et al.*, “DNA Translocation through Graphene Nanopores,” *Nano Lett.*, vol. 10, no. 8, pp. 3163–3167, 2010.
- [43] S. Garaj, W. Hubbard, A. Reina, J. Kong, D. Branton, and J. A. Golovchenko, “Graphene as a sub-nanometer trans-electrode membrane,” *Nature*, vol. 467, no. 7312, pp. 190–193, 2010.
- [44] A. T. Kuan, B. Lu, P. Xie, T. Szalay, and J. a. Golovchenko, “Electrical pulse fabrication of graphene nanopores in electrolyte solution,” *Appl. Phys. Lett.*, vol. 106, no. May, p. 203109, 2015.
- [45] A. V Eletsksii *et al.*, “Sub-5nm graphene nanopore fabrication by nitrogen ion etching induced by a low- energy electron beam.”
- [46] Y. Deng, Q. Huang, Y. Zhao, D. Zhou, C. Ying, and D. Wang, “Precise fabrication of a 5 nm graphene nanopore with a helium ion microscope for biomolecule detection,” *Nanotechnology*, vol. 28, no. 4, p. 45302, 2017.
- [47] K. Liu, J. Feng, A. Kis, and A. Radenovic, “Atomically Thin Molybdenum Disulfide Nanopores with High Sensitivity for DNA Translocation,” *ACS Nano*, vol. 8, no. Xx, pp. 2504–2511, 2014.
- [48] G. Danda *et al.*, “Monolayer WS₂ Nanopores for DNA Translocation with Light-Adjustable Sizes,” *ACS Nano*, vol. 11, no. 2, pp. 1937–1945, 2017.
- [49] N. Alem *et al.*, “Vacancy growth and migration dynamics in atomically thin hexagonal boron nitride under electron beam irradiation,” *Phys. Status Solidi - Rapid Res. Lett.*, vol. 5, no. 8, pp. 295–297, 2011.
- [50] S. Liu *et al.*, “Boron nitride nanopores: Highly sensitive DNA single-molecule detectors,” *Adv. Mater.*, vol. 25, no. 33, pp. 4549–4554, 2013.
- [51] Z. Zhou *et al.*, “DNA translocation through hydrophilic nanopore in hexagonal boron nitride,” *Sci. Rep.*, vol. 3, p. 3287, 2013.
- [52] T. Pham *et al.*, “Formation and Dynamics of Electron-Irradiation-Induced Defects in Hexagonal Boron Nitride at Elevated Temperatures,” *Nano Lett.*, vol. 16, no. 11, pp. 7142–7147, 2016.
- [53] Y. He, M. Tsutsui, S. Ryuzaki, K. Yokota, M. Taniguchi, and T. Kawai, “Graphene/hexagonal boron nitride/graphene nanopore for electrical detection of single molecules,” *NPG Asia Mater.*,

- vol. 6, no. 6, p. e104, 2014.
- [54] R. G. Amorim, A. R. Rocha, and R. H. Scheicher, “Boosting DNA Recognition Sensitivity of Graphene Nanogaps through Nitrogen Edge Functionalization,” *J. Phys. Chem. C*, vol. 120, no. 34, pp. 19384–19388, 2016.
- [55] L.-C. Yin, H.-M. Cheng, and R. Saito, “Triangle defect states of hexagonal boron nitride atomic layer: Density functional theory calculations,” *Phys. Rev. B*, vol. 81, p. 153407, 2010.
- [56] K. Liu *et al.*, “Geometrical Effect in 2D Nanopores,” *Nano Lett.*, p. acs.nanolett.7b01091, 2017.
- [57] S. M. Gilbert *et al.*, “Fabrication of Atomically Precise Nanopores in Hexagonal Boron Nitride,” vol. 1, pp. 4–8, 2017.
- [58] K. S. Novoselov *et al.*, “Electric field effect in atomically thin carbon films,” *Science (80-.)*, vol. 306, no. 5696, pp. 666–669, 2004.
- [59] C. Raillon, P. Granjon, M. Graf, L. J. Steinbock, and A. Radenovic, “Fast and automatic processing of multi-level events in nanopore translocation experiments,” *Nanoscale*, vol. 4, no. 16, pp. 4916–24, 2012.
- [60] S. J. Heerema, G. F. Schneider, M. Rozemuller, L. Vicarelli, H. W. Zandbergen, and C. Dekker, “1/F Noise in Graphene Nanopores,” *Nanotechnology*, vol. 26, no. 7, p. 74001, 2015.
- [61] N. C. Pagratis, “Rapid preparation of single stranded DNA from PCR products by streptavidin induced electrophoretic mobility shift,” *Nucleic Acids Res.*, vol. 24, no. 18, pp. 3645–3646, 1996.